HAL
open science

Frittage, cofrittage et maîtrise des microstructures de matériaux à base d'oxydes : zircone, alumine, spinelle, alumine-zircone, spinelle-alumine

Emre Yalamac

To cite this version:

Emre Yalamac. Frittage, cofrittage et maîtrise des microstructures de matériaux à base d'oxydes : zircone, alumine, spinelle, alumine-zircone, spinelle-alumine. Mécanique [physics.med-ph]. Institut National Polytechnique de Grenoble - INPG, 2010. Français. NNT : . tel-00521852

HAL Id: tel-00521852

https://theses.hal.science/tel-00521852v1

Submitted on 28 Sep 2010

HAL is a multi-disciplinary open access archive for the deposit and dissemination of scientific research documents, whether they are published or not. The documents may come from teaching and research institutions in France or abroad, or from public or private research centers.

L'archive ouverte pluridisciplinaire **HAL**, est destinée au dépôt et à la diffusion de documents scientifiques de niveau recherche, publiés ou non, émanant des établissements d'enseignement et de recherche français ou étrangers, des laboratoires publics ou privés.

N° attribué par la bibliothèque
|__|__|__|__|__|__|__|__|__|__|

THESE EN COTUTELLE INTERNATIONALE

pour obtenir le grade de

DOCTEUR DE l'Université de Grenoble (FR)
et
de l'IZMIR INSTITUTE of TECHNOLOGY (TR)

Spécialité : "Matériaux, Mécanique, Génie Civil, Electrochimie"

préparée au laboratoire "Science et Ingénierie des Matériaux et Procédés"
(SIMaP – UMR 5266) dans le cadre de l'Ecole Doctorale :
"Ingénierie – Matériaux, Mécanique, Energétique, Environnement, Procédés, Production"
(I – MEP2 N° 510)
et
au "Department of Mechanical Engineering"
dans le cadre de "The Graduate School of Science and Engineering,
Mechanical Engineering Department"

présentée et soutenue publiquement par

Emre YALAMAÇ

11 juin 2010

TITRE

Sintering, Co-sintering and Microstructure Control of Oxide based Materials : Zirconia, Alumina, Spinel, Alumina-Zirconia and Spinel-Alumina

Frittage, cofrittage et maîtrise des microstructures de matériaux à base d'oxydes : zircone, alumine, spinelle, alumine-zircone, spinelle-alumine

DIRECTEURS de THESE

Prof. Claude Paul CARRY (FR) & Prof. Sedat AKKURT (TR)

JURY

Prof. Muhsin CIFTCIOGLU, Président (TR)
Dr. Guillaume BERNARD-GRANGER, Rapporteur (FR)
Prof. Zafer EVIS, Rapporteur (TR)
Prof. Claude Paul CARRY, Directeur de thèse (FR)
Prof. Sedat AKKURT, Directeur de thèse (TR)

ACKNOWLEDGEMENTS

This thesis is a co-tutelle PhD thesis, therefore I studied in two universities: Université de Grenoble in France and Izmir Institute of Technology in Turkey. The laboratory in the former was "Science and Engineering of Materials and Processes (SIMaP)" and Mechanical Engineering Department in the latter.

I deeply thank my advisors, Prof.Dr. Sedat Akkurt and Prof.Dr. Claude Paul Carry, whose motivation, advice and supervision were invaluable through this dissertation.

Special thanks are also due to Prof.Dr. Michel Duclot for his support and encouragement.

I would like to thank the IYTE-MAM research center staff; Duygu Oğuz and Gökhan Erdoğan for their help in SEM, Mine Bahçeci for her AFM analysis and Evrim Yakut for her help in sedigraph analysis.

I would like to acknowledge Prof. Dr. Muhsin Çiftçioğlu for his appreciable contribution on this thesis, especially his fruitful discussions on the powder and microstructure characterization techniques. I would like to also thank to Berna Topuz for her help in sedigraph analysis.

I am indebted to many of my colleagues to support me and for the moments that we shared together Levent Aydın, Bahar Bozkurt Baştürk, Meral Budak, Elif Aras Gültürk, Nurdan Yıldırım Özcan, Abdullah Tuğrul Seyhan, F. Erinç Sezgin, Mücahit Sütçü, Uğur Türkan, and Sinan Yüksel (in alphabetical order!).

I acknowledge the financial support of French Ministry of Foreign Affairs.

I am also thankful to CMTC-Grenoble research center staffs. Dr.Frédéric Charlot, Dr.Francine Roussel-Dherbey and Mme.Graziella Kavaklian, for assisting me in performing SEM. I would like to appreciate M. Stéphane Coindeau for his help in XRD analysis. I owe my deepest gratitude to Dr. Florence Robaut for her help in WDS and EBSD analysis.

Je remercie Mme. Nathalie Lombardo et M. Alain Domèyne et aussi le groupe PMD (Processus en Milieux Divisés), sans qui certains de mes travaux auraient été impossibles.

Je remercie mes amis et collègues; Valérie Bounhoure, Sylvain Charmond, Coraline Crozet, Céline Dargons, Grégory Largiller, Malika Perrier, Jean-Joel Raharijaona, Aurélie Thomazic, and Oussama Yousfi (par ordre alphabétique) avec qui j'ai partagé de bons moments, que ce soit à ski, à la montagne ou les repas et les soirées passés ensemble.

Je remercie aussi tout ceux qui m'ont accueilli en France et m'ont appris le français...☺

I would like to acknowledge my sweetheart, Behiye Sezmen for her incredible patience, selfless love and emotional support during this thesis.

This thesis would not have been possible without the support and encouragement of my parents "Sevim YALAMAÇ and Ahmet YALAMAÇ", my brother Arda, his wife Emel and my sister Jülide, throughout the years.

TABLE OF CONTENTS

CHAPTER 1. INTRODUCTION 1
1.1. General background 2
1.2. Objectives 4
1.3. Dissertation Outline. 5

CHAPTER 2. BACKGROUND INFORMATIONS FROM THE LITERATURE 7
2.1. Fundamental Concepts in Sintering of Ceramics 7
2.1.1. Solid-State Sintering and Viscous Sintering 8
2.1.2. Driving Forces for Sintering 9
2.1.3. Sintering with Chemical Reaction: Reaction Sintering 9
2.1.4. Stages of Sintering 11
2.1.4.1. The Initial Stage of Sintering 13
2.1.4.2. The Second or Intermediate Stage of Sintering 13
2.1.4.3. The Final Stage of Sintering 14
2.1.4.4. Grain Growth Kinetics 15
2.2. Point Defect Chemistry 16
2.3. Solid Solution Elements 18
2.4. Importance and Measurement of Sintering Parameters 19
2.4.1. Densification Rate 19
2.4.2. Apparent Activation Energy 20
2.4.2.1. Arrhenius Plots and Q Calculation 21
2.4.2.2. Master Sintering Curve (MSC) 23
2.5. Bi-materials 27
2.5.1. Metal-Metal Bi-materials 28
2.5.2. Oxide-Oxide Bi-materials 30
2.5.3. Metal-Oxide Bi-materials 31
2.6. Diffusion Couples and the Kirkendall Effect 32

CHAPTER 3. SINTERING AND DENSIFICATION BEHAVIOUR OF MONOMATERIALS: ZIRCONIA AND ALUMINA 35
3.1. Introduction 36

3.2. Powder Properties 39
3.3. Thermal Behavior of the Powders 42
3.4. Preparation of the Samples 43
3.5. Characterization of the Green Compacts 43
3.6. Sintering 46
3.7. Density Measurements 46
3.8. Microstructural Characterization 46
3.9. Shrinkage, Shrinkage Rate, Densification and Densification Rate Curves 47
3.10. Results 50
3.10.1. Effect of Dilatometer and Atmosphere 51
3.10.2. Alumina Powders 51
3.10.3. Zirconia Powders 54
3.10.4. Effect of Compaction Process and Pressure on Fired Density 56
3.10.5. Determination of Apparent Activation Energies for Densification 58
3.11. Conclusions 63

CHAPTER 4. SINTERING BEHAVIOR OF A MAGNESIUM ALUMINATE SPINEL POWDER 65
4.1. Introduction 67
4.2. Powder and Experimental Procedure 72
4.2.1. Powder 72
4.2.2. Microstructural Characterizations 74
4.3. Results and Discussion 79
4.3.1. Densification Behavior of the Powder Compacts 79
4.3.2. Grain Growth Kinetics of Spinel 80
4.3.3. Apparent Activation Energies for Spinel Densification 84
4.3.3.1. Arrhenius Plots for Calculation of Activation Energies (Qd) ... 84
4.3.3.2. Calculation of Activation Energy (Qd) with Master Sintering Curve 85
4.3.3.3. Assesment and Discussion on Apparent Activation Energy of Spinel Densification 87
4.3.4. Coarsening Pre-treatment of Spinel Compacts 88

4.3.5. Two-Step Sintering of Spinel 95
4.4. Conclusions 98

CHAPTER 5. CO-PRESSING, CO-SINTERING AND CHARACTERIZATION OF BI-MATERIALS 101
5.1. Introduction 102
5.2. Experimental Procedure 104
5.2.1. Bi-material Combinations 104
5.2.2. Co-Pressing Techniques of Bi-materials 105
5.2.2.1. Co-Pressing with Single-action Mode of Uniaxial Pressing 105
5.2.2.2. Uniaxial Co-Pressing with Floating Die (Co-UPFlo) 105
5.2.2.3. Co-Pressing with Cold Isostatic Pressing after Uniaxial or Floating Die Mode of Pressing (Co-UP or UPFlo+ CIP) 107
5.2.3. Co-Sintering 107
5.3. Results 108
5.3.1. Comparison of the Densification Behaviors of Mono-Materials 108
5.3.2. Calculation and Analysis of Strain and Strain Rate Mismatches 108
5.3.3. Results of Sintering of Bi-materials 113
5.3.4. Observation of Bonding of the Bi-materials 114
5.3.5. SEM images of Bi-materials 117
5.3.5.1. Alumina – Zirconia 117
5.3.5.2. Alumina – Spinel 120
5.4. Conclusions 124

CHAPTER 6. MICROSTRUCTURAL DEVELOPMENT OF INTERFACE LAYERS BETWEEN CO-SINTERED ALUMINA AND SPINEL COMPACTS 125
6.1. Introduction 126
6.2. Experimental Procedure 129
6.3. Results 131
6.3.1. Co-sintering at High Temperature (1500°C) of Green Compacts 131
6.3.2. Initial Stage of Co-sintering of Bi-material at Low Temperature 140

6.3.3. Co-sintering of Compacts by Two Isothermal Steps Sintering..... 141
6.3.4. Diffusion Couple Tests 145
6.4. General Interpretation and Discussion 155
6.5. Conclusions 158

CHAPTER 7. CONCLUSIONS 161
7.1. Summary and Conclusions 161
7.2. Future Work 163

REFERENCES 165

TABLE DES MATIERES

CHAPITRE 1. Introduction.....1
1.1. Contexte général.....2
1.2. Objectifs.....4
1.3. Aperçu general de la thèse.....5

CHAPITRE 2. Aperçu de l'état de l'art : extraits de la littérature.....7
2.1. Concepts de base du frittage des céramiques.....7
2.1.1. Frittage en phase solide et frittage visqueux.....8
2.1.2. Forces motrices de frittage.....9
2.1.3. Frittage avec réaction chimique : frittage réactif.....9
2.1.4. Stades de frittage.....11
2.1.4.1. Le stage initial du frittage.....13
2.1.4.2. Le second stade ou intermédiaire du frittage.....13
2.1.4.3. Le stade final du frittage.....14
2.1.4.4. Cinétiques de croissance granulaire.....15
2.2. Chimie des défauts ponctuels.....16
2.3. Eléments en solution solide.....18
2.4. Importance et mesure des parameters de frittage.....19
2.4.1. Vitesse de densification.....19
2.4.2. Energies d'activation apparentes.....20
2.4.2.1. Diagrammes d'Arrhenius et détermination d'énergie d'activation.....21
2.4.2.2. Courbe de frittage de référence.....23
2.5. Bi-matériaux.....28
2.5.1. Bi-matériaux metal-métal.....28
2.5.2. Bi-matériaux oxyde-oxyde.....30
2.5.3. Bi-matériaux métal-oxyde.....31
2.6. Couples de diffusion et effet Kirkendall.....32

CHAPITRE 3. Comportements en frittage et en densification de monomatériaux : zircones et alumines 35
3.1. Introduction 36
3.2. Propriétés des poudres 39
3.3. Comportement thermique des poudres 42
3.4. Préparation des échantillons 43
3.5. Caractérisation des corps crus 43
3.6. Frittage 46
3.7. Mesures de densités 46
3.8. Caractérisation des microstructures 46
3.9. Courbes de retrait, de vitesse de retrait, de densification et de vitesse de densification 47
3.10. Résultats 50
3.10.1. Effets du dialtomètre et de l'atmosphère 51
3.10.2. Poudres d'alumine 51
3.10.3. Poudres de zircone 54
3.10.4. Effet du mode et de la pression de compactage sur la densité frittée 56
3.10.5. Détermination des energies d'activation apparentes de la densification 58
3.11. Conclusions 63
CHAPITRE 4. Comportement en frittage d'une poudre de spinelle aluminate de magnésium 65
4.1. Introduction 67
4.2. Poudre et procedure expérimentale 72
4.2.1. Poudre 72
4.2.2. Caractérisations microstructurales 74
4.3. Résultats et discussion 79
4.3.1. Comportement en densification des comprimés de poudre 79
4.3.2. Cinétiques de croissance granulaire des matériaux spinelle 80
4.3.3. Energies d'activation apparentes de la densification de la spinelle 84
4.3.3.1. Diagrammes d'Arrhenius pour la détermination d'énergies d'activation (Qd) 84

4.3.3.2. Détermination d'énergie d'activation (Qd) à partir d'une courbe de frittage de référence *85*
4.3.3.3. Bilan et discussion sur les énergies d'activation apparentes de la densification de la spinelle *87*
4.3.4. Prétraitement de coalescence de comprimés de spinelle *88*
4.3.5. Frittage en deux étapes de comprimés de spinelle *95*
4.4. Conclusions *98*

CHAPITRE 5. Co-pressage, co-frittage Caractérisation de bi-matériaux *101*
5.1. Introduction *102*
5.2. Procédure expérimentale *104*
5.2.1. Combinaisons de bi-matériaux *104*
5.2.2. Techniques de co-pressage des bi-matériaux *105*
5.2.2.1. Co-pressage uniaxial en mode simple action *105*
5.2.2.2. Co-pressage uniaxial en matrice frlottante *105*
5.2.2.3. Co-pressage uniaxial en matrice flrottante suivi d'un pressage isostatique à froid *107*
5.2.3. Co-frittage *107*
5.3. Résultats *108*
5.3.1. Comparaison des conportements en densification des différents monomatériaux *108*
5.3.2. Calcul et analyse des écarts de deformation et de vitesse de déformation *108*
5.3.3. Résultats de frittage de bi-matériaux *113*
5.3.4. Observation de la liaison des bi-matériaux *114*
5.3.5. Micrographies MEB de bi-matériaux *117*
5.3.5.1. Alumine – zircone *117*
5.3.5.2. Alumine – spinelle *120*
5.4. Conclusions *124*

CHAPITRE 6. Développement et microstructures de couches d'interface entre des comprimés cofrittés d'alumine et de spinelle *125*
6.1. Introduction *126*
6.2. Procédure expérimentale *129*

6.3. Résultats *131*
6.3.1. Cofrittages à haute temperature (1500°C) de comprimés copressés *131*
6.3.2. Stade initial du co-frittage de bi-matériaux à basse température *140*
6.3.3. Co-frittage de comprimés en 2 étapes isothermes *141*
6.3.4. Essais de couple de diffusion *145*
6.4. Interprétation et discussion générales *155*
6.5. Conclusions *158*

CHAPITRE 7. Conclusions *161*
7.1. Sommaire et conclusions *161*
7.2. Travaux futurs *163*

Références *165*

CHAPTER 1

INTRODUCTION

Résumé

Cette introduction décrit dans un premier temps le contexte général dans lequel s'inscrit cette thèse. Les applications des céramiques techniques sont en constante progression grâce à la plus grande maîtrise de leurs propriétés et de leurs procédés de fabrication depuis les poudres, leurs frittages jusqu'à leurs microstructures. Les bi-matériaux céramiques permettent d'envisager des combinaisons de propriétés prometteuses sous réserve de maîtriser leurs élaborations par frittage.

Les objectifs de cette thèse sont :

- *l'étude et la caractérisation du comportement en frittage des poudres commerciales d'alumine, de zircone et de spinelle utilisées pour le co-frittage des bi-matériaux*
- *l'étude de la liaison et de la morphologie de l'interface de différentes combinaisons de bi-matériaux oxydes avec une attention particulière quant au procédé de co-compaction des poudres*
- *l'étude du développement de la microstructure à l'interface Alumine-Spinelle de bi-matériaux co-pressés et co-frittés en incluant les cinétiques de croissance de l'intercouche.*

L'aperçu général de la thèse présente la structure de ce mémoire en sept chapitres (y compris un chapitre d'introduction et un chapitre de conclusion générale. Le chapitre 2 présente l'état de l'art des différentes parties de cette thèse. Le chapitre 3 concerne le comportement en frittage des mono matériaux alumines et zircone. Le chapitre 4 est consacré au frittage et à la maîtrise de la microstructure de la spinelle $MgAl_2O_4$. Le chapitre 5 traite du co-frittage de différentes combinaisons d'oxydes et de l'effet du procédé de compaction sur la tenue et la morphologie de l'interface. Le chapitre 6 se focalise sur le développement de la couche d'interface dans les bi-matériaux Spinelle – Alumine.

1.1. General Background

Contexte général

Ceramics are inorganic, nonmetallic and man-made materials that are most generally known for their brittleness, hardness, chemical and thermal stability. Majority of ceramics are oxides while new ceramics are also made from synthetically derived materials of nonoxides like Si_3N_4, SiC, etc. The applications for these materials are diverse, from bricks, tiles, refractories, glasses, whitewares, biomaterials to electronic, optical and magnetic components. These applications use the wide range of properties exhibited by ceramics. Advanced ceramics are referred to as “special”, “technical”, or “engineering” ceramics. They exhibit superior mechanical properties, corrosion/oxidation resistance, or electrical, optical, and/or magnetic properties. They form the second largest sector (17%) of the ceramic industry after the glass industry (55%). Although glass dominates the global ceramics market, the most significant growth is in advanced ceramics (Carter and Norton 2007). This sector requires high purity raw materials with known sintering and densification behavior for reliable manufacture of components. Most ceramics cannot be produced by melting and casting into a mold due to prohibitively high melting temperatures as much as 2500°C. Therefore sintering of fine powder compact is utilized to produce the desired products with or without partial melting. Sintering is a process by which fine powder particles are bonded upon elevated temperature thermal treatment to produce a dense solid material. To reduce the cost of manufacture reasonably low sintering temperatures are needed. This is provided by the high surface area and low particle size of the starting powder. Consequently, there is a demand in the advanced ceramics industry for submicron grained, high purity powder. Examples for such powders are alumina, zirconia, spinel, titania and others supplied by various manufacturers (Aloca 2010, Baikowski 2010, Sumitomo Chemical 2010, Tosoh 2010). Ceramic products made from alumina (Al_2O_3), zirconia (ZrO_2) and spinel are widely used in various areas like biomaterials, armor, filter for metal casting, fluorescent lighting, spark plugs, oxygen sensors, laser components, fuel cells and so on. Alumina, for example, is used mainly for its high hardness and stiffness that require abrasion resistance. Zirconia is generally used for its desirable chemical and mechanical properties. Optical properties of spinel like its transparency to infrared radiation make them desirable materials.

Bi-materials have attracted attention due to favorable combination of properties that are offered by such geometries. They have functional properties, depending on mechanical, electrical and magnetic properties of their components. Their application areas are ranging from electronic packaging applications such as multi-layer ceramic capacitors to thin film-substrate systems used widely in the microelectronics industry (Boonyongmaneerat and Schuh 2006, Cai, et al. 1997a). A strong bond between two densely fired oxide ceramics can provide a substrate material over which another oxide ceramic layer with the desired properties is present. Examples for potential systems that can be studied are alumina, yttria-stabilized tetragonal zirconia (Y_2O_3-doped ZrO_2), and magnesium aluminate spinel ($MgAl_2O_4$). Similar bi-material systems were previously studied for metal-metal systems with magnetic metal on one end and non-magnetic metal on the other so that desired properties are exploited from the co-sintered composites (Simchi, et al. 2006a). But, developing the compatible combinations of materials (e.g., matching coefficients of thermal expansion) and understanding the interfaces and reducing the processing cost are the three important issues that must be carefully considered (Carter and Norton 2007).

Each combination of two of the above listed oxide ceramics has different set of chemical and physical properties. Spinel shows high resistance to attack by most of the acids and alkalis and has low electrical losses. Due to these desirable properties, it has a wide range of applications in structural, chemical, optical and electrical industry. It is used as a refractory lining in steel-making furnaces, transition and burning zones of cement rotary kilns (Bartha and Klischat 1999). In addition to these, much of the research has been motivated by the need to obtain transparent spinel ceramics (Li, et al. 2000, Meir, et al. 2009). Spinel has provided considerable challenges for reliable transparent ceramic applications. But there is still some disagreement in the literature on the densification behavior of spinel (Reimanis and Kleebe 2009). Yttria-stabilized tetragonal zirconia has proved to be an important structural ceramic with excellent mechanical properties, such as high fracture toughness, strength, hardness, and has been commercialized for products of the optical fiber connector, grinding media, and precision parts (Matsui 2007a). Although, sintering and densification behavior of these individual ceramic oxides have been studied to some extent, there is still a need for further study of the behavior of bi-materials that are sintered in contact. Two oxides can be bonded by bringing them into contact by tape casting or by dry pressing before co-sintering at elevated temperatures. The former, for example, was done by Cai et al.,

(1997a, 1997b) on multilayered alumina/zirconia laminates. Few studies are found in the literature on the latter. Especially the co-sintered bi-material composed of alumina and spinel has not been studied in the literature. Some studies are found on formation of spinel in-situ by reaction of MgO and Al_2O_3 at high temperatures in different atmospheres. But the samples in these studies were not co-sintered bi-materials but were rather diffusion couples. Hence, there is a necessity to well describe the sintering and densification behavior of bi-materials that are co-pressed and co-sintered. Dilatometric measurements, diffusion couple tests and microstructural analysis of the interface will shed light on the degree and quality of connection between the two ceramics. Other features like chemical distribution of elements in the interface area, adhesion mechanisms, analysis of new in-situ phase(s) formation and characterization of crack and crack like formations at the interface or components of the bi-materials will help understand the potential in these materials.

1.2. Objectives

Objectifs

The main objectives of this thesis are

- To study and characterize the sintering and densification behaviors of mono-materials of alumina, spinel and zirconia based on the commercial powders used to co-press and co-sinter the oxide bi-materials. This sintering aspect includes :
    - the activation energies for densification of the ceramics.
    - the influence of different compaction methods of the three sintered ceramics.
    - precoarsening treatments and two step sintering of spinel ceramics.
- To study the bonding ability and the interface morphology of different co-sintered bi-materials: alumina – zirconia and alumina – spinel including the effects of compaction process.
- To investigate the microstructural development at the interface between the end-members of alumina – spinel co-sintered bi-materials including the interlayer growth kinetics.

1.3. Dissertation Outline

Aperçu general de la thèse

In this thesis, sintering, densification and microstructural behavior of different powders were investigated either alone or in contact with another powder. The powders were zirconia, alumina and spinel which were all commercial products of relatively high purity. Because of the large volume of information in the thesis and the difficulty of presentation in a concise form, the thesis is subdivided into several chapters. In the second chapter background information from the literature is provided to help the reader to follow the rest of the dissertation easier. In the third chapter, sintering and densification behavior of mono-materials of alumina and zirconia are presented. In the fourth chapter, sintering and densification behavior of mono-material of spinel are given. The results of sintering experiments on spinel were too voluminous to be included in the third chapter. The purpose for separately studying the mono-materials of spinel, zirconia and alumina in chapter three and four was to first understand the sintering behavior of these mono-materials and to use this information to better investigate the bi-materials in the following chapters. Fifth chapter provides results of experiments on co-pressed and co-sintered bi-materials of alumina – spinel and alumina – zirconia. Sixth chapter includes a detailed presentation of the microstructure of co-pressed bi-materials spinel – alumina as well as corresponding diffusion couple tests. Finally in chapter seven a conclusion of the thesis is given along with suggestions for future work.

CHAPTER 2

BACKGROUND INFORMATIONS FROM THE LITERATURE

Aperçu de l'état de l'art : extraits de la littérature

Résumé

En se basant sur des extraits de la littérature ce chapitre rappelle les concepts de base du frittage des matériaux céramiques et présente les approches théoriques et expérimentales qui seront utilisées par la suite pour l'étude du frittage et de l'évolution microstructurale des matériaux et des bimatériaux à base d'oxydes.

In this chapter introductory information on sintering of ceramics, its theory, basic measurements for activation energies and bi-materials is given to help the reader to follow the thesis more easily.

2.1. Fundamental Concepts in Sintering of Ceramics

Concepts de base du frittage des céramiques

The sintering process plays a prominent role in the fabrication of ceramics. Almost all ceramic bodies must be fired at elevated temperatures to produce a microstructure with the desired properties. This widespread use of the sintering process has led to a variety of approaches to the subject. In practice, the ceramist, wishing to prepare a material with a particular set of properties, identifies the required microstructure. The objective of sintering studies should therefore be to understand how the processing variables influence the microstructural evolution during sintering. In this way, useful information can be provided for the practical effort of designing processing conditions for the production of the required microstructure (De Jonghe and Rahaman 2003).

2.1.1. Solid-State Sintering and Viscous Sintering

Frittage en phase solide et frittage visqueux

Although several fabrication routes are available for the production of ceramics with high density or a controlled grain size such as colloidal processing, pressure sintering, and the use of additives that are incorporated into solid solution or form a discrete second phase, e.g., liquid-phase sintering (Rahaman 1995), these fabrication routes can be uneconomical for many applications or can be difficult to apply successfully (e.g., choice of additives). Simple, economical routes to microstructural improvement are worthy of investigation (Lin, et al. 1997).

Solid-state sintering is one of the sintering mechanisms which is mainly concerned with changes in porosity, that is, the changes taking place during the transformation of an originally porous compact to a strong, dense ceramic (Kingery, et al. 1976).

The analysis of viscous sintering appears relatively simple in principle. Matter transport occurs by a viscous flow mechanism. The path along which matter flows is not specified explicitly. Instead, it is implicitly assumed to be the shortest path. The equations for matter transport are derived on the basis of an energy balance. The models that have been developed to approximate the complex geometry of the real powder system yield satisfactory results. Compared with viscous sintering, the sintering phenomena in polycrystalline materials are considerably more complex because of the crystalline nature of the grains and the presence of grain boundaries.

A few different approaches have been used to analyze the densification process. The analytical models have received the greatest attention and provided the basis for the present understanding of sintering. The microstructure of the powder system is approximated by a relatively simple geometrical model, and analytical expressions are derived for the sintering rate as a function of the primary variables such as powder particle size, sintering temperature, and applied pressure. The scaling laws do not assume a specified geometrical model; instead they predict a general way on the dependence of the sintering rate on the change of scale (i.e., particle size) of the powder system. Other approaches are potentially useful but have not achieved the popularity of the analytical models. These approaches include the use of numerical simulations, topological models, and statistical models. Phenomenological equations and sintering

maps attempt to represent sintering data in terms of equations or diagrams but provide very little insight into the process.

2.1.2. Driving Forces for Sintering

Forces motrices de frittage

Sintering of a compact is accompanied by lowering the free energy of the system due to the elimination of internal surface area. Solid-vapor interfaces are replaced by lower energy solid-solid or solid-liquid interfaces (Kingery, et al. 1976). There are three possible driving forces to reduce the energy of the system;

a) Surface Curvature: In the absence of an external stress and a chemical reaction, surface curvature provides the driving force for sintering.

b) Applied Pressure: In the absence of a chemical reaction, an externally applied pressure normally provides the major contribution to the driving force when the pressure is applied over a significant part of the heating process (e.g., in hot pressing, hot isostatic pressing or sinterforging). Surface curvature also contributes to the driving force, but for most practical situations its contribution is normally much smaller than that provided by the external pressure.

c) Chemical Reaction: it may also provide a driving force for sintering. The decrease in energy accompanying a chemical reaction is generally much greater than the driving force provided by an applied stress or is significantly greater than that provided by the surface curvature.

2.1.3. Sintering with Chemical Reaction: Reaction Sintering

Frittage avec réaction chimique : frittage réactif

Reaction sintering, sometimes referred to as *reactive sintering*, is a particular type of sintering process in which the chemical reaction of the starting materials and the densification of the powder compact are both achieved during a single firing process. There are two main classes depending on whether single-phase solids or composites are produced (De Jonghe and Rahaman 2003).

For a powder compact consisting of a mixture of two reactant powders, the simplest example of reaction sintering is shown in Equation (2.1) (Rahaman and Jonghe

1993) and Figure 2.1. During sintering, reaction between the two starting powders A (e.g., ZnO) and B (e.g., Fe_2O_3) and densification occurs to produce a polycrystalline, *single-phase* solid C (e.g., $ZnFe_2O_4$):

$$ZnO + Fe_2O_3 \rightarrow ZnFe_2O_4 \tag{2.1}$$

In the second class, during reaction between two starting powders, densification occurs to produce a *composite* solid consisting of two phases because the reaction sintering system is obtained when one of the product phases, is a liquid. This occurs when the sintering temperature is above an eutectic temperature and corresponds to the process of *liquid phase sintering*. Here, the discussion of reaction sintering was confined mainly to systems in which the products are solids at the sintering temperature.

The energy changes for chemical reaction are much larger than those for surface area changes, and it would be very desirable if the free energy of the reaction could be used to drive the densification process. Unfortunately, there is no evidence that the energy of the reaction can act directly as a driving force for densification. Reaction sintering has the benefit of eliminating the pre-reaction (or calcination) step in the formation of solids with complex composition (De Jonghe and Rahaman 2003).

In practice, reaction sintering has several shortcomings, so the process finds little use in the production of single-phase solids. As outlined earlier, the reactions involve energy changes that are considerably larger than the changes in surface energies, and as a result, they can lead to coarse microstructures that inhibit densification. Other shortcomings include the risk of chemically inhomogeneous products due to incomplete reaction and difficulties in controlling the microstructure as a result of the added complexity introduced by the reaction.

Qualitatively, it is convenient to consider the reaction and the densification as two separate processes, and put forth a conceptual diagram that illustrates some issues. Such diagrams have been proposed by Yangyun and Brook (1985) as shown in Figure 2.2. These conceptual arguments lead to the conclusion that the best process is one where densification is completed before reaction can interfere, assuming that there are no deleterious molar volume differences between products and reactants.

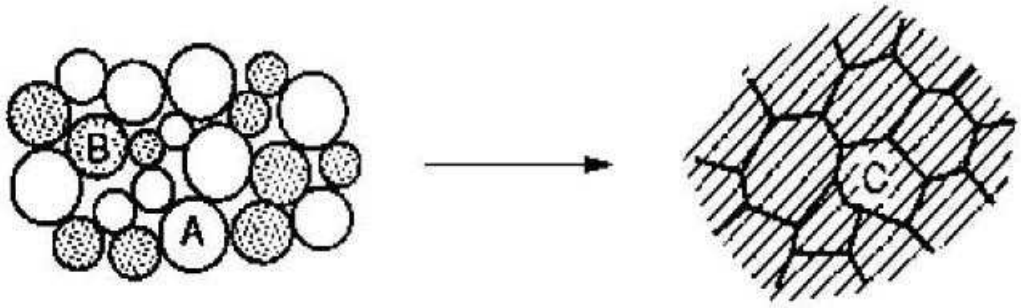

Figure 2.1. Schematic diagram illustrating the production of, a single-phase solid, C, by reaction sintering of a compacted mixture of two powders, A and B (Source: Yangyun and Brook 1985).

Schéma montrant l'élaboration d'un solid monophasé C par frittage réactif d'un comprimé de mélange de deux poudres A et B (Yangyun and Brook 1985).

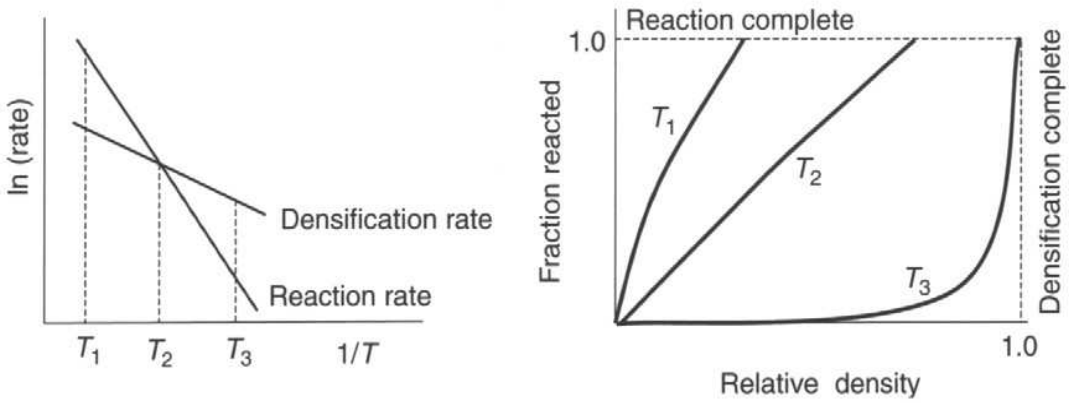

Figure 2.2. Schematic relationship between densification rate and reaction rate as a function of temperature T, and the resulting process trajectory. If the reaction rate is fast compared to densification, complete reaction can occur with limited densification (Source: Yangyun and Brook 1985).

Schéma de situation relative des vitesses de densification et et des vitesses de réaction en fonction de la température et leurs trajectoires respectives en fonction de la densité relaive. Si la vitesse de réaction est rapide vis à vis de celle de densification, la réaction peut être complète avec une densification limitée (de Yangyun and Brook 1985).

2.1.4. Stages of Sintering

Stades de frittage

In crystalline solids, matter is transported predominantly by diffusion of atoms, ions, or other charged species. Matter transport during sintering can occur by at least six

different paths that define the mechanisms of sintering. Some mechanisms (referred to as densifying mechanisms) lead to densification of the powder system, whereas others (nondensifying mechanisms) do not. In practice, more than one mechanism operates during any given sintering regime. All of the mechanisms lead to growth of the necks between the particles and so influence the densification rate. In Figure 2.3, six different mechanisms of sintering in polycrystalline materials are shown. As mentioned above, the growth of the necks take place by each mechanism. Only certain mechanisms, however, lead to shrinkage and densification. In these, matter is removed from grain boundaries (mechanisms 4 and 5) or from dislocations within the neck region (mechanism 6). In different publications, the mechanism 5 is called either lattice diffusion or volume diffusion. The mechanisms 1-3 do not cause densification. These nondensifying mechanisms however cannot be ignored. Because they reduce the curvature of the neck surface (i.e., the driving force for sintering) and so reduce the rate of the densifying mechanisms.

At high temperatures, densification can proceed by power-law creep or direct diffusional transport of material. Diffusional mechanisms tend to be favored at low pressures and in fine-grained materials, particularly in ceramic systems. Classical grain-boundary diffusion mechanism assumes that grain boundaries act as perfect sources and sinks for the diffusing atoms during the diffusion process and the energy provided is all available to drive the diffusional flux along the grain boundaries. In practice, however, some energy is expended for materials to be added to, or removed from, a grain boundary, i.e. an interface reaction occurs (He and Ma 2003a). The concept of interface reaction controlled sintering is not particularly new, and aspects of this idea have been developed by Ashby (1969) and Burton (1972). Experimental studies by He and Ma (2003b, 2005) have also shown the importance of interface reaction during the sintering of fine-grained ceramics. If the process of interface reaction is taken into account, the rate of densification can then be controlled either by the rate of diffusional transport between the sources and sinks, or the rate at which the sources and sinks can provide, or accept, material for the diffusional process, whichever is slower (He and Ma 2003a).

In order to accomplish theoretical analysis and quantitative modeling of sintering process, analytical models were developed. According to Coble (1962a), solid state sintering can be divided into three stages. A stage represents an interval of time or density over which the microstructure is considered to be reasonably well defined.

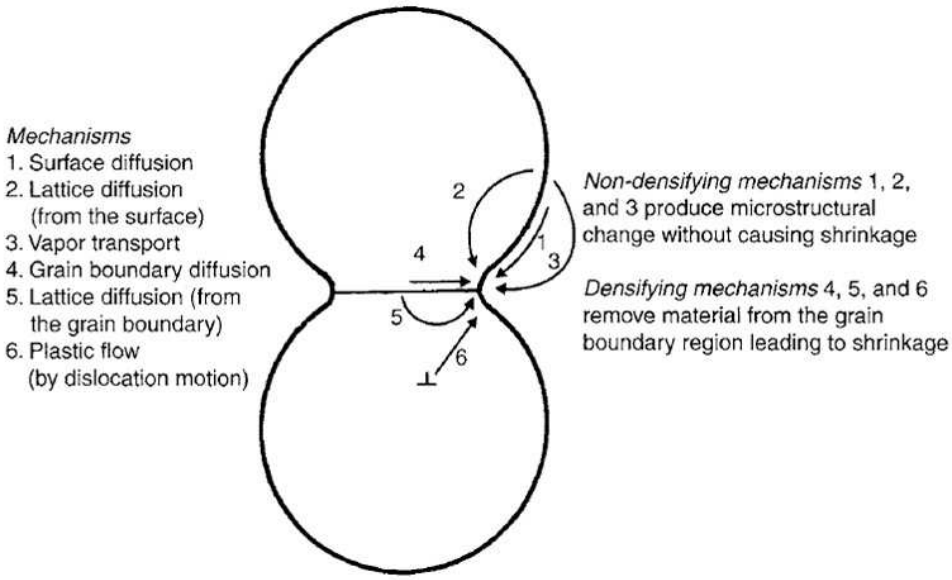

Figure 2.3. Six different mechanisms of sintering in polycrystalline materials (Source: De Jonghe and Rahaman 2003).

Six différents mecanismes de frittage dans matériau polycristallin (de De Jonghe and Rahaman 2003).

2.1.4.1. The Initial Stage of Sintering

Le stage initial du frittage

Some neck growth takes place between primary particles by diffusion, vapor transport and plastic flow. The contact area between the particles increases from zero (ideally point contact) to a value of ~0.4-0.5 of the particle radius. The large initial differences in surface curvature are removed and 3-5 % of linear shrinkage takes place in this stage, thus yielding an increase to roughly 0.65 of the theoretical density. The initial stage of sintering, as indicated by Coble, involves no grain growth.

2.1.4.2. The Second or Intermediate Stage of Sintering

Le second stade ou intermédiaire du frittage

It starts when grain boundaries are well formed. During this stage of sintering, grain boundaries form extensively but pores are still connected with each other and form a continuous pore network, i.e., pore channels exist, while the grain boundaries are still isolated and no continuous grain boundary networks are formed. Most densification

and microstructure changes take place in this stage of sintering. As pores become isolated and grain boundaries form a continuous network, the intermediate stage of sintering ends when a density of ~0.9 of the theoretical density and the third or final stage of sintering starts.

2.1.4.3. The Final Stage of Sintering

Le stade final du frittage

Isolated pores are located at grain boundaries (interfaces), or linear junctures of three grains or point junctures of four grains, and/or entrapped in grains. Density increases slightly but the microstructure develops (grains grow) very rapidly in this stage of sintering.

In order to obtain ceramics with pore-free, fine-grain structures by stress-free sintering, densification and grain growth phenomenon should be controlled. Control of the heating schedule to manipulate the microstructure during sintering is an approach that has long been known to have the advantages of simplicity and economy. In the simplest situations, there are two heating schedules commonly used in sintering experiments. Figure 2.4 shows the heating schedules. In one case, referred to as constant rate of heating (CRH); green compact is heated with fixed low heating rate to the required temperature, after which it is cooled. In the other case, referred to as isothermal heating; the compact is heated rapidly or at a controlled rate to an isothermal sintering temperature, held at this temperature for the required time to accomplish the desired density and finally cooled (Rahaman 1995).

In addition to these common heating schedules, a precoarsening step is added for sintering of alumina (Chu, et al. 1991, Lin, et al. 1997, Sato and Carry 1995). In the initial step, called the precoarsening treatment, the green compact is heated rapidly prior to densification and held there to improve the microstructural homogeneity. Subsequently the sample is heated to its final sintering temperature.

Another recent common method is known as two step sintering (TSS) which involves heating the sample to the first target temperature, rapidly cooling to the final sintering temperature and soaking there for the required amount of time (Figure 2.4). More details about this are given in Section 4.1.

The final densification of powder compacts is strongly affected by the sintering atmosphere because the atmospheric gas is entrapped within pores as they are isolated. In the case of a fast diffusing gas, full densification is possible, but this is impossible in a slowly diffusing or inert gas unless a high external pressure is applied. At this stage, when pore coalescence occurs, sintered density decreases (dedensification) (Coble 1962a, Demartin, et al. 1997).

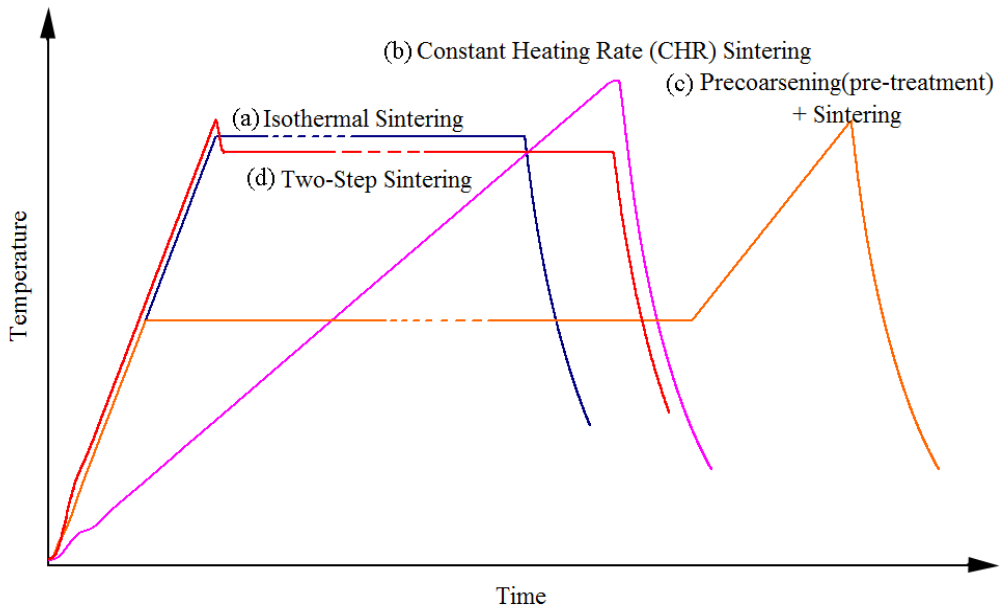

Figure 2.4. Sketch of the temperature-time schedule in a) isothermal, b) constant heating rate c) precoarsening (pretreatment) and d) two-step sintering.

Schema de profiles temperature –temps pour des frittages a) isotherme, b) à vitesse de montée en température constante c) avec un prétraitement de coalescence et d) à 2 étapes.

2.1.4.4. Grain Growth Kinetics

Cinétiques de croissance granulaire

Grain growth describes the increase in the average grain size of a polycrystalline material. Grain growth in ceramics is generally divided into two types: (i) normal grain growth and (ii) abnormal grain growth, which is sometimes referred to as exaggerated grain growth or discontinuous grain growth. In normal grain growth, the average grain size increases with time but the grain size distribution remains self-similar (invariant in time). Abnormal grain growth is the process whereby a few large grains grow rapidly at

the expense of the smaller grains, giving a bimodal grain size distribution (De Jonghe and Rahaman 2003).

Normal grain growth in pure, dense, single-phase materials has been analyzed by a number of different approaches (Atkinson 1988). More recently, the use of computer simulations has provided a valuable technique for the analysis of grain growth. The simulations of Srolovitz et al., (1984) and Anderson et al., (1984) employed a Monte Carlo method that allows topological requirements to be taken into account to provide realistic pictures of grain growth.

The grain growth models predict a kinetic equation of the form,

$$(d)^m-(d_o)^m=Kt \qquad (2.2)$$

d_o : Initial grain size (Primary crystallite size)

t : Soak time at specified sintering temperature

K : Constant,

m : Grain growth exponent ranging from 2 to 4.
is 2 for the normal grain growth, 3 for grain boundary segregation and
4 for grain boundary precipitation.

In the literature, several researchers published estimates of grain growth exponents for different powders.

2.2. Point Defect Chemistry

Chimie des défauts ponctuels

The rates of kinetic processes such as precipitation, densification, grain coarsening, and high-temperature creep deformation are determined by mass transport due to defects.

Points defects defined as deviations from the perfect atomic arrangement: missing ions, substituted ions, interstitial ions, and their associated valance electrons, occur (to greater or lesser degrees) in all crystalline materials. Diffusion of solids into other solids is influenced by deviations from the ideal crystalline state. Defect chemistry

provides immensely useful tools for understanding the properties of crystals containing point defects.

A standard notation used for the description of defects in ionic materials is Kroger-Vink notation, in which a defect is described by three parts. The main body of the notation identifies whether the defect is a vacancy “V”, or an ion such as “Mg”. The subscript denotes the site that the defect occupies, either the normal atom sites of the host lattice or an interstitial site “i”. The superscript identifies the effective charge (or relative charge) of the defect relative to the perfect crystal lattice. For this part of the notation, dots (˙) represent positive effective charges, dashes (´) represent negative charge, and x’s are sometimes used to show neutrality (Chiang, et al. 1997).

Starting with a perfect crystal, one can only form atomic defects with an expenditure of energy which is most commonly thermal. The increased energy and amplitude of lattice vibrations at elevated temperatures increase the probability that an atom will be displaced from its lattice position. Thus formation of atomic defects is a thermally activated process.

In many ceramic systems, significant concentrations of defects are formed only at temperatures well above half the melting point. The two most common types of crystalline defects in ionic materials are Frenkel and Schottky defects. These are intrinsic defects since they can be thermally generated in a perfect crystal, as opposed to extrinsic defects, which are formed only by the addition of impurities or solutes.

A Frenkel defect (Figure 2.5(a)) is formed when an atom is displaced from its normal site onto an interstitial site forming a defect pair: a vacancy and an interstitial. The Schottky defect is unique to ionic compounds and is represented by the simultaneous creation of both cation and anion vacancies, which is illustrated in Figure 2.5(b) The vacancies must be formed in the stoichiometric ratio in order to preserve the electrical neutrality of the crystal (Carter and Norton 2007).

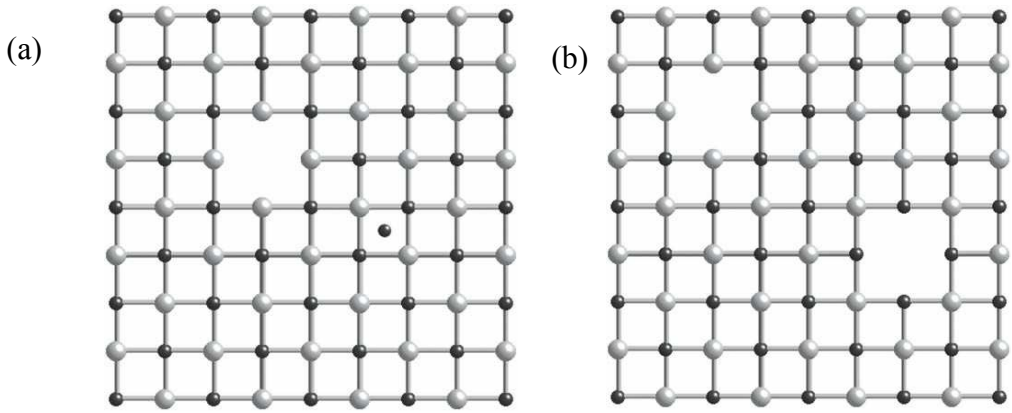

Figure 2.5. Schematic of (a) a Frenkel defect and (b) a Schottky defect drawn in 2D (Source : Carter and Norton 2007).

Schéma de défauts ponctuels a) défauts de Frenkel et b) défauts de Schottky (de Carter and Norton 2007).

2.3. Solid Solution Elements

Eléments en solution solide

Solutes may enter solid solution in crystals as either substitutional or interstitial species. Consider the dissolution of Al_2O_3 in MgO. Based on the similarity in ionic radii between Al^{3+} and Mg^{2+} in six-fold coordination, their radiuses are 0.054 and 0.072 nm, respectively. Assuming that aluminium substitutes for magnesium, an additional vacant magnesium site is needed in order to satisfy the site and charge balance. The basic crystal of MgO has a 1:1 cation-anion stoichiometry, whereas alumina dissolution creates a 2:3 site ratio. The oxygen ions are likely to occupy additional oxygen lattice sites. At this point;

$$Al_2O_3 = 2Al^{\bullet}_{Mg} + 3O^{x}_{O} + V''_{Mg} \tag{2.3}$$

Consider the incorporation of MgO into Al_2O_3. In this instance, the Mg ions may enter the solid solution substitutionally or interstitially; it is not exactly clear which is the lower energy option. If it is substitutional, a possible reaction is

$$2MgO = 2Mg'_{Al} + 2O^{x}_{O} + V^{\bullet\bullet}_{O} \tag{2.4}$$

And if it is interstitial,

$$3MgO = 3Mg_i^{\bullet\bullet} + 3O_O^x + 2V_{Al}''' \tag{2.5}$$

A third possibility is that magnesium is self-compensating and forms both the interstitial and substitutional defect:

$$3MgO = 2Mg'_{Al} + Mg_i^{\bullet\bullet} + 3O_O^x \tag{2.6}$$

Experimental data and calculations of the relative energies for these incorporation mechanisms suggest that at high temperatures magnesium is self-compensated to a large extent, but that some minor compensation by cation vacancies or oxygen interstitials also exists. That is, the net incorporation reaction can be considered to be mostly reaction in Equation (2.6), plus some fraction of reactions in Equations (2.4) and (2.5) (Chiang, et al. 1997).

2.4. Importance and Measurement of Sintering Parameters

Importance et mesure des parameters de frittage

2.4.1. Densification Rate

Vitesse de densification

The kinetic data for the densification of the powder compact during sintering is important practically and theoretically. They can be obtained as functions of time or temperature by two methods: i) intermittently, density of compacted powder is measured after firing at the selected temperatures for a determined period of time, ii) continuously, by the technique of dilatometry (Rahaman 1995). Shrinkage ($\Delta L/L_o$) is determined from the measured length change in the sample in a dilatometer in comparison to the initial compact size. Computer collected shrinkage and temperature data are accumulated constantly during the heating process. Shrinkage reflects the direct action of densification mechanisms like grain boundary diffusion; although simultaneous coarsening processes alter the driving force (Hillman and German 1992).

Densities, $\rho(T)$, and densification rate curves are computed from the recorded shrinkage data and from final density ρ_f measurements using the following formula:

$$\rho(T) = \rho_f \left(\frac{1 + \frac{\Delta L_f}{L_o}}{1 + \frac{\Delta L_{(T)}}{L_o}} \right)^3 \tag{2.7}$$

in which L_o is the initial sample length, L_f is the final sample length and L(T) is the sample length at the temperature T (Legros, et al. 1999). Final densities were measured by the classical Archimedes method on cooled samples.

To obtain the densification rate, temperature derivative of relative density ρ is taken

$$\frac{d\rho_{(T)}}{dT} = -3 * \frac{d\left(\Delta L_{(T)} / L_0\right)}{dT} * \frac{\left(1 + \frac{\Delta L_{(f)}}{L_0}\right)^3}{\left(1 + \frac{\Delta L_{(T)}}{L_0}\right)^4} * \rho_f \tag{2.8}$$

2.4.2. Apparent Activation Energy

Energies d'activation apparentes

Sintering involves competing mechanisms, each of which individually obeys Arrhenius' equation, the dependence of the combined rate on temperature is in general not of this type. However, apparent activation energies can be measured. The apparent activation energy for densification (Q) is usually found empirically from constant heating rate experiments.

In the beginning of densification of most materials, sintering is controlled by a mixture of volume and grain-boundary diffusions and grain growth can also significantly affect the theoretical activation energy for these diffusion mechanisms, so the apparent activation energy for densification often deviates from reported activation energy for grain-boundary or volume diffusion.

Generally, activation energy characterizes the temperature dependence of the rate of a thermal event. For instance, the activation energy for grain-boundary diffusion is a temperature-independent term that governs the rate at which grain boundary diffusion takes place at different temperatures. The thermal events occurring during sintering take place simultaneously, therefore the activation is called ''apparent'' as it

only gives an empirical indication of the temperature dependence of sintering densification by attending diffusion mechanisms (Blaine, et al. 2009).

Activation energy is described by the Arrhenius equation or Master Sintering Curve (MSC) models.

2.4.2.1. Arrhenius Plots and *Q* Calculation

Diagrammes d'Arrhenius et détermination d'énergie d'activation

Young and Cutler (1970) proposed a technique to measure activation energy for reaction rate phenomena at constant rates of heating. Because, it was hoped that CRH techniques would help to solve the problems encountered in isothermal work and that the experimental conditions would more nearly approach those encountered in industry.

But this technique is sensitive to surface properties and particle size distribution in a material. Wang and Raj (1990) improved the method by applying careful green-state processing to eliminate the grain size variability. Therefore, the following approach was used to analyze the data. The densification rate is written below to measure the activation energy for sintering of pure alumina and alumina doped with zirconia or titania.

$$\dot{\rho} = \mathrm{A}\frac{e^{-Q/RT}}{T}\frac{f(\rho)}{d^{n}} \tag{2.9}$$

Here, $\dot{\rho} = d\rho/dt$ is the rate of densification, d is the grain size, n is the grain size exponent, Q is the activation energy, $f(\rho)$ is a function only of density and A is a material parameter that is insensitive to d, T, or ρ. In their work, grain growth was avoided by employing cold-isostatic pressing of green compacts so that dense and uniform packing were obtained. In addition, a constant value of relative density could be obtained by changing the heating rate. Thus, d and $f(\rho)$ are assumed to be constant values. Diffusion mechanisms can be predicted by calculating grain size exponent (n). The densification rate is controlled by lattice diffusion (n = 3) or by grain-boundary diffusion (n = 4) depending on the value of n.

The densification rate may be written as;

$$\dot{\rho} = \frac{d\rho}{dt} = \frac{d\rho}{dT}\dot{T} \tag{2.10}$$

Where $\dot{T}$=dT/dt, the heating rate, is held constant during the experiment. Substituting Equation (2.10) into Equation (2.9) and taking logarithms. Finally, the Equation (2.11) is obtained for calculation of activation energy.

$$\ln\left(T\dot{T}\frac{d\rho}{dT}\right) = -\frac{Q}{RT} + \ln \mathrm{A} - n\ln d \tag{2.11}$$

A plot of the left-hand side vs. 1/T would give a value for Q provided that the data points are taken at a constant value of ρ and d. As a result, apparent activation energies at several densities are calculated from Arrhenius plots of the densification rates at different heating rates (Wang and Raj 1990).

As an illustration of the procedure for calculation of the activation energy, the calculation of Wang et.al is summarized below. The results of sintering pure alumina for two heating rates of 5°C/min and 20°C/min are given in Figure 2.6(a). A third heating rate is needed to calculate the activation energy more precisely. Wang et.al also tested an intermediate heating rate of 10°C/min the results of which are not given in Figure 2.6 probably for the sake of clarity of the graphs. The derivatives of ρ with respect to temperature are shown in Figure 2.6(b).

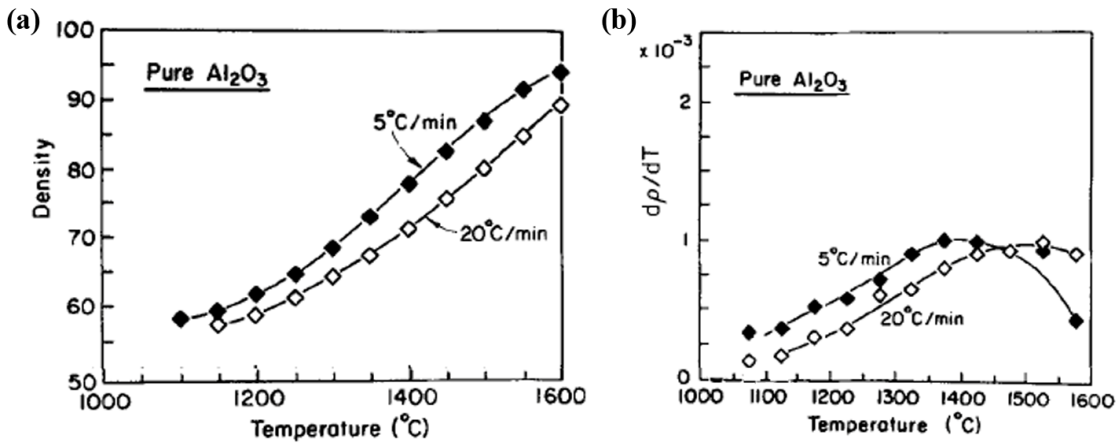

Figure 2.6. Relative density (a) and densification rate (b) versus temperature graphs of alumina (Source: Wang and Raj 1990).

Courbes de densité relative a) et de vitesse de densification b) en fonction de la température pour de l'alumine pure (de Wang and Raj 1990).

The Equation (2.11) is applied to data in Figure 2.6(b) in the following way. First a density value is determined and its corresponding temperature is read from Figure 2.6(a). Then the dρ/dT value is read from Figure 2.6(b) for the same temperature. Five such readings for five different densities (ρ=0.65 to 0.85) at three different heating rates are used to plot Figure 2.7. These fifteen values are plotted in an Arrhenius plot to find the value of the activation energy for pure alumina. The average and the spread in the values of the activation energy are also calculated.

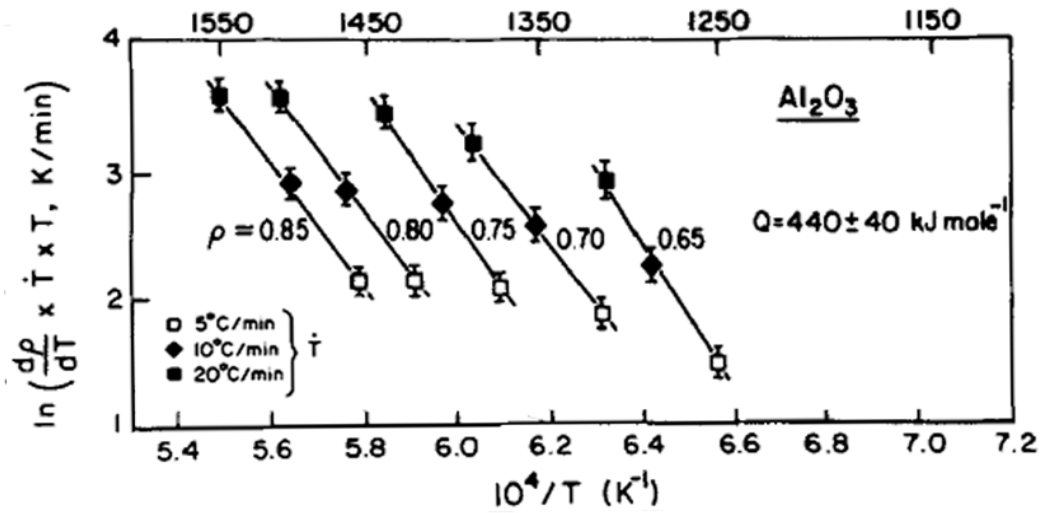

Figure 2.7. Arrhenius plots of alumina and the estimated activation energy using the method described in the text (Source: Wang and Raj 1990).

Diagrammes d'Arrhenius pour de l'alumine et énergie d'activation estimée par la méthode décrite dans le texte (de Wang and Raj 1990).

2.4.2.2. Master Sintering Curve (MSC)

Courbe de frittage de référence

In order to produce quality materials within specified density and dimensional limits, shrinkage and densification of particulate materials should be monitored and controlled. One of the simplest and most functional sintering models is Master Sintering Curve (MSC), developed by Su and Johnson (1996). The MSC model enables to predict the densification behaviour under arbitrary time-temperature excursions following a minimal set of preliminary experiments. Through the MSC, the density of the material is predicted at any point during any sintering cycle.

Su and Johnson (1996) derived the master sintering curve from the densification rate equation of combined stage sintering model proposed by Hansel et al., (1992) The model originated from instantaneous linear shrinkage rate equation

$$-\frac{dL}{Ldt}=\frac{\gamma\Omega}{kT}\left(\frac{\Gamma_v D_v}{G^3}+\frac{\Gamma_b \delta D_b}{G^4}\right) \tag{2.12}$$

In the equation (2.12),

γ : the surface energy

Ω : the atomic volume

T : the absolute temperature

G : the mean grain diameter

D_v and D_b : the coefficients for volume and grain boundary diffusion, respectively

δ : the width of the grain boundary

Γ : the lumped scaling parameters,

For isotropic shrinkage, the linear shrinkage rate can be converted to the densification rate by

$$-\frac{dL}{Ldt}=\frac{d\rho}{3\rho dt} \tag{2.13}$$

where ρ is the bulk density. The equation (2.12) can be simplified by assuming only one dominant diffusion mechanism (either volume or grain-boundary diffusion) governs the densification. Thus Eq. (2.12) becomes

$$\frac{d\rho}{3\rho dt}=\frac{\gamma\Omega(\Gamma(\rho))D_o}{kT(G(\rho))^n}\exp\left(-\frac{Q}{RT}\right) \tag{2.14}$$

Equation (2.14) can be rearranged and integrated as follows:

$$\int_{\rho_o}^{\rho}\frac{(G(\rho))^n}{3\rho\Gamma(\rho)}d\rho=\int_0^t\frac{\gamma\Omega D_o}{kT}\exp\left(-\frac{Q}{RT}\right)dt \tag{2.15}$$

The right-hand side (rhs) of Eq. (2.15) are related to the dominant atomic diffusion process and is independent of the character of the powder compact. The terms on the lhs defines the microstructural evolution. With slight further rearrangement, the lhs of Eq. (2.15) becomes

$$\Phi(\rho) = \frac{k}{\gamma\Omega D_o} \int_{\rho_o}^{\rho} \frac{(G(\rho))^n}{3\rho\Gamma(\rho)} d\rho \tag{2.16}$$

Which includes all microstructural and materials properties,
Except for Q. The rhs is

$$\Theta(t,T) \equiv \int_{t_0}^{t} \frac{1}{T} \exp\left[-\frac{Q}{RT}\right] dt \tag{2.17}$$

which depends only on Q and the time-temperature profile.
Thus Equation (2.15) becomes

$$\Phi(\rho) = \Theta(t, T(t)) \tag{2.18}$$

The relationship between ρ and $\Phi(\rho)$ is defined as the master sintering curve. The MSC is unique for a given powder and green-body process, including fixed green density, and it is independent of the sintering path, given the assumption described above.

Su and Johnson suggested not to include data taken at high densities (>95% of theoretical density) because exaggerated grain growth may take place for some materials at these densities and the sintering data points do not converge very well.

Su and Johnson applied their model for different materials. Here is the example of relative densities versus temperature curves of alumina pellets, sintered at heating rates of 8, 15, 30 and 45°C/min, shown in Figure 2.8. MSCs were constructed from the densification data displayed in Figure 2.8. Figure 2.9(a) shows that the individual sintering curves converged reasonably close to a single curve. This indicated that there must be a general curve, regardless of the sintering path.

Initially, an estimate is made for the activation energy Q, and the MSCs for all heating profiles are computed using Equation (2.17). If the correct value of Q has been given,

all of the data converge to a single curve. A curve (a polynomial function) can be fitted to all the data points, and then the convergence of the data to the fitted line can be quantified through the sum of the residual squares (sum of residual squares divided by total number of data points) is a minimum. The results for such an exercise for the alumina sintering data of Figure 2.8 is shown in Figure 2.9(b). The minimum is reached at ~440 kJ/mol, indicating the estimated apparent activation energy. This is in reasonable good agreement with the results of Wang and Raj (1990) (see in Figure 2.7).

The MSC has successfully been applied for calculation of activation energy of many materials like thorium dioxide (ThO_2) (Kutty, et al. 2004), nanocrystalline and microcrystalline ZnO (Ewsuk, et al. 2006) and TiO_2 (Li, et al. 2008).

Teng et al., (2002) redefined the shape of MSC and wrote a computer program in order to improve the predictive accuracy of the MSC model and make application of MSC easier in addition to predicting the sintering results of various heating profiles.

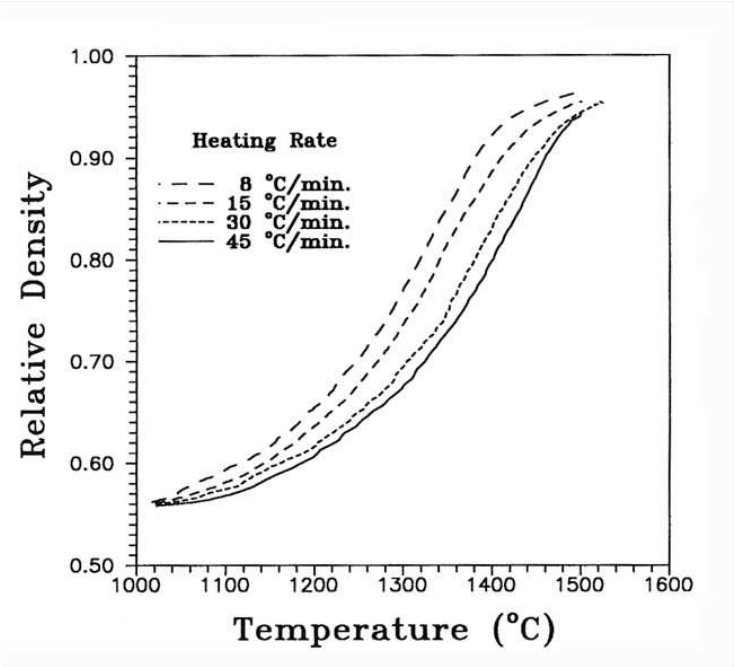

Figure 2.8. Relative densities versus temperature curves of alumina, sintered with different heating rates (Source: Su and Johnson 1996).

Courbes de densité relative en function de la température pour de l'alumine frittée avec différentes vittesses de chauffage (de Su and Johnson 1996).

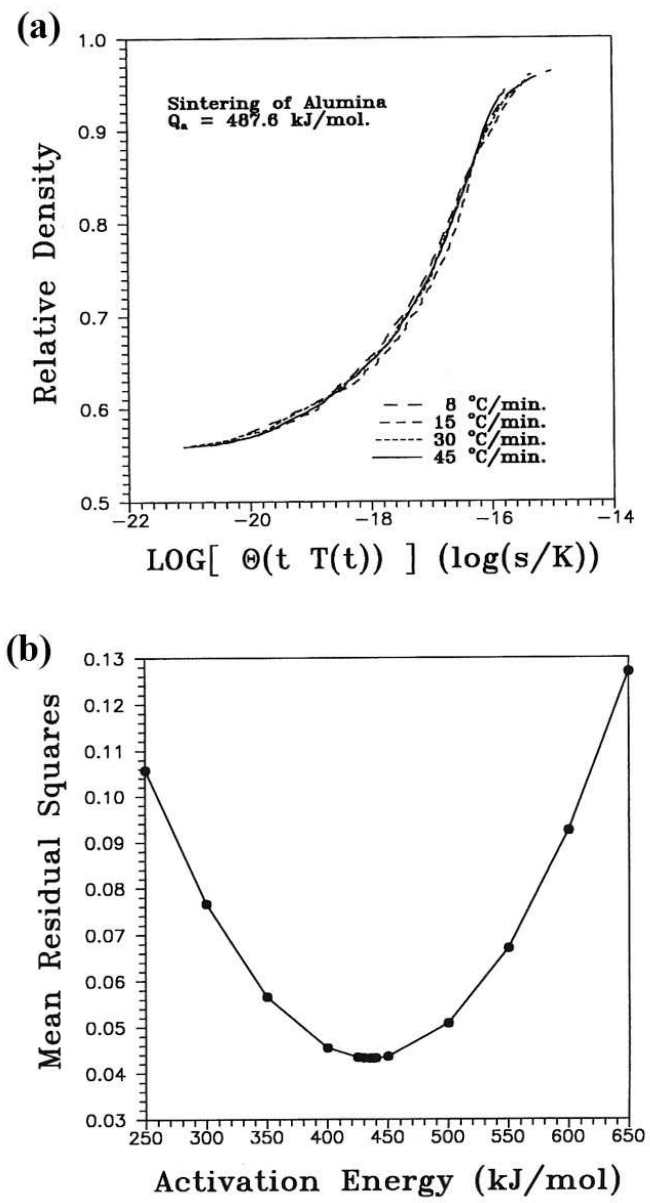

Figure 2.9. (a) Master Sintering Curves of alumina and (b) Mean of Residual Square versus activation energy (Source: Su and Johnson 1996).

Courbes de frittage de reference pour de l'alumine a) et écart type moyen en function de l'énergie d'activation (de Su and Johnson 1996).

2.5. Bi-materials

Bi-matériaux

Bi-materials are composed of at least two layers or parts which are made of different materials or different compositions. They have functional properties, depending on mechanical, electrical and magnetic properties of their components. Their application areas range from electronic packaging applications such as multi-layer

ceramic capacitors to thin film-substrate systems used widely in the microelectronics industry (Boonyongmaneerat and Schuh 2006) and (Simchi, et al. 2006a). Production of the bi-material by different methods and with various components is an interesting subject for the researchers.

There are many types of bi-materials; metal-metal (Simchi 2006b, Simchi, et al. 2006a), metal-oxide (Boonyongmaneerat and Schuh 2006) and oxide-oxide (Cai, et al. 1997a, Cai, et al. 1997b) and (Sun, et al. 2008). They are mostly produced by tape casting method (Cai, et al. 1997a) and co-pressing method (Simchi 2006b, Simchi, et al. 2006a).

2.5.1. Metal-Metal Bi-materials

Bi-matériaux metal-métal

Co-pressing technique is the main method for production of bi-materials. According to *ASM Metals Handbook* (1990), "co-molding" is possible when materials have either compatible or overlapping process parameters (Baumgartner and Tan 2002). It means that the process is applicable for materials having same or similar matrix, sintering behavior, coefficient of thermal expansion, etc. Meanwhile, it is believed that co-sintering of the molded parts is the key stage in the manufacturing route. Therefore, optimization of the sintering parameters is of crucial importance.

Simchi et al., (2006a) evaluated the micro-structural modification and density profile during co-sintering of magnetic 17-4PH and non-magnetic 316L stainless steel powders. The major aim of their study was to produce a component in a way that magnetic properties were induced to one side of the resulting structure, so were non-magnetic properties to the other side of the corresponding structure. In fact, co-sintering process offers some advantages, including lower cost and simple manufacturing step compared to other fabrication methods such as joining. Hence, they prepared bi-layer (the authors use the term "bimaterial" instead) powder compact through dry pressing. For that purpose, first powder was poured into alumina tube and the die was slightly tapped to spread the powder uniformly at its bottom. Afterwards, the second powder was subsequently poured on top of the previous layer. The powders were eventually pressed together into pellets.

Non-isothermal sintering behavior of the composite layers was studied by dilatometric method under either hydrogen or low pressure vacuum atmosphere. In their corresponding study, they measured densification rate and characterized the microstructure of bi-layers.

Figures 2.10(a) and (b) show the calculated mismatch strain and strain rate of bi-layer during non-isothermal sintering in hydrogen atmosphere. They were obtained by taking the shrinkage and shrinkage rate of each material followed by subtraction of their values from each other. Consequently, the bilayers sintered in a hydrogen atmosphere were found to show maximum strain incompatibility of 0.5 %, while those sintered in low pressure atmosphere exhibited higher strain incompatibility. From that point of view, it is reasonable to infer that sintering in hydrogen atmosphere is much better than that in low pressure atmosphere in order to achieve an enhanced bonding at the interlayer.

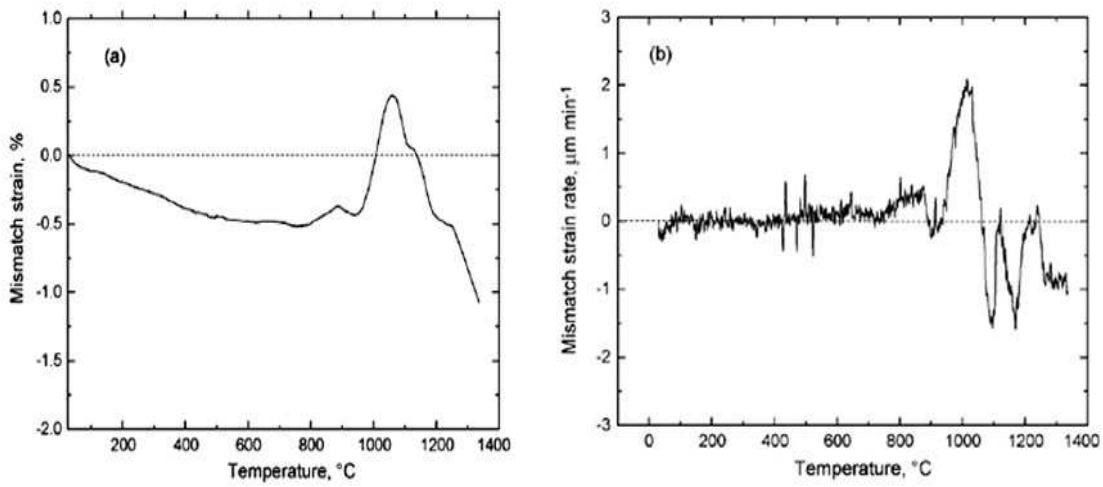

Figure 2.10. Mismatch strain (a) and strain rate (b) between 17-4PH and 316L stainless steel layers during non-isothermal sintering in hydrogen. (Source : Simchi, et al. 2006a).

Ecarts de retrait a) et de vitesse de retrait entre des couches d'aciers inoxydables 17-4PH et 316L lors d'un frittage anisotherme sous hydrogène (de (Simchi, et al. 2006a).

In his other work, two-layer stepwise graded Ni-based superalloys were co-pressed by the same production method in their previous study and then the green compacts were co-sintered in a laboratory furnace under reduced pressure of argon (0.1 mbar) in the temperature range from 1250°C through 1300°C for 60 minutes (Simchi 2006b).

2.5.2. Oxide-Oxide Bi-materials

Bi-matériaux oxyde-oxyde

Cai et al., (1997a) fabricated asymmetric and symmetric bi-layers of Alumina-Zirconia by conducting tape casting and lamination methods. Although their samples were actually multi-layered ceramics, they called them bi-layers in their publication. They examined the type of cracks and crack-like defects which occurred as a consequence of mismatch stress in film-substrate systems or ceramic multi-layers during sintering and cooling periods. As a result, they eventually observed that debonding cracks occurred at the interface of both symmetric and asymmetric bi-layers of alumina and zirconia. They also revealed that channel cracks along the zirconia layers in the asymmetric bi-layers are principally noticeable, while interlayer and transverse cracks are, however, visible in alumina side of symmetric layers of alumina and zirconia. Figures 2.11(a) and (b) give the channel cracks and transverse cracks in the asymmetric and symmetric bi-layers of alumina and zirconia, respectively. For the purpose of strengthening the interlayer bonds and layer densities between alumina and zirconia, various amounts of alumina were also incorporated into zirconia. SEM micrographs showing the interlayer of neat alumina-neat zirconia and 30 wt. % of alumina added zirconia-neat alumina are given in Figures 2.12(a) and (b), respectively. They eventually concluded that it is highly reasonable to provide a precise control for heating and cooling rates during sintering process in order to achieve defect-free bi-layers of alumina and zirconia.

Sun et al., (2008) studied to eliminate cracks and chambers in three-layered Al_2O_3/ZrO_2 functionally graded materials (FGMs). The green bodies were composed of alumina, a mixture of alumina and zirconia, and zirconia layers that were compacted in a single-action die and co-sintering at different heating regimes. Two distinct alumina powders and two distinct zirconia powders were mixed to change powder characteristics. Low compaction pressure (at 60 MPa) and modified interface profile by using jagged surface punch at compaction and low cooling rate (4^oC/min) are the optimized processing parameters for crack free FGMs. They compared a smooth interface and an occlusive interface derived from the jagged punch surface.

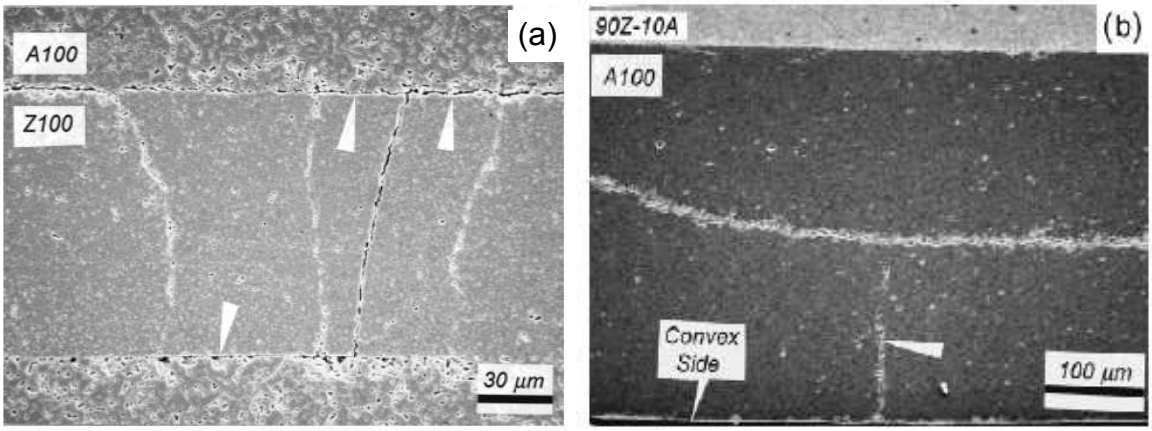

Figure 2.11. Typical defects observed in the symmetric laminates: (a) debonding cracks and (b) channel cracks (Source : Cai, et al. 1997a).

Défauts caractéristiques observés dans des structures feuilletées (alumine-zircone) symétriques a) fissures interfaciales b) fissures transverses (de Cai, et al. 1997a).

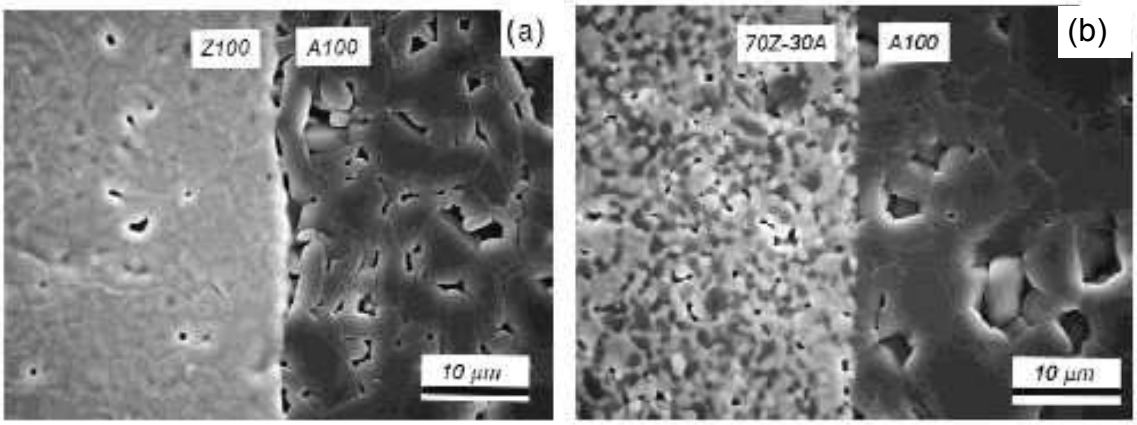

Figure 2.12. SEM micrograph showing the microstructure of (a) A100/Z100, and (b) A100/Z70 symmetric laminates (Source : Cai, et al. 1997a).

Micrographies électroniques à balayage montrant des microstructures de structures lamellaires symétriques a) A100/Z100 et b) A100/Z70 (de Cai, et al. 1997a).

2.5.3. Metal-Oxide Bi-materials

Bi-matériaux métal-oxyde

Boonyongmaneerat and Schuh (2006) studied tungsten(W)/alumina (Al_2O_3) metal-oxide system, which is used to a great extent, especially for electronic packages and metal brazing applications; (Kohl 1964, Tummala 1988). They prepared two-layer compacts by pouring Al_2O_3 and W powders sequentially into a die of rectangular cross-section and cold pressed without binders using a single-action press at 80 MPa. These

green specimens were then co-fired in a furnace at 1177°C for 1 hour, followed by slow furnace cooling. The test specimens are shown in Figure 2.13(a). In Figure 2.13(b), a magnified view of the interfacial region between W and Al_2O_3 is shown in a scanning electron micrograph. It has been found that no primary chemical interaction occurs along the W/Al_2O_3 interface, and mechanical interlocking is the main mechanism that controls adhesion. The sintering kinetics of W particles can be dramatically changed by the addition of very small quantities of transition metals, such as Ni, Fe, and Pd, through the process of activated sintering. They used four-point bending delamination experiments to evaluate the strength and adhesion of co-sintered W/Al_2O_3 bi-material (Boonyongmaneerat and Schuh 2006).

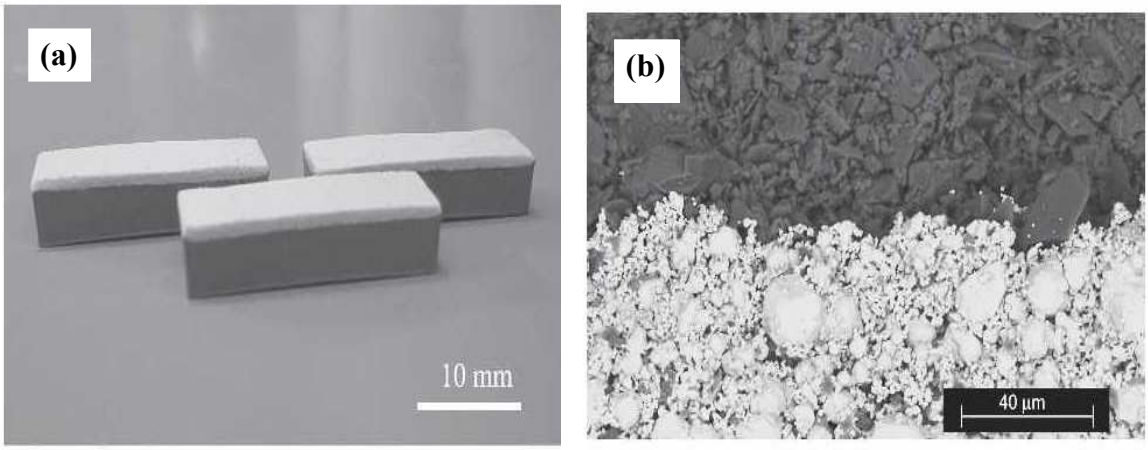

Figure 2.13. W/Al_2O_3 bilayer specimens, (a) a macroscopic view and (b) a micrograph of the interfacial region (Source: Boonyongmaneerat and Schuh 2006).

Echantillons bi-couches W/Al_2O_3 a) vue macroscopique et b) micrographie de la zone interfaciale (de Boonyongmaneerat and Schuh 2006).

2.6. Diffusion Couples and the Kirkendall Effect

Couples de diffusion et effet Kirkendall

Diffusion couple test is a useful and common technique to understand the growth of intermediate new phases between the two end members (components) which were previously shaped and sintered to some extent. It has been used by many researchers (Buscaglia, et al. 1997, Pettit, et al. 1966, Siao, et al. 2009, Watson and Price 2002) in the literature.

One of the most significant experiments in the field of solid state diffusion was conducted by Smigelkas and Kirkendall in 1947 (Smigelkas and Kirkendall 1947). In

their experiment, a rectangular bar of wrought brass (70wt%Cu-30wt%Zn) was ground and polished and then wounded with molybdenum wires, which are inert to the system. They are used as markers. Then the bar was encapsulated in a block of pure copper (Cu), as shown in Figure 2.14. This couple was cross-sectioned into small pieces, they were subjected to annealing at 785°C for different annealing times. After annealing, each annealed part was polished and etched; the distance between the markers was measured. After measuring, it was clear that with increasing annealing time, the distance between markers decreases parabolically with time. This is because $D_{Zn}>D_{Cu}$ and the zinc atoms diffuse out of the central block faster than they are replaced by copper atoms diffusing in the opposite direction. This shift was explained as Kirkendall effect. When initial interface is shifting, diffusion porosity may develop and locate in the side containing faster moving atom (Siao, et al. 2009).

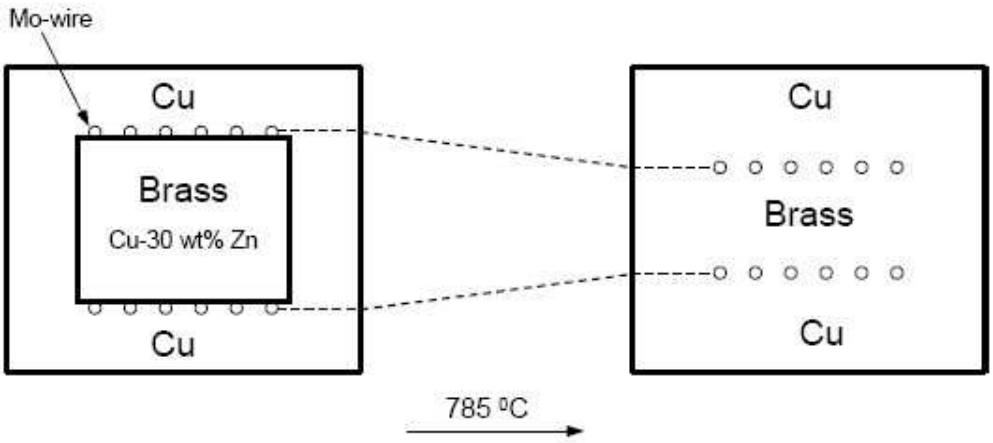

Figure 2.14. Schematic representation of a cross-section of the diffusion couples before and after annealing at 785°C (Source: Smigelkas and Kirkendall 1947).

Représentation schématique de la section transverse de couples de diffusion avant et après recuit à 785 °C (de Smigelkas and Kirkendall 1947).

CHAPTER 3

SINTERING AND DENSIFICATION BEHAVIOUR OF MONOMATERIALS : ZIRCONIA AND ALUMINA

Comportements en frittage et en densification de monomatériaux : zircones et alumines

Résumé

Dans ce chapitre les propriétés physico-chimiques des poudres commerciales d'alumines et de zircones ainsi que leurs comportements en frittage ont été caractérisés. Toutes ces poudres sont de haute pureté avec des surfaces spécifiques (BET) élevées comprises entre 13 et 32 m^2/g. Ces poudres sont des poudres granulées avec des tailles de granules de quelques dizaines de microns. Leurs courbes de compressibilité montrent que ces granules se briseraient pour des pressions supérieures à 200 MPa. L'alumine non dopée en magnésium présente un retrait linéaire total d'environ 18 % après un frittage jusqu'à 1500°C ; ce niveau de retrait correspond à une densité relative finale de 97%. Pour une vitesse de chauffage de 3,3°C/min le pic de vitesse de densification se situe at 1250°C.

Pour les mêmes conditions de chauffage la poudre de zircone à 3 mole% d'oxyde d'yttrium présente un épaulement inhabituel dans les courbes de vitesses de densification en fonction de la température. Cet épaulement de vitesse de densification serait dû à la fraction non négligeable de cristallites nanométriques de cette poudre. Les courbes de vitesse de densification en fonction de la température de la poudre de zircone à 2 mole % d'oxyde d'yttrium sont plus régulières avec des pics de vitesses de densification entre 1200 et 1300°C selon la vitesse de chauffage.

Les microstructures des matériaux frittés ont été observées soit sur des surfaces de rupture soit sur des sections polies et attaquées thermiquement. L'alumine dopée à la magnesie présente une taille de grains moyenne de 0.9 µm alors que l'alumine non dopée frittée dans les mêmes conditions présente une taille de grains moyenne de 2.0 µm. Les poudres d'alumine dopée (A) ou non dopée (B) en magnésie présentent des

énergies d'activation apparentes de densification très peu différentes de respectivement 680 et 660 kJ/mol. Pour les poudres de zircone yttriée les énergies d'activation apparentes moyennes de la densification sont respectivement de 530 kJ/mol pour la poudre Z-3Y et de 840 kJ/mol pour la poudre Z-2Y. Des déterminations plus précises de ces énergies d'activation apparentes avec une large gamme de vitesse de chauffage ont permis de confirmer des valeurs plus élevées au tout début de la densification et décroissantes quand la densité relative augmente. De telles énergies d'activation très élevées en tout début de frittage de ces poudres nanométriques de zircone seraient à relier à des cinétiques de densification gouvernées par un mécanisme du type réaction d'interface tant que la taille des cristallites resterait inférieure à 100 nm.

3.1. Introduction

Introduction

The chemical and physical properties of all four powders of alumina A, alumina B, Zirconia TZ-2Y and Zirconia Z-3Y were determined. The experimental procedure for the preparation of compacted mono-materials, composed of only one oxide powder, is presented in this chapter. Before doing any study on bi-materials (Chapters 5 and 6), it was necessary to characterize the sintering and densification behaviors of all four mono-materials. A literature review is summarized below about the sintering and densification behaviour of alumina and zirconia.

The effect of magnesia on the sintering and microstructure of alumina has been extensively studied since the discovery of the Lucalox process by Coble in 1961 (Coble 1962b). Bennison and Harmer (1990) has published in 1990 a review of the literature on this topic.

Young and Cutler (1970) investigated the sintering behavior of alumina, zirconia and titania via constant rate of heating (CRH) experiments. Hillman et.al. later applied dilatometer and gas adsorption measurements for analysis of the sintering mechanisms of alumina. According to their results, simultaneous surface diffusion and grain boundary diffusion were the sintering mechanisms and their activation energies were 508 and 440 kJ/mol, respectively (Hillman and German 1992).

Sato and Carry (1996) investigated the effect of magnesia and yttria doping on the sintering behavior of alumina using constant-heating rate dilatometric experiments.

They observed that doping of magnesia into alumina decreases the activation energy for densification. Yttria doping, on the other hand, delays densification on heating due to increased apparent activation energy for the intermediate stage of sintering of alumina. Activation energy increases from 740 to 870 kJ/mol after 1500 ppm Y_2O_3 is added to undoped alumina.

Recently, Shao et al., (2008) studied the calculation of apparent activation energy of α-alumina based on Arrhenius theory at constant heating-rates sintering from dilatometric results. Their findings supported the previous results on activation energy, dependent on relative density of sintered alumina (Wang and Raj 1990). The procedure used in calculation of activation energies and the densification rate curves are given in Chapter 2 of this thesis.

Matsui et.al. made many contributions to sintering kinetics of zirconia. They investigated the effect of Al_2O_3 on the initial sintering stage of fine zirconia powder and sintering kinetics at constant rate of heating. They determined the activation energies at the initial stage of sintering by analyzing the densification curves. They found that the activation energy of powder compact including Al_2O_3 was lower than that of a powder compact without Al_2O_3. The diffusion mechanisms at the initial sintering stage were determined using the new analytical equation applied for CRH techniques. This analysis exhibited that Al_2O_3 included in a powder compact changed the diffusion mechanism from grain boundary to volume diffusion (VD). Therefore, it is concluded that Al_2O_3 addition enhanced the densification rate because of a decrease in the activation energy of VD at the initial sintering stage (Matsui, et al. 2005). In another study, the effect of specific surface area on the initial sintering stage of fine zirconia powder and sintering kinetics at isothermal heating was investigated (Matsui 2007a).

For yttria stabilized zirconia, apparent activation energy values of 615-650 kJ/mol are commonly reported (Matsui, et al. 2005, Wang and Raj 1991). Recently, Bernard-Granger and Guizard (2007b) have studied the densification behavior of zirconia and they calculated the apparent activation energy for zirconia from Arrhenius plots. The obtained straight lines were not parallel. So they unambiguously concluded that the apparent activation energy of the mechanism controlling densification, Q, was a direct function of the relative density. They confirmed their idea by demonstrating apparent activation energy versus relative density plot as shown in Figure 3.1. It is observed that the apparent activation energy value is decreasing linearly with the increase of the relative density. They explained the reason of activation energy increases

for lower values of the relative density with a point defect formation step and grain boundary diffusion of Zr^{4+} cations. This defect formation step or defect absorption steps could be the limiting step of sintering kinetics especially for ultrafine grained compacts (nano structured materials) in which the diffusion distance is also nanometric. By analogy with interface reaction controlled creep, such sintering kinetic can be named as "interface reaction controlled sintering".

Bernard-Granger and Guizard (2007a) attempted to identify the control mechanism(s) of densification during spark plasma sintering (SPS) experiments. They proposed different mechanisms controlling the densification of yttria stabilized zirconia powder during SPS. When the applied compaction stress is low and/or the sintering temperature is low, a pure bulk diffusion mechanism is probably responsible for the densification. At intermediate compaction stresses and/or medium temperatures, according to apparent activation energy of 450 kJ/mol, densification proceeds by grain boundary sliding accommodated by an in-series (interface-reaction/lattice diffusion of the Zr^{4+} and/or Y^{3+} cations) mechanism controlled by the interface-reaction step. For high temperatures and/or high stresses, densification proceeds by a dislocation-climb-controlled mechanism.

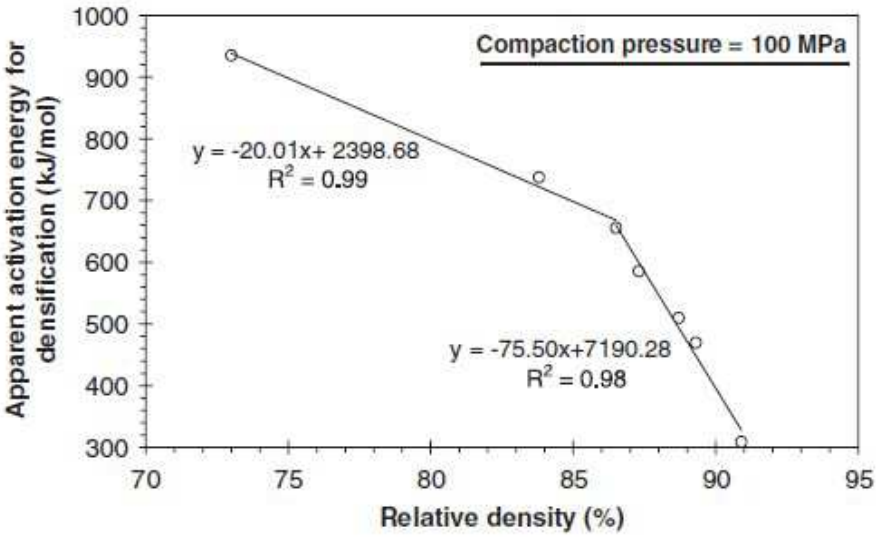

Figure 3.1. Apparent activation energy versus relative density for for yttria-doped zirconia (Source: Bernard-Granger and Guizard 2007b).

Energie d'activation apparente en fonction de la densité relative pour de la zircone yttriée (de Bernard-Granger, 2007b).

3.2. Powder Properties

Propriétés des poudres

Zirconia (ZrO_2) TZ-2Y (TOSOH) powder with uniform dispersion of 2 mol % yttria, and zirconia Z-3Y (Batch n°16129 Baikowski, France) powder with uniform dispersion of 3 mol % yttria powders were used. Two kinds of commercial grade submicron-grained alumina were used in this thesis. One of them was 550 ppm magnesium-doped (Batch n° 660J CR 15 MgO-doped, Baikowski) alumina powder (alumina A) while the other powder was a non-doped α-alumina (alumina B) (Batch n° 14406 BMA15, Baikowski). Designations along with some physical and chemical properties of the powders are given in Tables 3.1 and 3.2.

The SEM images of the powders are shown in Figure 3.2. Alumina B powder is softly agglomerated, alumina A powder had nearly the same form therefore its SEM image was not displayed. Zirconia powders were in a granulated form. Zirconia TZ-2Y powders have spherical shape and average granular size is 40 µm. On the other hand, zirconia Z-3Y granules were doughnut shaped with a diameter of about 20 µm.

Particle size distributions of the powders were analyzed by sedigraph method (Sedigraph 5100, Micromeritics). Results are given in Figure 3.3. The Sedigraph particle size measurement covers the size range from 300 to 0.10 µm equivalent spherical diameter. So the finer particle starts from 0.10 µm for each powder. According to the results, zirconia TZ-2Y powder is slightly finer than the other powders and alumina A powder is coarser than the others respectively.

Table 3.1. Designations of powders.

Désignation des poudres.

Name of powder	**Zirconia** (doped 2 mol.% yttria) (TOSOH)	**Zirconia** (doped 3 mol.% yttria) (Baikowski)	**Alumina** (CR15- 550 ppm MgO-doped) (Baikowski)	**Alumina** (BMA15, (Baikowski)	**Spinel** (S30CR) (Baikowski)
Designation	Zirconia TZ-2Y	Zirconia Z-3Y	Alumina A	Alumina B	Spinel

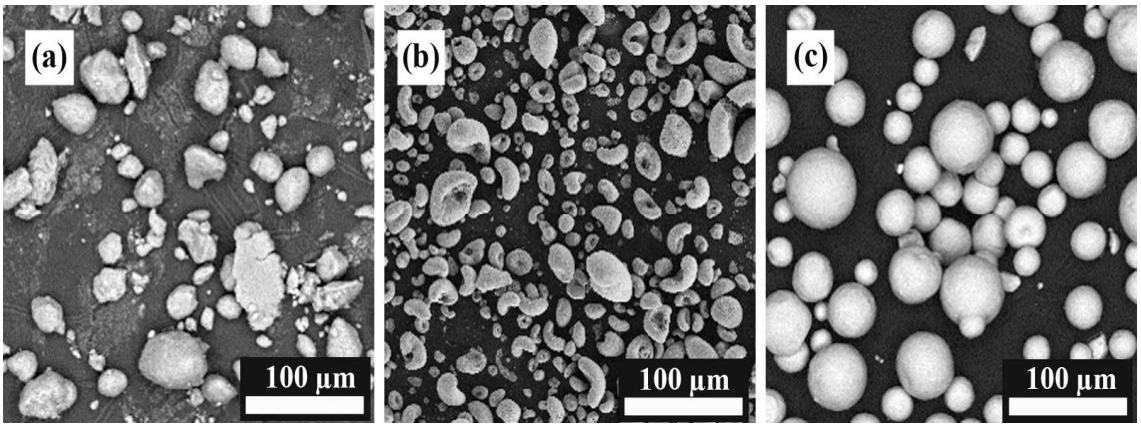

Figure 3.2. SEM images of the powders (a) alumina B, (b) zirconia Z-3Y and (c) zirconia TZ-2Y.

Micrographies en Microscopie Electronique à Balayage (MEB) des poudres granulées a) alumine B, b) zircone Z-3Y et c) zircone Z-2Y.

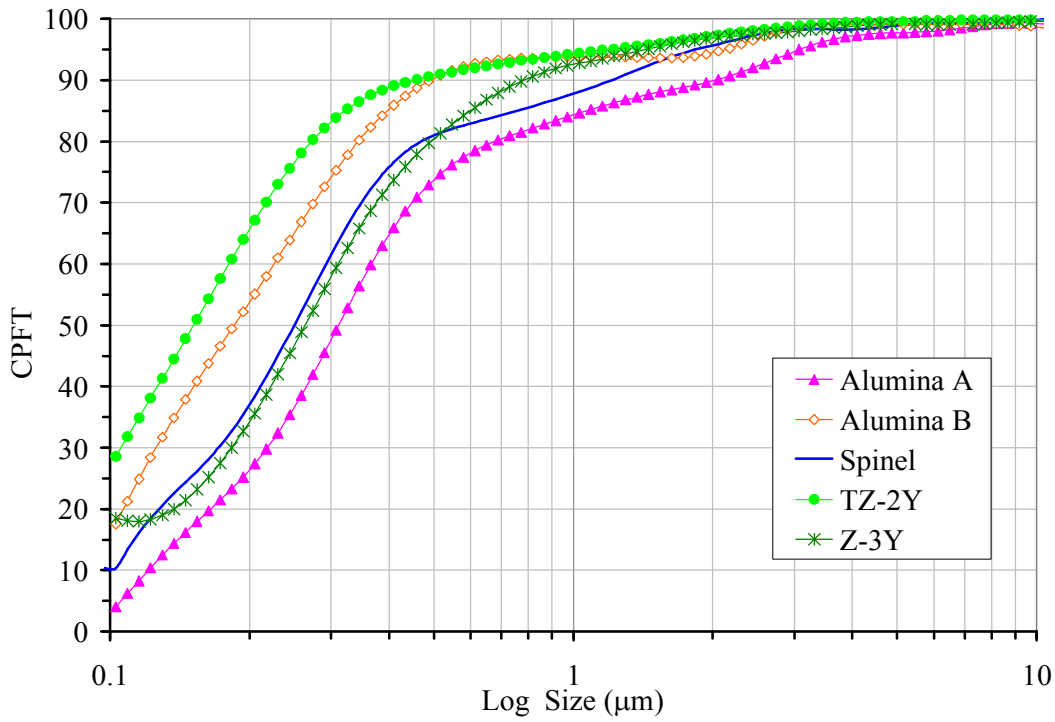

Figure 3.3. Particle size distribution curves of the powders.

Courbes de distribution cumulée en taille des particules de poudres (mesure par vitesse de sédimentation).

Figures 3.4(a), (b), (c) and (d) show the SEM images of primary particles of alumina A, alumina B, zirconia Z-3Y and TZ-2Y, respectively. According to the SEM images, the elementary particle sizes of zirconia Z-3Y and zirconia TZ-2Y are nearly 60 and 80 nm, respectively.

Specific surface area (SSA) of the powders, green compacts and partially densified compacts were measured by the BET method. The SSA results of the powders are given in Table 3.2.

Assuming that the elementary particles are spherical and dense, an equivalent BET grain size can be estimated from the Equation (3.1)

$$d_{BET} = \frac{6}{(SSA * \rho_{th})} \tag{3.1}$$

where ρ_{th} is the theoretical density of the solid.

So by this method particle size of the green compacts and partially densified compacts were also calculated from Equation (3.1).

These BET grain sizes are not significantly different than those of SEM elementary particle sizes (Figure 3.4). The difference between such elementary particle sizes and the D_{50} sedigraph value is probably due to the aggregate of elementary particles.

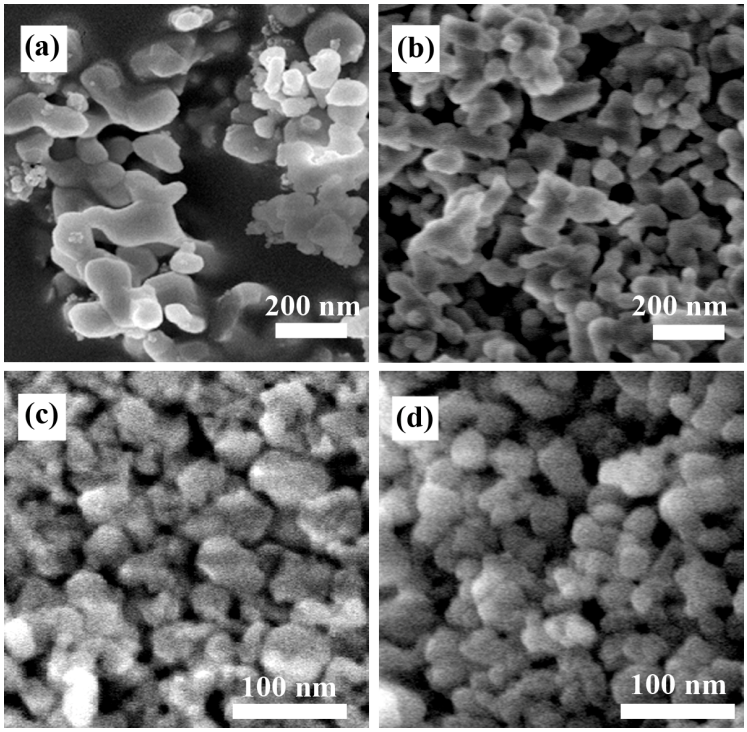

Figure 3.4. The primary particles of powders SEM images of (a) alumina A, (b) alumina B, (c) zirconia Z-3Y and (d) zirconia TZ-2Y.

Micrographies MEB montrant la taille des particules primaires (cristallites) des poudres : a) alumine A, b) alumine B, c) zircone Z-3Y et d) zircone 2Y.

Table 3.2. Chemical and physical properties of the powders (Baikowski 2010).

Caractérisitiques physico-chimiques des poudres mises en oeuvre.

		Alumina A	Alumina B	Zirconia Z-3Y	Zirconia TZ-2Y	Spinel
D_{50} (µm)		0.35	0.18	0.26	0.15	0.25
Specific Surface area BET (m^2/g)		14.3	13.3	31.76	19.65	31.0
Theoretical density (g/cm^3)		3.97	3.97	6.09	5.987	3.55
d_{BET} (µm)*		0.105	0.113	0.031	0.051	0.055
Granular Particle size (SEM) (µm)		-	-	20	42	-
Chemical Analysis (ppm)	Na	20	7.1		160**	10
	K	39	28		-	
	Fe	6	4.6		<20**	10
	Si	35	7.7		<20**	20
	Ca	3	1.8		-	5
	MgO	550	-		-	
	Y_2O_3	-	-		2.01	
	Al_2O_3	-	-		<50	

*calculated from BET data as described in the text.
** oxides.

3.3. Thermal Behavior of the Powders

Comportement thermique des poudres

To investigate the organic binders or additives inside the powders, thermal gravimetric analysis (TGA) (SETARAM, TG/DTA Setsys) were done. The powders were heated up to 700°C with 5°C/min heating rate. The results are shown in Figure 3.5. Zirconia Z-3Y and the spinel powders had the highest weight losses while alumina B powder had the lowest weight loss. The weight losses of both zirconia powders probably originated from loss of binder in the granulated powder. Spinel weight loss was probably derived from loss of sulphur during heating.

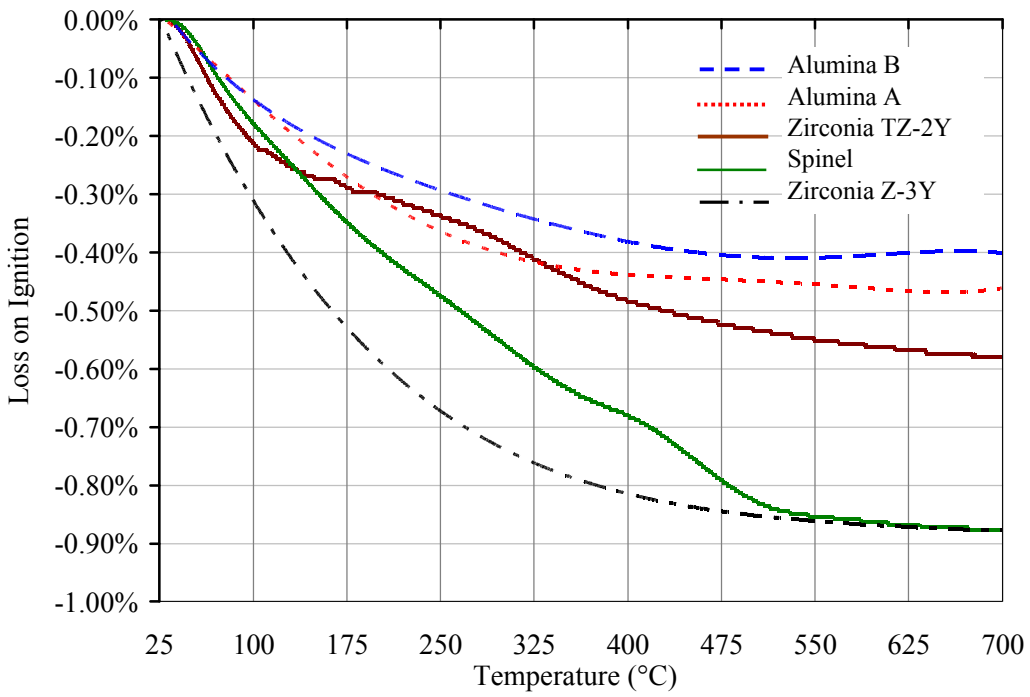

Figure 3.5. TGA results of the powders.

Analyse ThermoGravimétrique (ATG) des poudres.

3.4. Preparation of the Samples

Préparation des échantillons

Green bodies of the mono-materials were prepared by different compaction techniques. In the first method, green compacts were prepared by cold-isostatic pressing (CIP) (ACB ALSTHOM, Nantes-France) at a pressure of 150 or 250 MPa. The powders were also uniaxially pressed (UP) (PW-10 model, P/O/Weber) at different pressures of 150 or 250 MPa in a stainless steel die (ϕ: 8 mm).

3.5. Characterization of the Green Compacts

Caractérisation des corps crus

To investigate the compaction behaviour of the powders, the compaction diagrams were constructed. Single action-mode uniaxial compaction diagrams of powders were carried out in the steel cylindrical die up to 350 MPa by using on-line computer analysis of the powder densification (via a punch displacement) versus change of compaction pressure. The compaction diagrams are shown in Figure 3.6.

The density of the compact as a function of the applied pressure is commonly used to characterize the compaction behavior. The data can be easily measured and can find use in process optimization and quality control. The compaction data for granules often show two straight lines with two different slopes separated by a break point. Compaction is interpreted to occur by rearrangement in the low-pressure linear region and by deformation in the high-pressure linear region. Powders consisting of primary particles show a single line, whereas an agglomerated powder may show two lines with different slopes, with the break point determined by the strength of the agglomerates (Niesz, et al. 1977, Rahaman 1995). The zirconia powders used in this study were all agglomerated and showed this characteristic in their compaction behavior curves in Figure 3.6.

According to the compressibility curves, alumina B had the highest green density and alumina A had the lowest green density values. Spinel showed the highest gain in green density upon application of higher pressures. So warping phenomenon probably was expected during firing of that powder after single action mode uniaxial pressing. Because major causes of warping during firing is density variations in the green state. In single action mode uniaxial pressing of powder, pressure variations in the die cause different amount of compaction at different parts of the green pellet. Top part of the pellet in contact with the punch that applied the force had higher green density than the rest of the pellets. Therefore, higher firing shrinkage is expected for the parts that had lower green density. To avoid this type of problem and to provide better packing homogeneity, double-action mode compaction is preferred and this mode is commonly used in industry (Rahaman 1995). In this thesis most of the samples were compressed with floating die method (UPFlo), a very similar technique to double-action mode as well as by CIP (cold isostatic pressing).

The relative densities of green bodies of the powders at different applied pressures of 150 and 250 MPa are given in Table 3.3. Spinel showed the highest green density difference (5%) when pressure was increased.

SEM images of green compacts of alumina B and zirconia TZ-2Y which were cold isostatic pressed (CIP) at 250 MPa are shown in Figure 3.7. According to the images, zirconia TZ-2Y elementary particles are finer than alumina B and they have 100 nm and 50 nm average particle sizes, respectively in agreement with the SEM observation of non-compacted powders.

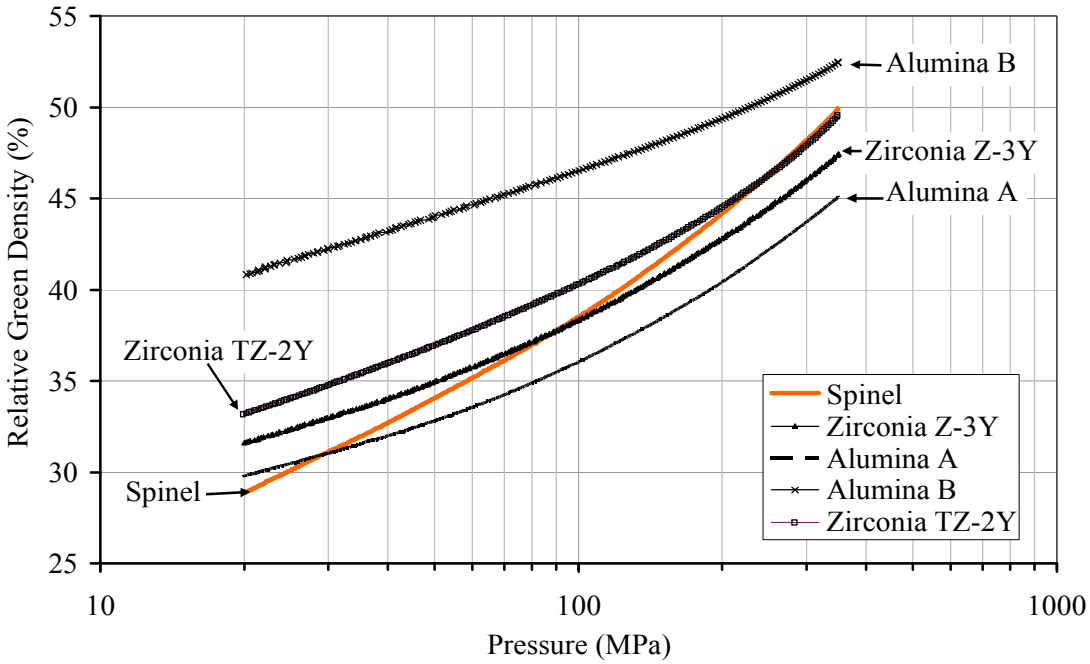

Figure 3.6. The compaction diagrams of powders with single action mode uniaxial pressing.

Courbes de compressibilité des poudres en mode uniaxial simple effet.

Table 3.3. Relative densities of compacts after uniaxial pressing (UP).

Densités relatives des comprimés de pressage uniaxial.

Compaction Pressure	Alumina A	Alumina B	Zirconia TZ-2Y	Zirconia Z-3Y	Spinel
150 MPa	38.3 %	48.3 %	43 %	41 %	42 %
250 MPa	42.5 %	51 %	47 %	44 %	47 %

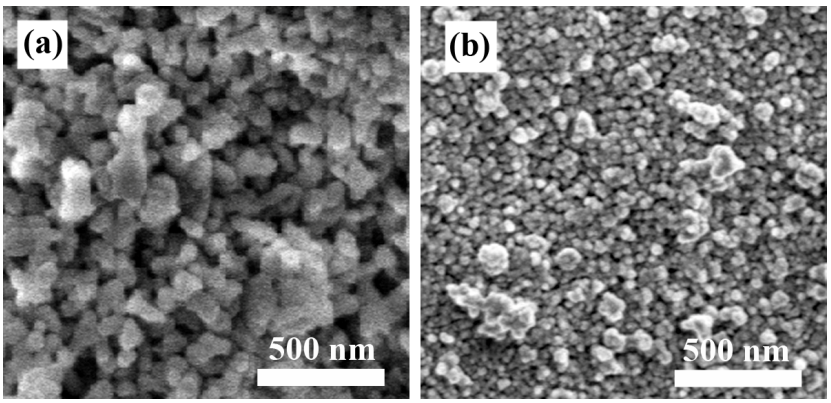

Figure 3.7. SEM images of powder compacts, CIPed at 250MPa (a) alumina B, (b) zirconia TZ-2Y.

Micrographies MEB de comprimés de poudres (pressage isostatique à froid sous 250 MPa) a) alumine B, b) zircone TZ-2Y.

3.6. Sintering

Frittage

In this study two different dilatometers were used to investigate the sintering behavior of the mono-materials. The first one was a vertical dilatometer (DHT2050K, Setaram, France) that can be heated up to 1550°C. The samples were sintered under constant heating rate conditions at various rates from 1 to l0°C/min up to 1550°C for 1 to 16 hours (or no-soaking time) under static air atmosphere. The dimensional change was measured in situ using pure alumina probes with a constant load 0.05 N, which corresponds to a pressure of about 1 kPa on a cylindrical sample with 8 mm diameter.

The second one was also a vertical dilatometer (L75VS-1750, Linseis, Germany) that could be heated up to 1750°C. The samples were sintered under constant heating rate conditions at various rates from 1 to l0°C/min up to 1580°C for 5 hours or no-soaking time under flowing argon atmosphere. In this dilatometer the load on the sample was also constant (0.1 N).

3.7. Density Measurements

Mesures de densités

The final density was measured by the Archimedes method (ASTM C 20-87). The immersion liquid was Xylene or water. The theoretical density of alumina and zirconia are 3.98 and 6.05 g/cm^3, respectively (Rahaman 1995).

3.8. Microstructural Characterization

Caractérisation des microstructures

A variety of techniques was used to characterize the microstructure of the green compacts and the sintered samples. The microstructures of the fracture surfaces, polished surfaces, and polished and thermally or chemically etched surfaces were observed by SEM.

Average grain size measured on the polished and thermally etched surface by the mean intercept area on a plane section technique, is demonstrated in Equation (3.2) (Bernard-Granger, et al. 2008a)

$$\bar{D} = 1.38 * \sqrt{\frac{L * h}{\left(N1 + N2/2\right)}} \tag{3.2}$$

N1 represents the number of grains which are completely inside the image and N2 represents the number of grains which are not completely inside the image. L is equal to length of image and h is related to height of image.

3.9. Shrinkage, Shrinkage Rate, Densification and Densification Rate Curves

Courbes de retrait, de vitesse de retrait, de densification et de vitesse de densification

In this section, shrinkage, shrinkage rate, densification and densification rate curves are explained using one of the powders as the example: alumina B. The shrinkage behavior of alumina B was obtained from dilatometer measurements. During the test, the sample under static air atmosphere was first heated up to 800°C and subsequently to 1500°C with constant heating rates of 10°C/min and 3.3°C/min, respectively. The blank test was performed by utilizing the same test conditions as in the dilatometer measurements. To get the correct shrinkage data, the blank test was subtracted from sample raw data.

$$\Delta L_{corrected} = \Delta L_{sample} - \Delta L_{blank} \tag{3.3}$$

The calculated relative shrinkage ($\Delta L_{(T)}/L_o$) of alumina B with respect to temperature is shown in Figure 3.8. Temperature dependent derivative of shrinkage $\frac{d\left(\Delta L_{(T)}/L_o\right)}{dT}$, in other words, shrinkage rate of sample was subsequently obtained from the data given in Figure 3.8 by taking into account any instant change in shrinkage profile of the sample during on-line measurements. The shrinkage rate curve of alumina B is shown in Figure 3.9.

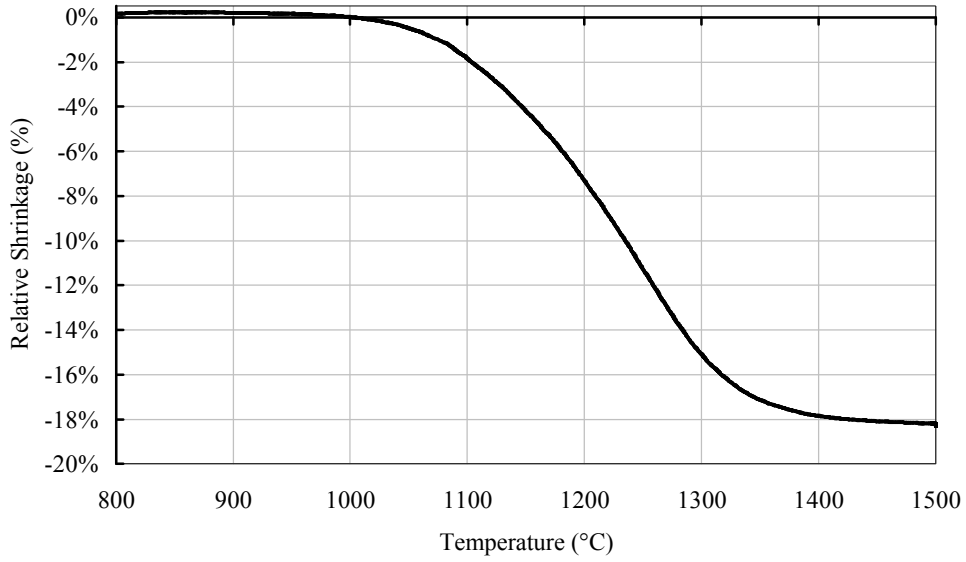

Figure 3.8. Relative shrinkage curve for powder compacts (CIP 250 MPa) of alumina B during sintering at a heating rate of 3.3°C/min.

Courbe de retrait de comprimés (CIP 250 MPa) de poudre d'alumine B pendant un essai de frittage anisotherme avec une vitesse de chauffage de 3,3°C/min jusqu'à 1500°C.

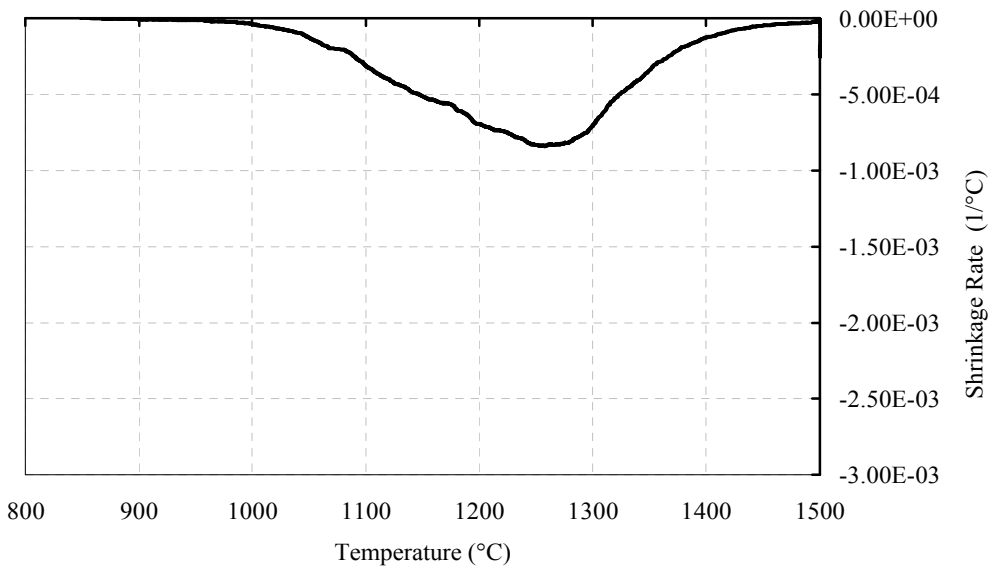

Figure 3.9. Shrinkage rate curve for powder compacts of alumina B (CIP 250 MPa) during sintering at a heating rate of 3.3°C/min.

Courbe de vitesse de retrait de comprimés (CIP 250 MPa) de poudre d'alumine B pendant un essai de frittage anisotherme avec une vitesse de chauffage de 3,3°C/min jusqu'à 1500°C.

The relative density (ρ) and its temperature derivative ($d\rho/dT$) are computed in accordance with Equations (2.7) and (2.8), respectively, which are already elucidated in Section 2.4.1. Relative density profile and densification rate of the corresponding

alumina B sample with respect to temperature are shown in Figures 3.10 and 3.11, respectively. Consequently, at the intended experimental conditions, the achieved final density for the sample was revealed to be 0.97, while the maximum densification rate was observed approximately at the temperature of 1280°C.

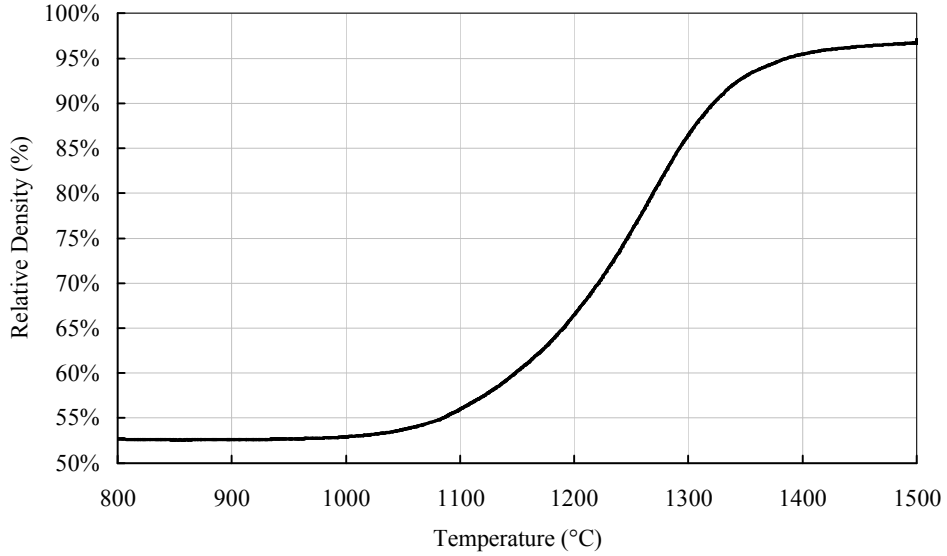

Figure 3.10. Relative density curve for powder compacts (CIP 250 MPa) of alumina B during sintering at a heating rate of 3.3°C/min.

Courbe de densification relative de comprimés (CIP 250MPa) de poudre d'alumine B pendant un essai de frittage anisotherme avec une vitesse de chauffage de 3,3°C/min jusqu'à 1500°C.

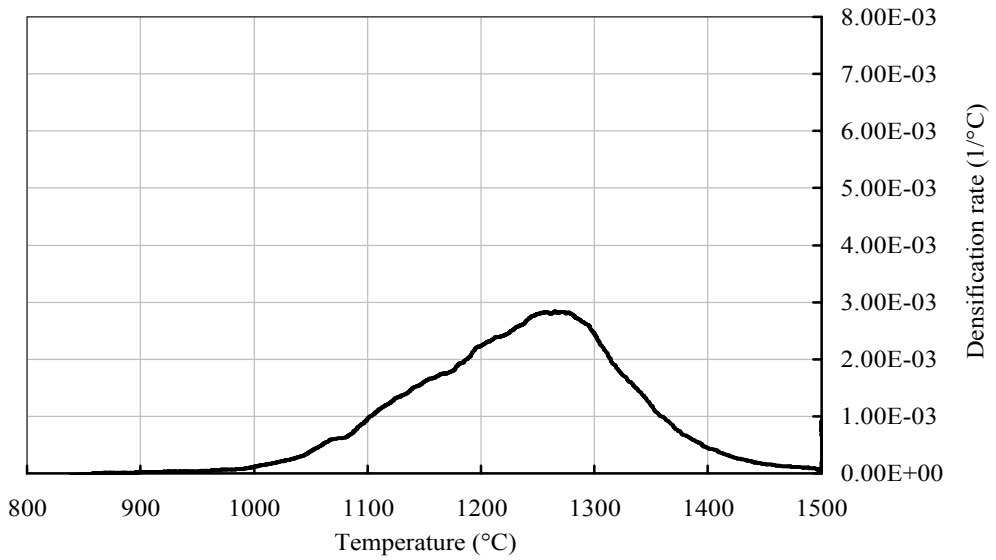

Figure 3.11. Densification rate curve for powder compacts of alumina B (CIP 250 MPa) during sintering at a heating rate of 3.3°C/min.

Courbe de vitesse de densification relative de comprimés (CIP 250MPa) de poudre d'alumine B pendant un essai de frittage anisotherme avec une vitesse de chauffage de 3,3°C/min jusqu'à 1500°C.

3.10. Results

Résultats

In this part, the sintering, densification behaviors and microstructures of mono-materials were investigated by dilatometers and by SEM to achieve more appropriate combination of bi-materials with higher densities and higher chemical and physical bonding by optimizing sintering parameters.

3.10.1. Effect of Dilatometer and Atmosphere

Effets du dialtomètre et de l'atmosphère

First of all the consistency of the dilatometers was tested. To compare Setaram and Linseis dilatometers and their atmosphere, alumina B samples were prepared at 250 MPa by cold isostatic pressing, and they were separately sintered in both dilatometers up to 1500°C with 3.3°C/min heating rate without a soaking time.

Figure 3.12 shows relative density (densification) and densification rate curves of alumina B samples after testing in each dilatometer. Their curves showed exactly the same behavior independent of the dilatometer or sintering atmosphere conditions.

Especially in the case of advanced ceramics, the sintering atmosphere can have a significant effect on microstructural evolution. Thus control of oxygen or nitrogen partial pressure as a function of temperature may in some cases be beneficial (De Jonghe and Rahaman 2003). Insoluble gases trapped in closed pores may obstruct final stages of densification or lead to post-densification swelling and, in these cases, a change of sintering atmosphere or vacuum sintering is indicated (Coble 1962a). In our cases pressure was not varied inside the dilatometers and there was no significant effect on sintering behavior of the powders from the type of the atmosphere.

3.10.2. Alumina Powders

Poudres d'alumine

Figure 3.13 shows relative density and densification rates of alumina A and alumina B samples at different heating rates. Alumina A powder contained 550 ppm of MgO while alumina B had none. So these two alumina powders might show different

effects when sintered in contact with other powders like spinel. According to the graphs (Figure 3.13), when heating rate decreases from 10 to 1°C/min, the temperature at which the maximum densification rate is observed to shift lower temperatures.

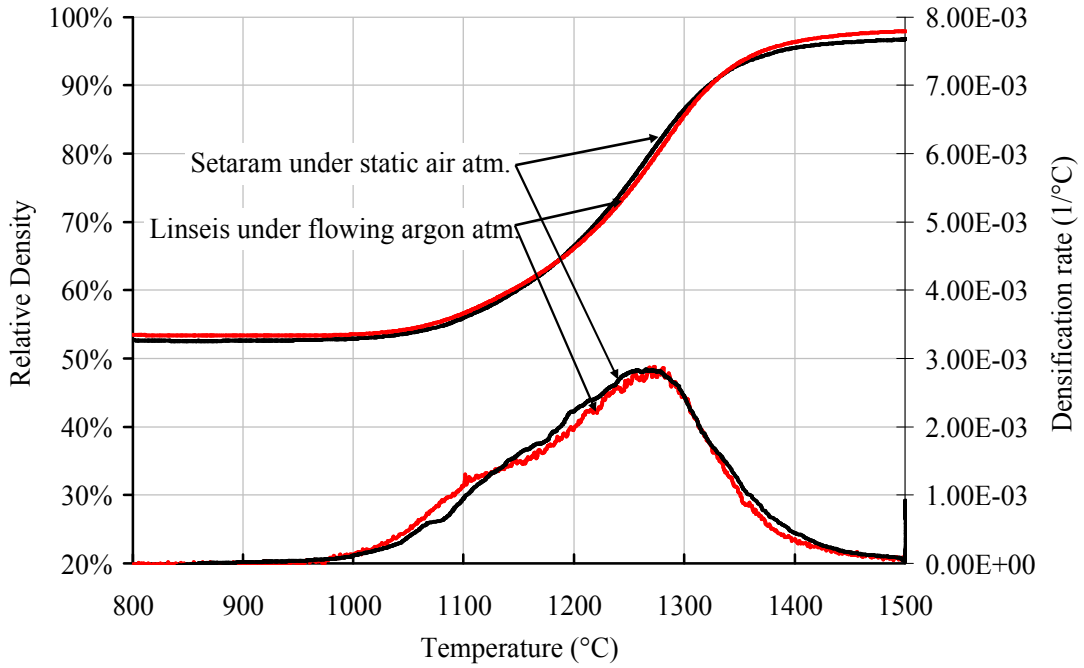

Figure 3.12. Comparison of the dilatometers and atmosphere effects on the densification and densification rate curves for powder compacts of alumina B (CIP 250 MPa and sintered with a 3.3 °C/min heating rate up to 1500°C).

Comparaison des effets du modèle de dilatomètre et de l'atmosphère sur les courbes de densification et de vitesse de densification de comprimés de poudre d'alumine B (CIP 250 MPa et fritté avec une vitesse de chauffage de 3,3°C/min jusqu'à 1500°C)

The SEM images of alumina powders are shown in Figure 3.14. In the alumina B sample (Figure 3.14(a)), which had 1°C/min of heating rate, grain size was larger than the same powder that was heated faster (Figure 3.14(b)).

Figure 3.15 shows the cross section of polished and thermally etched surfaces of alumina ceramics. They were both sintered with a heating rate of 1°C/min for soaking time of 1 hour at 1500°C. In consequence, alumina A was found to have a final density of 96 %, while alumina B had a density of 98%. However, the average grain size (0.9 μm) of alumina A was about two times smaller than that (2 μm) of alumina B. This difference may be due to the well known hindering effect of MgO additives on the grain growth in the alumina A powder (Bennison and Harmer 1990). In a similar manner,

Bateman et al., (1989) reported that very low content (0.1%) of MgO is capable of retarding the grain growth in alumina.

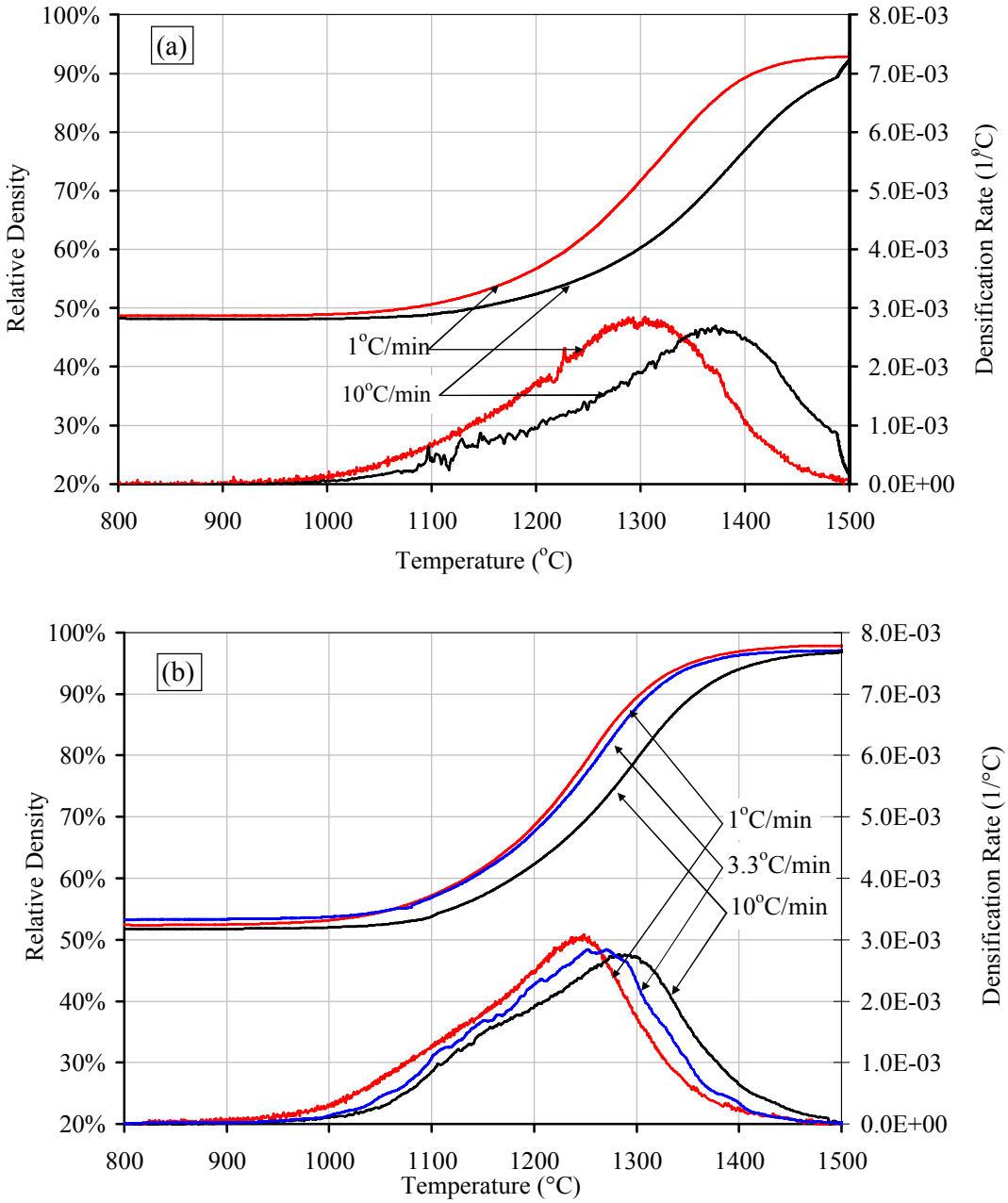

Figure 3.13. Densification curves during sintering at heating rates of 1, 3.3 and 10°C/min for powder compacts of (a) alumina A and (b) alumina B. The upper and lower curves in all (a) and (b) are the relative densities, ρ, and their temperature derivatives, $d\rho/dT$, respectively (all the samples were CIPed at 250 MPa).

Courbes de densification pour des essais de frittage à des vitesses de chauffage de 1, 3,3 et 10°C/min de comprimés de poudre de a) alumine A (dopée en MgO) et b) alumine B (non dopée). Les courbes du haut et du bas de la figure correspondent respectivement aux densités relatives et à leurs dérivées en température. Tous les échantillons avaient été Comprimés Isostatiquement à froid sous 250 MPa.

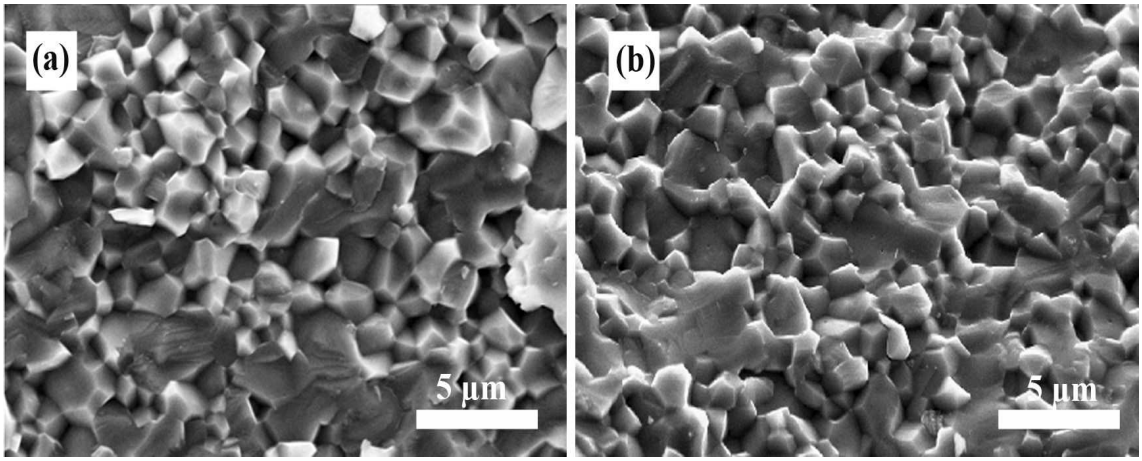

Figure 3.14. SEM micrographs of fracture surfaces of sintered alumina B powder specimens (CIP 250 MPa) treated at different heating rates (a) 1°C/min and (b) 10°C/min, without a soaking time at 1500°C.

Micrographies MEB de surfaces de rupture d'échantillons frittés d'alumine B (non dopée) (CIP 250 MPa) et frittés avec des vitesses de chauffage de a) 1°C/min et b) 10°C/min jusqu'à 1500°C sans temps de maintien à 1500°C.

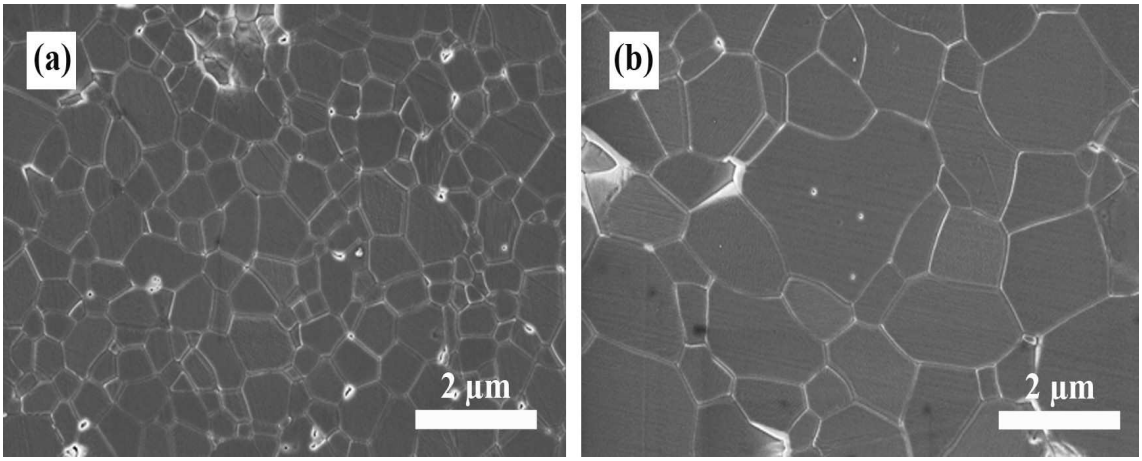

Figure 3.15. SEM images of polished and thermal etched surfaces of sintered powder specimens (a) alumina A and (b) alumina B (CIP 250 MPa), treated with 1°C/min heating rate for 1 hour soaking time at 1500°C.

Micrographies MEB de sections polies et attaquées thermiquement d'échantillons (CIP 250 MPa) de a) alumine A (dopée MgO) et b) alumine B (non dopée) frittés 1 heure à 1500°C avec une vitesse de chauffage de 1°C/min.

3.10.3. Zirconia Powders

Poudres de zircone

Sintering behaviors of zirconia TZ-2Y and zirconia Z-3Y powders were also investigated by plotting their densification curves. Figures 3.16(a) and (b) show the densification and densification rate curves of zirconia TZ-2Y and zirconia Z-3Y, respectively. For TZ-2Y powder, the densification and relative density curves shifted to lower temperatures, when heating rate decreased. On the other hand, zirconia Z-3Y powder showed an unexpected densification curve for the experiment at 1°C/min of heating rate. There was a hunch like shape (second maxima) at the lower temperature end of its densification rate curve (Figure 3.16(b)). This kind of behavior on the densification rate curves especially at very low heating rate (~1°C/min) conditions is probably due to very fine grained powders.

Zirconia Z-3Y had the finest grain size as mentioned in Section 3.2. According to SSA analysis and the resulting calculations, its primary crystallite size was around 31 nm which was very fine. In the literature, densification mechanism for very fine grained powders is reported to be controlled by interface reaction (He and Ma 2003a).

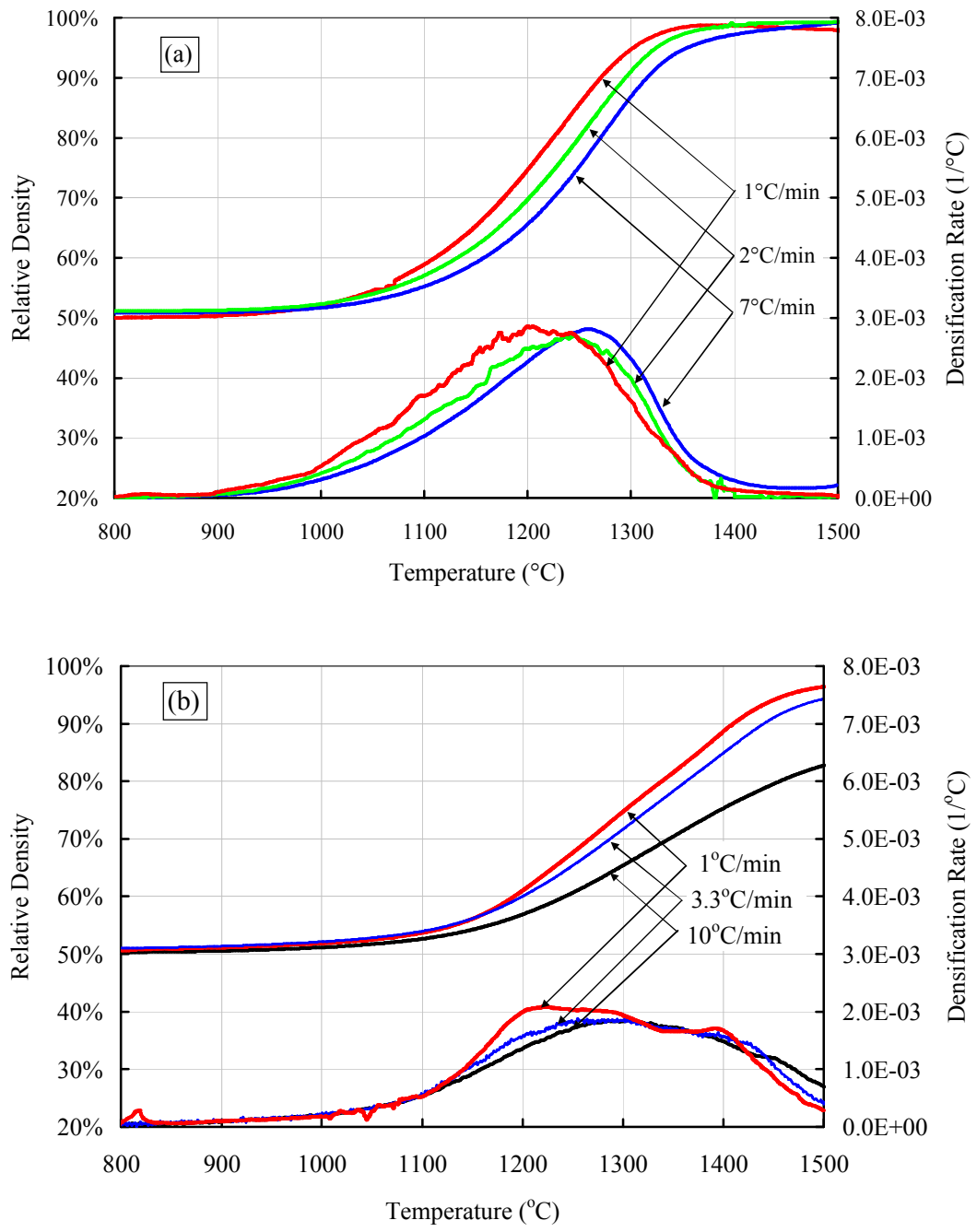

Figure 3.16. Densification curves during sintering at different heating rates for powder compacts of (a) zirconia TZ-2Y and (b) zirconia Z-3Y. In both graphs, the upper curves are the relative densities, ρ, and the lower curves are their temperature derivatives, $d\rho/dT$, respectively.

Courbes de densification pour des essais de frittage à des vitesses de chauffage de 1, 3,3 et 10°C/min de comprimés de poudre de a) zircone TZ-2Y et b)zircone Z-3Y). Les courbes du haut et du bas de la figure correspondent respectivement aux densités relatives et à leurs dérivées en température.

3.10.4. Effect of Compaction Process and Pressure on Fired Density

Effet du mode et de la pression de compactage sur la densité frittée

Uniaxial pressing in a die and isostatic pressing are commonly used for the compaction of dry powders. Die compaction is one of the most widely used operations in the ceramics industry. It allows the formation of relatively simple shapes rapidly and with accurate dimensions. The agglomeration of dry powders combined with the nonuniform transmission of the applied pressure during compaction leads to significant variations in the packing density of the green body. Isostatic pressing produces better uniformity in the packing density and can be used for the production of green bodies with complex shapes (Rahaman 1995).

In this section, the effects of applied compaction pressure and the type of compaction process are compared to evaluate the forming methods. The effect of compaction pressure on the sintering behavior of powders was investigated in the case of zirconia TZ-2Y powder. The powder was cold isostatically pressed (CIP) at two different levels of 150 and 250 MPa. The compacts were sintered in dilatometer at 1500°C for 1 hour with 1°C/min heating rate. The densification and densification rate results are shown in Figure 3.17. According to the results, there was no significant difference on the sintering curves of 150 MPa and 250 MPa. As was expected, initial green density of the low pressure compacted sample was slightly lower than that of the high pressure compacted one. Eventually, their final densities were the same at the end of the sintering process. For Uniaxial Pressing (UP) conditions the initial relative densities were respectively 43% and 47% (Table 3.2). As mentioned above, the applied pressure is not transmitted uniformly to the powder due mainly to friction between the powder and the die wall that leads to significant variations in the packing density of the green body. On the other hand, CIP produces better uniformity in the packing density, therefore TZ-2Y powder has higher green density values after CIP than UP at the same applied pressures.

The scanning electron microscopy images of sintered zirconia powders are shown in Figure 3.18. The samples were broken to observe their fracture surfaces. No significant difference was observed between the microstructures of the two zirconia powder samples as shown in Figure 3.18. In brief, the selected compaction pressures did not affect the densification behavior of zirconia powder significantly.

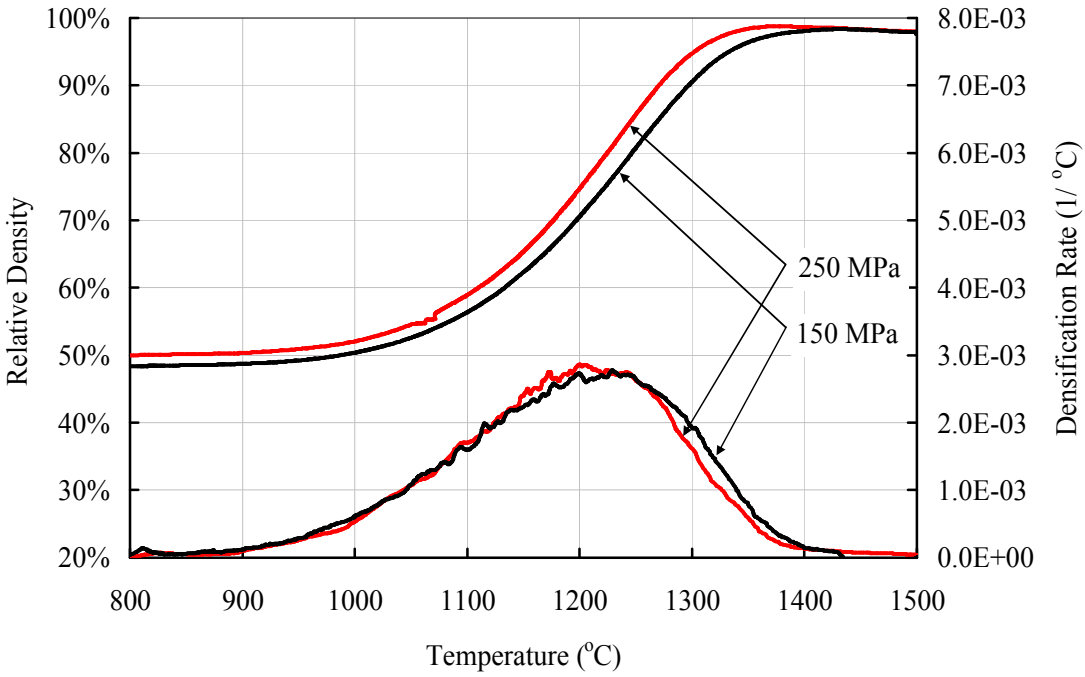

Figure 3.17. Effect of CIP compaction pressure on the sintering of zirconia TZ-2Y, 1°C/min heating rate.

Effet de la pression de compactage en compression isostatique à froid sur le frittage de la poudre TZ-2Y avec une vitesse de chauffage de 1°C/min.

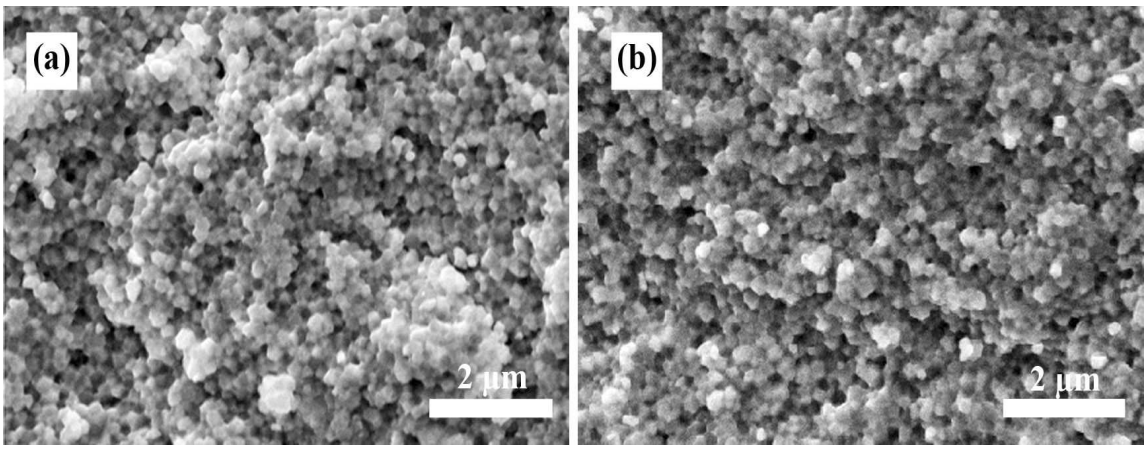

Figure 3.18. SEM micrographs of sintered zirconia TZ-2Y powder specimens, compacted at different pressures of (a) CIP 150 MPa and (b) CIP 250 MPa, were sintered at 1500°C with 1°C/min heating rate.

Micrographies MEB de surface de rupture après chauffage à 1°C/min jusqu'à 1500°C d'échantillons de zircone TZ-2Y comprimés isostatiquement à froid sous a) 150 MPa et b) 250 MPa.

The compaction techniques of CIP and UP were compared on the shrinkage curves of alumina A compacts. As discussed above, their initial green densities as well as their final densities were considerably different shown in Figure 3.19.

The shrinkage of spinel was tested for anisotropy. It was found that there was no significant difference between the longitudinal and transverse axis. This result was also recently confirmed by another study on the same spinel powder (Benameur, et al. 2010).

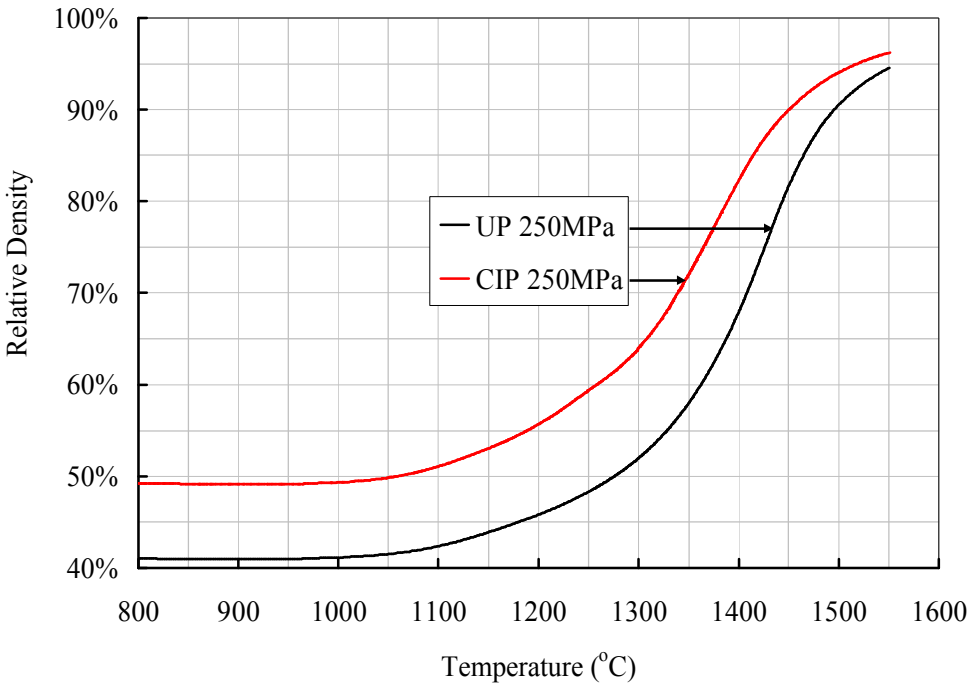

Figure 3.19. Effect of compaction process on the sintering of alumina A compacts, sintered with 3.3°C/min constant heating rate up to 1550°C.

Effet du mode de compactage sur le frittage de comprimés d'alumine A frittés jusqu'à 1550°C avec une vitesse de chauffage de 3,3°C/min.

3.10.5. Determination of Apparent Activation Energies for Densification

Détermination des energies d'activation apparentes de la densification

In this section, the activation energies of alumina B and zirconia Z-3Y powders are displayed to understand more clearly the densification behaviors of the two powders. For the sake of brevity, the Arrhenius plots of the other powders (alumina A and zirconia TZ-2Y) are given in Appendix A. Arrhenius plots were drawn by using Equation (2.11) at different relative densities of 0.60, 0.65, 0.70, 0.75, 0.80, and 0.85.

The Arrhenius plots of alumina A and alumina B are depicted in Figure 3.20. The slopes of the plots allow calculation of the activation energies, giving values of 660 kJ/mol and 680 kJ/mol, respectively. But usually, activation energies are determined from sintering experiments within an error of 3 to 20% despite all precautions to ensure ideal conditions (German 1996). The activation energy measurements for intermediate-stage sintering of alumina were in good agreement with the literature (Wang and Raj 1990). Alumina A doped with 550 ppm magnesia had the nearly same value with alumina B. So, magnesia doping was found not to significantly affect the activation energy. This result was also consistent with the literature (Sato and Carry 1996).

Figure 3.21 shows the Arrhenius plots of zirconia Z-3Y and TZ-2Y. The slopes of the plots allow calculation of the activation energies, giving values of 530 kJ/mol and 840 kJ/mol, respectively. The straight lines were not parallel to each other. This signifies unambiguously that the apparent activation energy of the mechanism controlling densification, Q_d, is a direct function of the relative density (Figure 3.22). It was observed that the apparent activation energy value of zirconia Z-3Y decreased linearly with an increase in the relative density. As mentioned in Section 3.1. concerning the densification of zirconia powders, Granger and Guizard explained the relation of activation energy increases with the relative density via a point defect formation step and grain boundary diffusion of Zr^{4+} cations (Bernard-Granger and Guizard 2007b). This defect formation step or defect absorption steps could be the limiting step of sintering kinetics especially for ultrafine grained compacts (nano structured materials) in which the diffusion distance is also nanometric. Zirconia Z-3Y had a large interval for the apparent activation energy (300-700 kJ/mol) value which includes the traditional 615–650 kJ/mol range commonly reported for pure TZ-3Y material (Matsui, et al. 2005, Wang and Raj 1991). For the case of zirconia TZ-2Y, the same parallel trend for each density value was observed similar to alumina powders (Figure 3.23).

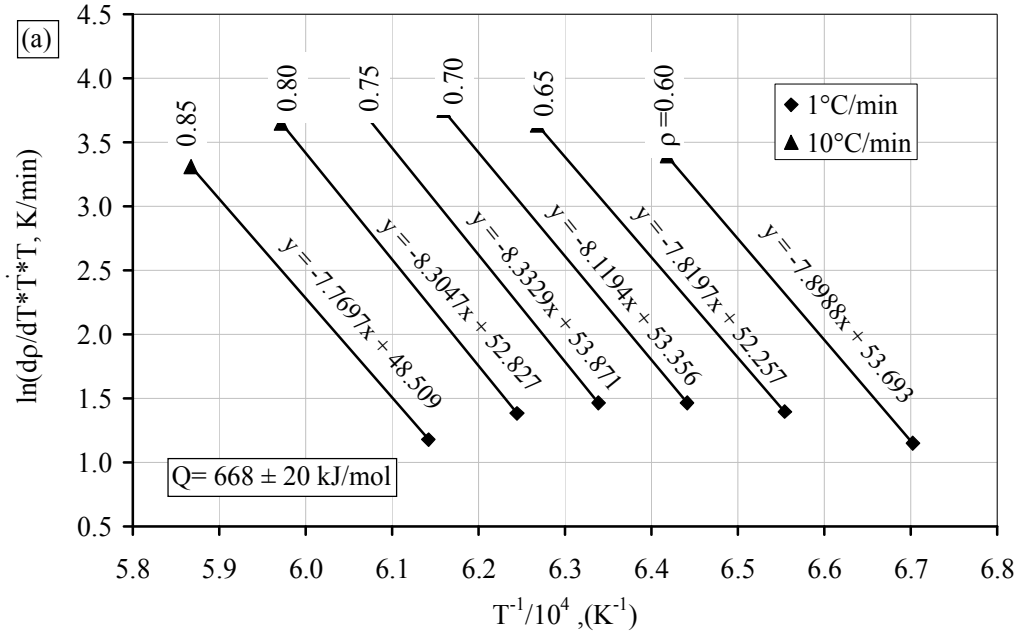

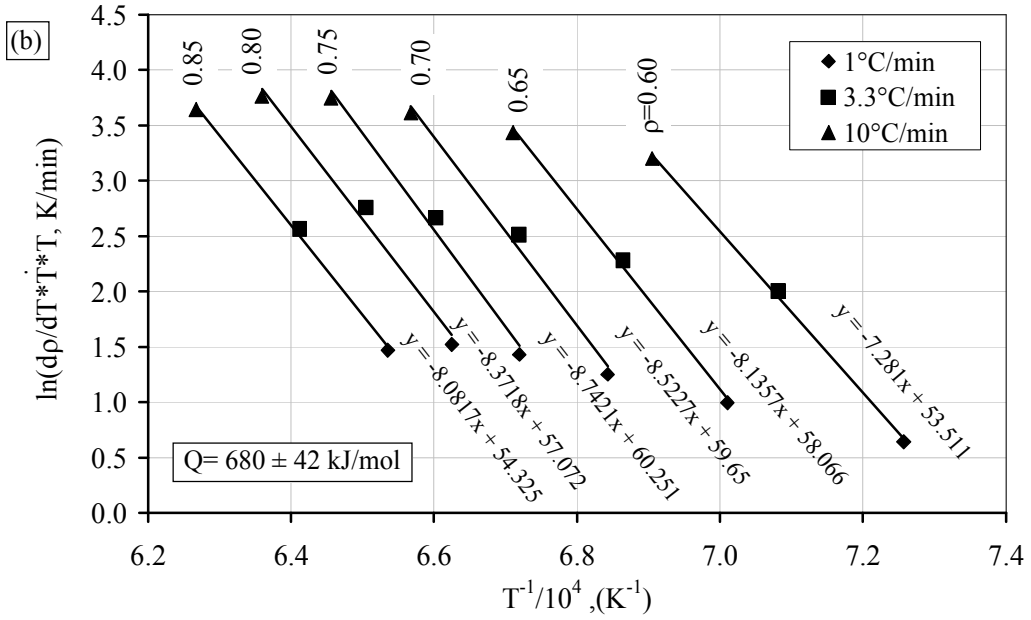

Figure 3.20. Arrhenius plots of constant heating rate sintering for pellets (CIP 250 MPa) of alumina A and (b) alumina B.

Diagrammes d'Arrhenius des vitesses de densification d'essais de frittage à vitesses de chauffage constantes de a) l'alumine A (dopée MgO et b) l'alumine B (non dopée).

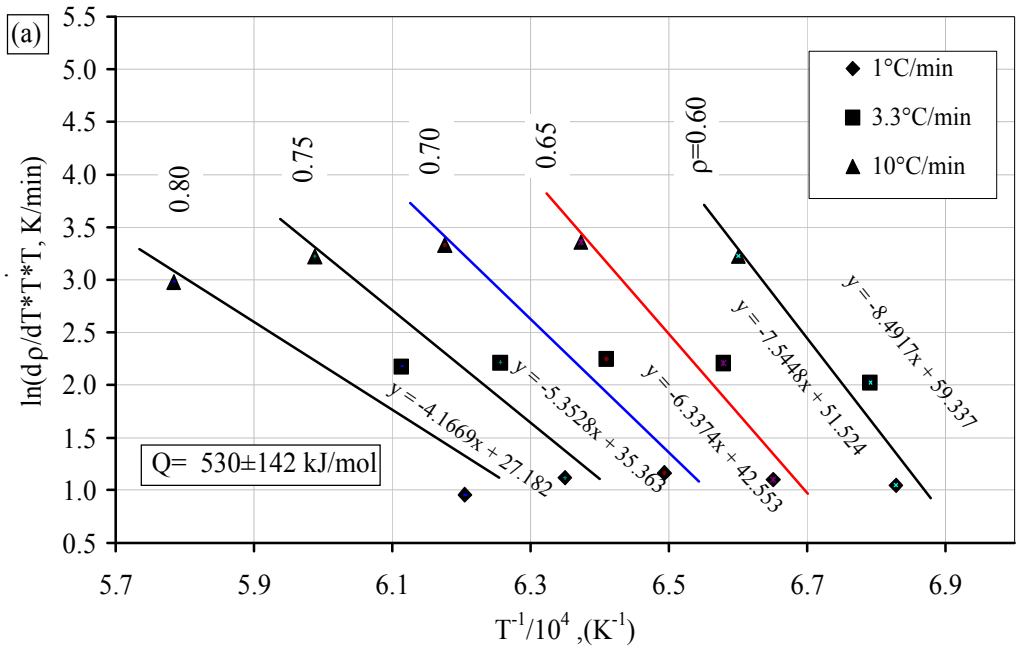

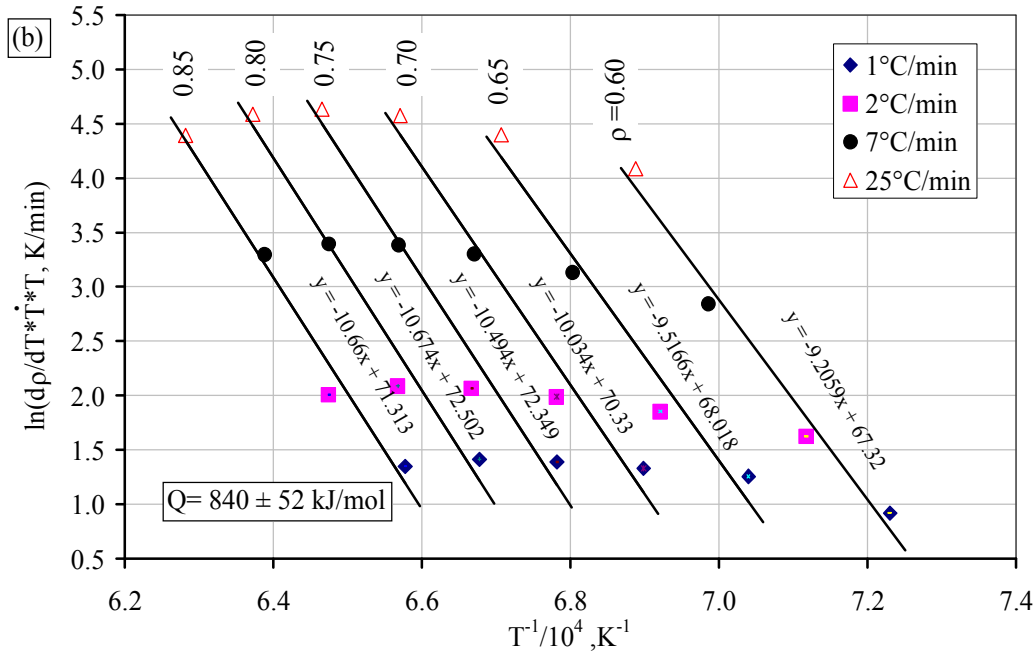

Figure 3.21. Arrhenius plots of constant heating rate sintering for pellets (CIP 250 MPa) of (a) zirconia Z-3Y and (b) zirconia TZ-2Y.

Diagrammes d'Arrhenius des vitesses de densification d'essais de frittage à vitesses de chauffage constantes de a) zircone Z-3Y et b) zircone TZ-2Y.

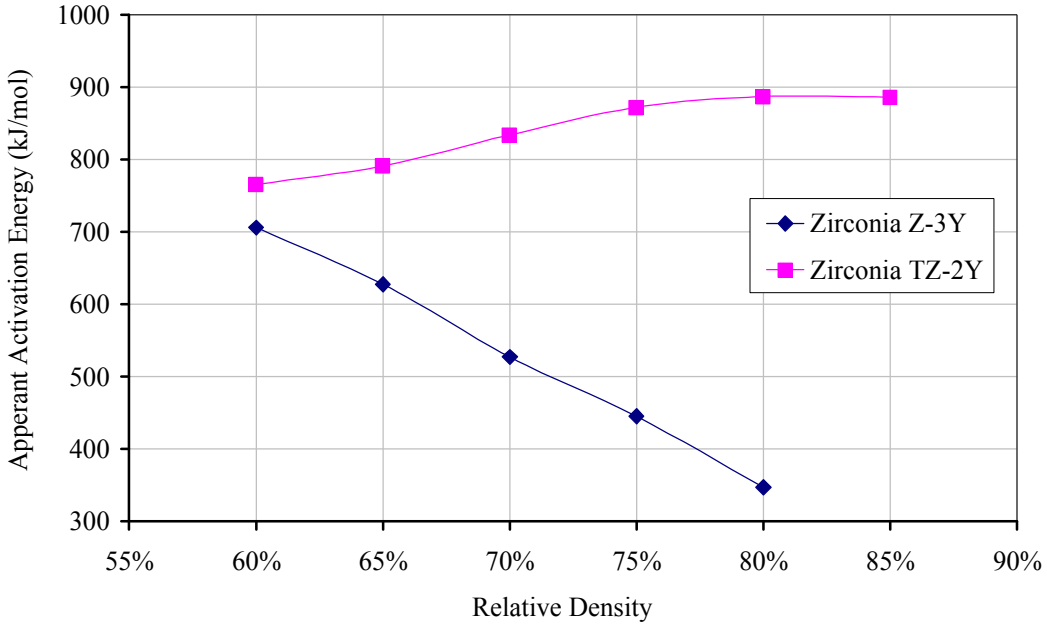

Figure 3.22. Apparent activation energies for densification versus relative densities of zirconia Z-3Y and TZ-2Y powders.

Energies d'activation apparentes de la densification en fonction de la densité relative pour les poudres de zircone Z-3Y et TZ-2Y.

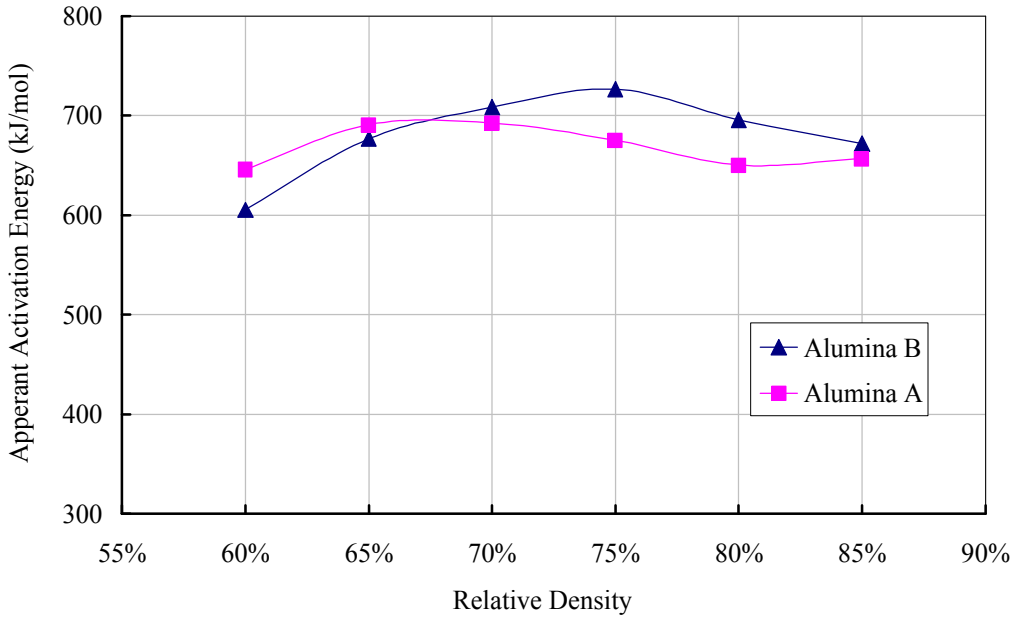

Figure 3.23. Apparent activation energies for densification versus relative densities of alumina A and alumina B powders.

Energies d'activation apparentes de la densification en function de la densité relative pour les poudres d'alumine A (dopée MgO) et B (non dopée).

3.11. Conclusions

Conclusions

In this chapter, physical and chemical properties of alumina and zirconia powders and their sintering behaviors were characterized. All powders were found to be high purity with a large BET surface area between 13 and 32 m^2/g. Consequently, zirconia powders were all agglomerated with spherical or doughnut shapes. The sintering behaviors of the mono-material as tested in a dilatometer showed that alumina B shrank by 18% after exposure to 1500°C and maximum densification rate for 3.3°C/min of heating rate occurred at 1250°C for this powder. A total relative density of 97% could be achieved.

When the same tests were done on Z-3Y powder an unexpected bump was observed in the shrinkage rate versus temperature diagrams. This bump was thought to originate from the very fine particle size fraction of the powder. Zirconia powder showed the maxima in its densification rate versus temperature diagram at 1200 to 1300°C depending on the heating rate.

Sintered microstructures of the powders were investigated from fractured surfaces as well as polished and thermally etched surfaces. MgO doped alumina was found to have a grain size of 0.9 µm while the undoped alumina had 2.0 µm. The apparent activation energies (Q_d) of powders were calculated. Alumina A and alumina B powders had nearly the same apparent activation energies of 680 and 660 kJ/mol, respectively. The activation energy value for zirconia was 530 kJ/mol for the Z-3Y powder. TZ-2Y powder had an activation energy value of 840 kJ/mol. More experiments at different heating rates could provide more precise activation energy measurements and confirm the decrease of apparent densification activation energies of zirconia for increasing relative density. Such high apparent activation energies at the beginning of the densification could be related to an interface reaction controlled mechanism as long as the crystallite sizes are lower than 100 nm.

CHAPTER 4

SINTERING BEHAVIOR OF A MAGNESIUM ALUMINATE SPINEL POWDER

Comportement en frittage d'une poudre de spinelle aluminate de magnésium

Résumé

Le comportement en densification de comprimés de poudre de spinelle a été caractérisé lors d'essais avec suivi du retrait par dilatométrie verticale. Deux pics séparés par un léger minimum sont observes sur les courbes de vitesse de densification en fonction de la température. Pour une vitesse de chauffage de 1°C/min ces pics de vitesse se situent respectivement à 1240°C et 1370°C. L'allure de ces courbes de vitesse de densification semble probablement caractéristique de la poudre commerciale utilisée. La croissance granualaire a été étudieé par des essais isothermes à 1500°C et une valeur de l'expoant m de la loi classique $(d)^m-(d_o)^m=Kt$ *a été estimée à 2,75. Cette valeur est différente de celles rapportées dans la littérature et pourrait être due à la présence de pores ou d'impuretés résiduels. Benamuer et al., (2010) ont observélors d'une étude sur le même type de poudre commerciale de spinelle que le taux d'impureté diminuait significativement pendant le cycle de frittage. Des énergies d'activation apparentes pour la densification de comprimés de poudre de spinelle ont été déterminées par deux approches expérimentales différentes lors d'essais de frittage en conditions anisothermes avec des vitesses de montée en température constante allant de 1 à 10°C/min. Sur la base de la pente de diagrammes d'Arrhenius à densité relative constante, une énergie d'activation apparente moyenne de 860 kJ/mol a été estimée. Cette énergie d'activation apparente semble décroitre quand la densité relative augmente jusqu'à 80 % et ensuite augmenter très nettement pour les densités relatives plus élevées. L'approche par la technique de la courbe de frittage de référence a conduit à une valeur d'énergie d'activation apparente de 863 kJ/mole très proche de*

celle de déterminée à partir des diagrammes d'Arrhenius. Ces énergies d'activation apparentes sont proches de celles rapportées par Benameur et al.(Benameur, et al. 2010) pour une poudre commerciale de même origine. Ces énergies d'activation seraient caractéristiques de cette poudre. Les valeurs élevées pour les faibles densités relatives (début du frittage) pourraient être liées aux très petites tailles intiales des cristallites de spinelle et traduire une cinétique de densification gouvernée par une réaction d'interface. Les distances de diffusion étant très courtes la cinétique de frittage ne dépendrait plus de la cinétique de diffusion mais de la réaction de création ou d'adsorption des espèces diffusantes dans les zones source ou puit.

La caractérisation des microstructures de frittage des échantillons de spinelle de densité supérieure à 80 % a mise en évidence les biais de mesure de taille de grains engendrés par la technique de révélation des microstructures par attaque thermique. L'attaque thermique de surfaces polies (classiquement une vingtaine de minutes à une température de 50°C inférieure à la température maximum du cycle de frittage) présente deux inconvénients : la fermeture ou le comblement des pores et une possible recristallisation- croissance granulaire. Pour des échantillons de spinelle à 85% ou à 99 % de densité relative des temps d'attaque dans l'acide orthophosphorique à chaud de respectivement 10 et 15 minutes donnent les meilleurs résultats ; les niveaux de porosité mesurés soit par analyse d'image soit par immersion dans un liquide sont en très bon accord.

Dans la seconde partie de ce chapitre l'effet sur la microstructure de cycles de frittage non classiques a été étudié pour approcher des cycles de frittage conduisant aux meilleurs compromis densité relative - taille de grains. Des traitements de précoalescence de huit à dix heures dans la gamme de temperature 1100 – 1200°C ont conduit à la disparition du premier pic de vitesse de densification : cette disparition de pic serait due à la coalescence des grains les plus petits sur les plus gros qui entrainerait un resserrement de la distribution en taille des cristallites. Des cycles de frittage en deux étapes ont été pratiqués avec trois différents cycles thermiques. Une augmentation de la densité relative jusqu'à 96 % a été observée sans augmentation notable de la taille de grains (460 nm). Des densités relatives légèrement plus élevées sont possibles par une combinaison de prétraitements de coalescence et de cycle en deux étapes. La densité la plus élevée a été obtenue par un prétraitement à 1200°C suivi d'un frittage à 1500°C pendant 10 heures mais au détriment d'une certaine croissance granulaire.

4.1. Introduction

Introduction

Magnesium aluminate spinel, $MgAl_2O_4$ (called spinel, hereafter) is an attractive material due to its desirable thermal (Bartha and Klischat 1999) and optical properties (Mroz, et al. 2005). Because of its wide range of applications, numerous studies on spinel are published each year. At the beginning, the articles were focused on understanding the fundamental densification and microstructure evolution mechanisms. But later in the last ten years, production of transparent spinel with different production methods like hot-press sintering (Kleebe, et al. 2005, Ting and Lu 1999a), spark plasma sintering (Bernard-Granger, et al. 2009, Morita, et al. 2009) etc. has become the main objective of the studies. Recently, Reimanis and Kleebe (2009) published a comprehensive review on the sintering and microstructure development of transparent spinel. They reported a thorough literature review of densification behaviour of transparent spinel with or without additives.

In the literature of spinel, most of the studies on densification mechanisms utilized reactive sintering process (Chiang and Kingery 1989, Chiang and Kingery 1990, Ting and Lu 1999a, Ting and Lu 1999b, Ting and Lu 2000). It is a particular type of sintering process in which the chemical reaction of the starting powders and the densification of the powder compact are both achieved during a single firing process.

In practice, reaction sintering has several shortcomings, so the process finds little use in the production of single-phase solids. The reactions involve energy changes that are considerably larger than the changes in surface energies, the classical driving force of non reactive solid phase sintering, and as a result, they can lead to microstructures that inhibit densification. Other shortcomings include the risk of chemically inhomogeneous products due to incomplete reaction and difficulties in controlling the microstructure as a result of the added complexity introduced by the reaction (Rahaman 1995).

Ting and Lu extensively studied the sintering kinetics of spinel based on atomic defect reactions. They produced stoichiometric and nonstoichiometric magnesium aluminate spinel by reaction between MgO and Al_2O_3 powders during conventional sintering process. So synthesis and densification mechanisms take place during constant heating rate period. Using densification rate versus grain size plots they calculated a 499

kJ/mol of activation energy value and grain-size exponents "*n*" (in Equation (2.9)) of 2.35 and 2.47 for nonstoichiometric and stoichiometric spinel, respectively. As a result, they suggested that the rate controlling mechanism is lattice oxygen diffusion through vacancies. The discrepancy between their *n* values and that for lattice-diffusion-controlled densification (n=3) was attributed to the concurrent mechanisms during sintering (Ting and Lu 1999b).

In another study, Ting and Lu (2000) investigated the effect of sintering atmosphere (vacuum sintering) on the sintering kinetics of stoichiometric and nonstoichiometric spinel. According to their results, MgO rich spinel showed higher densification rate than Al_2O_3-rich or stoichiometric spinel independent of the sintering atmosphere. They observed nearly 50 µm thick abnormal grain growth region at the surface of the sample due to MgO evaporation from the surface (Ting and Lu 2000).

Rozenburg and co-workers (Rozenburg, et al. 2008) determined the optimum sintering processing conditions for a hot-pressed magnesium aluminate spinel containing LiF. In order to drive densification mechanisms, they calculated activation energy for undoped and LiF doped spinel samples from measurement of shrinkages of samples during hot-press sintering. The pure spinel (no LiF) activation energy was found to be 500 kJ/mol at 33 MPa under hot-pressing, which was the highest energy for specimen with or without additives. They used master sintering curve (MSC) method to calculate the activation energy values.

Bratton studied the grain growth kinetics of spinel and found that the grain growth exponent, *m*, in equation (2.2) should be 2 (Bratton 1969, Bratton 1971). He concluded that if the ceramic is porous, the value of *m* is more likely to be 3. He determined that volume diffusion mechanism was operating for both initial and intermediate stages of densification and oxygen ions were the rate-controlling species during the sintering of spinel. A similar study on spinel was made later by Chiang and Kingery who showed again that *m* is equal to 2 (Chiang and Kingery 1989).

Recently, Benameur et al., (2010) investigated pressureless-sintering behavior of a stoichiometric commercially available fine-grained spinel powder which is the same spinel powder (S30-CR, Baikowski) that is used in this study. They observed peaks and shoulders on the densification rate curves of the spinel powder at different constant heating rate sintering tests and plotted the sintering path of the powder (grain size versus relative density trajectory) to determine the control mechanisms for densification and grain growth. Sintering path results were tested and fitted with their established

theoretical expression (Bernard-Granger and Guizard 2008b). As a result, they determined that grain growth was controlled by grain boundary diffusion and densification was controlled by either volume diffusion or grain boundary diffusion. They calculated activation energies for densification and grain growth by using the Arrhenius plots and Master Sintering Curve (MSC) methods. Their calculated activation energy results were not in agreement with the previous literature results (Rozenburg, et al. 2008, Ting and Lu 1999a) as shown in Table 4.1. They proposed that the difference was due to the motion of the Frenkel defects associated to O^{2-} anions in both mechanisms.

Table 4.1. Calculation of activation energies for densification and grain growth controlling mechanisms of a commercial spinel powder (Source : Benameur, et al. 2010).

Estimation des énergies d'activation des mécanismes gouvernant la densification et la croissance granulaire d'une poudre commerciale de spinelle (de Benameur et al. 2010).

	Applied Methods	
	Arrhenius Plots	Master Sintering Curve
For Densification Controlling Mechanisms	875 kJ/mol	950 kJ/mol
For Grain Growth Controlling Mechanisms	1070 kJ/mol	1100 kJ/mol

Dense spinel ceramics are increasingly investigated for different potential applications. Nonuniformities in green bodies, particle packing and degree of agglomeration of the starting powder lead to nonuniformities in the fired product which eventually prevents full densification (Shaw 1989). A particle size distribution can have significant effects on sintering. When the starting powder has a bimodal particle size distribution, for example, the densification behavior of the ceramic during sintering will be different from a powder with monomodal size distribution. For a few oxide ceramics, the use of a precoarsening step prior to densification has been observed to produce an improvement in the microstructural homogeneity during subsequent sintering (Chu, et al. 1991, Lin, et al. 1997, Sato and Carry 1995). Nano-sized particles in the powder coarsen while the average larger particle size does not increase significantly. Precoarsening pretreatment of ceramics is usually done for better microstructural

homogeneity via enhanced neck formation between the particles to obtain a stronger compact and for elimination of smallest particles (Lin, et al. 1997). In the remaining part of sintering the compact is better able to resist differential densification by eliminating local densification of finest particles.

Chu et al., (1991) investigated the effect of low temperature pre-treatment of Al_2O_3, MgO and ZnO green compacts without densification. They observed that compacts produced by pre-treatment have more uniform microstructures than the initial ones. They, however, gave neither detailed observation nor clear explanation on how the densification proceeded and the microstructure developed during the subsequent sintering. Sato and Carry (1995) applied precoarsening process for two kinds of commercial, submicron-grained, nondoped α-alumina powders. The shoulder in the subsequent densification rate versus temperature curves was eliminated due to the disappearance of nano-particles during the pre-treatment process. They observed that the final microstructure is slightly coarser than the conventionally sintered (i.e., without the initial heat treatment step) one after pre-treatment process. A study by Lin et.al., (1997) involved the effect of a precoarsening step (50 hours at 800°C) on the subsequent densification and microstructural evolution of alumina (Al_2O_3) powder compacts during constant-heating-rate sintering (4°C/min to 1450°C). They observed that compared to conventional sintering, after the precoarsening step, the average pore size was increased while the pore size distribution became narrower. A comparably higher final density, a smaller average grain size, and a narrower distribution in grain sizes were achieved with precoarsening.

Achieving a high density and at the same time, a small grain size is very important for ceramic materials because it gives an improvement of mechanical properties. For example, in order to improve mechanical strength, some efforts have been focused on minimizing final grain size of spinel (Patterson, et al. 2003). In addition to improvement of mechanical properties dense spinel was studied for optical transparency applications as well (Li, et al. 2000).

Two Step Sintering (TSS) is the most widely applied sintering process to obtain relatively dense and small grain size materials. It was first suggested by Chen and Wang (2000) to produce fully dense cubic Y_2O_3 with a grain size of 60 nm. In this technique, the powder compact is heated to a temperature (T1) which is generally 50-100°C higher than the soak temperature (T2). First step from time zero to T1 temperature is done to obtain 75% relative density after which the temperature is decreased sharply to T2

where the material is soaked until full density with limited growth of grains is obtained. Since it was a new kind of sintering technique, it has been applied to various ceramic materials such as Al_2O_3 (Bodisova, et al. 2007, Hesabi, et al. 2009), yttria stabilized ZrO_2 (Wang, et al. 2009), Y_2O_3 (Wang, et al. 2006a) and $BaTiO_3$ (Wang, et al. 2006b), etc. The efficiency of TSS method was also tested on different types of crystal structures (cubic, tetragonal and hexagonal) (Maca, et al. 2010).

Studies involving sintering and densification behavior of spinel as mentioned above (Bernard-Granger, et al. 2009, Chiang and Kingery 1989, Ting and Lu 2000) depend critically on the ability to correctly measure the grain size and porosity on polished and etched cross sections of samples. Because ceramics are brittle materials it is significantly more difficult to prepare samples compared to metals (Cook, et al. 1995). They are more stable, more brittle and harder. The difficulty arises during cutting, grinding, polishing and etching. If the researcher is not careful, artifacts can be easily mistaken for true microstructures. Inaccurate measurement of grain size or porosity can produce misleading results that are difficult to interpret on scientific grounds. Pull-outs and fragmentation of grains are common in ceramics during cutting, grinding and polishing. Deformation twins and dislocations can also develop during grinding (Elssner, et al. 1999). But there is additional potential problem that arises during etching of the polished cross sections as explained below.

Sintered spinel ceramics are generally etched by thermal etching at temperatures 50-300°C lower than the sintering temperature (Ting and Lu 2000). During thermal etching, loss of material occurs through vapor phase transport from the grain boundaries leaving a groove behind that makes observation of the grain boundaries possible. But chemical etching (Chiang and Kingery 1989) is also performed on polished samples with hot orthophosphoric acid (H_3PO_4) at 180°C for several minutes. Acid attack occurs preferentially on the grain boundaries because of the loosely bonded higher energy atoms there. Resulting dissolution of material from the grain boundary leaves a groove behind. Chemical etching methods are many and varied; however, highly aggressive and hazardous reagents are mostly used in extreme conditions for extended treatment durations.

In this chapter, sintering and densification behavior of a commercial spinel powder was studied. The measurement and calculation of the activation energy for densification was performed by both conventional techniques and by MSC analysis. Grain growth kinetics was also analyzed. Observations of microstructural behavior of

the spinel powder are discussed. A comparison of density measurements done by Archimedes method and microstructural observations was done.

In the second part of this chapter, the effects of pretreatments on sintering behavior and on microstructural development using non-doped, submicron-grained spinel powder are reported. Adopting a constant heating rate condition allows the shrinkage behavior in the intermediate stage of sintering to be observed. As mentioned above, the TSS technique was adapted for many powders, but no one tested the effect of TSS on microstructural development of spinel. Further results of the combined use of TSS and precoarsening are also given.

4.2. Powder and Experimental Procedure

Poudre et procedure expérimentale

4.2.1. Powder

Poudre

Commercially available spinel ($MgAl_2O_4$) (S30-CR, batch n° 061674 Baikowski) powder was used as the starting material in this study. The main impurities in the spinel powder, given by the supplier (Baikowski 2010), are (in wt ppm): Na: 10, Fe: 10, Si: 20, and Ca: 5. Baikowski also reports a d50 value of 350 nm with a mean agglomerate size of ~ 2.5 µm and a specific surface area of 30 m^2/g (Rozenburg, et al. 2008). No second phase MgO was present in the spinel. Residual sulfur of around 400 ppm was detected (Bernard-Granger, et al. 2009). Our measured BET, X-ray diffraction (XRD) and thermogravimetric analysis (Figure 3.5) results were coherent with their results.

Figure 4.1 shows the particle size distribution of the spinel powder measured by Sedigraph method (Sedigraph III, Micromeritics). The powder consisted of mainly submicron-sized particles with mean diameter of 0.25 µm (supplier also reports a d_{50} value of 350 nm with a mean agglomerate size of 2.5 µm and a specific surface area of 30 m^2/g). As seen in Figure 4.1, spinel particle size distribution is not mono-modal.

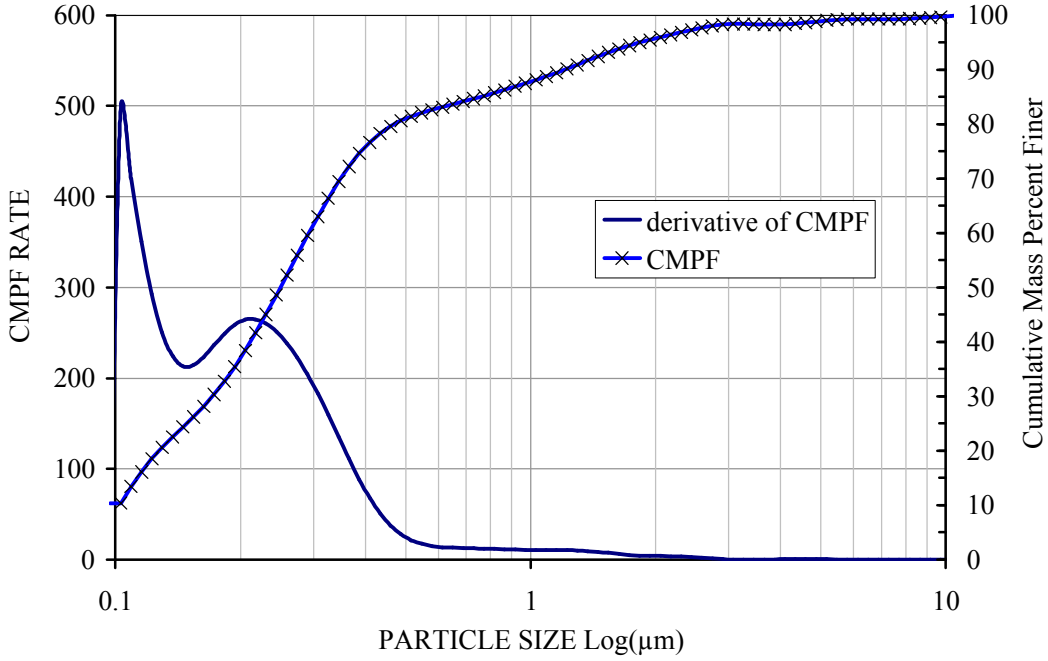

Figure 4.1. Particle size distribution of spinel powder measured by Sedigraph method.

Distribution en taille de particules de la poudre de spinelle mesurée par sédimentation.

The SEM images of spinel powder are shown in Figures 4.2(a) and (b). The spinel powders were in a softly agglomerated form and initial particle size of spinel was finer than 50 nm as seen in the SEM images. According to measured specific surface area of spinel (31 m^2/g), if the particle shape is assumed spherical, calculated particle size d_{BET} is about 55 nm from specific surface area (Equation 3.1). So this BET results are coherent with SEM observations.

Powder compacts for sintering were formed by uniaxial pressing in a stainless steel die, followed by cold isostatic pressing (CIP) under high pressure; no binder was used in the process. Die pressing was performed under a pressure of ~50 MPa to produce compacts (8 mm in diameter × 8.2 mm height) with a density that was 37% of the theoretical density of spinel (3.55 g/cm^3). After cold isostatic pressing under a pressure of ~250 MPa, the relative density (ρ_{rel}) of the compacts increased to 0.50. This relative density is higher than the deduced one from compaction curve (Figure 3.6).

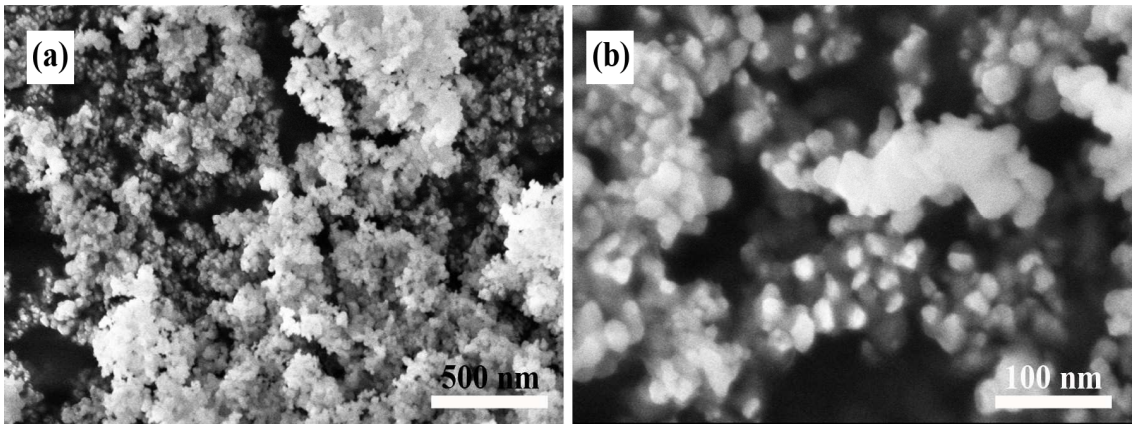

Figure 4.2. SEM images of spinel powder with different magnifications.

Micrographies MEB de la poudre de spinelle à différents grandissements.

In this study two different vertical dilatometers were used to investigate the sintering behaviour of spinel (L75VS-1750, Linseis, Germany) and (DHT2050K, Setaram, France). The two machines were tested and found to provide the same data (see in Section 3.10.1). Green Compacts were sintered at temperatures up to 1500°C for different soaking times of 0 to 16 hours with different heating rates (1 to 10°C/min.) under air flow atmosphere.

Densities, $\rho(T)$, and densification rate curves were computed from the recorded shrinkage data and from final density ρ_f measurements using the Equation (2.7). Archimedes method was applied on cooled samples. To plot the densification rate, temperature derivative of relative density ρ was taken as in Equation (2.8).

In mercury-porosimetry experiments, the pore diameter was determined from the pressure of intrusion by using the Washburn Equation and assuming values of 140° for the contact angle and 480 ergs/cm² for the surface tension of mercury. The pore-size distributions follow from the derivative of the volume that was intruded, with respect to the pore diameter. A Quantachrome 60 device was used for porosimetry measurements.

4.2.2. Microstructural Characterizations

Caractérisations microstructurales

A variety of techniques was used to characterize the microstructure of the green compacts and the sintered samples. Microstructures of the fracture surfaces, polished surfaces, and polished-and-thermally or chemically-etched surfaces were observed by SEM.

Average grain size was measured on the polished and thermally etched surface by the mean intercept area on a plane section technique (Bernard-Granger, et al. 2008a).

To investigate the microstructures, the pellets were vertically cut into two halves with a diamond disc saw. After cutting, half of them were mounted into polyester resin before grinding and polishing. Fine polishing was done with 0.02 μm alumina suspension.

In order to reveal the microstructure of polished ceramics, different thermal etching treatments were applied with respect to sintering conditions of samples. For example, the first sample (99% relative density) was fed by pushing slowly (~3.3 mm/s) inside the centre of the horizontal tube furnace (Carbolite STF15/450) which was maintained at 1450°C. Samples were removed after 1 hour of soak. The second sample (85% relative density) was fed the same way and was kept in the furnace at 1300°C (50°C below the sintering temperature) for 1 hour, and then removed.

The thermally etched samples, with respect to their sintering conditions, were observed with SE detector (Figure 4.3). Structures were pore-free and the average grain sizes of spinel samples were around 840 nm and 200 nm, in the 99% dense and the 85% dense samples, respectively in Figures 4.3(a) and (b). According to Figure 4.3(b), the spinel density unexpectedly looked like almost 99%. But the final Archimedes' density of this sample was measured to be 85%.

During polishing a large amount of deformation and accompanied defect population is induced on the specimen surface. When thermal energy is supplied to the specimen, this highly deformed surface is given the opportunity to rearrange by recrystallization through nucleation and growth of a new generation of strain-free grains (Kingery, et al. 1976). Some grain size coarsening and pore elimination can then be expected to occur during thermal etching.

In both cases, thermal etch lines and formation of kinks on the thermally etched surfaces of samples was observed (Figure 4.3). These kinks and steps on the grains were also observed by Jalota et.al., (2007) in their study on Ti foam metallic samples during thermal treatment. The effect of thermal etching on the surface roughness of nearly fully dense ceramic was analyzed by the Atomic Force Microscope (AFM). Figures 4.4(a) and (b) show the image of as-polished surface and thermally etched surface, respectively. Roughness (Rms) of surface sharply increased from 3 nm to 22 nm after thermal etching.

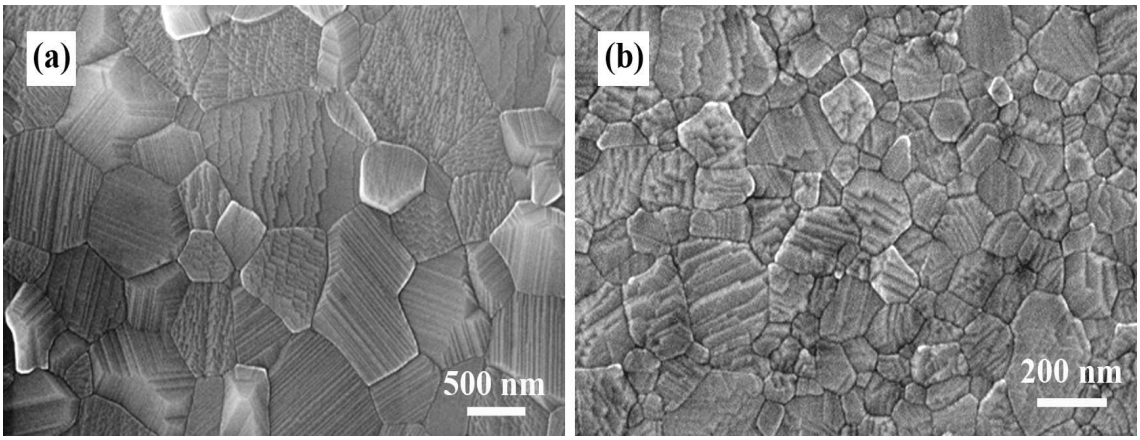

Figure 4.3. Thermally etched surface of spinel ceramics (a) spinel has 99% relative density and (b) spinel has 85% relative density.

Surfaces polies et attaquées thermiquement de céramiques spinelle a) matériau avec une densité relative de 99% b) matériau avec une densité relative de 85%.

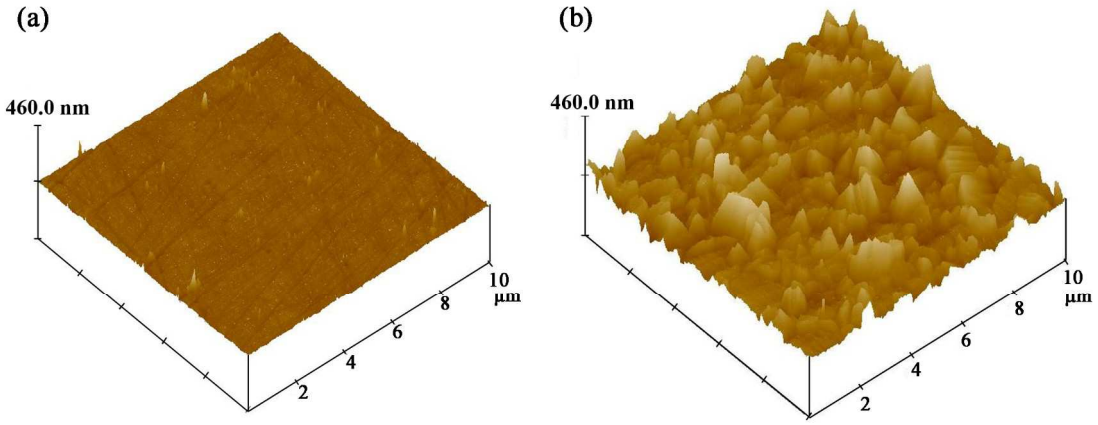

Figure 4.4. Effect of thermal etching on the roughness of spinel (99% dense) surface (a) as-polished and un-etched surface and (b) thermally etched surface.

Effet d'attaque thermique sur la rugosité de surface d'une spinelle (99% dense) a) surface polie non attaquée b) surface attaquée thermiquemen.

In order to further understand the discrepancy between Archimedes measurement and Figure 4.3(b), two more observations were made. The first involved observation of the as-polished sample surface (Figure 4.5(a)) and the second involved observation of the fracture surface of the same sample (Figure 4.5(c)). According to Figure 4.5(a), spinel density strangely looks again like ~99%. But it was known that the final Archimedes' density was 85% as supported by Figure 4.5(c) which shows that the sample was really porous in agreement with the Archimedes test result. Thus, thermal etching performed 50°C below the sintering temperature for this sample modified the

microstructure and produced misleading information. The surface of the ceramic sample was possibly covered by debris removed during polishing which smeared on the surface (Figure 4.5(a)) and recrystallized (Figure 4.5(b)) during thermal etching, eventually covering the pores.

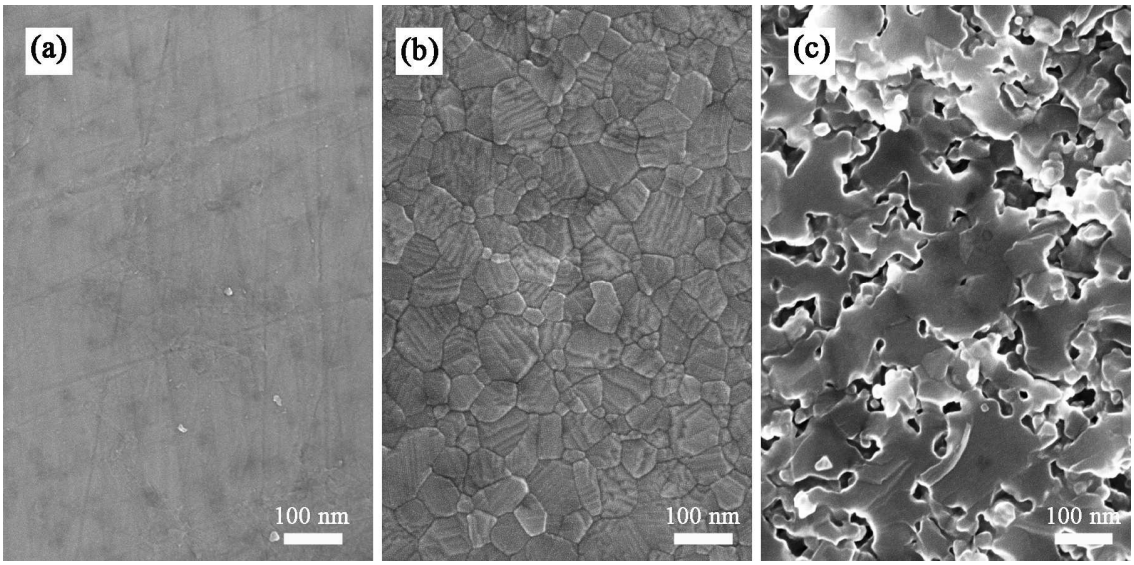

Figure 4.5. Scanning electron micrographs of (a) polished, (b) polished and thermally etched and (c) fractured surfaces of spinel ceramic sintered at 10°C/min until 1350°C for 10 hours, the specimen has the final relative density of 85%.

Micrographies MEB de surfaces d'une céramique spinelle frittée 10 heures à 1350°C (vitesse de chauffage 10°C/min) a) polie b) polie et attaquée thermiquement et c) surface de rupture.

In order to clarify the conflicting micrographs in Figure 4.5, chemical etching was applied for comparison with thermal etching. Chemical etching of the polished samples was done with hot orthophosphoric acid (H_3PO_4) at 140°C for several minutes. The effect of soaking time on the etching process was also tested. The polished samples were held for 10, 15 and 20 minutes inside hot orthophoshoric acid. The chemically etched surfaces were investigated under SEM (Figure 4.6). After 10 minutes of holding inside the etchant, the microstructure of low density ceramic (Figure 4.6(a)) was significantly different from the as polished surface (Figure 4.5(a)). Porosity of the order of about 15% was observed and grain boundaries were slightly visible compared to Figure 4.5(b). This microstructure was more realistic and more in line with the Archimedes measurement. The 99% dense sample in Figure 4.6(b) showed small amount of porosity, as expected, but duration of soak was not enough to reveal the grain

boundaries of fully dense ceramic (Figure 4.6(b)). When the etching duration was increased up to 15 minutes, acid strongly attacked the surface of the 85% dense sample and dissolved the material which resembled a sponge (Figure 4.6(c)). On the other hand, the same durations perfectly revealed the grain boundaries of fully dense spinel ceramic (Figure 4.6(d)), which easily enable the measurement of average grain size to be 660 nm. However, further soaking (20 min) inside the etchant led to accelerated dissolution for both samples (Figures. 4.6(e) and (f)). Therefore, optimum etching duration in hot acid is 15 min for the 99% dense sample and around 10 min for the 85% dense sample.

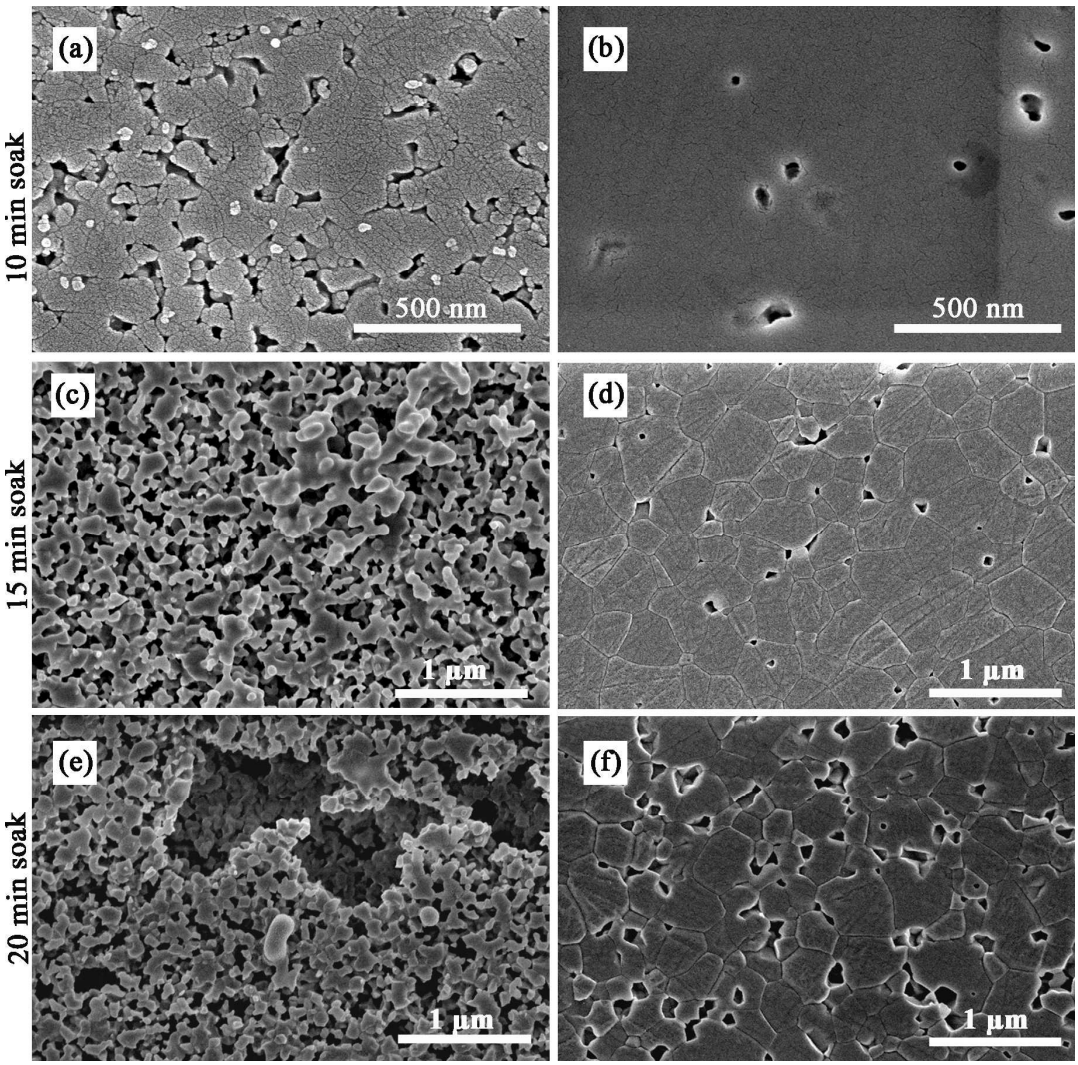

Figure 4.6. Surfaces of chemically etched spinel ceramics; (a), (c), (e) 85% relative density and (b), (d), (f) 99% relative density, they were held 10, 15 and 20 min inside the hot acid from top row to bottom row, respectively.

Surfaces polies et attaquées chimiquement de spinelle ; a), c), e) avec une densité relative de 85 % et b), d), f) avec une densité relative de 99%. Ces surfaces polies ont été attaquées pendant 10, 15 et 20 minutes pour respectivement les rangées de micrographies de haut en bas de la figure.

4.3. Results and Discussion

Résultats et discussion

Densification behaviour of spinel was investigated using the dilatometers with different heating regimes of constant heating rate (CHR) and isothermal heating. Figure 4.7 shows the thermal regimes of spinel sintering. Calculations of apparent activation energy values were based on those fractions of lines up to points A, B, C and D in Figure 4.7.

4.3.1. Densification Behavior of the Powder Compacts

Comportement en densification des comprimés de poudre

Densification behavior of spinel powder compacts was investigated using dilatometer and general densification behavior of spinel at constant heating rates of 1 and 3.3, 5.7 and 10°C/min up to 1500°C are illustrated in Figure 4.8. Maximum density of 0.907 was obtained for the sample sintered with 1°C/min heating rate. So, none of these specimens completed the full densification cycle under the present conditions. Densification of the samples showed the common three distinct stages as a function of temperature. In the first stage not much densification occurs with spinel up to roughly 900°C. In the second stage between 900 and 1500°C, densification rate is significant. In the final region beyond roughly 95% density other phenomena like exaggerated grain growth may occur. Therefore, we focused on intermediate sintering region up to 90% density. Two peaks were observed on the densification rate curves of spinel as different from general powder densification behavior. There was a dip (minima) between two peaks around 0.67 relative densities on the densification rate curves (See Figure 4.8). This spinel powder densification behavior was investigated under hot-pressing in previous studies (Reimanis and Kleebe 2009) but this type of densification behavior was not mentioned in their study. The dip (minima) shifts slightly to lower temperatures with decreasing heating rates.

Bernard-Granger et al., (2009) also analyzed the densification mechanism of the same spinel powder (S30-CR) for different spark plasma sintering temperatures as a function of soak time. They observed wavy shaped densification curves during soaking time and they mentioned them as uncommon densification behaviour compared to other

powders like zirconia or alumina which shows continuous densification curves (Bernard-Granger and Guizard 2007b). A similar slightly wavy behavior was observed in this study on the ramp up part of the plots (Figure 4.8). This could be attributed to a characteristic of the Baikowski powder S30-CR as no such behavior was reported by Ting and Lu (2000).

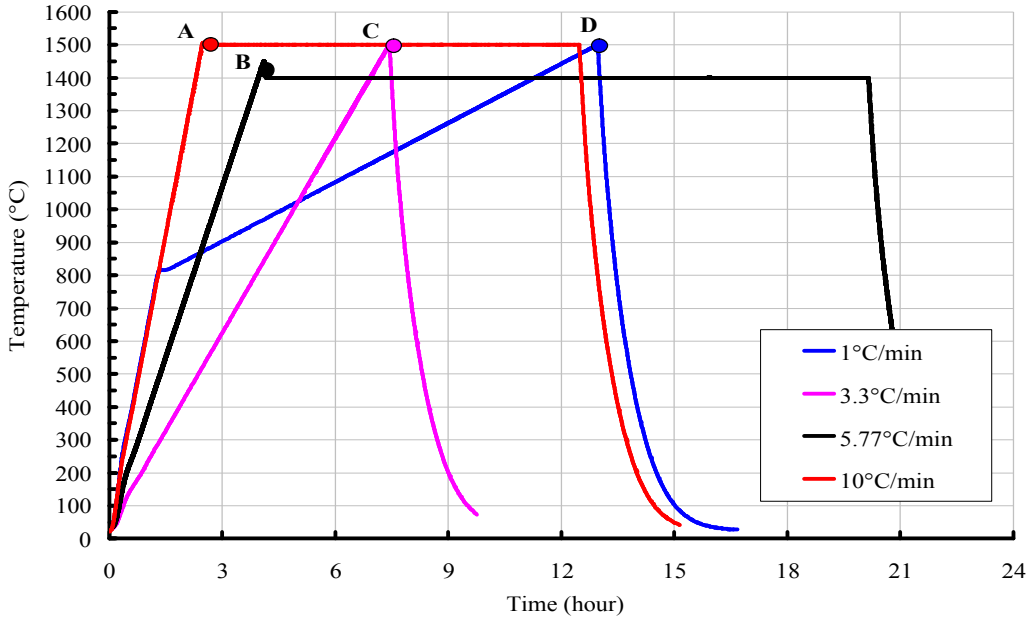

Figure 4.7. Temperature versus time schedules of sintering tests.

Programmes temps – temperature des essais de frittage.

4.3.2. Grain Growth Kinetics of Spinel

Cinétiques de croissance granulaire des matériaux spinelle

Grain growth kinetics of spinel was analyzed. The grain growth analysis was performed by using Equation (2.2). Figure 4.9 shows the densification and densification rate curves of spinel with respect to time. Spinel compacts were sintered at 3.3°C/min until 1500°C where they were soaked for 1 hour, 4 hours and 16 hours. After 1 hour soak time, the spinel had the final density of 0.935. During the prolonged soaking time from 4 hours to 16 hours, the relative density increased from 0.955 to 0.985, respectively. Again densification rate curves of these samples showed two separate peaks. So this behaviour was characteristic of this commercial spinel powder (S30CR, Baikowski).

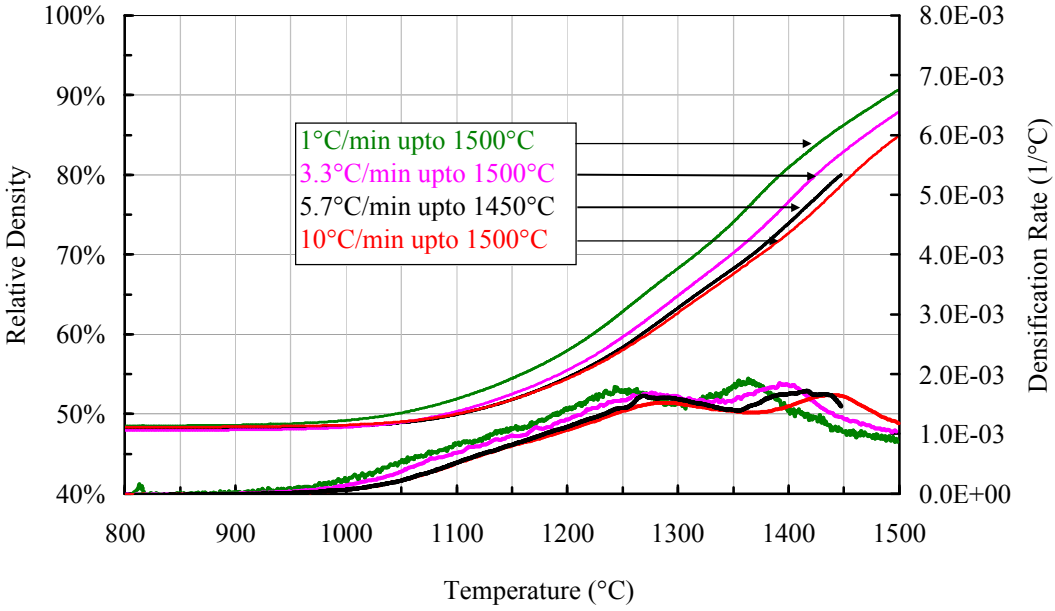

Figure 4.8. Densification and densification rate curves of spinel powder compacts (50 MPa Uniaxial Pressing + 250 MPa Cold Isostatic Pressing).

Courbes de densification et de vitesse de densification de comprimés de poudre de spinelle (Pressage Uniaxiale PU 50 MPa + Pressage Isostatique à Froid PIF 250 MPa).

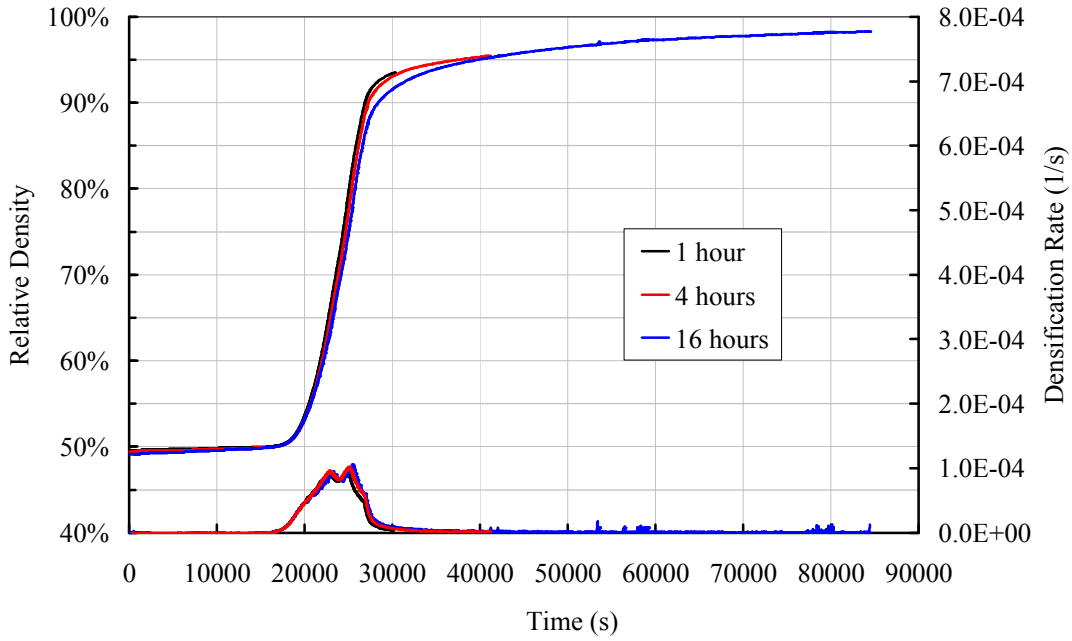

Figure 4.9. Densification and densification rate curves during isothermal sintering cycles at 1500°C for the study of spinel grain growth (3.3°C/min heating rate up to 1500°C).

Courbes de densification et de vitesse de densification pendant des cycles de frittage isotherme à 1500°C pour l'étude de la croissance granulaire dans la spinelle (vitesse de chauffage 3,3°C/min jusqu'à 1500°C).

Representative images of polished and thermally etched sintered spinel ceramics are given in Figure 4.10. Grain size increased gradually from 1 hour soaking time to 16 hours. As seen in the densification curves (Figure 4.9), sintered spinel ceramics could not reach full density at the end of the sintering process, their microstructures, however, represented full densities in Figure 4.10. Again there was a discrepancy between the Archimedes and the results in Figure 4.10. This was discussed in Section 4.2.2. The measured average grain sizes with the applied thermal cycle are given in Table 4.2.

The *m* exponent in Equation (2.2) can be measured by plots of G^m-G_o^m against soaking time at 1500°C (Figure 4.11). Slopes of the graphs give the *m* exponent. None of the G^m-G_o^m vs time plots for our data followed a straight line through the origin. But $G^{2.5}$-$G_o^{2.5}$ vs time and G^3-G_o^3 vs time plots were very close to the origin. In this case m was around 2.75. So, grain growth kinetics of stoichiometric spinel is possibly not governed completely by normal grain growth.

In the literature, *m*=2 for spinel (Bratton 1971, Chiang and Kingery 1989) there are different proposed mechanisms like porosity and impurities that affect the value of *m*.

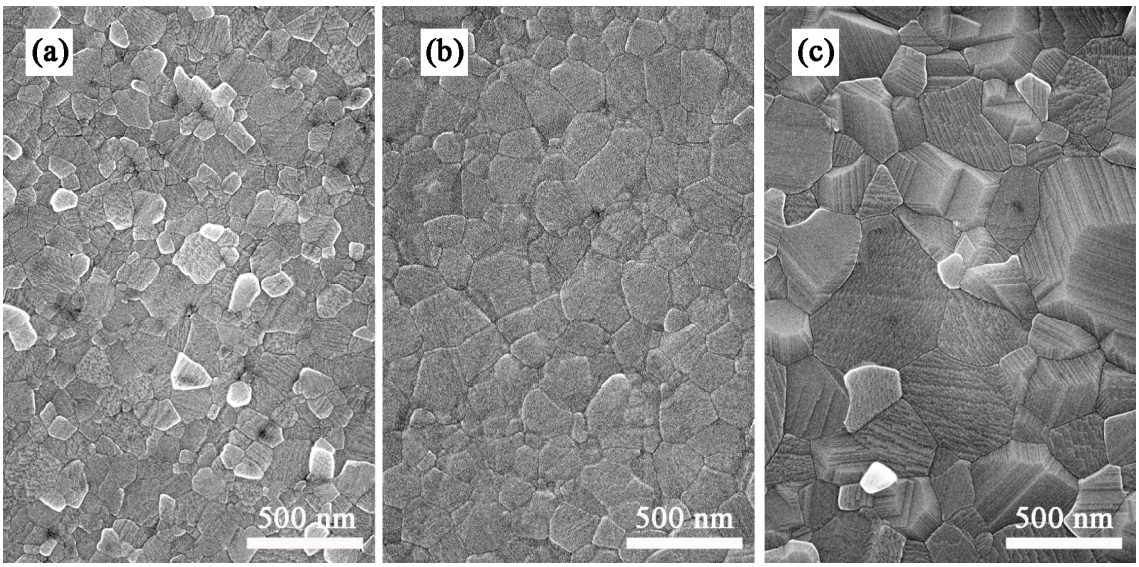

Figure 4.10. Scanning electron micrographs of spinel ceramic sintered at 1500°C for (a) 1 hour, (b) 4 hours and (c) 16 hours (3.3°C/min heating rate up to 1500°C).

Micrographies MEB de spinelle frittées à 1500°C pendant a) 1 heure, b) 4 heures et c) 16 heures (vitesse de chauffage de 3,3°C/min jusqu'à 1500°C).

Table 4.2. Thermal cycles and average grain sizes.

Cycles thermiques et tailles moyennes de grains.

	1500°C, 3.3°C/min		
Soaking Time (hour)	1	4	16
Relative Density (%)	93.4	95.5	98.5
Average Grain size (µm)	0.342	0.500	0.840

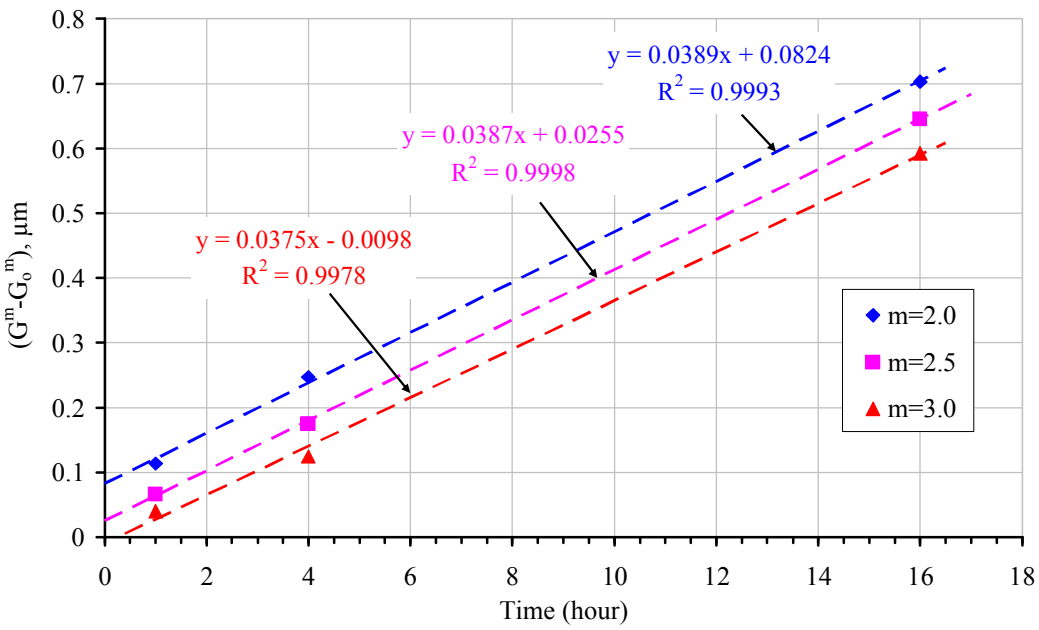

Figure 4.11. Grain growth laws at 1500°C of sintered spinel material.

Lois de croissance granulaire à 1500°C pour des spinelles frittées.

Microstructures of nearly fully dense (99%) spinel ceramics were examined (Figure 4.3). The grain size was observed to be smaller in the interior and larger close to the surface. In the literature, abnormal grain growth layer at the surface of spinel ceramic due to loss of MgO by evaporation was reported (Ting and Lu 2000). Ting and Lu also mentioned another fine grain size (G_{av}<1 µm) region at the surface of spinel under vacuum atmosphere sintering at low sintering temperatures (e.g. 1600°C). However, in our case we did not observe any such layer. The white arrows in Figures 4.12(a) and (b), indicate the direction of interior of spinel. At the surface of spinel around 50 µm thick abnormal grain growth region was observed. The average grain size was around 2 µm on the surface and 0.56 µm in the interior.

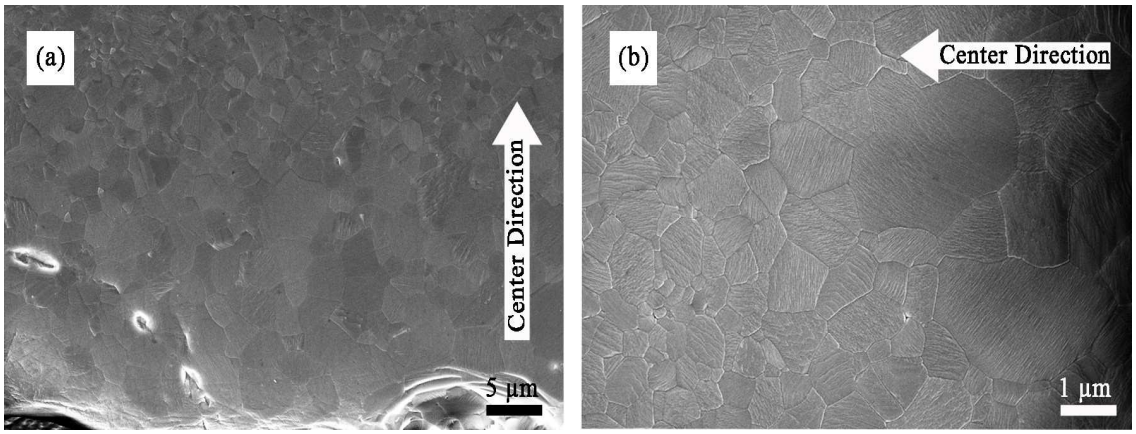

Figure 4.12. SEM images of polished cross sections of a 96% dense sintered spinel samples close to their outer edges (10°C/min at 1500 C for 10 hours).

Micrographies MEB proches de la partie extérieure d'échantillons de spinelle frittée (10°C/min 10 heures à 1500 °C) avec une densité relative de 96%.

4.3.3. Apparent Activation Energies for Spinel Densification

Energies d'activation apparentes de la densification de la spinelle

In this section, apparent activation energy of spinel was calculated by employing two different calculation methods. The first calculation is based on Arrhenius plots of densification rate versus reciprocal temperature per Equation (2.11). The second one is based on MSC method (Section 2.4.2.2). The results were compared with the literature as mentioned in the introduction part. Both techniques were outlined in Chapter 2.

4.3.3.1. Arrhenius Plots for Calculation of Activation Energies (Q_d)

Diagrammes d'Arrhenius pour la détermination d'énergies d'activation (Q_d)

General densification behavior of spinel at four different constant heating rates is illustrated in Figure 4.8. In the literature, generally three different constant heating rates were employed (Bernard-Granger and Guizard 2007b, Rozenburg, et al. 2008). For spinel powder, Arrhenius plots were drawn from densification and densification rate curves (Figure 4.8). Figure 4.13 shows the plots of ln(dρ/dT* $\dot{T}$ *T) as a function of 1/T for different relative densities of 0.60, 0.65, 0.70, 0.75, 0.80 and 0.85. Where $\dot{T}$ is the heating rate, T is the absolute temperature in Kelvin. The slopes of the plots for these six different densities allow calculation of the apparent activation energies as was proposed by Wang and Raj (1990). In this study, average value of activation energy was

found to be 863 kJ/mol. But usually, activation energies determined from sintering experiments are in error by 3 to 20 %, depending on the precautions to ensure ideal conditions (German 1996). Figure 4.14 shows a plot of the relative density versus apparent activation energy.

4.3.3.2. Calculation of Activation Energy (Q_d) with Master Sintering Curve

Détermination d'énergie d'activation (Q_d) à partir d'une courbe de frittage de référence

In this section, the activation energy of spinel was calculated by master sintering curve (MSC) method. In order to compare MSC with the conventional calculation of Q_d on Arrhenius plots, the same experimental results as in Section 4.3.3.1 were used. Thus plotted in Figure 4.15 is the MSC constructed from the data displayed in Figure 4.8. In addition, Figure 4.16, which was derived from Figure 4.15, shows the average residual square versus Q_d where the activation energy was found to be 833 kJ/mol.

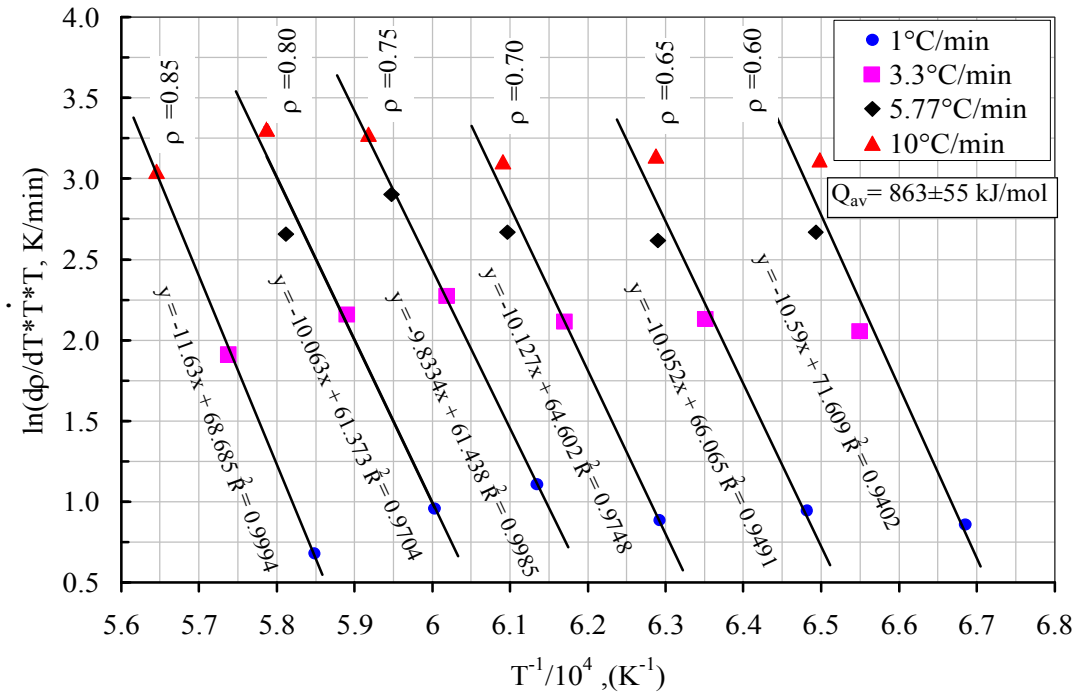

Figure 4.13. Arrhenius plots at various relative densities of powder compacts of spinel; from data of constant heating rate sintering tests.

Diagrammes d'Arrhenius de vitesses de densification à différentes densités relatives de comprimés de spinelle ; à partir des données d'essais de frittage sous différentes vitesses de chauffage.

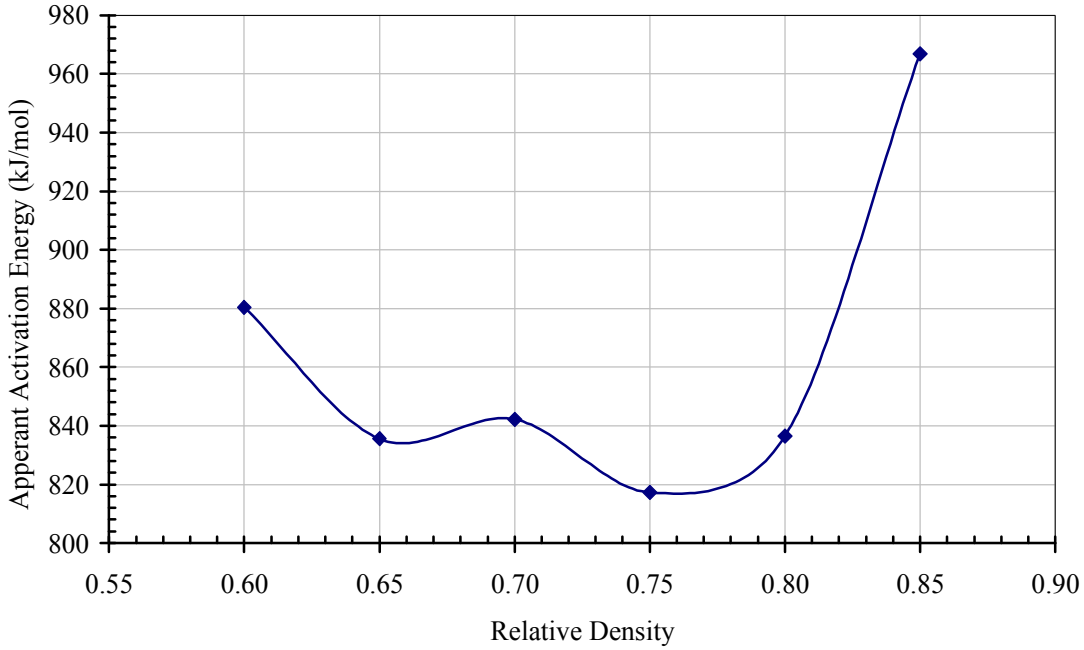

Figure 4.14. Apparent activation energy for densification versus relative density.

Energie d'activation de la densification en function de la densité relative.

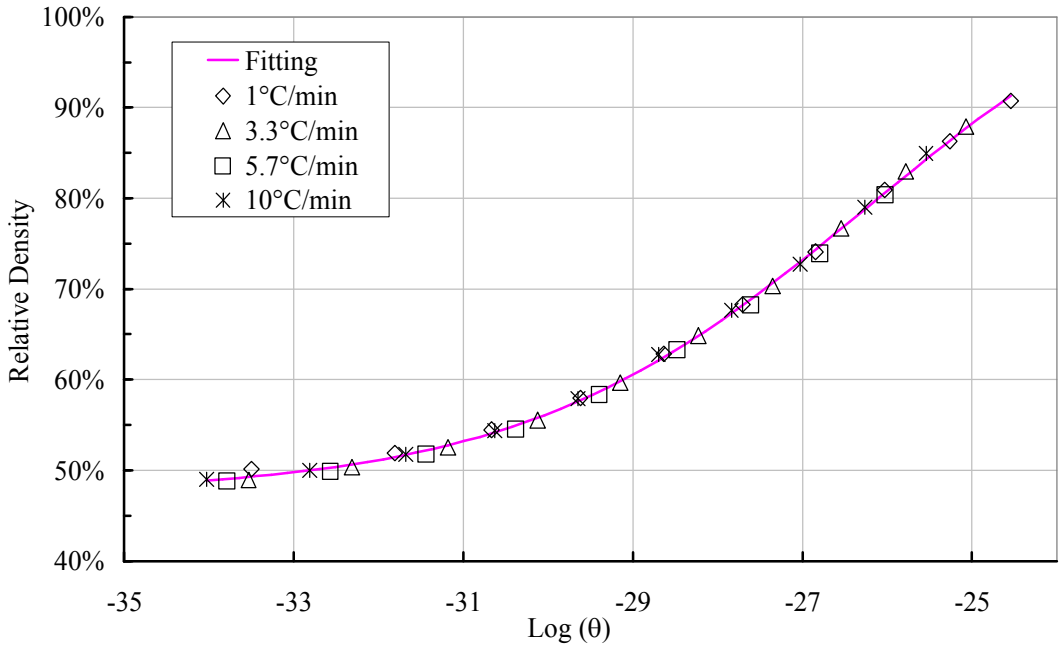

Figure 4.15. Master Sintering Curve of spinel compacts : Relative density as a function of the master sintering variable (cold pressing conditions : UP 50 MPa + CIP 250 MPa).

Courbe de frittage de référence de comprimés de spinelle : densité relative en fonction de la variable de frittage de référence (conditions de pressage à froid UP 50 MPa + CIP 250 MPa).

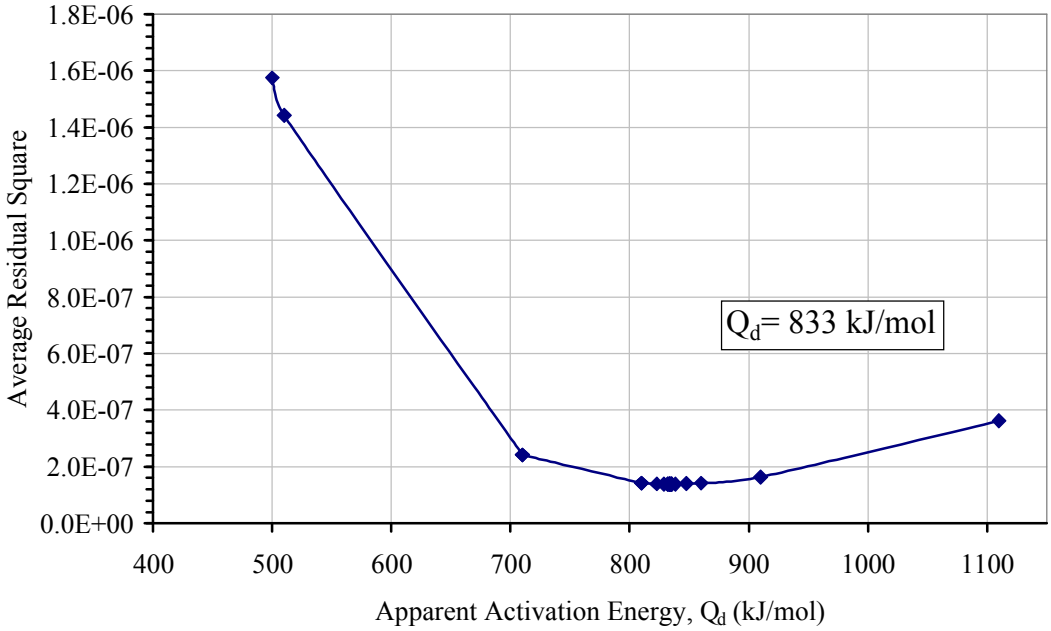

Figure 4.16. Master Sintering Curve : Average residual square versus apparent activation energy (Q_d).

Courbe de Frittage de Référence : écart quadratique moyen en function de l'énergie d'activation apparente (Q_d).

4.3.3.3. Assesment and Discussion on Apparent Activation Energy of Spinel Densification

Bilan et discussion sur les énergies d'activation apparentes de la densification de la spinelle

Apparent activation energy for densification of spinel was calculated from Arrhenius plots. Below is given a discussion of the results and comparison with the literature.

The activation energy for intermediate-stage sintering of spinel was fairly different from literature. The apparent activation energy values measured in this study were not in agreement with the traditional 350–500 kJ/mol values that are commonly reported for pure spinel material (Rozenburg, et al. 2008, Ting and Lu 1999b). This much of difference cannot be explained by error from experimental procedure neither did Benameur et.al. observe the 350-500 kJ/mol values. Their value was 875 kJ/mol (Table 4.1) which was very close to our value of 863 kJ/mol (Benameur, et al. 2010). In evaluating our result, several factors have to be considered. First, the wavy shape of the densification rate behavior of this spinel powder might effect the apparent activation energy calculation.

It is clear that the straight lines in Figure 4.13 are not parallel. So, the apparent activation energy of the mechanism controlling densification, Q_d, is a direct function of the relative density. This is clearly confirmed in Figure 4.14 by plotting relative density versus apparent activation energy. It is observed that the apparent activation energy value varies with the relative density with a large increase beyond 0.85 relative density. Bernard-Granger and Guizard (2007b) in their study for yttria stabilized zirconia made a similar observation. They explained the reason for activation energy increases for lower values of the relative density with a point defect formation step and grain boundary diffusion of Zr^{4+} cations. So the activation energy behavior of spinel can be associated with point defect formation step.

In this part of the discussion the results obtained from MSC for estimating the apparent activation energy for densification of spinel is presented.

The fact that the apparent activation energy for densification is a direct function of the relative density allows the master sintering curve analysis. Indeed, this kind of analysis supposes that the activation energy for densification has a single value whatever is the relative density. Apparent activation energy was calculated from a computer program written by Teng et al., (2002). Figure 4.16 shows the average residual square versus Q_d where the activation energy was found to be 833 kJ/mol. This value was the minimum average residual square value for the best Q_d. This result is nearly the same as the activation energy found from Arrhenius plots. But our result of activation energy for densification controlling mechanism is slightly different than the result of Benameur et al. that is also tabulated in Table 4.1 (Benameur, et al. 2010).

4.3.4. Coarsening Pre-treatment of Spinel Compacts

Prétraitement de coalescence de comprimés de spinelle

In order to understand the formation mechanism of the two peaks in Figures 4.8 and 4.9 and to determine which peak is the main densification peak, a precoarsening step was applied. Figure 4.17 shows the heating regimes of constant heating rate and applied precoarsening experiments. In conventional sintering, the compact is heated with constant heating rate at 3.3°C/min to 1500°C. This sample was coded sample K. Furthermore, three different pre-treatments were applied by heating to 1100°C, 1150°C and 1200°C and by holding at these temperatures for 10, 9 and 8 hours, respectively. If

the soak time at these temperatures was zero these samples were coded 1100L, 1150L or 1200L, depending on the precoarsening temperature. But if the soak time was 10, 9 or 8 hours then these samples were coded 1100M10, 1150M9 and 1200M8, respectively. Finally, the samples were heated at 3.3°C/min to 1500°C after the precoarsening step. These samples were coded 1100N, 1150N and 1200N, depending on the precoarsening temperature.

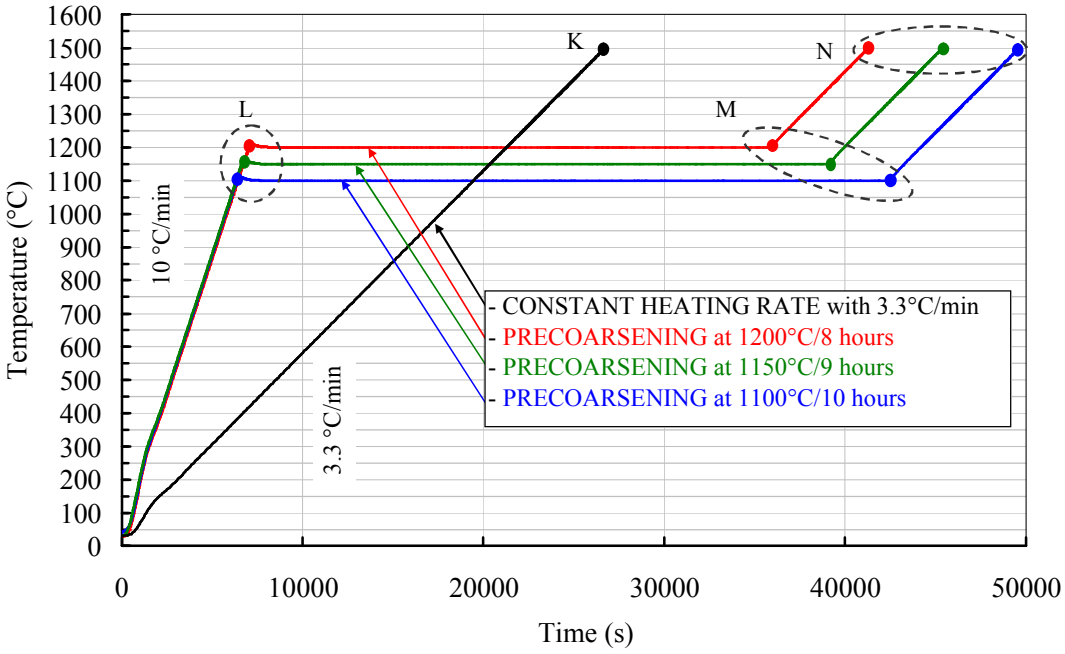

Figure 4.17. Heating schedules of precoarsening treatments on spinel compacts. Sample K was heated at constant heating rate (3.3°C/min) up to 1500°C. Samples of the group L were heated at 1100°C, 1150°C and 1200°C and were cooled without a soaking time. Samples of the group M were soaked at these temperatures for 8-10 hours and then cooled. Samples of the group N after same group M soaking time were directly heated at a rate of 3.3°C/min up to 1500°C and cooled without soaking time at 1500°C.

Cycles thermiques de traitement de précoalescence de comprimés de spinelle. L'échantillon K a été chauffé à vitesse de chauffage constante (3,3 °C/min) jusqu'à 1500°C. Les échantillons du groupe L ont été chauffés jusqu'à 1100, 1150 et 1200°C puis refroidis sans maintien à ces températures. Les échantillons du groupe M ont été maintenus à ces températures pendant des temps allant de 8 à 10 heures puis refroidis. Les échantillons du groupe N après le même traitement en température que ceux du groupe M ont été chauffés directement à 3,3°C/min jusqu'à 1500°C et refroidis sans maintien à 1500°C.

Figures 4.18(a) and (b) show the effect of precoarsening step on the densification and densification rate of spinel. Three different pre-treatments were applied. As seen in Figure 4.18, no significant differences appeared between the samples K and 1100N in their densification rate curves which showed double peaks and a dip in the middle. The only difference between these samples was observed in slight densification of sample 1100N at the precoarsening temperature of 1100°C. But when the precoarsening temperature was increased to 1150°C, the first peak turned to a shoulder form (Figure 4.18(b)). The shoulder disappeared completely after 8 hours of pre-treatment at 1200°C (1200N). This can be seen in Figure 4.18(b) clearly.

A variety of techniques was used to characterize the microstructure of the green compacts and the sintered samples. The microstructures of the fracture surfaces, and polished and thermally etched surfaces of all samples were observed by SEM. But only a few selected micrographs are given in Figure 4.19 for the fracture surfaces of samples. Evolution of sintering during pre-treatment as a function of soak temperature and soak time is shown in Figure 4.19. Micrograph of the as-received material (Figure 4.19(a)) is compared to that heated to 1100°C(1100L) with ρ_{rel}~53% and to 1200°C(1200L) with ρ_{rel}~55% in Figures 4.19(b) and (c). The same samples were also observed after 10 hours (1100M10) and 8 hours (1200M8) of soak time at the pre-treatment temperatures in Figures 4.19(d) and (e), respectively. These images correspond with the elimination of first peak on the densification rate curve of spinel, in Figure 4.18(b). After sintering at 1100°C the relative density slightly increased about 3%. There was no significant increase in average particle size (Figure 4.19(b)). A compact that has been precoarsened for 10 hours at 1100°C, showed appreciable microstructural change accompanied by the disappearance of more than half of the nano-sized particles (Figures 4.19(b) and (d)). Figure 4.19(c) shows the compact that was heated conventionally to 1200°C. The particles showed more rounding of the edges and corners, and the finest particles have completely disappeared. After the pre-treatment at 1200°C for 8 hours, considerable matter transport has occurred in the compact. The relative density reached 68% and the rounded grains grew. A partially bonded network of particles seemed to have a narrower size distribution at a very similar size of about 0.12 μm as seen in the micrograph (Figure 4.19(e)).

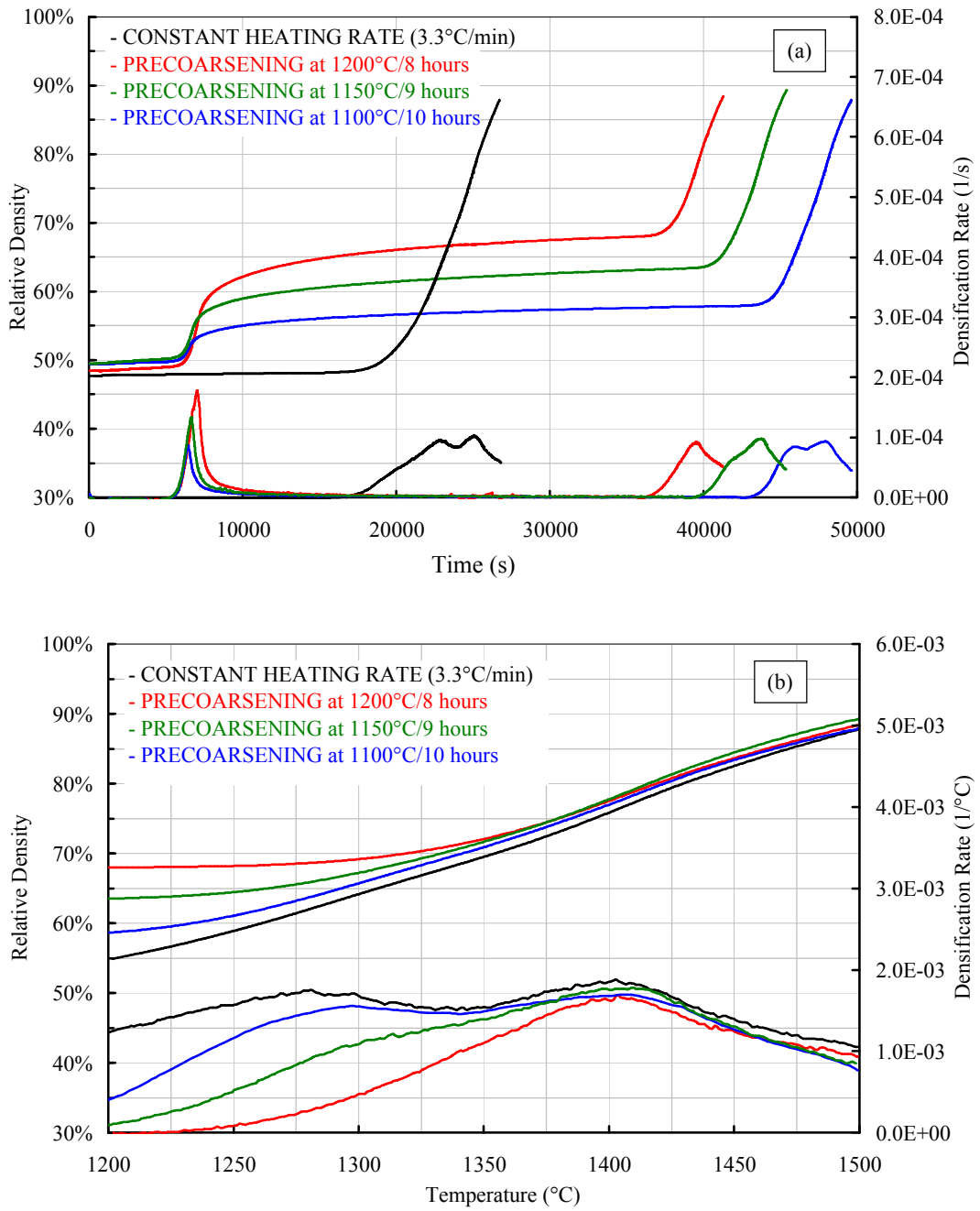

Figure 4.18. Densification and densification rate curves during sintering at a heating rate of 3.3°C/min for powder compacts of spinel with and without coarsening pre-treatments (a) The upper and lower curves are the relative densities, ρ, and their time derivatives, $d\rho/dt$, respectively respect to time (b) The upper and lower curves are the relative densities, and their temperature derivatives, $d\rho/dT$, respectively respect to temperature from 1200 to 1500°C.

Courbes de densification et de vitesse de densification pendant un frittgae à 3°C/min de comprimés de spinelle avec et sans pré-traitments de coalescence. a) les courbes en haut et bas de la figure correpondent respectivement aux densités relativse et aux vitesses de densification en fonction du temps. b) les courbes en haut et en bas de la figure correspondent respectivement aux densités relatives et aux vitesses de densification dans l'interval de température de 1200 à 1500°C.

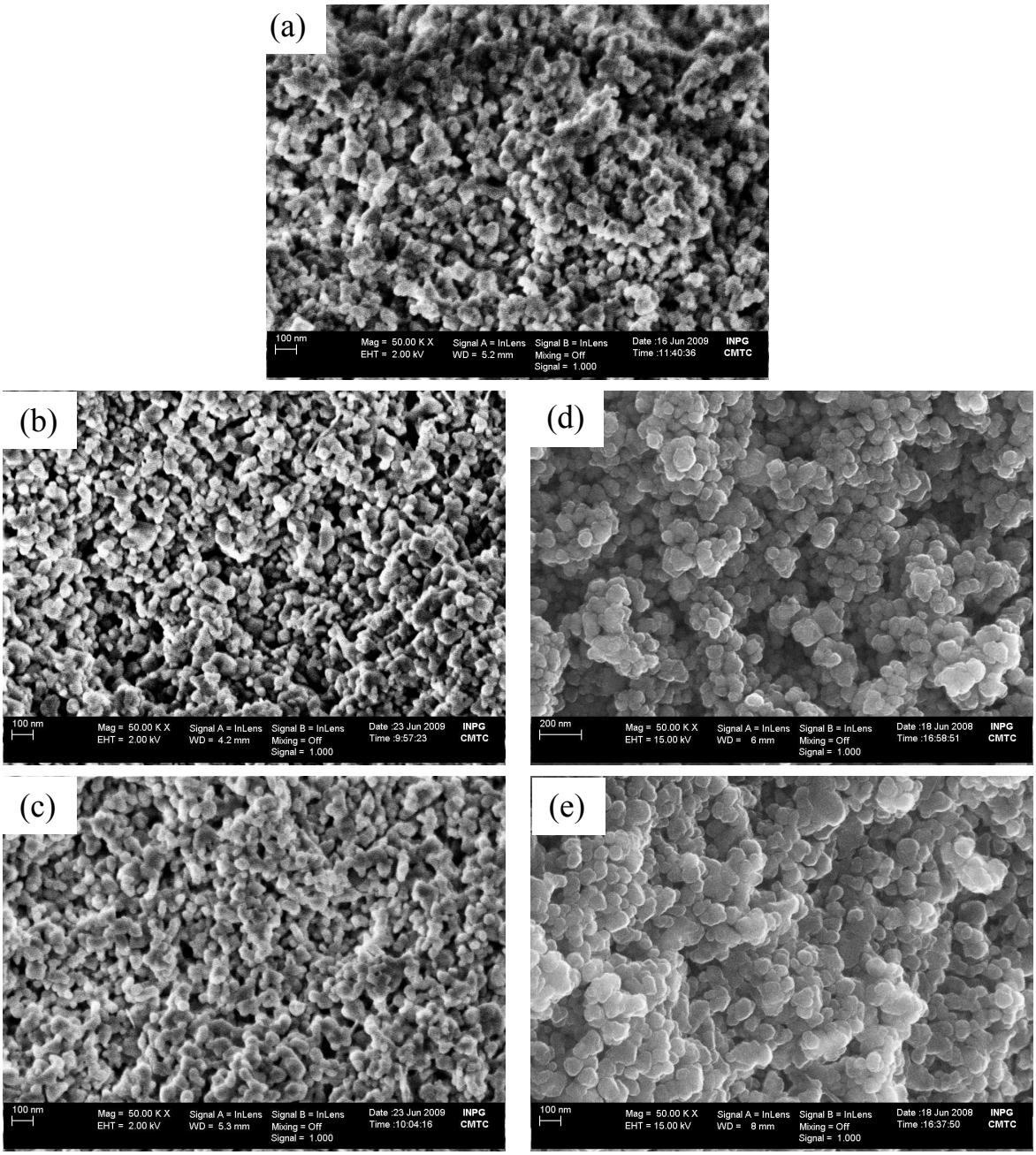

Figure 4.19. Scanning electron micrographs of fracture surfaces of spinel compacts showing the effect of the pretreatment on the microstructure before the sintering step at high temperature: (a) as compacted, (b) and (c) heated at 10°C/min until 1100°C (1100L) and 1200°C (1200L), respectively (d) and (e) pre-treated at 1100°C for 10 hours (1100M10) and at 1200°C for 8 hours (1200M8), respectively.

Micrographies MEB de surface de rupture de comprimés de spinelle montrant l'effet du prétraitement de coalescence sur la microstructure avant le frittage à haute température : a) état brut de compactage, b) et c) chauffés à 10°C/min jusqu'à respectivement 1100°C (1100L° et 1200°C (1200L) , d) et e) prétraités respectivement 10 heures à 1100°C (1100M10) et 8 heures à 1200°C.

Three samples were selected for analysis by mercury porosimetry; these were samples 1100L and 1200M8. The pore-size distribution measurement results are given in Figure 4.20. It was found from data in Figure 4.20 that when the pretreatment temperature was increased, both the proportion and size of the pores decreased significantly. Average pore sizes, in the major part of the samples, were 38 nm and 35 nm for samples pretreated at 1100°C and 1200°C, respectively. The pore size distributions of the samples were monomodal both before and after pretreatment. Lin et.al., (1997) however, observed larger median pore size with narrower distribution in their study on alumina. This difference with Lin's study may arise from partial densification in our samples during pretreatment as shown in Figure 4.18(a).

The mercury porosimetry measured also the total porosities of the samples. Figure 4.21 shows relative density and total porosity values for each sample which are theoretically expected to add up to 100% when there is no closed porosity. According to these results, precoarsened sample has increasing amount of closed porosity with increasing soaking time at the pretreatment temperature.

Figure 4.22 shows the grain size versus relative density. Grain size values for sintered compacts with low densities were calculated from BET measurements. These low density samples were pretreated samples. In this method, the particle shape was assumed spherical, and particle sizes, d_{BET}, were calculated. In addition, grain sizes were measured from polished and thermally etched surfaces of the samples that were heated to 1500°C. All results are combined in Figure 4.22. Ideally, the desirable area of the diagram in Figure 4.22 is the lower right part where density is maximum with little grain growth.

The shoulder (peak) in the densification rate versus temperature diagram was completely eliminated by precoarsening pretreatment at 1200°C for 8 hours. The finest particles were therefore eliminated. Sato and Carry (1995) obtained similar results to eliminate the shoulder as a result of pretreatment.

The subsequent sintering process was therefore expected to provide a more uniform microstructure. Total amount of porosity in the sample after 1200°C pretreatment was found to be lower than that pretreated at 1100°C. Pore size distribution was not observed to change much, but the pore size was smaller unlike the observation by Lin et.al., (1997). The purpose was eventually to produce ceramics with high density without much grain growth. But the contribution derived from precoarsening pretreatment was not very significant to achieve this.

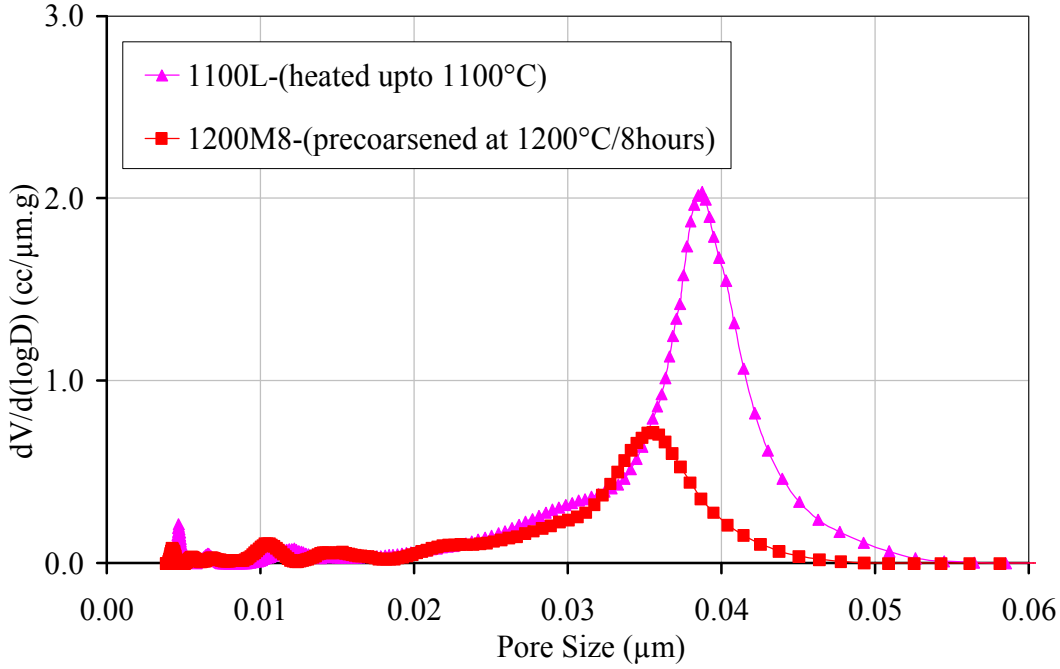

Figure 4.20. Effect of pretreatment on the pore-size distribution of spinel samples (mercury porosimetry).

Effet d'un prétraitment sur la distribution en taille des pores (Porosimétrie à mercure).

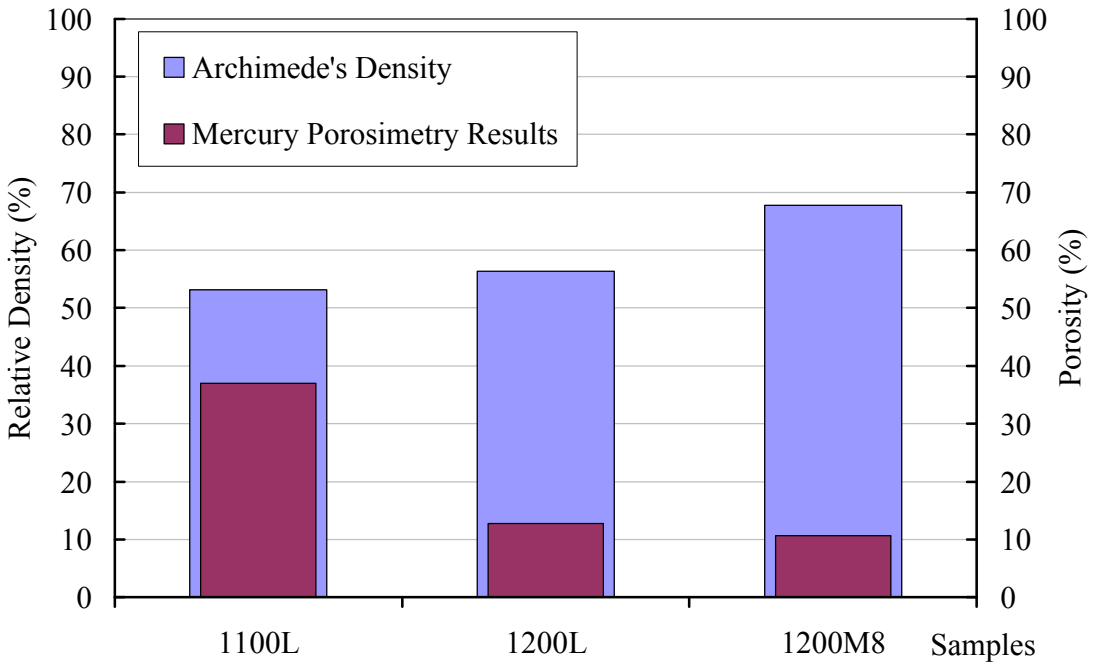

Figure 4.21. Density and porosity measurements (Archimedes and Mercury) showing the effect of a pretreatment on the structure of spinel compacts.

Mesures de densité et de porosité (Archimède et Mercure) montrant l'effet d'un prétraitement sur la structure de comprimés de spinelle.

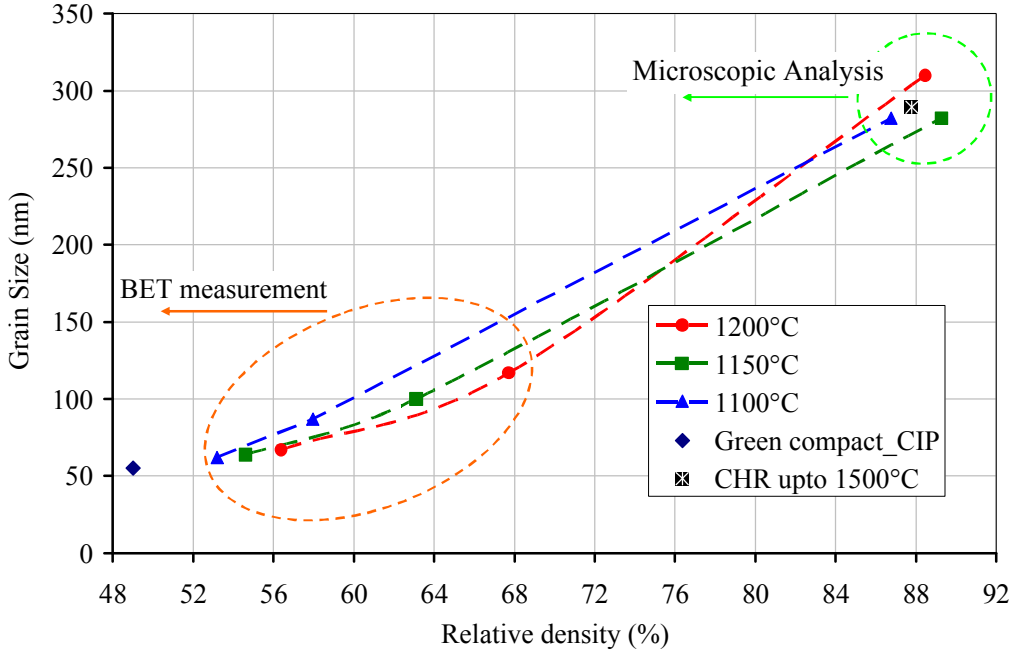

Figure 4.22. Effect of pretreatment on sintering path of spinel compacts : grain size versus relative density.

Effet de prétraitement sur la trajectoire de frittage de comprimés de spinel : taille de grains en function de la densité relative.

4.3.5. Two-Step Sintering of Spinel

Frittage en deux étapes de comprimés de spinelle

In order to achieve fine grain size and higher density spinel ceramics, two-step sintering method was applied for different temperatures (1500-1400°C) and heating rates (10 and 5.7°C/min) with different soaking times. Heating schedules for the two-step sintering (TSS), for the isothermal single step sintering (SSS) and a precoarsening followed TSS and a precoarsening followed SSS tests are illustrated in Figure 4.23. Each line represents an example of different applied heating regime group. The heating conditions for the three different two-step sintering (TSS), two different isothermal single step sintering (SSS) and a precoarsening followed TSS and a precoarsening followed SSS tests are tabulated in Table 4.3. The temperatures of the first sintering step (T1) were chosen on the basis of the evaluation of dilatometric measurements (see Figure 4.7). So according to these temperatures, minimum relative density (ρ_{rel}~80%) at first sintering step (T1) was obtained in the TSS-II test. In addition, a plot is given in Figure 4.24 showing all precoarsening pretreatments as well as SSS and TSS results in terms of density versus grain size graph. Figures 4.25(a) and (b) show SEM images of

polished and chemically etched surfaces of spinel ceramics with the heating regimes of SSS-I and TSS-I, respectively.

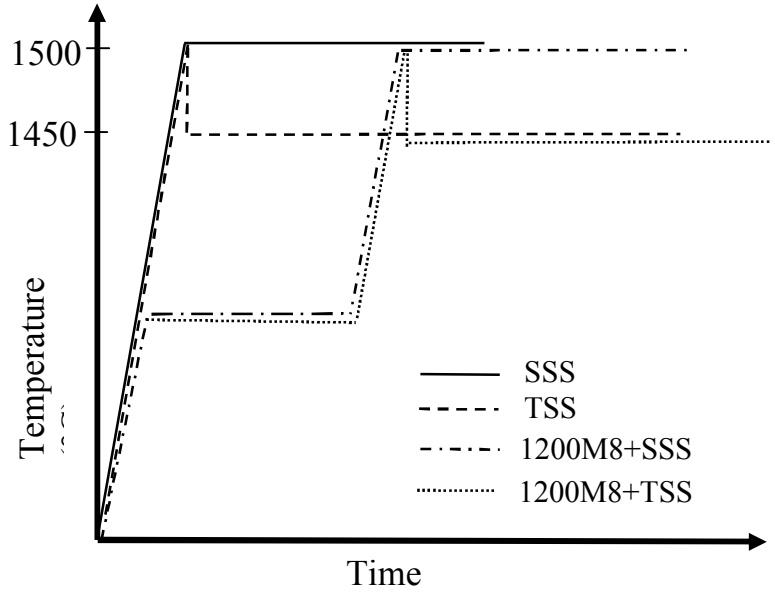

Figure 4.23. Heating regimes used in two-step sintering experiments as well as in the isothermal sintering and combination of precoarsening and single or two steps sintering tests.

Cycles de chauffage des essais de frittage en deux étapes, de frittage isotherme et combinant un traitement de pre-coalescence avec un frittage en deux étapes.

Table 4.3. Heating conditions of two-step sintering, single step sintering and combination of precoarsening and single or two steps sintering tests.

Conditions de chauffage des frittages en deux étapes, en une seule étape et combinant un prétraitement et un cycle en deux étapes.

Description of the heating regime	**Code**	**Precoarsening step (Temperature/time)**	**T1** (°C)	**T2** (°C)	**Soaking Time (hours)**
Two steps sintering I	TSS-I	None	1500	1450	16
Two steps sintering II	TSS-II	None	1450	1400	24
Two steps sintering III	TSS-III*	None	1450	1400	16
Single step sintering I	SSS-I	None	1450	1450	16
Single step sintering II	SSS-II	None	1500	1500	10
Precoarsening followed by single step sintering I	1200M8+ SSS-II	1200°C/8 hours	1500	1500	10
Precoarsening followed by two steps sintering I	1200M8+ TSS-I	1200°C/8 hours	1500	1450	16

* Exception of the TSS-III (5.7°C/min), heating rates of all the samples were 10°C/min.

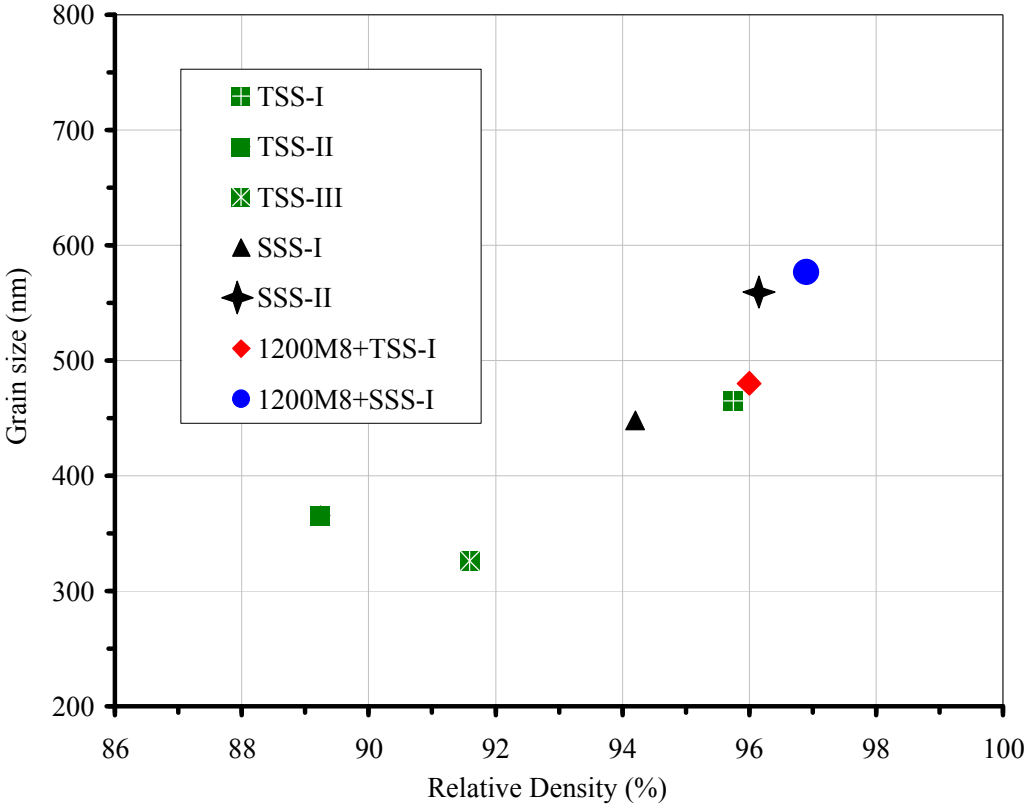

Figure 4.24. Sintering paths of spinel specimens : grain size vs. relative density for Single Step Sintering (SSS) and Two Steps Sintering (TSS).

Trajectoire de frittage d'échantillons de spinelle : taille de grains en function de la densité relative pour des frittages en une seule étape et en deux étapes.

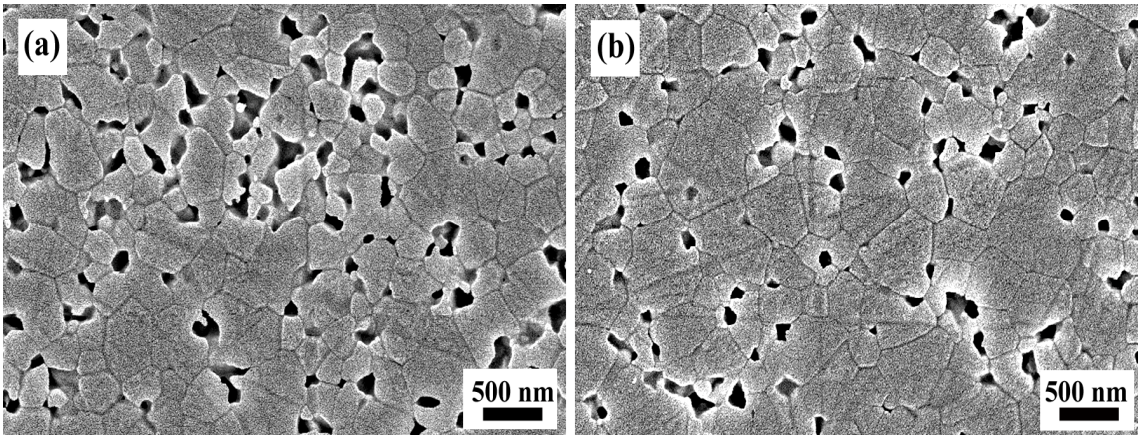

Figure 4.25. SEM images of the spinel specimens sintered with (a) SSS-I and (b) TSS-I.

Micrographies MEB d'échantillons de spinelle frittés suivant les cycles thermiques a) SSS-I et b) TSS-I.

According to the results shown in Figure 4.24, TSS clearly achieved a higher density than conventional single step isothermal sintering with a small increase in grain size. TSS-1 sample, for example, had 94.3% relative density after isothermal sintering at 1450°C with a mean grain size of 450 nm. When the same soak temperature of 1450°C was reached after a first heating step at T1=1500°C, the relative density was found to rise to 95.7% with a small increase in grain size of up to 465 nm. For comparison purposes three additional data points are plotted in Figure 4.24 for samples heated by SSS-I. These data points indicated that it was possible to reach densities higher than 97% but at the expense of higher grain growth.

Figures 4.25(a) and (b) show SEM images of polished and chemically etched surfaces of spinel ceramics with the heating regimes of SSS-I and TSS-I, respectively. Both samples were chemically etched in the same etching conditions. Thermal etching was also done but was found to produce incorrect results as discussed in Section 4.2.2. According to image analysis and average grain size calculation, the SSS sample had nearly 6% porosity and 465 nm of average grain size, while the TSS sample had about 3% porosity and 470 nm of average grain size. The porosity analyses were coherent with Archimedes results of the samples.

4.4. Conclusions

Conclusions

Densification behavior of the spinel powder was investigated using vertical dilatometers. Two bumps and a minimum in-between were observed in the densification rate versus temperature plots of the powder. There were two distinct peaks at the densification rate versus temperature plots at 1240°C and 1370°C for 1°C/min of heating rate. This is probably a characteristic of the powder studied. Grain growth kinetics was also studied. A value of m=2.75 was found for the grain growth exponent versus time. This result was different from those reported in literature possibly due to the presence of pores and impurities. Benamuer et al. (Benameur, et al. 2010) observed that impurity levels of their spinel significantly decreased during the sintering process. Apparent activation energy for densification of the powder was measured and calculated using two different techniques. First method involved the use of densification rate versus reciprocal temperature diagrams to calculate the activation energy from slopes to

be 863 kJ/mol. The activation energy was found to gradually decrease by increasing the relative densities up to 0.80 and then to increase significantly at higher (ρ_{rel}=0.85) relative densities. Another technique used for calculation of activation energy was the master sintering curve (MSC) method which yielded an activation energy value of 833 kJ/mol. The two values for Q were interestingly in good agreement. The activation energy values reported in the study of Benameur et al., (2010) are also in agreement with the results reported here. A potential explanation could be the characteristic of the powder used in the study which was also manifested in its sintering behavior. Microstructures of the ceramics were also observed and grain growth near the surface was determined. MgO evaporation on the surface of spinel might be the reason for this abnormal grain growth.

For nearly fully dense spinel ceramic, 15 minutes of chemical etching in orthophosphoric acid gave the best etching results. Thermal etching led to two major problems: pore closure and some grain growth. The surface roughness of spinel was also significantly affected by thermal etching at high temperature treatment conditions. Chemical etching also provided good results for low density spinel ceramics (85% density) for a limited soak time range around 10 minutes. For these samples, however, fracture surfaces can give more accurate information on porosity and average grain size. If 85% dense spinel is excessively soaked in acid for etching, it rapidly dissolves and can produce significantly misleading microstructures. Finally, care should be taken to adapt the correct etching schedule.

In the second part of this chapter, sintering characteristics of spinel was investigated. Precoarsening treatments at 1100-1200°C were applied and the lower temperature peak was found to disappear. Microstructural development was investigated on fracture surfaces of these pretreated samples. Grains were found to coarsen with increasing soak time at the soak temperature. Increasing temperature from 1100°C to 1200°C also produced the same effect. Mercury porosimeter measurements indicated a monomodal pore size distribution both before and after pretreatment. An increase in the proportion of closed pores was observed when the pretreatment temperature was elevated. Two step sintering technique was tested on three different thermal treatment schedules and an increase in relative density up to 96% was measured without an increase in grain size (460 nm). A slightly higher density was possible with combined use of pretreatment and TSS. Best density was achieved in 1200°C pretreated sample when fired at 1500°C for 10 hours but this time grain growth occurred.

CHAPTER 5

CO-PRESSING, CO-SINTERING AND CHARACTERIZATION OF BI-MATERIALS

Co-pressage, co-frittage

Caractérisation de bi-matériaux

Résumé

Deux différents systèmes de bi-matériaux à base d'oxydes ont été étudiés. Après co-frittage les bi-matériaux alumine B (non dopée) – zircone TZ-2Y présentent des interfaces très peu solides, alors que les interfaces des paires alumines –spinelle semblent relativement très résistantes. Ces échantillons présentent des mécanismes de tenue mécanique à l'interface entre les deux parties différents. Dans le premier cas la faible liaison mécanique résulterait d'un simple emboitement mécanique des grains. Alors que dans le second cas la bonne tenue mécanique de l'interface serait due à une liaison « chimique » par diffusion lors du co-frittage. Dans le cas des combinaisons alumine B – zircone Z-3Y les deux parties sont même séparées après le cycle de co-frittage ; cette séparation peut s'expliquer par les écarts de retrait de frittage très prononcés entre ces matériaux

Les observations en micorscopie électronique à balayage montrent pour les couples alumines – spinelle co-frittés une couche intermédiaire de grains colonnaires de spinelle avec quelques micro-fissures dans la partie alumine qui semblent dépendre de la séquence de compactage pour la combinaison alumine B – spinelle. Dans les bi-matériaux zircone TZ-2Y – alumina B, après co-frittage des fissures perpendiculaires à l'interface sont observées dans la partie zircone ; ces fissures seraient apparues au refroidissement à cause du coefficient de dilatation de la zircone plus élevé que celui de l'alumine.

Différentes techniques de co-pressage ont été mises en œuvre pour obtenir des bi-matériaux à cru plus homogènes et sans fissure. Des séquences de pressage comprenant un presage uniaxial simple effet ou en matrice flottante sous faible contrainte suivi d'un pressage isostatique à froid sous plus forte contrainte ont permis

de minimiser la fissuration au niveau de l'interface. Un essai mécanique sur un bi-matériau alumine A – spinelle co-fritté a montré qu'il supporterait une contrainte de traction d'au moins 10 MPa.

5.1. Introduction

Introduction

The sintering and densification behaviors of mono-materials via different heating regimes are reported in the previous chapters. Bi-materials and their sintering behavior, however, are the core of this thesis due to a combination of properties that they can offer. A strong bond between two co-sintered oxide ceramics can provide novel properties.

Bi-materials have functional properties, depending on mechanical, electrical and magnetic properties of their components. Their applications areas are ranging from electronic packaging applications such as multi-layer ceramic capacitors to thin film-substrate systems used widely in the microelectronics industry (Boonyongmaneerat and Schuh 2006, Cai, et al. 1997a). There are many types of bi-materials; metal-metal (Simchi, et al. 2006a, Simchi 2006b), metal-oxide (Boonyongmaneerat and Schuh 2006) and oxide-oxide (Cai, et al. 1997a, Cai, et al. 1997b, Sun, et al. 2008).

Die compaction of layers (powder stacking) is a simple and well established method. The disadvantages of the process are limited number of layers (not more than two or three in potential fabrication), limited size of the part (<100 cm^2) due the limits of compaction forces. Nevertheless this method allows effective laboratory studies of layered materials (Kieback, et al. 2003).

Ravi and Green (2006) analyzed distortion in the bi-layer configurations. Because when a powder is consolidated, variations in green density are known to arise (Lannutti, et al. 1997). These density variations impart a difference in shrinkage strain from one region to another. The corresponding differential strain rate between these regions is expected to produce densification stresses and/or warpage during sintering (Kellett and Lange 1984). In order to characterize these density gradients and relate them to the microstructure, properties and tolerances of the final sintered part, experiments were performed on model bi-layer structures in which there is a green density difference between the layers (Ravi and Green 2006).

Co-sintering process is to sinter two materials to one piece while they have contact with each other, relatively common technique to fabricate bi-material. The advantage of co-sintering is that it allows both slurry-based and compaction-based processing routes (Boonyongmaneerat and Schuh 2006). On co-sintering two different powder materials must match in shrinkage to minimize differential strains. Otherwise cracks and cracklike defects are commonly observed in these systems as a result of mismatch stresses. One reason of these stresses is thermal expansion difference between constituent layers, which occurs during the cooling stage when materials are brittle. Mismatch stress also can be generated during sintering process when the co-sintering layers have different densification kinetics (Cai, et al. 1997a).

Cai et al., (1997a) fabricated bi-layers of alumina-zirconia by tape casting and lamination methods. They examined the type of cracks and crack-like defects which occurred as a consequence of mismatch stress during sintering and cooling periods. For the purpose of strengthening the interlayer bonds and layer densities between alumina and zirconia, various amounts of alumina were also incorporated into zirconia. They eventually concluded that it is highly reasonable to provide a precise control of heating and cooling rates during sintering process in order to achieve defect-free bi-layers of alumina and zirconia. Their other study (Cai, et al. 1997b) involved the analytical expressions for the viscoelastic mismatch stresses that are established between alumina – zirconia symmetric bi-material layers. The uniaxial viscosity and Young's modulus for the heating cycle have been measured by cyclic dilatometry. The calculated stresses at different stages of processing are analyzed with respect to the possible corresponding failure mechanisms.

Further, co-sintering is used in sintering the functionally gradient materials. These are transition materials; for example, one end is 100% metallic and gradual thin steps are used to progress to 100% ceramic (German 1996). Sun et al., (2008) studied to eliminate cracks and chambers in three-layered Al_2O_3/ZrO_2 functionally graded materials (FGMs). The green bodies composed of alumina, mixture of alumina and zirconia and zirconia layers were compacted in a single-action die and co-sintering at different heating regimes. Two distinct alumina powders and two distinct zirconia powders were mixed to change powder characteristics. Low compaction pressure (at 60 MPa) and modified interface profile by using jagged surface punch at compaction and low cooling rate (4°C/min) are the optimized processing parameters for crack free FGMs.

Simchi et al., (2006a) evaluated the microstructure and density profile during co-sintering of magnetic and non-magnetic stainless steel powders. Co-sintering process offers some advantages, including lower cost and simple manufacturing step compared to other fabrication methods such as joining. They produced green bilayer compacts by uniaxial dry pressing method. In their corresponding study, considering the shrinkage curves obtained from dilatometer, they calculated also mismatch strain and strain rate of bilayer during co-sintering process.

In this chapter, different types of bi-materials are studied. These are alumina – zirconia and alumina – spinel bi-materials. Different co-pressing techniques and the resulting co-sintering behaviors are tested to produce crack-free bi-materials. Final microstructures and microstructural interactions on the interfaces of the two different bi-combinations which were co-pressed and co-sintered oxide materials, are analyzed, interpreted and discussed considering their strain (or shrinkage) mismatches, strain rates and thermal expansion mismatches as well as diffusion and interdiffusion kinetics between the components of the bi-materials. Adhesion strength and mechanisms between the two component powders are investigated.

5.2. Experimental Procedure

Procédure expérimentale

5.2.1. Bi-material Combinations

Combinaisons de bi-matériaux

The mono-materials, introduced in Chapters 3 to 4, were used as components of the potential bi-materials. In this study, production and characterization of four different types of bi-materials were investigated. But considering the compaction order for example, if alumina A was the first powder and spinel was the second one that was filled into the compaction die, A/S bi-material designation was used. On the other hand, the designation S/A means that the bi-material was prepared in the green state by placing the spinel first into the die mold cavity and alumina later. All possible combinations are listed in Table 5.1. Not all of them, however, are used in this thesis. Details of the production process of co-pressed and co-sintered materials are described in the next section.

Table 5.1. Produced bi-materials and their components.

Bi-matériaux étudiés et leurs composants.

#	Bi-material Combination	Code
1	Alumina A – Spinel	A/S or S/A
2	Alumina B – Spinel	B/S or S/B
3	Alumina B – Zirconia TZ-2Y	B/TZ-2Y or TZ-2Y / B
4	Alumina B – Zirconia Z-3Y	B/Z-3Y or Z-3Y /B

5.2.2. Co-Pressing Techniques of Bi-materials

Techniques de co-pressage des bi-matériaux

Green compacts of the bi-materials were produced with different co-pressing techniques. They were all described in the following subsections.

5.2.2.1. Co-Pressing with Single-action Mode of Uniaxial Pressing

Co-pressage uniaxial en mode simple action

The bi-materials pellets were prepared by single action-mode of uniaxial pressing at two different pressures: 150 MPa and 250 MPa. The co-pressing method is illustrated in Figure 5.1. The first powder was poured into die cavity and was settled down uniformly at its bottom by tapping with a metal rod. Afterwards, the second powder was subsequently poured on top of the previous layer and the powders were eventually co-pressed together into pellets. This compaction technique was designated as; Co-UP.

5.2.2.2. Uniaxial Co-Pressing with Floating Die (Co-UPFlo)

Co-pressage uniaxial en matrice frlottante

The bi-materials pellets were also prepared by floating die-mode of uniaxial pressing at a pressure of 250 MPa. The co-pressing method with floating die mode is illustrated in Figure 5.2. The same procedure was used as in single-action-mode of

uniaxial pressing. Except, there is a spring between die and bottom punch. So the die also moves by tightening of spring when the top punch is moving under applied pressure but the bottom punch is fixed. This compaction technique was designated as Co-UPFlo.

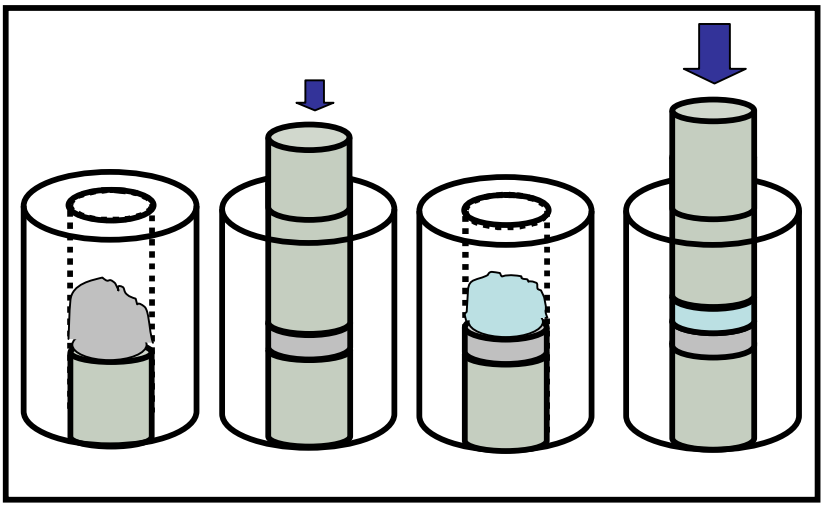

Figure 5.1. Schematic illustration of uniaxial single action co-pressing method (Co-UP).

Illustration de la méthode de co-pressage uniaxial en mode simple action.

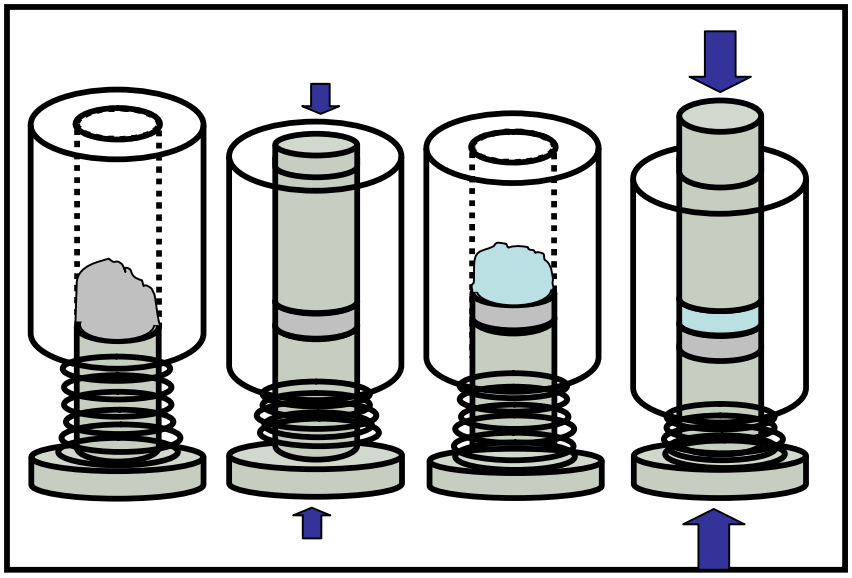

Figure 5.2. Schematic illustration of co-pressing method with floating die mode of pressing (Co-UPFlo).

Illustration de la méthode de co-pressage uniaxial en matrice flottante.

5.2.2.3. Co-Pressing with Cold Isostatic Pressing after Uniaxial or Floating Die Mode of Pressing (Co-UP or UPFlo+ CIP)

Co-pressage uniaxial en matrice flrottante suivi d'un pressage isostatique à froid

The bi-materials pellets were previously produced at low pressures (50 or 100 MPa) with single-action mode of uniaxially pressing or floating die-mode of uniaxial pressing as described in previous sections and then they were compacted under CIP at 250 MPa. These bi-material green body production techniques were designated as Co-UPFlo+CIP or Co-UP+CIP depending on the initial pressing methods.

5.2.3. Co-Sintering

Co-frittage

In the first set of experiments, all bi-materials were prepared by utilizing the single action-mode of uniaxial pressing at different pressure values as mentioned in Section 5.2.2. Various types of bi-material green compacts were produced via single action-mode of uniaxial pressing by switching compaction order of bi-material components. The resulting green compacts were then co-sintered with different constant heating rates (1 and 3.3°C/min) upto 1580°C, using a vertical dilatometer. In addition to bi-materials, green compacts of zirconia, alumina and spinel mono-materials were pressed at 250 MPa and then fired at selected same heating conditions. Therefore, sintering behaviors of all oxides were studied by themselves or in combination with other oxides as couples. A photograph of a co-sintered alumina – spinel bi-material is shown in Figure 5.3.

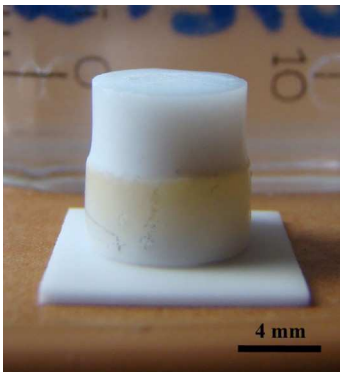

Figure 5.3. Photograph of a co-sintered alumina – spinel bi-material (1500°C – 4 hours) : the upper part is the spinel part.

Photographie d'un bimatériau alumine – spinelle cofritté (1500°C – 4 heures) : la partie supérieure correspond à la spinelle.

5.3. Results

Résultats

5.3.1. Comparison of the Densification Behaviors of Mono-Materials

Comparaison des conportements en densification des différents mono-matériaux

Combinations of bi-materials were examined by comparing and analyzing their shrinkages and shrinkage rates. The sintering behavior of powders was investigated separately. Figure 5.4(a), gives the relative shrinkage curves of all powder samples as a function of temperature. Based upon the related values obtained from the corresponding graph, each powder type studied was indicated to exhibit shrinkage values between more or less 17 and 25 %. Sintering of zirconia TZ-2Y occurs at lower temperatures, thus exhibiting a relatively high densification rate, as compared to the other powders. Of all, alumina A and alumina B have the highest and lowest relative shrinkage values, respectively. Shrinkage behaviors of alumina A and alumina B powders are distinctly different from each other. This trend is also valid for zirconia powders such that zirconia TZ-2Y shows highly different behaviour than zirconia Z-3Y.

Time dependent shrinkage rate results of mono-materials are given in Figure 5.4(b). As seen in this graph, alumina A has a significant shrinkage rate than the others.

Provided that the same type of powders such as alumina A and alumina B are not co-sintered, any bi-combination of these powders were experimentally investigated and intensively discussed in the following sections. Moreover, mismatches that occurred during co-sintering were calculated based on the relative shrinkage and shrinkage rate values of each powder given in Figure 5.4(a) and (b). The basics of these calculations were also highlighted under the subsequent title in details.

5.3.2. Calculation and Analysis of Strain and Strain Rate Mismatches

Calcul et analyse des écarts de deformation et de vitesse de déformation

As depicted in Figure 5.4, each type of powder features distinct shrinkage behavior with respect to the temperature applied. This dissimilarity between individual layers causes mismatch strain to occur at the interface during co-sintering of the

bilayers, leading to interfacial cracking. The mismatch strains and strain rates were computed for any bi-material by using the below formula as follows.

$$\text{Mismatch strain} = \left(\frac{\Delta L_{(T)}}{L_o}\right)_{Powder-A} - \left(\frac{\Delta L_{(T)}}{L_o}\right)_{Powder-B} \tag{5.1}$$

$$\text{Mismatch strain rate} = \left(\frac{d\left(\Delta L_{(T)} / L_o\right)}{dt}\right)_{Powder-A} - \left(\frac{d\left(\Delta L_{(T)} / L_o\right)}{dt}\right)_{Powder-B} \tag{5.2}$$

According to Equation 5.1, shrinkage values of each individual layer at any specified temperature ranging from 20 to 1580°C are subtracted from one another. Figures 5.5(a), and (b) show the calculated mismatch strain values for bi-combinations of alumina – zirconia, and alumina – spinel, respectively. As seen in Figure 5.5(a), bi-combinations including alumina B – zirconia TZ-2Y and alumina B – zirconia Z-3Y exhibited distinctly different behavior. On the other hand, alumina A – spinel and alumina B – spinel bi-combinations up to almost 1050°C show the same response such that no significant mismatches took place in between (in Figure 5.5(b)). However, zirconia Z-3Y – spinel and zirconia TZ-2Y – spinel bi-combinations demonstrated the same behavior as alumina – zirconia bi combinations already given in Figure 5.5(a).

Mismatch strain rate results are also important to understand the incompatibility between the layers during sintering. They can be calculated by subtracting time dependent strain rate of components from each other (in Equation 5.2). The results of mismatch strain rates are given in Figures 5.6(a) and (b). These findings are critical to evaluating the potential performance of the bi-materials to be produced. Alumina B–zirconia TZ-2Y bi-materials showed smaller differences in mismatch strain rates compared to alumina B – zirconia Z-3Y. Alumina A – spinel and alumina B – spinel pairs showed larger differences in shrinkage mismatch strain rates.

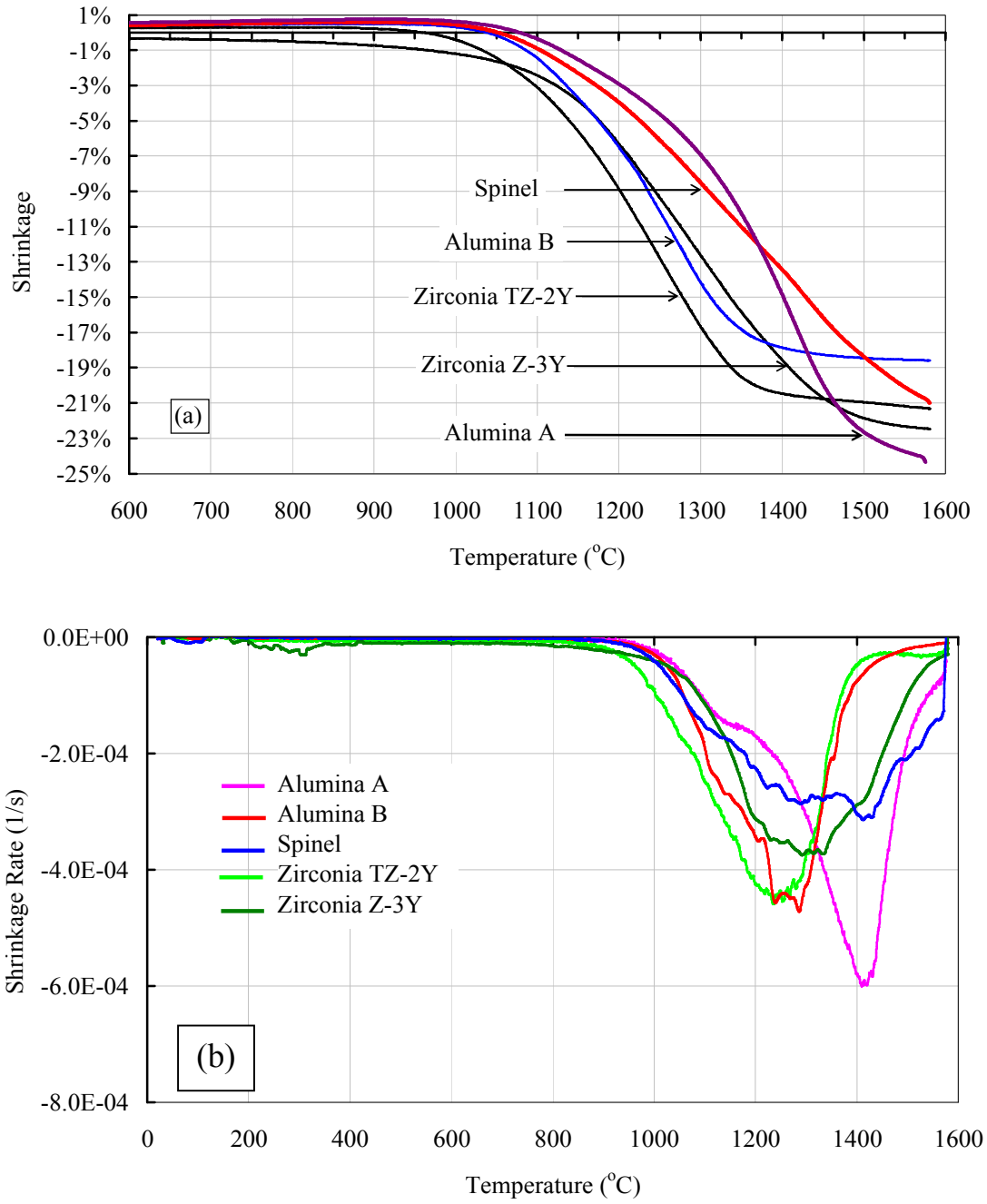

Figure 5.4. Shrinkage behaviors of powder compacts (UP 250MPa) of alumina B, alumina A, zirconia Z-3Y, zirconia TZ-2Y and spinel (a) relative shrinkage and (b) shrinkage rate curves during sintering up to 1580°C with heating rate of 3.3°C/min.

Comportements en retrait comparés de comprimés de poudre (UP 250 MPa) d'alumine B, d'alumine A, de zircone Z-3Y, de zircone TZ-2Y et de spinelle : courbes a) de retrait et b) de vitesse de retrait pour un frittage anisotherme jusqu'à 1580°C avec une vitesse de chauffage de 3,3°C/min.

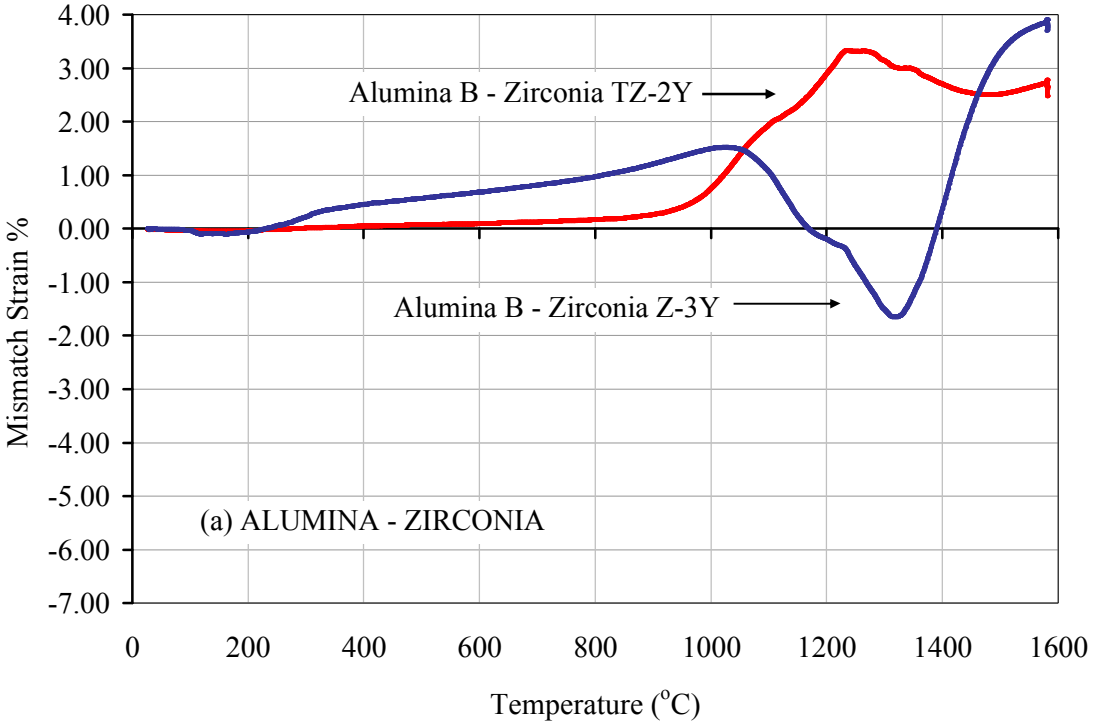

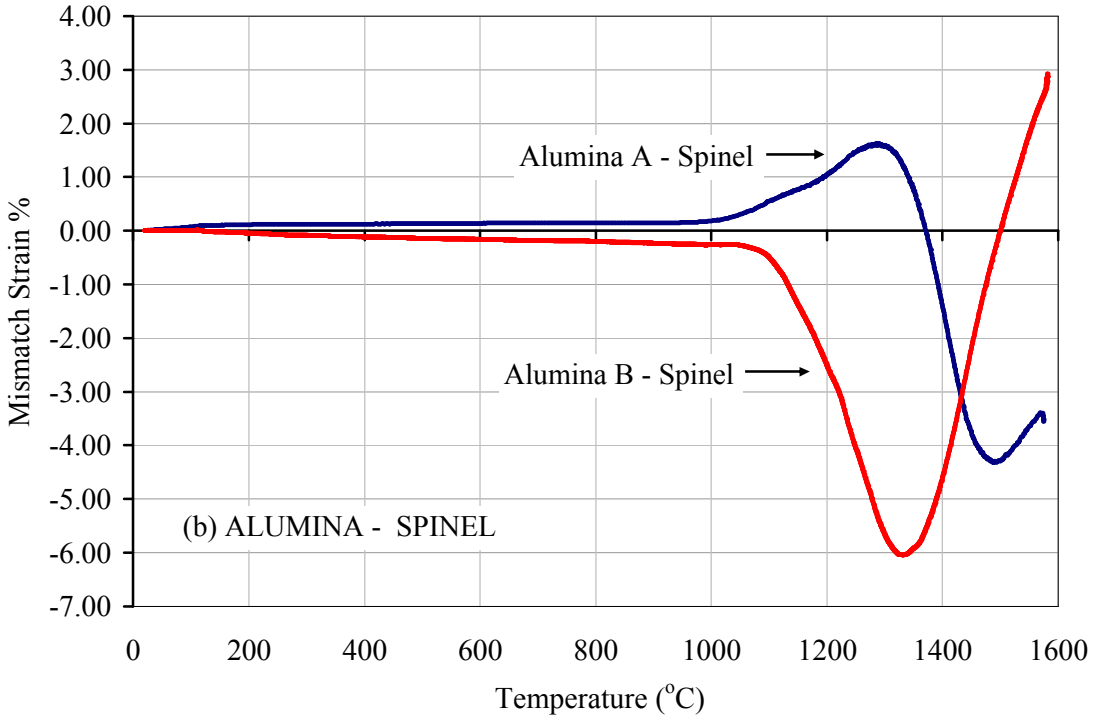

Figure 5.5. Mismatch strains of individual powder compacts of (a) alumina – zirconia, alumina – spinel, (UP 250 MPa) sintered at 1580°C with heating rate of 3.3°C/min.

Ecart de deformation entre des comprimés de a) alumines – zircone b) alumines –spinelle (UP 250 MPa) frittés individuellement jusqu'à 1580°C avec une vitesse de chauffage de 3,3°C/min.

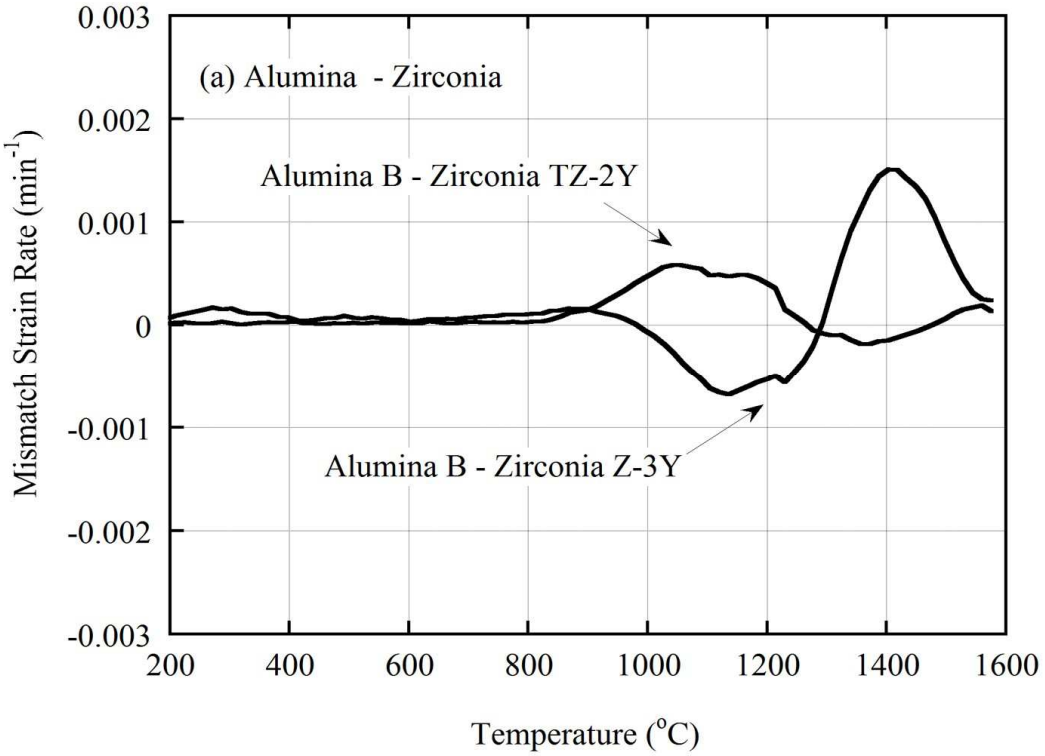

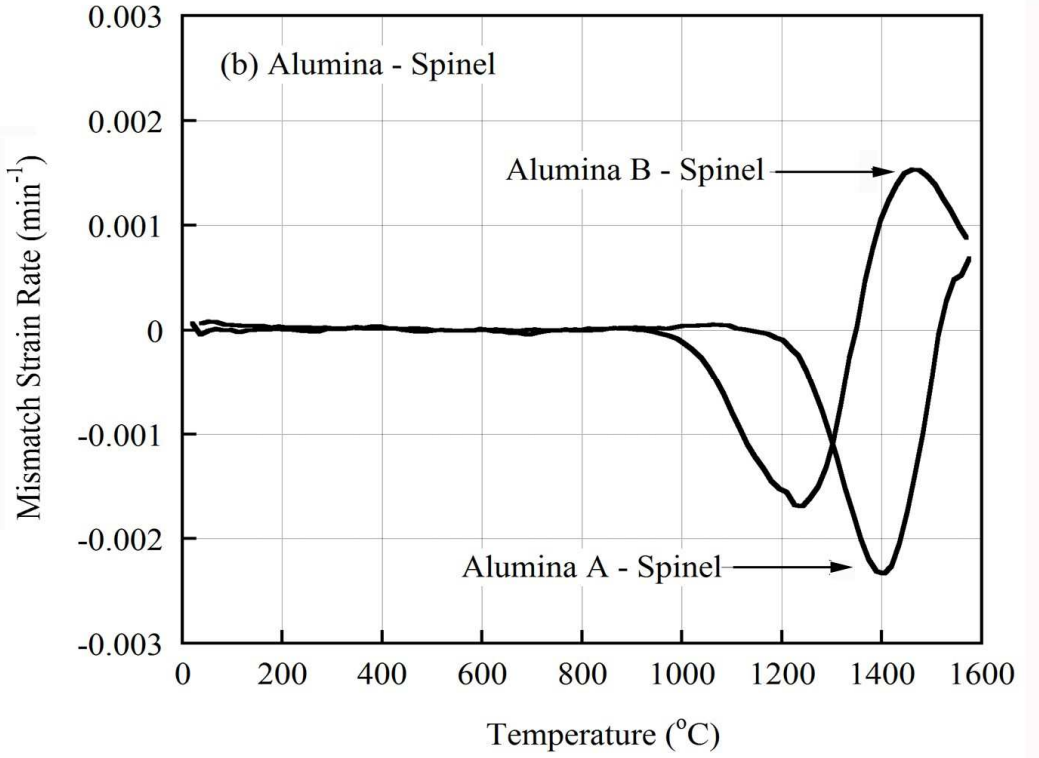

Figure 5.6. Mismatch strain rates of individual powder compacts (UP 250 MPa) of (a) alumina – zirconia, (b) alumina – spinel sintered up to 1580°C with heating rate of 3.3°C/min.

Ecart de vitesse déformation entre des comprimés de poudre (UP 250 MPa) de a) alumines – zircones b) alumines –spinelle (UP 250 MPa) frittés individuellement jusqu'à 1580°C avec une vitesse de chauffage de 3,3°C/min.

5.3.3. Results of Sintering of Bi-materials

Résultats de frittage de bi-matériaux

As mentioned in Section 5.3.1, there are four different types of bi-materials but considering the compaction order the total number of bi-material couples tested was seven. The results observed for each bi-material by bare eye at each given condition are given in Table 5.2. In the table, symbol "X" refers to those bi-material samples that fractured and separated at the interface after co-sintering, while the other symbol "+" means a well-bonded interface.

Consequently, spinel – alumina A, spinel – alumina B and alumina B – zirconia TZ-2Y pairs were observed to bond well relative to the other pairs studied including zirconia Z-3Y – alumina B. These pairs separated after co-sintering process. The reason for separation of these bi-combinations can be explained by mismatch strains and mismatch strain rates between components of these pairs. Their mismatch strain rate fluctuation is relatively higher than the bonded alumina – zirconia TZ-2Y pairs.

Table 5.2. Observations of uniaxial co-pressed bi-materials pellets after co-sintering.

Observations après co-frittage des échantillons de bi-matériaux co-pressés uniaxialement.

#	Code	Bi-combinations and compaction order	1580°C			
			1°C/min		3.3°C/min	
			150 MPa	250 MPa	150 MPa	250 MPa
1	(A/S)	Alumina A Spinel		+		+
2	(S/A)	Spinel Alumina A		+		+
3	(B/S)	Alumina B Spinel	+	+	+	+
4	(S/B)	Spinel Alumina B		+		+
5	(TZ-2Y/B)	Zirconia TZ-2Y Alumina B	+		+	
6	(B/TZ-2Y)	Alumina B Zirconia TZ-2Y		+		+
7	(Z-3Y/B)	Zirconia Z-3Y Alumina B	X	X		X

5.3.4. Observation of Bonding of the Bi-materials

Observation de la liaison des bi-matériaux

General shapes of zirconia TZ-2Y – alumina B and spinel – alumina B bi-materials are shown in Figures 5.7(a) and (b), respectively. The bi-material green body productions were done as mentioned in Section 5.2.2 For the bi-materials in Figure 5.7(a), zirconia was the first powder (bottom part) and alumina B was the second one (top part). It was uniaxially pressed at 150 MPa by single-action die mode. For the alumina – spinel bi-material (in Figure 5.7(b)), spinel was the first powder on the compaction and alumina B was the second one which was compacted at 250 MPa. The green compacts of bi-materials were sintered up to 1580°C with various heating rates including 1°C/min. Regardless of the type of powder, powder order or compaction pressure, interface was curved with center of curvature in the second powder (Figures 5.7(a) and (b)). This can be attributed to the compaction process of powders. The compaction was done by single-action mode so the pressure was applied only by the top punch. Some cracks in the zirconia parts are observed by naked-eye independent of compaction pressure (150 or 250 MPa). In the alumina – spinel type of bi-materials, some visible cracks were also detected, particularly in the spinel regions through the interface.

In order to eliminate the curvature of the interface in the bi-materials and also to produce crack-free bi-materials, other types of green compaction methods were applied. Figures 5.8(a), (b), (c) and (d) give the cross sectional images of alumina A – spinel bi-materials, produced with different green compaction methods (as mentioned in Section 5.2.2). In Figure 5.8 the bottom halves of the bi-materials were always alumina. Classical single action-mode of uniaxial pressing resulted in a curved interface (Figure 5.8(a)). Figure 5.8(b) shows the cross sectional image of alumina A – spinel bi-material, produced by co-pressing with floating die mode of uniaxial pressing at 250 MPa. The curvature of the interface was eliminated by this production method, and the interface was parallel to the top and bottom sides. Moreover, no cracks were observed at the center of interface or at the components near the center of interface but there are still some cracks around the edge of interface by bare eye observation.

Unfortunately, in the die compaction, the crack formation is common and unavoidable when the disk sample with a height-to-diameter ratio is higher than 0.5–1.0

due to significant variations in the packing density of the green body during pressing. Therefore, in order to minimize the density variations, cold isostatic pressing was applied to produce better uniformity in the packing density and also it can be used for the production of green bodies with complex shapes and with much higher height-to-diameter ratios. For that reason, the bi-materials green compacts firstly were produced by die compaction method at low pressures then the green compacts were cold isostatically pressed at 250 MPa. These methods are explained in detail in Section 5.2.2. The produced bi-material green compacts were co-sintered at different sintering regimes.

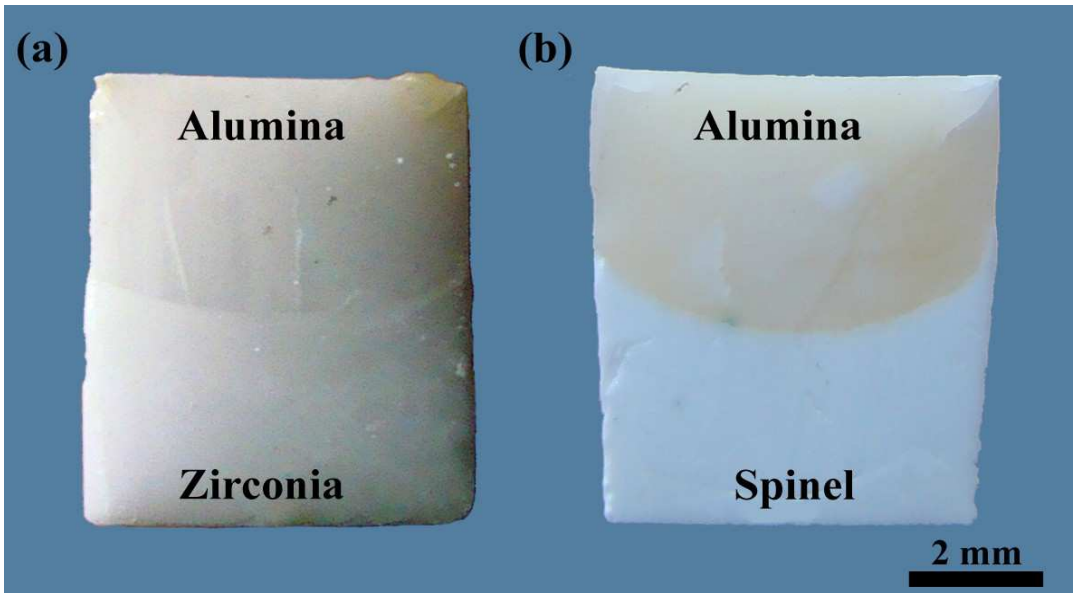

Figure 5.7. Shapes of the bi-materials (a) zirconia TZ-2Y – alumina B (Co-UP 150 MPa), (b) spinel – alumina B (Co-UP 250 MPa). (alumina part at the top in all photos). Co-sintering conditions : 1°C/min up to 1580°C.

Morphologie des bi-matériaux a) zircone TZ-2Y – alumine B (Co-UP under 150 Mpa) , b) spinelle – alumine B (Co-UP 250 Mpa). (la partie alumine est située en haut dans les deux cas). Cycle de co-frittage : 1°C:min jusqu'à 1580°C.

The question now emerges as to what happens when CIP is done after either UP or UPFlo. Figure 5.8(c) shows the cross-section of the bi-material produced by UP followed by CIP at 250 MPa. Cracks were not observed around the interface of the bi-materials. This interface was compared to the other sample, shown in Figure 5.8(d), which was produced via UPFlo followed by CIP. The only difference between the two bi-materials was the shape of the interface. The interlayer was wavy for UP+CIP samples. Another observation was that spinel compacted better after CIP (Figures 5.8(c) and (d)).

Figures 5.9(a) and (b) give the optical microscope images of the bi-materials. According to these images, completely crack free bi-materials were produced by these green body production methods independent of sintering regime and there is good adhesion at the center and edges of the interface. Some pore-like black spots on the surfaces of alumina B parts were observed that are unpolished, artifact points but on the surface of spinel part rarely no such observations because it was polished better than alumina part due to their hardness difference (Spinel: 1050 HV, Alumina: 2100 HV, (Navias 1961)). In early production methods, cracks probably might be observed at the center, edges or corners of bi-materials, because of green body inhomogeneity.

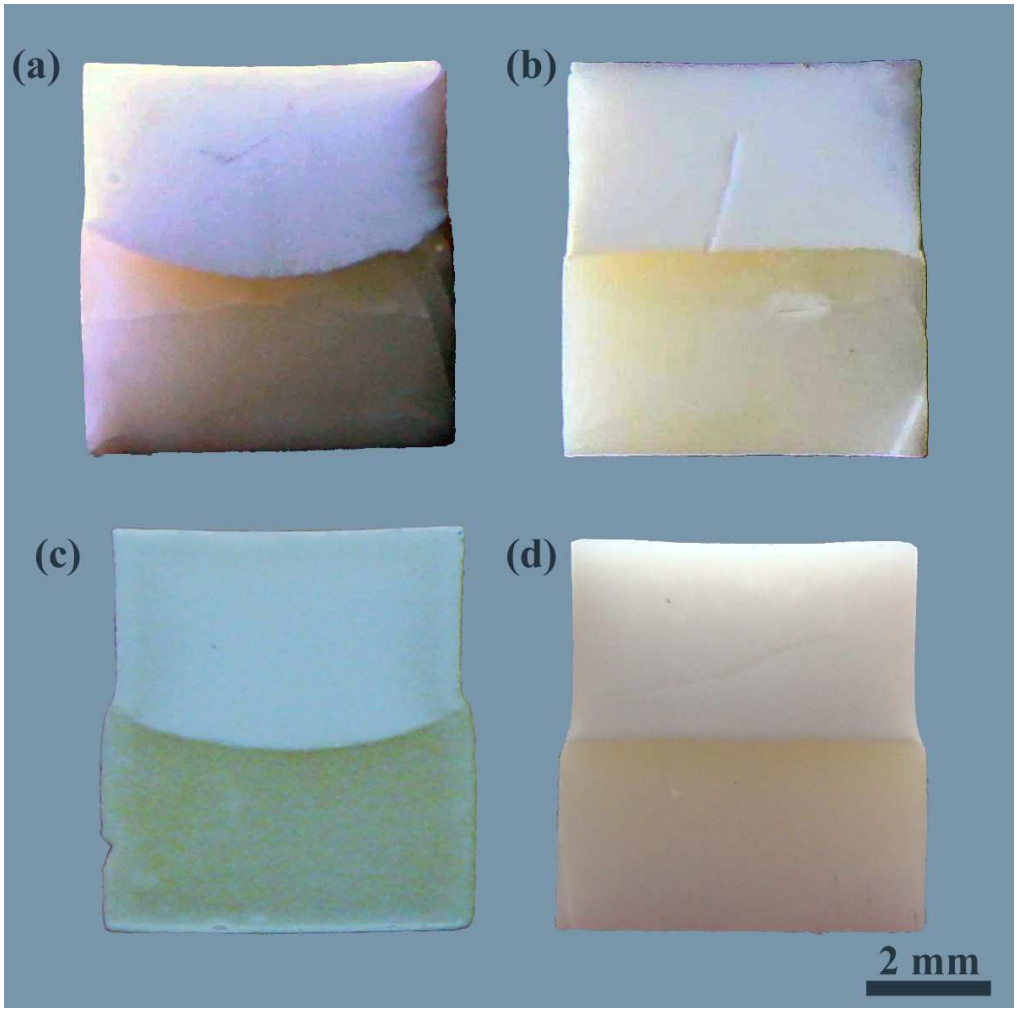

Figure 5.8. Shape of alumina B – spinel bi-materials, produced by different co-pressing techniques at final pressure of 250 MPa (a) Co-UP, (b) Co-UPFlo, (c) Co-UP+CIP and (d) Co-UPFlo+CIP. (Spinel part at the top in all photos) Co-sintering conditions : 1°C/min up to 1580°C.

Morphologie des bi-matériaux alumina B – spinelle, préparés par différentes techniques de co-pressage sous une pression finale de 250 MPa a) Co-UP, b) Co-UPFlo c) Co-UP + CIP and d) Co-UPFlo + CIP. Dans tous les cas la partie spinelle était situé en haut. Conditions de co- frittage : 1°C/min jusqu'à 1580°C.

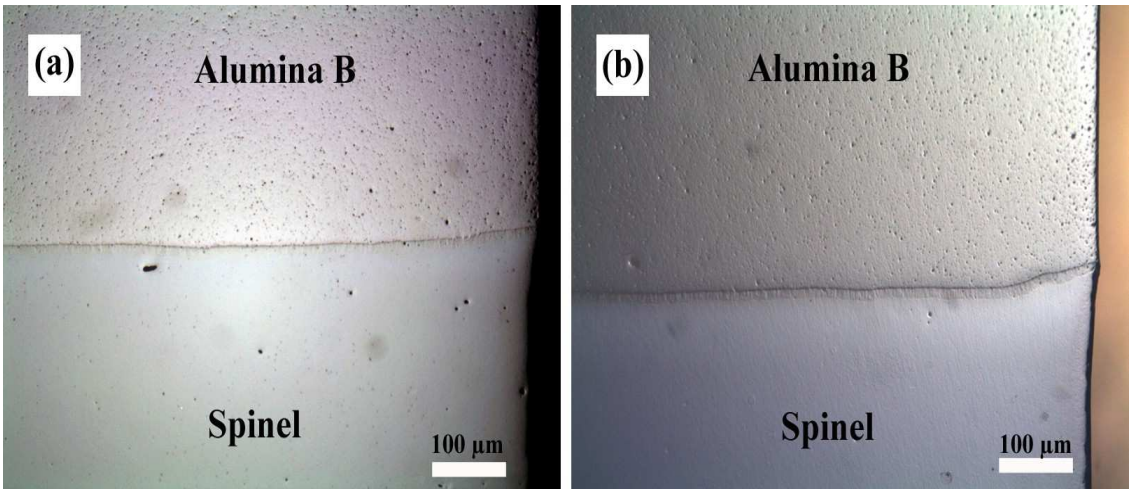

Figure 5.9. Optical Microscope image of bonding regions of spinel – alumina B bi-materials, produced by single-action mode of uniaxial pressing at 100 MPa followed by cold isostatic pressing at 250 MPa (Co-UP+CIP). They were co-sintered at 1500°C for (a) 4 and (b) 16 hours.

Micrographies optiques des régions de liaison de bi-matériaux spinelle – alumine B préparés par co-pressage uniaxial simple effet sous 100 MPa suivi d'un pressage isostatique à frois sous 250 MPa (Co-UP + CIP). Ces bi-matériaux ont été co-frittés à 1500°C pendant a) 4 et b) 16 heures.

5.3.5. SEM images of Bi-materials

Micrographies MEB de bi-matériaux

5.3.5.1. Alumina – Zirconia

Alumine – zircone

Microstructures of alumina B – zirconia TZ-2Y bi-materials were investigated by SEM. In order to observe the interface, the bi-materials were vertically cut into two parts and half of them were polished and thermally etched. The bonding structure, mechanisms and the effect of compaction order between alumina B and zirconia TZ-2Y powders were examined. Polished cross sections of the two types of bi-materials are shown in Figures 5.10(a) and (b). As seen in the Figure 5.10(a), intense cracks arising occurred at the interface region and systematically within the zirconia part perpendicular to the interface. Coefficients of Thermal expansion (CTEs) of the materials from the literature are given in Table 5.3. Figure 5.11 shows linear thermal expansion coefficient (CTE) of mono-materials up to 1100°C. CTE values were measured by using the dilatometer. The results are well-matched with the literature results given in Table 5.3. Zirconia TZ-2Y had the highest CTE value, while alumina A

and alumina B had similar CTE values. So the cracks perpendicular to the interface in the zirconia materials are a consequence of the tensile stress state which develops in zirconia on cooling due to the higher CTE of zirconia.

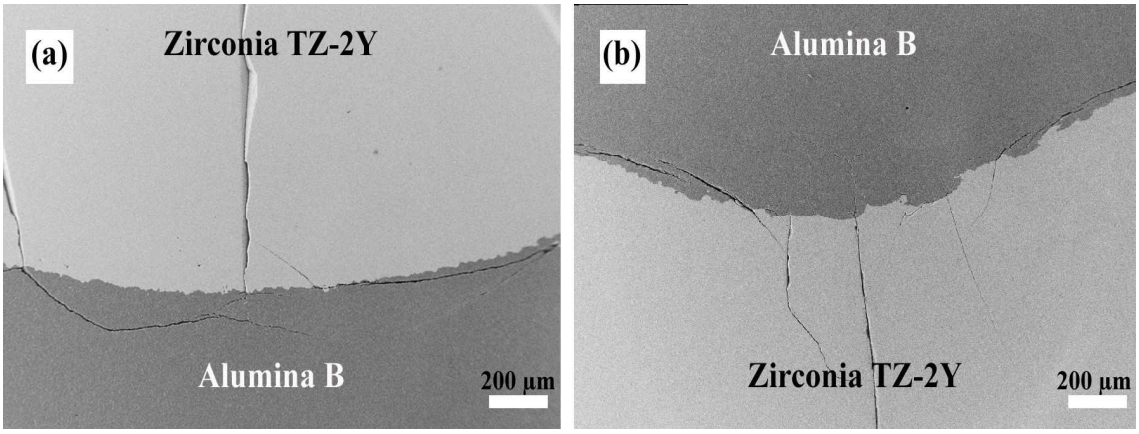

Figure 5.10. Compaction (Co-UP 250 MPa) order and cracks formation on the alumina B – zirconia TZ-2Y bi-materials (a) alumina B – zirconia TZ-2Y bi-material, (b) zirconia TZ-2Y – alumina B bi-material.

Effet de séquence de compaction (Co-UP 250 MPa) et formation de fissures dans des bi-matériaux alumine B – zircone TZ-2Y a) alumine B – zircone TZ-2Y et zircone – TZ-2Y.

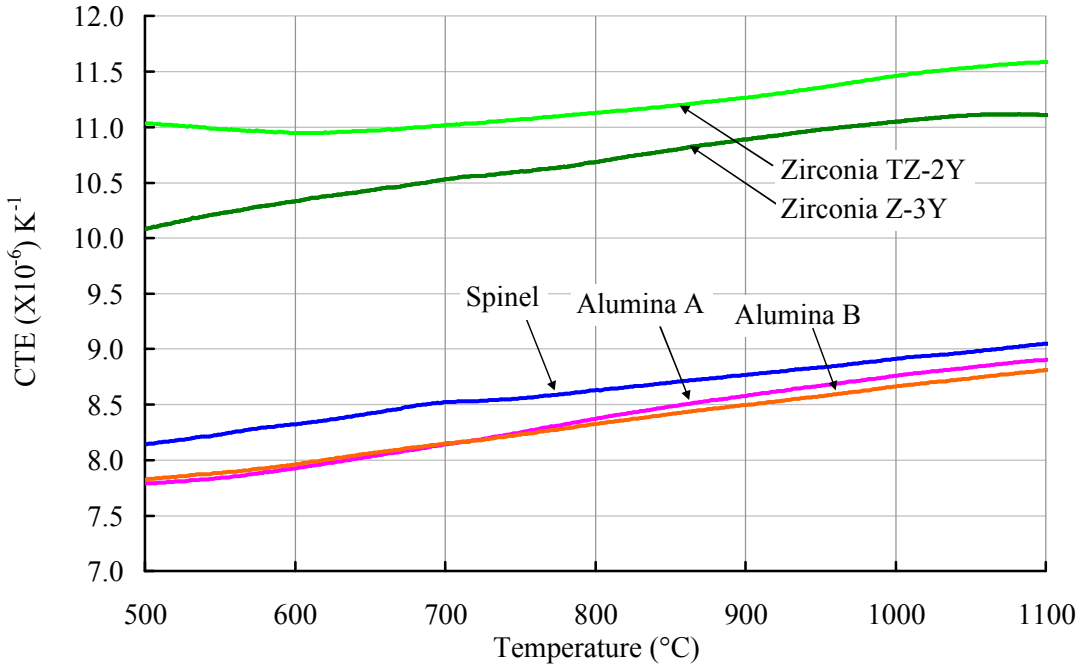

Figure 5.11. Thermal Expansion Coefficients of mono-materials up to 1100°C. Dilatometric data obtained with nearly fully dense samples during the heating step of a thermal cycle (10°C/min).

Coefficients de dilatation thermique des mono-matériaux de cette étude entre 500 et 1000°C. Données dilatométriques obtenues pendant le chauffage à 10°C/min d'échantillons frittés presque totalement denses.

To interpret the mechanism for the formation of interfacial bonding, the alumina – zirconia interface was intensively studied. Figures 5.12(a), (b), (c) and (d) are the SEM micrographs showing the microstructures of alumina B – zirconia TZ-2Y bi-material interface and the individual components at different magnifications, respectively. Highly rough and wavy interface is clearly visible in Figure 5.12(a). This roughness may assist in enhancement of interlocking and mechanical adhesion at the interface of alumina – zirconia bi-materials. In addition, zirconia and alumina B were found to exhibit an average grain size of 200 nm and 2 μm, respectively.

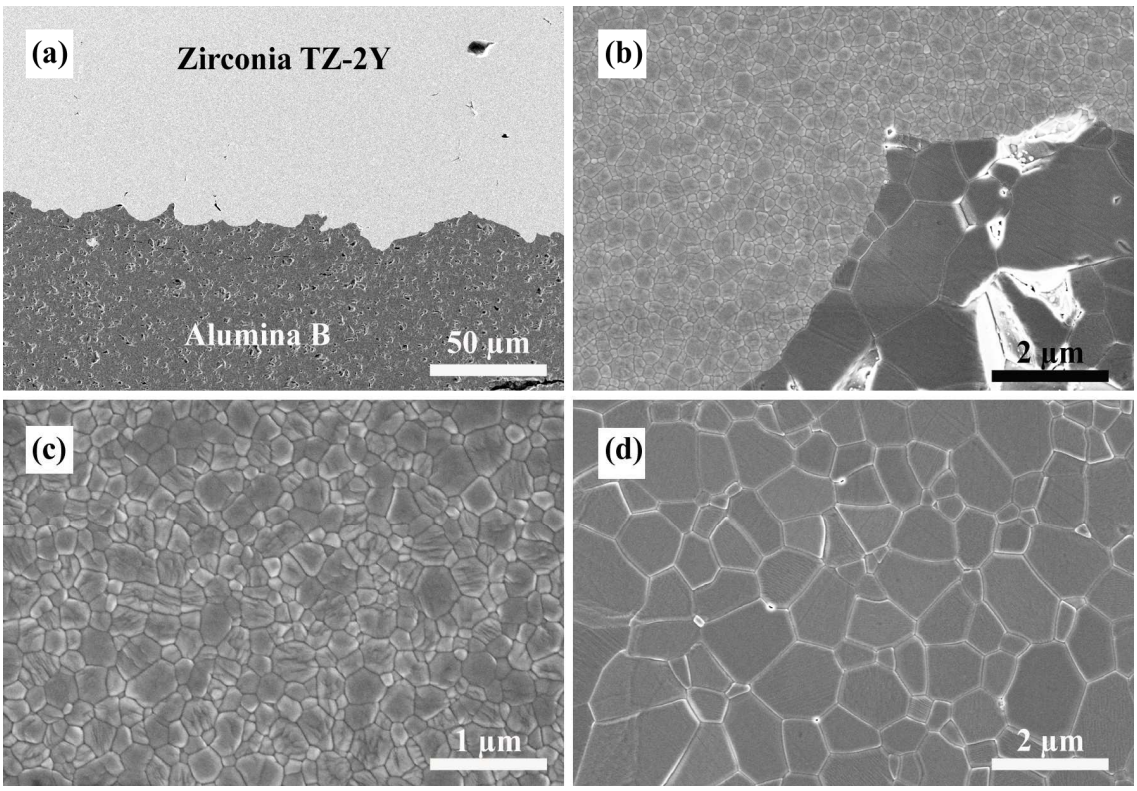

Figure 5.12. SEM micrographs of alumina B – zirconia TZ-2Y bi-material interface and components (a) interface, (b) interface at higher magnification, (c) zirconia TZ-2Y region, (d) alumina B region. (Co-UP at 250 MPa) and co-sintered up to 1580°C at 3.3°C/min.

Micrographies MEB de bi-matériaux alumine B – zircone TZ-2Y (Co-UP 250 MPa) a) zone de l'interface b) zone de l'interface à plus fort grandissement c) partie zircone TZ-2Y et d) partie alumina B. Co-frittage anisotherme à 3,3°C/min jusqu'à 1580°C.

Table 5.3. Mean linear thermal expansion coefficients of materials (Morrell 1985).

Coefficients de dilatation moyens des oxides étudiés (de Morell 1985).

Material	Mean linear thermal expansion coefficient (10^{-6} K^{-1}) over temperature range from 25°C to		
	500°C	1000°C	1500°C
Alumina 99%	7.0	8.0	9.0
Spinel	7.6	8.4	10.2
Zirconia (partially stabilized)	8-9	9-10	-

5.3.5.2. Alumina – Spinel

Alumine – spinelle

The interface microstructures of spinel – alumina A and spinel – alumina B bi-materials and their individual components are reported in this section. Compaction order effect on the microstructure of alumina B and spinel bi-combinations are compared in Figure 5.13. In alumina B – spinel bi-combinations, some cracks were observed in the alumina parts (in Figure 5.13(a)) on the other hand, in spinel – alumina B bi-combinations (reversed compaction order), there was no crack of this type (in Figure 5.13(b)). Thus when the alumina was in the lower part, it had some cracks but when it was in the upper part, there was no crack. Therefore, these cracks depended on the compaction order. In the case of alumina A – spinel bi-combinations, interface was almost crack-free in samples where spinel was on top (Figure 5.13(c and d)).

As discussed in Chapter 3, if height-to-diameter ratio of uniaxially pressed green compact is high (H/D>1) significant variations in the packing density of the green body occurs. In this thesis, there were more than one type of powder and higher height-to-diameter ratio was unavoidably necessary for dilatometric studies. Therefore, each powder had different initial green density due to position of powder inside the compaction die (bottom or top). The powders compaction behaviors are given in Figure 3.6 and initial green density differences are tabulated in Table 3.3. This difference reached 5% in the spinel powder. As a result of these density distinctions, each green bi-material showed different sintering paths and there were cracks depending on the position of the powder in the die.

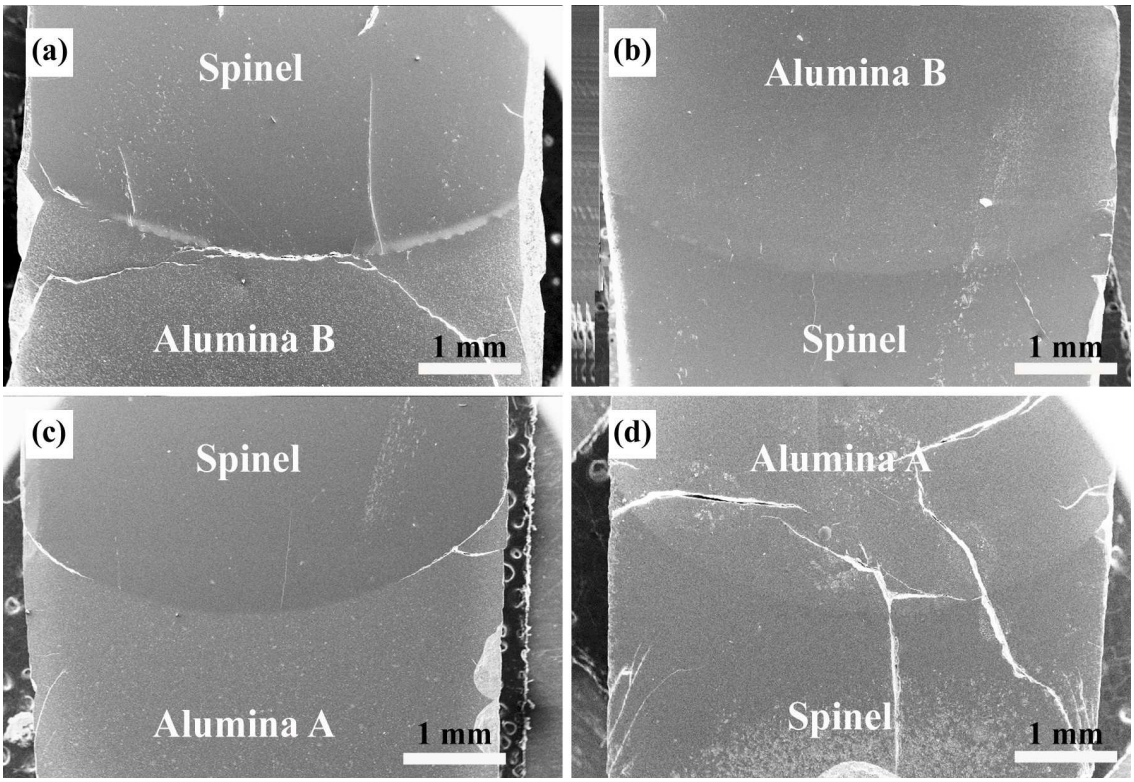

Figure 5.13. Compaction order of alumina and spinel bi-combinations, produced by single-action mode of uniaxial pressing at 250 MPa (Co-UP) (a) alumina B – spinel bi-material, (b) spinel – alumina B bi-material, (c) alumina A – spinel bi-material, (d) spinel – alumina A bi-material. Sintering conditions : 3.3°C/min up to 1580°C.

Effet de séquence de compaction de bi-matériaux co-pressés en pressage uniaxial simple effet sous 250 MPa (Co-UP) : a) Alumine B – spinelle, b) spinelle – alumine B, c) alumine A – spinelle, d) spinelle – alumine A. Friitage anisotherme à 3,3 °C/min jusqu'à 1580°C.

SEM analysis was conducted to examine the interface of spinel – alumina B bi-materials sintered up to 1580°C with a heating rate of 3.3°C/min. Figures 5.14(a) and (b) give the SEM micrographs showing the interlayer that occurred between alumina and spinel with different magnifications, respectively. As seen in Figure 5.14(b), the single interlayer comprised of elongated grains formed with thicknesses of about 12 µm. Nearby the interlayer, fine grains with about 200 nm average grain size are observable (Figure 5.14(c)) in spinel region, while this value switches to 2500 nm in the alumina region (Figure 5.14(d)).

Spinel – alumina bi-materials were compacted with floating die-mode of uniaxial pressing at 250 MPa (Co-UPFlo) before being sintered at 1500°C for 16 hours with 3.3°C/min heating rate. SEM image of polished and thermally etched bi-material surface is given in Figure 5.15. General view of the interlayer is given in Figure 5.15(a).

The thickness of the flat interlayer was nearly 35 µm (Figure 5.15(b)). The picture was taken at the interface between spinel and the interlayer. Columnar grains were detected. The grain sizes of spinel and alumina parts near the interlayer are given in Figures 5.15(c) and (d), respectively. As seen in the figure, the grain size of alumina was significantly larger than spinel one.

Figures 5.16(a) and (b) give SEM images of the polished and thermally etched surfaces of the bi-materials, firstly compacted at low pressure either by single-action mode (Co-UP) or by floating die mode (Co-UPFlo) of uniaxial pressing then each sample was cold isostatically pressed. There were no interlayer cracks between alumina and the interlayer. The SEM images also confirmed the elimination of cracks in the interlayer. More discussion of the interlayer formation and the resulting microstructure is presented in Chapter 6.

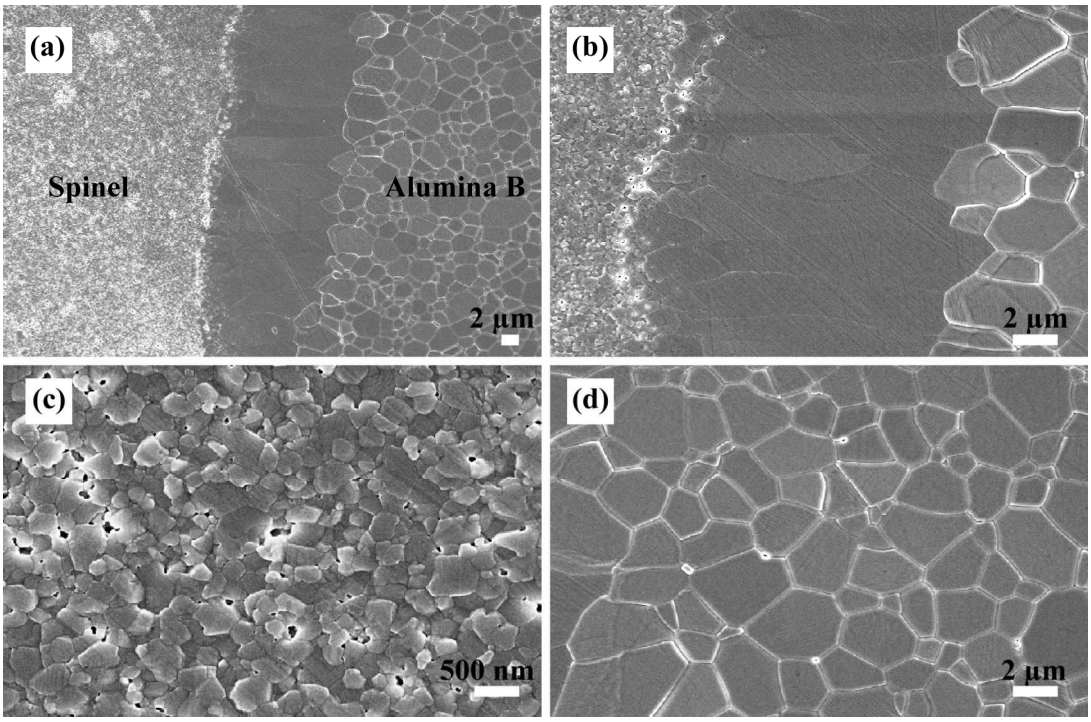

Figure 5.14. Spinel – alumina B bi-material, produced by single-action mode of uniaxial pressing at 250 MPa (Co-UP), (a) interlayer, (b) higher magnification of the interlayer, (c) spinel region close to interface, (d) alumina B region. Co-sintering conditions : 3.3°C/min up to 1580°C.

Bi-matériau alumine B – spinelle co-pressé uniaxialement en matrice simple effet sous 250 MPa (Co-UP), a) zone interfaciale b) zone interfaciale à plus fort grandissement, c) partie spinelle proche de l'interface d) partie alumine B. Cycle de co-frittage : à 3,3 °C/min jusqu'à 1580°C.

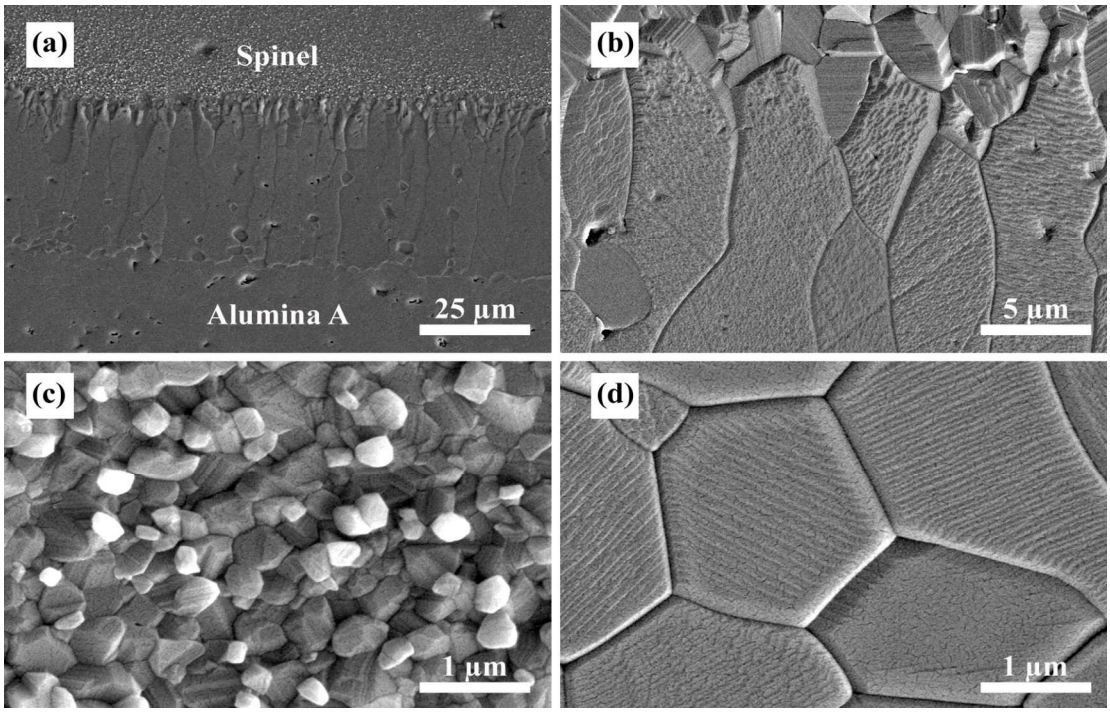

Figure 5.15. Alumina A – spinel bi-material, produced by double-action mode of uniaxial pressing at 250 MPa (Co-UPFlo) (a) general view of interlayer, (b) columnar grains at the interlayer (c) spinel grains in spinel and (d) alumina grains in alumina. Co-sintering conditions : 1500°C for 16 hours.

Bi-matériau alumina A – spinelle, co-pressé en pressage uniaxialement en matrice flrottante sous 250 MPa (Co-UPFlo) a) vue générale de la couche interfaciale, b) grains colonnaires de la couche interfaciale, c) grains de spinelle dans la partie spinelle et d) grains d'alumine dans la partie alumine. Conditions de co-frittage :1500°C pendant 16 heures.

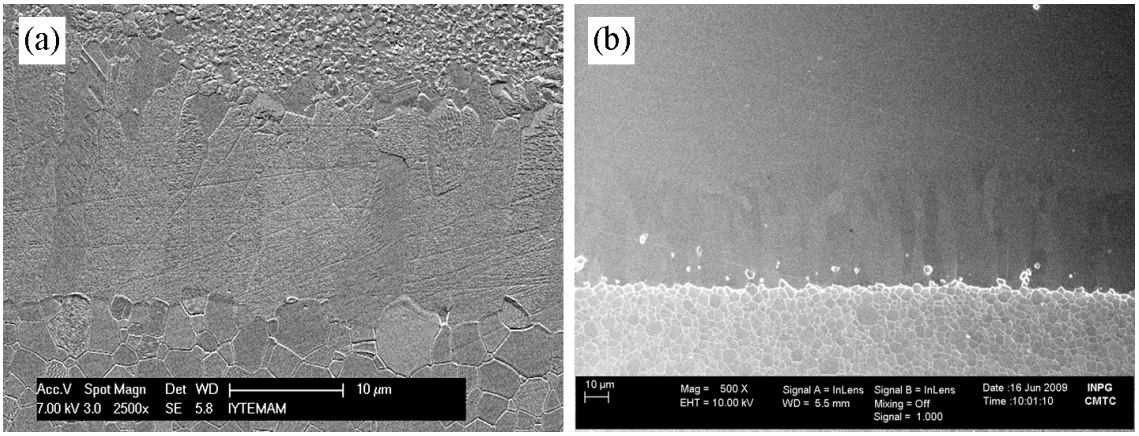

Figure 5.16. SEM images of alumina B – spinel bi-materials produced by (a) single-action mode and (b) floating die mode, of uniaxial pressing followed by cold isostatic pressing at 250 MPa. (Spinel part at the top in all photos). Co-sintering conditions: (a) 1°C/min up to1580°C, (b) 1500°C for 16 hours.

Micrographies MEB de bi-matériaux alumine B – spinelle co-pressé uniaxialement a) en mode simple effet et b) en matrice flottante suivi d'un pressage isostatique à froid sous 250 MPa (dans tous les cas la partie spinelle est en haut). Conditions de co-frittage : a) à 1 °C/min jusqu'à 1580°C, b) 1500°C pendant 16 heures.

5.4. Conclusions

Conclusions

Two different bi-material oxide systems were investigated. The alumina B – zirconia TZ-2Y bi-material yielded poor adhesion at the interface while alumina – spinel pair possessed relatively strong adhesion at the interface. Samples had different types of adhesion mechanisms at the interfaces of the bi-materials. In the first case, mechanical bonding by interlocking was the adhesion mechanism. On the other hand, in the second case, chemical bonding by diffusion was the adhesion mechanism. However, alumina B – zirconia Z-3Y pairs separated after co-sintering process. The reason for separation of these bi-combinations can be explained by severe shrinkage mismatches between these pairs.

According to SEM observation, the interlayer was composed of columnar grains of spinel and some minor cracks were observed in the alumina part, which was dependent on the compaction order in alumina B – spinel bi-materials. In the zirconia TZ-2Y – alumina B bi-materials, some cracks were observed in the zirconia parts due to significant differences in thermal expansion coefficients. Different co-pressing techniques were applied to produce more homogeneous green body and consequently crack free bi-material. Single action mode or double action mode uniaxial pressing and cold isostatic pressing samples had less cracks in the interface.

CHAPTER 6

MICROSTRUCTURAL DEVELOPMENT OF INTERFACE LAYERS BETWEEN CO-SINTERED ALUMINA AND SPINEL COMPACTS

Développement et microstructures de couches d'interface entre des comprimés cofrittés d'alumine et de spinelle

Résumé

Ce chapitre décrit et analyse les expériences et les observations microstructurales menées sur des bi-matériaux alumine-spinelle : co-frittage d'échantillons co-pressés ou couple de diffusion entre des échantillons prédensifiés. Les essais de co-frittage ont été réalisés en conditions isothermes (après une montée en température à 3°C/min) à 1400°C et à 1500°C pour des temps de maintien en température allant jusqu'à 16 heures.

Les observations des sections transverses des bi-matériaux co-frittés à 1500°C pendant 16 heures ont montré le développement dans la partie alumine à partir de l'interface initiale alumine-spinelle d'une couche grains colonnaires de spinelle dont l'épaisseur croit avec le temps suivant une loi parabolique caractéristique d'un mécanisme de diffusion. Sur la base de l'ensemble des observations de ces couches de grains colonnaires de spinelle, des coefficients de diffusion et les énergies d'activation apparentes correspondantes ont été estimés. Ces énergies d'activation apparentes de l'ordre de 450 kj/mole et les coefficients de diffusion estimés correspondraient d'après la littérature à l'énergie d'activation de la diffusion en volume des anions oxygène. Les cations Mg^{2+} diffusant en phase solide plus rapidement que l'oxygène, ce serait la diffusion en volume de l'oxygène depuis la partie spinelle qui gouvernerait la cinétique de croissance ce cette couche de grains colonnaires de spinelle dans la parie alumine des bi-matériaux co-frittés.

Dans la partie spinelle des bi-matériaux co-frittés une zone poreuse de grains fins a été mise en évidence ; dans cette zone pouvant s'étendre sur plusieurs centaines

de microns à partir de l'interface initiale, la porosité décroit et la taille des grains de spinelle augmente au fur et à mesure que l'on s'éloigne de l'interface. Cette zône poreuse peut s'expliquer par un passage et une diffusion rapide en phase vapeur du magnésium d'autant plus marqués que la température est élevée et ce tant que la porosité reste ouverte dans la partie spinelle. Cette zône poreuse étendue masquerait une zone poreuse plus limitée liée à un « pur » effet Kirkendal de diffusion du magnésium en phase solide.

Les essais de co-frittage en deux étapes isothermes (1400°C 4 à 16 heures + 1500°C 4 à 16 heures) ont révélés une microstructure en deux partie de la couche d'interface de grains de spinelle colonnaires : l'une au voisinage de l'interface initiale correspondrait à la couche formée à 1400°C et l'autre correspondrait à la croissance à 1500°C.

Les essais de couple de diffusion à 1500°C entre des comprimés prédensifiés à 95 % de spinelle et d'alumine ont révélés dans la partie alumine en contact avec la partie spinelle le développement d'une couche de grains colonnaires de spinelle très semblable à celles observées lors des essais de co-frittage. L'épaisseur de cette couche n'est pas significativement différente de celles observées en co-frittage pour une même durée de maintien à haute température (40 µm après 16 heures à 1500°C) La largeur des grains colonnaires de spinelle est elle plus grande (8 µm par rapport à < 5 µm) ; ceci peut s'expliquer par une densité de sites de germination de grains colonnaires plus faible dans la cas des couples prédensifiés avec des tailles de grains plus élevées. A l'extrémité des grains colonnaires de spinelle côté alumine le centre de courbure des interfaces avec les grains d'alumine est le plus souvent situé dans les grains d'alumine ; ceci serait un élément de plus en faveur d'une réaction de formation de la phase spinelle localisée à l'extrémité des grains colonnaires.

6.1. Introduction

Introduction

When magnesia (MgO) and alumina (Al_2O_3) are heated together, a spinel ($MgO.Al_2O_3$) phase forms in the middle. The extent of the formation of the spinel phase or the interface between magnesia (MgO) and alumina (Al_2O_3) have been studied from different perspectives in order to understand if a good bond can be achieved between

the two or to investigate the diffusion behaviors of the components (Rossi and Fulrath 1963, Watson and Price 2002, Zhang, et al. 1996). Most of these studies involved heating of diffusion couples, some others involved heating of single/poly crystals of a component in contact with a powder of the second component. In the literature, sintering behavior of co-pressed and co-sintered powders of oxide/oxide, metal/oxide and metal/metal pairs are reported (Boonyongmaneerat and Schuh 2006, Simchi, et al. 2006a, Sun, et al. 2008).

Co-sintering process is to sinter two materials together when they are in contact with each other, relatively common technique to fabricate bi-materials. These materials are functionally graded materials, which mean that their gradient properties depend on mechanical, electrical and magnetic properties of their components and also on continuous or stepwise production processing (Sun, et al. 2008).

Diffusion couple test is a useful and common technique to understand the growth of intermediate new phases between the two end-members (components) which were previously shaped and sintered to some extent. For example, solid state reactions and solid-gas reactions between Y_2O_3 and Fe_2O_3 systems were studied by Buscaglia et.al. who used different types of diffusion couples (Buscaglia, et al. 1997). They observed growth of different dense ternary phases at the interfaces. An interlayer phase including columnar type elongated grains gained strong adherence between the end-members. Smigelkas and Kirkendall (1947) studied the diffusion couples in metals that produce porosity in the interface. More recently similar porosity in oxide – oxide based diffusion couples was observed (Siao, et al. 2009).

Reaction paths at the interfaces AO-B_2O_3 and AB_2O_4 – B_2O_3 (e.g. A=Mg, B=Al) are discussed by Kingery et.al., (1976). Although these reactions were originally proposed for NiO – Al_2O_3 interface (Pettit, et al. 1966), they are equally applicable to the interfaces between MgO and Al_2O_3. So at the $MgAl_2O_4$ – Al_2O_3 interface oxygen and cation transport through $MgAl_2O_4$ produces the following reaction

$$Mg^{2+} + O^{2-} + Al_2O_3 = MgAl_2O_4 \tag{6.1}$$

Carter investigated the solid-state reaction mechanisms between magnesium oxide and aluminum oxide in his inert marker experiments at high temperature (Carter 1961). He observed that the solid-state reactions forming $MgAl_2O_4$ occurs by counterdiffusion of the Mg^{2+} and Al^{3+} ions through the relatively rigid oxygen lattice of

the spinel at the Al_2O_3/MgO-gas interface. He suggested that spinel forms at the Al_2O_3 – $MgAl_2O_4$ interface in an amount three times higher than at the MgO – $MgAl_2O_4$ interface. This was later confirmed by other studies on $MgAl_2O_4$ spinel (Rossi and Fulrath 1963, Watson and Price 2002) as well as for $NiAl_2O_4$ spinel (Pettit, et al. 1966). A High Resolution Electron Microscope study of the interface was carried out by Li et.al., (1992).

The interdiffusion of polycrystalline MgO and Al_2O_3 under atmospheric pressure in the range of 1200 to 1600°C with and without dopant additions was studied by Zhang et.al., (1996). Spinel growth showed parabolic law as measured from the ratio of spinel layer thickness versus time. Chemical diffusion coefficient of Mg^{2+} ions must be somewhat higher than that of the Al^{3+} ions. Because they found the measured average concentration gradient of Mg^{2+} to be less than one-and-a-half times that of Al^{3+} ions (Zhang, et al. 1996).

In another study, spinel phase formation by reaction of either single or polycrystalline periclase with single-crystal corundum was investigated under high pressure and at elevated temperatures (Watson and Price 2002). Spinel composition showed linear variation across the spinel layer from periclase side to corundum side. They observed two different microstructural spinel phase formations, one of them was equiaxed type grains near the periclase side, on the other hand, there were columnar type grains near the corundum side. The ratio of equiaxed to columnar grain region was around 1:3. So they concluded that spinel grows in both directions by consuming periclase and corundum. Thus spinel was formed by counterdiffusion of Al^{3+} and Mg^{2+} ions through spinel lattice. At the end of their paper these authors recalled that their model and the data on which it is based do not require mobile oxygen; but they mentioned that "it seems likely that oxygen was mobile in our experiments, although its mobility is not required for spinel growth". Spinel layer formation was significantly effected by applied pressure, temperature and soaking time (Watson and Price 2002). A similar interlayer was observed for $NiAl_2O_4$ growth between diffusion couples of NiO and Al_2O_3 (Pettit, et al. 1966). Whitney and Stubican studied the interdiffusion between MgO and $MgAl_2O_4$ (Whitney and Stubican 1971) to compare with other studies for MgO – Al_2O_3 interfaces (Carter 1961, Watson and Price 2002, Zhang, et al. 1996) but without reporting any interface layer microstructural observation and without considering the necessary mobility of oxygen for spinel layer growth.

Diffusion between AO and B_2O_3 type of oxides in systems of MgO – Al_2O_3 (Li, et al. 1992, Rossi and Fulrath 1963, Watson and Price 2002, Zhang, et al. 1996) and NiO – Al_2O_3 (Pettit, et al. 1966) were studied using diffusion couples. Some other studies involved vapour phase transport of Mg to form $MgAl_2O_4$ (Carter 1961, Navias 1961). Okada et.al., investigated spinel formation from different sized powders of ZnO and Al_2O_3 (Okada, et al. 1985). The spinel phase in these studies formed in-situ. These studies were more concerned with physical development of this interlayer from kinetic aspect without much attention on the microstructures (Carter 1961, Zhang, et al. 1996).

In this study, commercial spinel and alumina powder compacts are used as end-members during co-sintering and diffusion couple tests as opposed to the above studies which produced spinel in-situ. Apart from that, the microstructural development between $MgAl_2O_4$ and Al_2O_3 is studied with special attention to the interlayer. This study follows another study done by the authors on different bi-material oxide systems (alumina – zirconia and alumina – spinel) aimed at investigating the mechanical and chemical aspects (Chapter 5 of this thesis) and other detailed studies on sintering of spinel powder (Chapter 4 of this thesis).

6.2. Experimental Procedure

Procédure expérimentale

Two different commercially available submicron-grained alumina powders were used in this study. The first powder, coded alumina A, was a MgO doped Baikowski product (Batch n° 660J CR15 MgO-doped, Baikowski) while the second powder was a non-doped α-alumina, coded alumina B, powder (Batch n° 14406 BMA15, Baikowski). Spinel ($MgAl_2O_4$) powder was also a Baikowski product (S30-CR, Baikowski). Some physical, and chemical properties of the powders used in this study are shown in Table 3.2.

In order to achieve a good bond between alumina and spinel the interface development must be understood very well. Hence, three different sets of tests were planned. The first involved co-sintering of alumina – spinel pairs of co-pressed pellets. The second set was performed to see if two co-sintering steps would influence the interface layer microstructure. The third one was run to collect complementary

information about the interface layer which develops between predensified alumina and spinel samples during the diffusion couple tests.

The green bi-material cylindrical samples (8 mm diameter) were previously produced at low pressures of 50 or 100 MPa with single-action (UP) or floating die (UPFlo) mode of uniaxial pressing. The first powder was poured into die cavity and was settled down by tapping with a metal rod before the second powder was added and co-pressed together. Then they were compacted under cold isostatic pressure at 250 MPa. More experimental detailed about green compact preparation can be seen in Chapter 5. Prepared green compacts of bi-materials were sintered in a vertical dilatometer (DHT2050K, Setaram, France) at 1400°C and 1500°C for 1 to 16 hours with 3.3°C/min of heating rate. This way, co-densification behaviors of the compacts were investigated. The sintered samples were cooled in furnace with 30°C/min cooling rate.

In order to investigate the microstructures of the interface and components of the bi-materials after co-sintering, sintered pellets were cut parallel to the cylinder axis into two parts. Half of them were mounted into polyester resin before being ground and polished by conventional sample preparation methods. To reveal the morphology and microstructural alteration at the interface, bi-materials were thermally etched at about 100°C below the sintering temperatures. Microstructures of the polished and thermally etched surfaces were observed by SEM (scanning electron microscope, Zeiss, Ultra 55). Chemical etching with hot orthophosphoric acid was also done for some of the samples.

Co-pressed alumina and spinel compacts were sintered in two isothermal steps to understand the nucleation step of the columnar grains structure and the evolution of microstructures in the interface. Co-pressed samples were heated up to 1400°C for 4-16 hours with 3.3°C/min of heating rate followed by another heating step at 1500°C for 4-16 hours. The purpose was to see if new generation columnar spinel grains emerge at the interface.

In addition to co-sintering process, to understand and determine more clearly the diffusion mechanisms between alumina and spinel pellets during co-sintering, diffusion couples of spinel and alumina were tested. The green compacts of alumina A and spinel were separately sintered at 1500°C for 30 minutes and 4 hours, respectively. Soaking times were so selected to achieve matching fired densities at 95% of theoretical density. Theoretical densities for spinel and alumina were taken as 3.55 and 3.987 g/cm^3, respectively. Therefore both alumina A and spinel end-members were predensified to 95% density before the diffusion couple test. The purpose was to leave some room for

further densification when the two pellets were in contact during heating. Another reason was to use pores as markers for future observation (Carter 1961). In order to obtain two end-members of alumina and spinel for diffusion couple tests, cylindrical sintered samples were cut into two pieces from the centers of the pellets horizontally. And then each of the cut surfaces was ground and well polished with 1 μm diamond. Once well polished surfaces were obtained, two separate diffusion couple tests were done as listed in Table 6.1. In the first experiment both end-members were predensified to 95% density before the diffusion couple test. In the second diffusion couple test, however, spinel was in the green state with about 50% density while alumina A (the other half of the previous alumina A sample) pellet was 95% dense. Contact surface of green spinel compact was smoothed as much as possible with fine SiC griding paper.

Table 6.1. Diffusion couple test samples.

Echantillons des essais de couples de diffusion.

Diffusion couple test	Densities of pellets before diffusion couple experiment	
	Alumina A	Spinel
Experiment No 1	95%	95%
Experiment No 2	95%	50% (green)

In the diffusion couple tests predensified pellets of alumina and spinel were placed face to face to bring polished surfaces in contact. In order to increase the contact and to decrease the diffusion gap between the end-members an external pressure (300 g ~ 0.1 MPa) was applied. Diffusion couple tests were done in the dilatometer. This way, co-densification behaviors of the couples were investigated. The couples were heated up to 1500°C for 16 hours with 3.3°C/min of heating rate.

6.3. Results

Résultats

6.3.1. Co-sintering at High Temperature (1500°C) of Green Compacts

Cofrittages à haute temperature (1500°C) de comprimés copressés

Alumina A and spinel co-pressed green compact was co-sintered up to 1500°C at a heating rate of 3.3°C/min for 16 hours before analysis of the interface in SEM. An

interlayer composed of new generation columnar spinel grains was observed to form between the alumina and spinel (Figure 6.1). The interlayer thickness was about 40 μm depending on the sintering regime (1500°C for 16 hours soaking time). The grains were elongated in this layer in contrast to the equiaxed grains in the neighboring spinel and alumina. When spinel starts to densify from green state, a fine spinel (d~400 nm) region was observed in the parent spinel near the in-situ columnar spinel interlayer as shown in Figure 6.1(b). The thickness of fine and porous spinel region (~200 μm in this case) was much higher than columnar spinel interlayer (~40 μm). This porous and fine grained spinel region is discussed further in this chapter. Size of the spinel grains far away from the interlayer and around in the center of the spinel body was roughly about 800 nm (Figure 6.2). On the other hand, grain size of the spinel closer to the external surface was nearly 3000 nm probably due to evaporation of Mg and resultant formation of excess O^{2-} vacancies in the spinel grains of the external surface region (Ting and Lu 2000). This will be further discussed below. The microstructural schematic of this bi-material (alumina A – spinel) co-sintered at 1500°C for 16 hours is illustrated in Figure 6.2. Grain sizes of alumina near the interlayer and in the bulk were 3400 nm (Figure 6.2). The width of columnar spinel grains were less than 5 μm.

Crystal orientation of columnar spinel grains was investigated by electron backscattered diffraction (EBSD) method. Alumina A and spinel interlayer formation is demonstrated in Figure 6.4. According to the results, each columnar grain shows different color which means that they have the same cubic crystal structure with random crystallographic orientations. So there is no specific orientation in the growth of columnar spinel grains in the interlayer. This is due to the nucleation of these columnar grains from the spinel part that consisted of randomly oriented equiaxed fine grains. Formation and growth of the interlayer is thought to proceed as follows. First, new generation of spinel forms at the spinel-alumina interface. Because the spinel grains are randomly oriented and provide the nuclei for formation of the interlayer, the initial set of spinel grains in the interlayer grow randomly into alumina along with the concentration gradient of Mg. After some growth, new in situ formed spinel grains compete with each other and those favorably oriented grains grow faster and wider. The less fortunate grains that are oriented sideways fade out as they cannot be supplied with sufficient Mg.

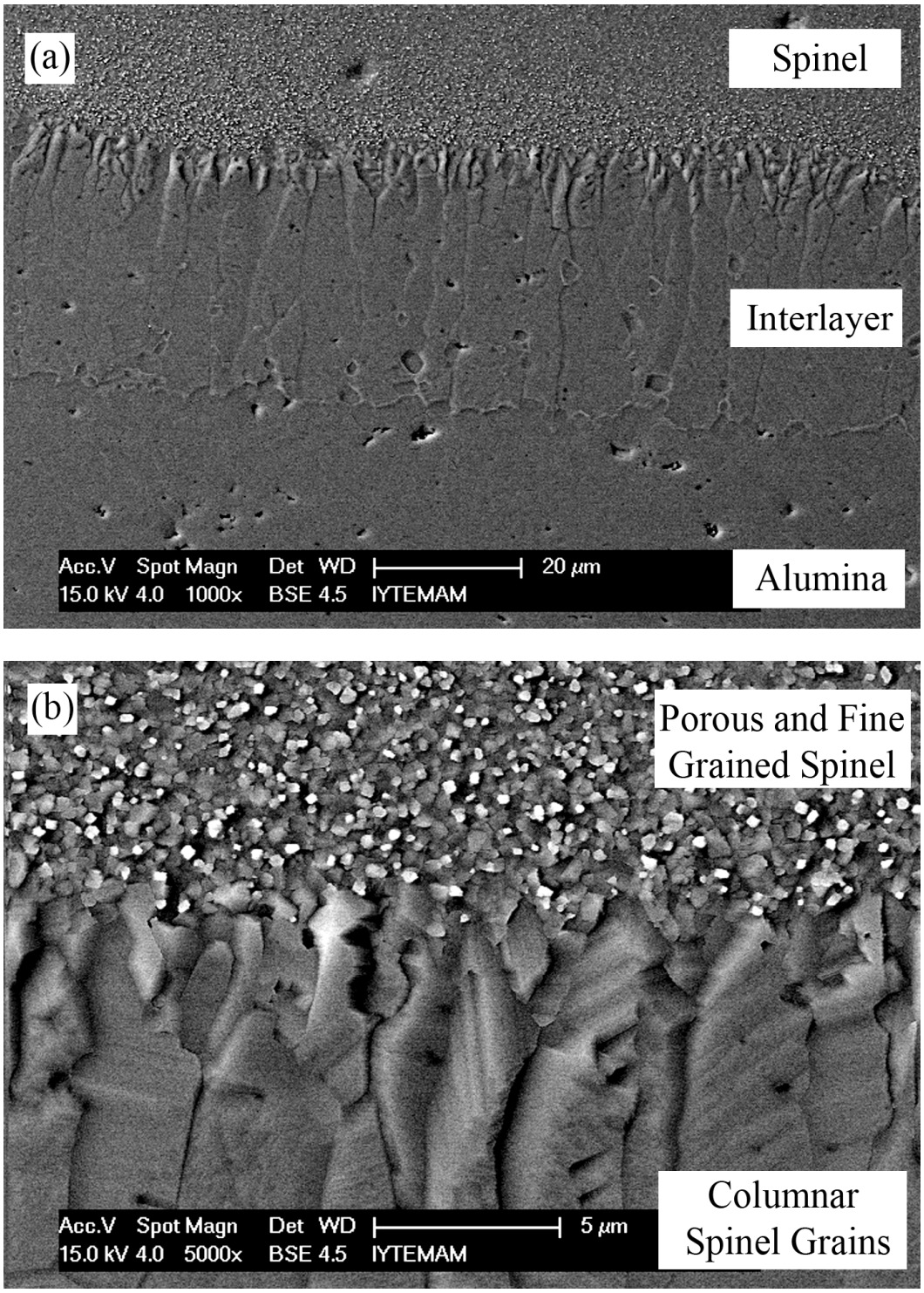

Figure 6.1. Interface microstructure of spinel – alumina A bi-material co-sintered for 16 hours at 1500°C with 3.3°C/min heating rate: (a) general view (b) a closer view of the porous and fine grained parent spinel and in-situ grown columnar grained spinel.

Microstructure de l'interface d'un bi-matériau Spinelle – Alumine A cofritté 16 heures à 1500°C (vitesse de chauffage 3,3°C/min) a) vue générale b) vue détaillée de la région entre la partie spinelle poreuse à grains fins et la région à grains colonnaires de spinelle qui se sont développés in-situ.

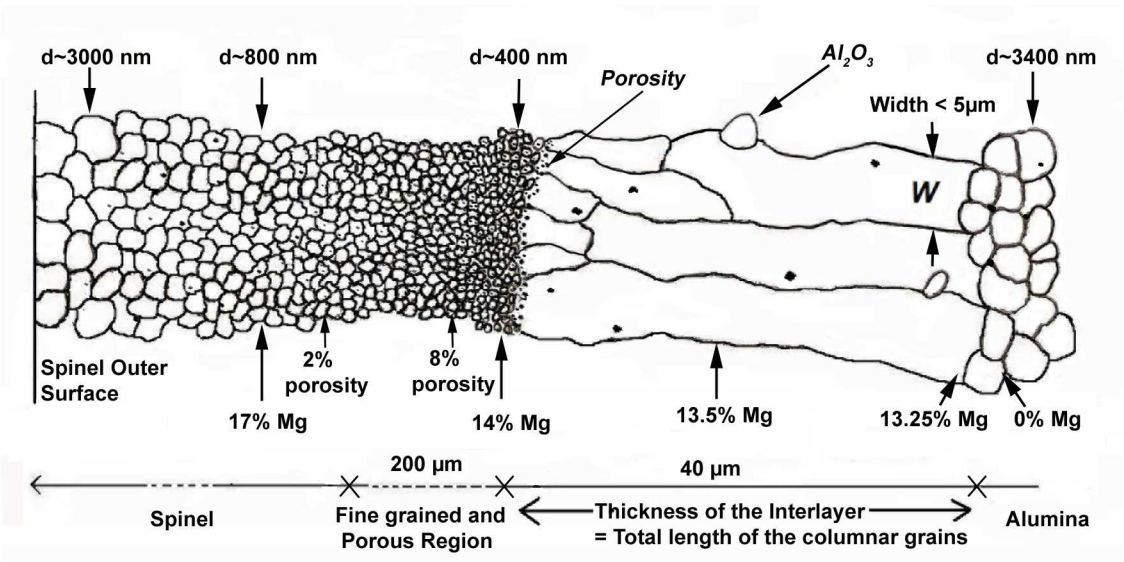

Figure 6.2. Schematic illustration of bi-material (alumina A – spinel) microstructure co-sintered for 16 hours at 1500°C.

Schéma général de la microstructure d'un bi-matériau (alumine A – spinelle) co-fritté à 1500°C pendant 16 heures.

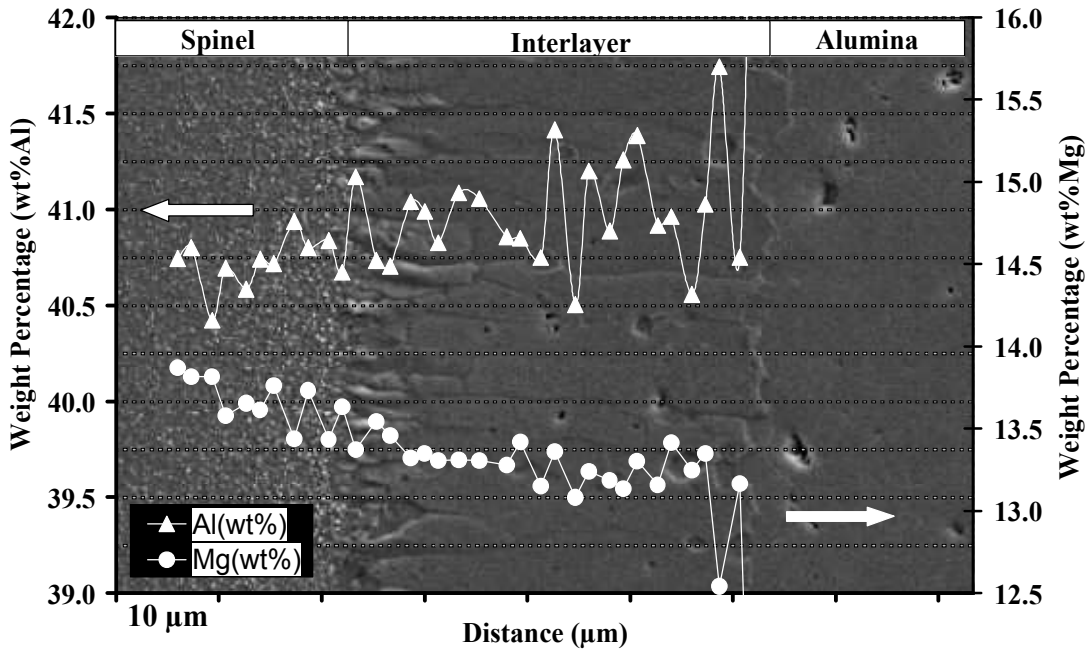

Figure 6.3. WDS analysis of the interlayer between spinel and alumina. Mg concentration slightly decreases from left to right. Al concentration increases in the same direction. Alumina A – spinel co-sintered samples (1500°C, 16 hours).

Profils de concentrations (analyse WDS) en magnesium et en aluminium à l'interface entre la spinelle – l'alumine dans un échantillon co-fritté 16 heures à 1500°C. La concentration en magnésium décroit légèrement de la gauche vers la droite alors que la teneur en aluminium croit.

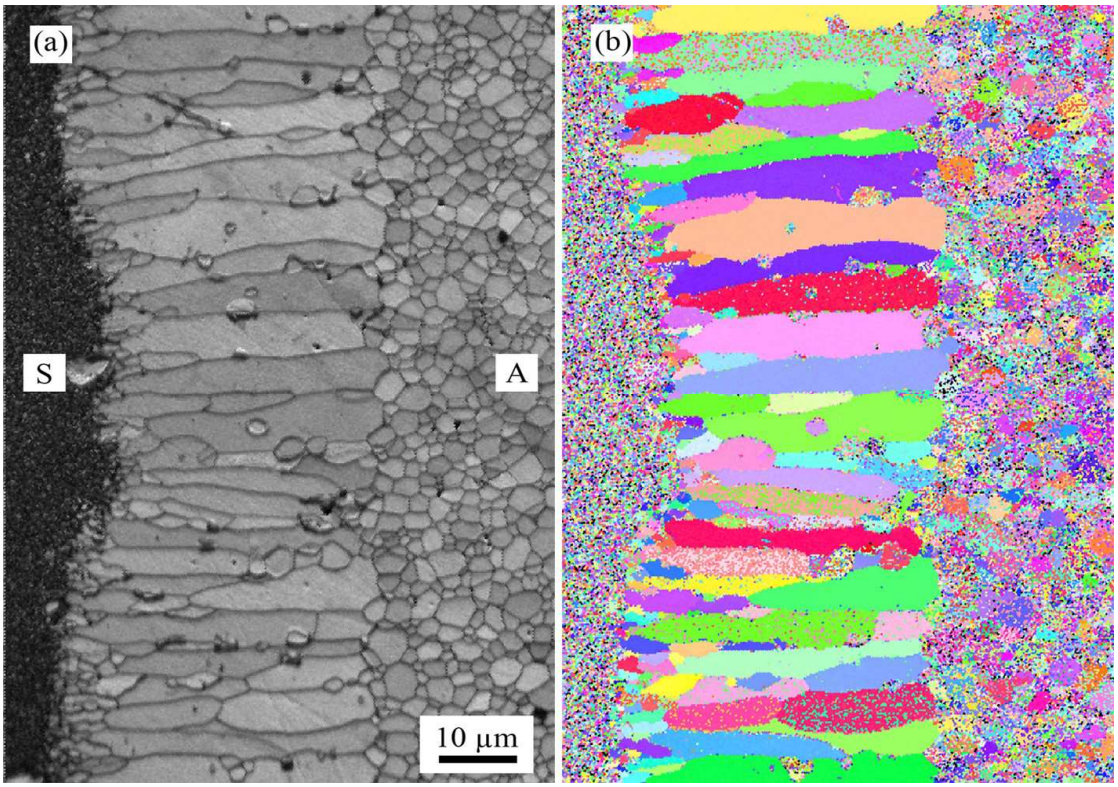

Figure 6.4. (a) Secondary electron SEM image and (b) EBSD image of interlayer of alumina A – spinel bi-material co-sintered at 1500°C for 16 hours.

Micrographies de la couche interfaciale d'un bi-matériau alumine A –spinelle co-fritté 16 heures à 1500°C a) image en électrons secondaires b) image en canalisation d'électrons rétrodiffusés (EBSD).

The amount of porosity in spinel was observed to decrease from the interface to the bulk of the spinel. Maximum porosity was present in the interface between parent spinel and columnar spinel in the interlayer.

Spinel grain size evolution was followed with SEM in the bi-material alumina B – spinel which was sintered at 1500°C for 16 hours. Figure 6.5 shows the increasing spinel grain size in moving away from the interface to the interior of spinel. In the same direction, pores almost completely disappeared 90 µm away from the interface (Figure 6.5(c)). Nearly 360 µm away from the interface, the grain size roughly became two times bigger than that near the interface (Figure 6.5(d)).

The grain size distribution profiles from interface to interior of spinels for each type of bi-material are given in Figure 6.6. Both co-sintered bi-materials have nearly the same grain size at the center of the spinel part but they have slightly different grain size near the interface.

A question came up then if grain growth, pore closure or new grain formation occurred during thermal etching, thereby leading to biased results. Chemical etching with orthophosphoric acid at 140°C was performed to verify data in Figures 6.5 and 6.6.

The same trend in grain sizes was observed on the samples that were chemically etched with slightly smaller grain size measurements. Chemical etching also revealed that porosity in parent spinel was higher than that observed in Figure 6.5. Some porosity values are indicated in Figure 6.2 and results on fine and porous spinel part will be further discussed in Section 6.2.3.

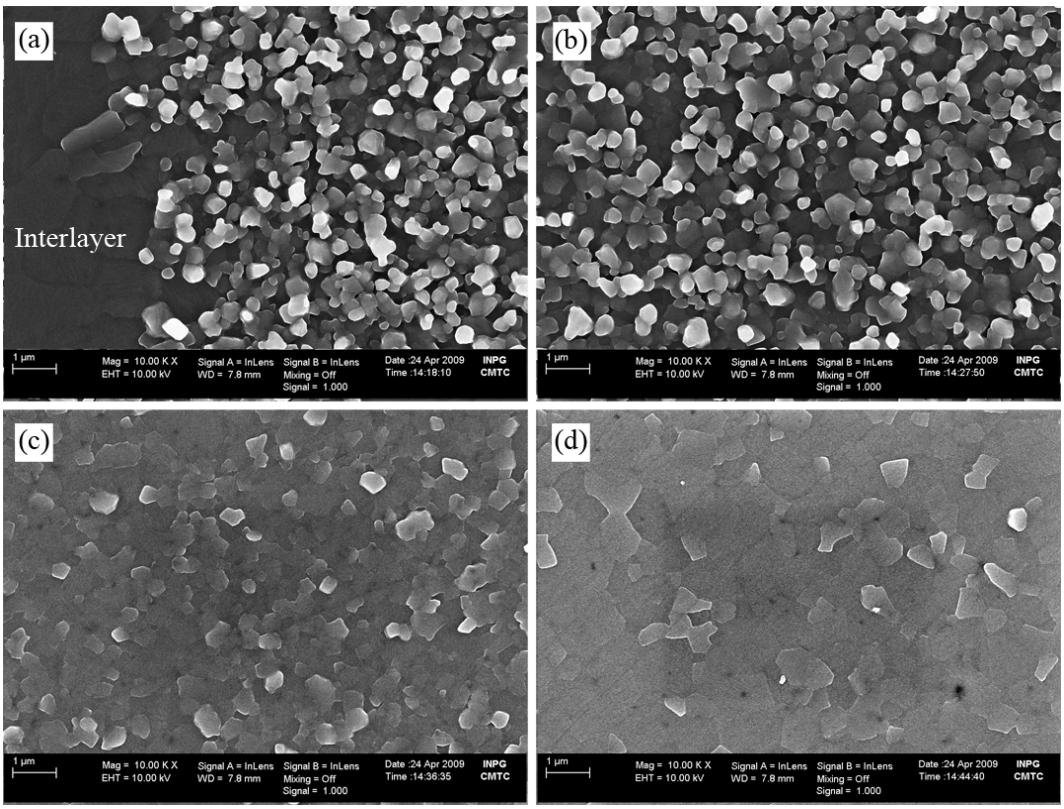

Figure 6.5. Porous region in parent spinel end-member in alumina B – spinel bi-material (a) near the interlayer, (b) 40 µm, (c) 90 µm, and (d) 360 µm away from the interlayer into bulk of the parent spinel. The bi-material was co-sintered at 1500°C for 16 hours with 3.3°C/min heating rate.

Région poreuse dans la partie spinelle initiale d'un bi-matériau alumine B – spinelle co-fritté 16 heures à 1500°C (vitesse de chauffage 3,3°C /min) a) près de l'interface b) à 40µm, (c) 90µm, and (d) 360µm de l'interface.

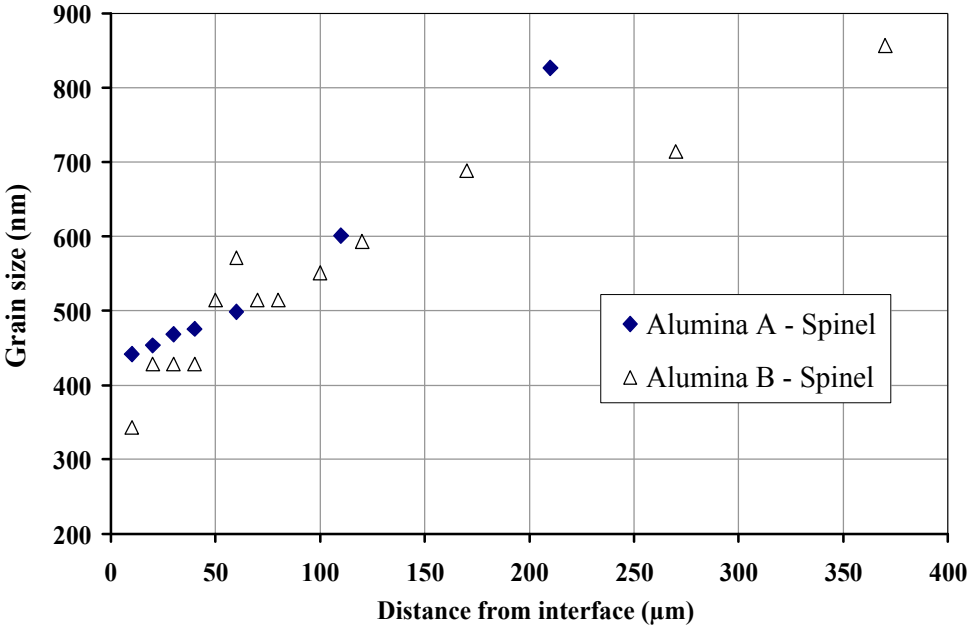

Figure 6.6. Spinel grain size profiles from interface to interior of spinels for each type of co-sintered bi-material for 16 hours at 1500°C. Polished cross sections were thermally etched at 1450°C for 30 min.

Profils en taille de grains dans la partie spinelle à partir de l'interface pour les deux types de bi-matériaux co-frittés 16 heures à 1500°C. Mesures faites sur des sections transverses polies et attaquées thermiquement 30 minutes à 1450°C.

The effects of pressing method, sintering temperature, soaking time, and type of alumina (550 ppm magnesium-doped or non-doped) on the spinel columnar grains interlayer thickness of spinel – alumina co-sintered bi-materials were evaluated. The results of all the interlayer thicknesses are given in Figure 6.7. The co-pressed bi-materials were co-sintered at 1400°C or 1500°C with 3.3°C/min heating rate for different soak times. The interlayer thicknesses are found to be directly proportional to the square root of soaking time. These results are in reasonable agreement with a parabolic diffusion Equation (6.2). The main effect was obtained from the soaking temperature. Other factors were not significantly effective. Type of alumina (whether doped with MgO or not) was found not to have a significant effect on the extent of the formation of columnar spinel grain layer (Carry, et al. 2010).

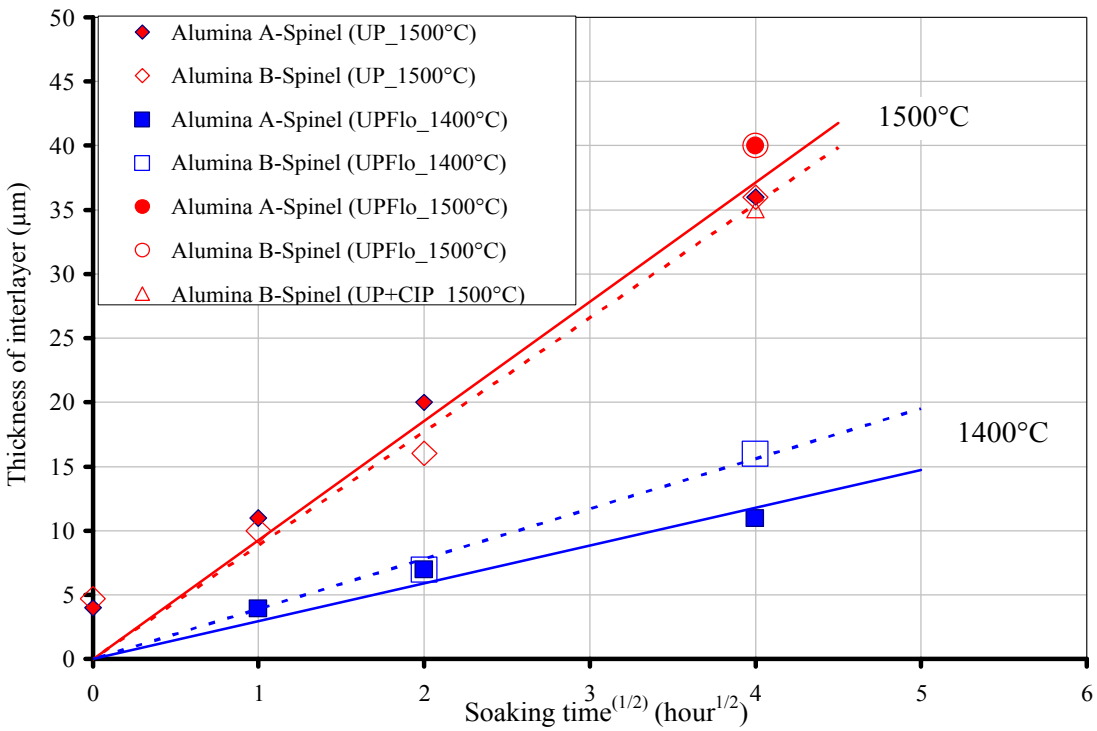

Figure 6.7. Effect of soaking time, pressing method and temperature on the interlayer thickness of alumina – spinel co-sintered bi-materials.

Effets du temps de frittage, du procédé de presage et de la température sur l'épaisseur de la couche interfaciale de grains colonnaires de spinelle dans des bi-matériaux co-frittés alumine – spinelle.

Experimental apparent diffusion coefficients (*D*) of columnar grained spinel layer were calculated by using thickness versus square root of soak time results of bi-materials according to equation;

$$x = k\sqrt{Dt} \tag{6.2}$$

x: thickness of spinel columnar grained interlayer (µm)

t: soaking time at specified temperature (hour)

D: Diffusion coefficient

Calculated interlayer growing activation energy and corresponding apparent diffusion coefficients of bi-materials are tabulated in Table 6.2. As a result of calculations, the apparent activation energy (Q_d) of alumina A – spinel and alumina B – spinel were 450 and 425 kJ/mol, respectively. And their diffusion coefficients (*D*) were 2.6 x 10^{-14} m^2/s and 2.2 x 10^{-14} m^2/s at 1500°C.

The calculated activation energy for grain growth of columnar grains are in good agreement with the literature but is completely different from the activation energy of densification of spinel (as mentioned in Section 4.3.3).

In the spinel literature, several scientists reported values of the diffusion coefficients (D_o) of Al, Mg and O^{2-} ions. Reimanis and Kleebe (2009) tabulated the diffusion coefficients and related the activation energy results. When compared with literature (Reimanis and Kleebe 2009), lattice O^{2-} ion diffusion could be the limiting diffusion mechanism of growth of the spinel columnar grained interlayer because of its low diffusion coefficient, limiting the diffusion process. As Mg^{2+}diffuse much faster than O^{2-} ion, the solid state chemical reaction (6.1) at the end of spinel columnar grains on the alumina side appears to be limited by the O^{2-} ion bulk diffusion.

Table 6.2. Diffusion coefficients and apparent activation energies deduced from the growth kinetics of the columnar grained spinel interlayer during bi-material co-sintering.

Coefficients de diffusion et energies d'activation apparentes déduits des vitesses de croissance de la couche de grains colonnaires de spinelle pendant le co-frittage de bi-matériaux.

Type of Bi-material	**Apparent Diffusion Coefficients of Bi-materials at Temperature**		**Apparent Activation Energy of Interlayer Growth (kJ/mol)**
	1400°C	**1500°C**	
Alumina A-Spinel	3.9×10^{-15}	2.6×10^{-14}	450
Alumina B-Spinel	4.0×10^{-15}	2.2×10^{-14}	425

Columnar spinel grains in the interlayer are thought to nucleate from initial fine spinel grains and to grow toward alumina. Evidence for this preposition can be seen in Figures 6.1(a), 6.3 and 6.4(a) where the grain phase boundaries between columnar spinel grains and alumina are almost always curved with their centers of curvature in alumina grains. As these images were taken after 16 hours of soak period at 1500°C, further soak at this temperature is expected to advance the boundary into alumina. Therefore, the interlayer grows into alumina away from spinel. Further evidence for this argument will be presented in Section 6.3.4.

6.3.2. Initial Stage of Co-sintering of Bi-material at Low Temperature

Stade initial du co-frittage de bi-matériaux à basse température

The interlayer formation, extent of sintering, and adhesion mechanisms were investigated at very low temperatures. Figure 6.8 depicts the alumina – spinel bi-material fracture surface. The left side of the image is the alumina part. The sample was co-sintered at 1150°C for 16 hours. Maximum shrinkage of the bi-material was about 8 % and its components of alumina and spinel have also individually nearly the same shrinkage values as their bi-material (Carry, et al. 2010). The grain sizes of alumina and spinel were 200 nm (Figure 6.8(a)) and 80 nm (Figure 6.8(b)), respectively. Thus the grain size of both materials almost doubled. The diffusion rate is also low between the components, but the some necking contact between alumina and spinel can still be partially established as shown in Figures 6.8(c) and 6.8(d) at different magnifications.

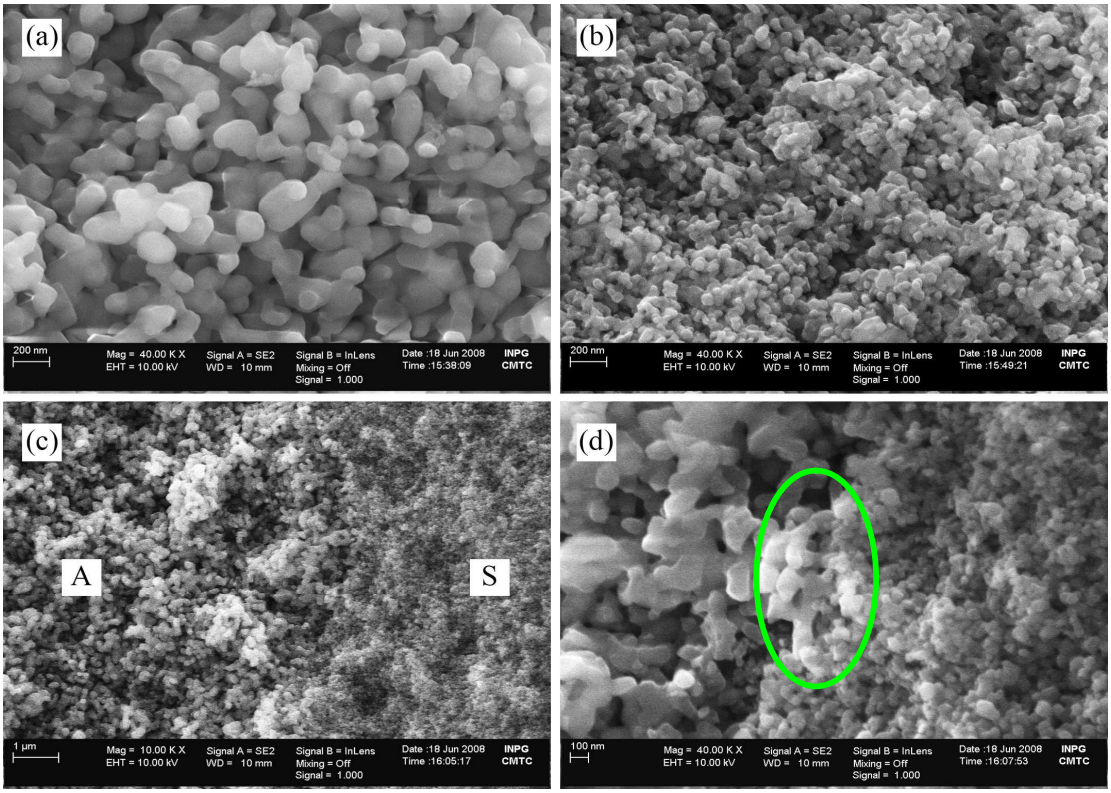

Figure 6.8. SEM image of the fracture surface of alumina – spinel bi-material co-sintered at 1150°C for 16 hours. (a) and (b) show the initial stage sintering of alumina and spinel part, (c) and (d) the interface region between alumina and spinel at different magnifications. A: alumina and S: spinel.

Micrographies MEB de surface de rupture transverse de bi-matériaux alumina – spinelle co-frittés 16 heures à 1150°C. a) et b) stade de frittage initial dans les parties alumine et spinelle, c) et d) la région à l'interface alumine – spinelle à différents grandissements.

6.3.3. Co-sintering of Compacts by Two Isothermal Steps Sintering

Co-frittage de comprimés en 2 étapes isothermes

The next set of experiments was done to determine if two isothermal steps co-sintering would lead to a different interlayer microstructure. Each type of bi-material was sintered by two isothermal steps sintering. The two sintering steps were done at 1400°C for either 4 hours or 16 hours followed by another sintering at 1500°C for 16 hours. The thicknesses of the interlayer and their microstructures were investigated from polished and thermally etched surfaces of bi-materials. Thicknesses of the interlayer and the type of the bi-materials after two isothermal step co-sintering are tabulated in Table 6.3. Thicknesses of the interlayers were slightly higher than the interlayer thickness of single isothermal step co-sintered bi-materials. So, in each isothermal step, depending on the duration, interlayer grew by diffusion of matter.

Table 6.3. Thickness of interlayer after two isothermal steps co-sintering.

Epaisseur de la couche interfaciale après un co-frittage en deux étapes isothermes.

Two isothermal steps Co-sintering Conditions	**Type of Bi-materials**	
	Alumina A – Spinel	**Alumina B – Spinel**
1400°C/4 hours + 1500°C/16 hours	40 µm	44 µm
1400°C/16 hours + 1500°C/16 hours	47 µm	47 µm

SEM micrographs of thermally or chemically etched samples of alumina A – spinel bi-material, sintered at 1400°C for 16 hours and then at 1500°C for 16 hours are given in Figure 6.9. Interestingly, the interlayer was found to consist of two separate easily distinguishable areas. On the left of the Figure 6.9(a), a band of first generation columnar spinel interlayer was observed. Same observation was made on another half of the polished and chemically etched surface of the sample (Figure 6.9(b)). Total thickness of the interlayer was nearly 5 µm after the first isothermal step (1400°C) and was 40 µm after the second isothermal step (1500°C) sintering. A thin porous layer is

observed in the spinel part just near the interface; this porous layer is much less extended than in the case of the samples co-sintered directly at 1500°C.

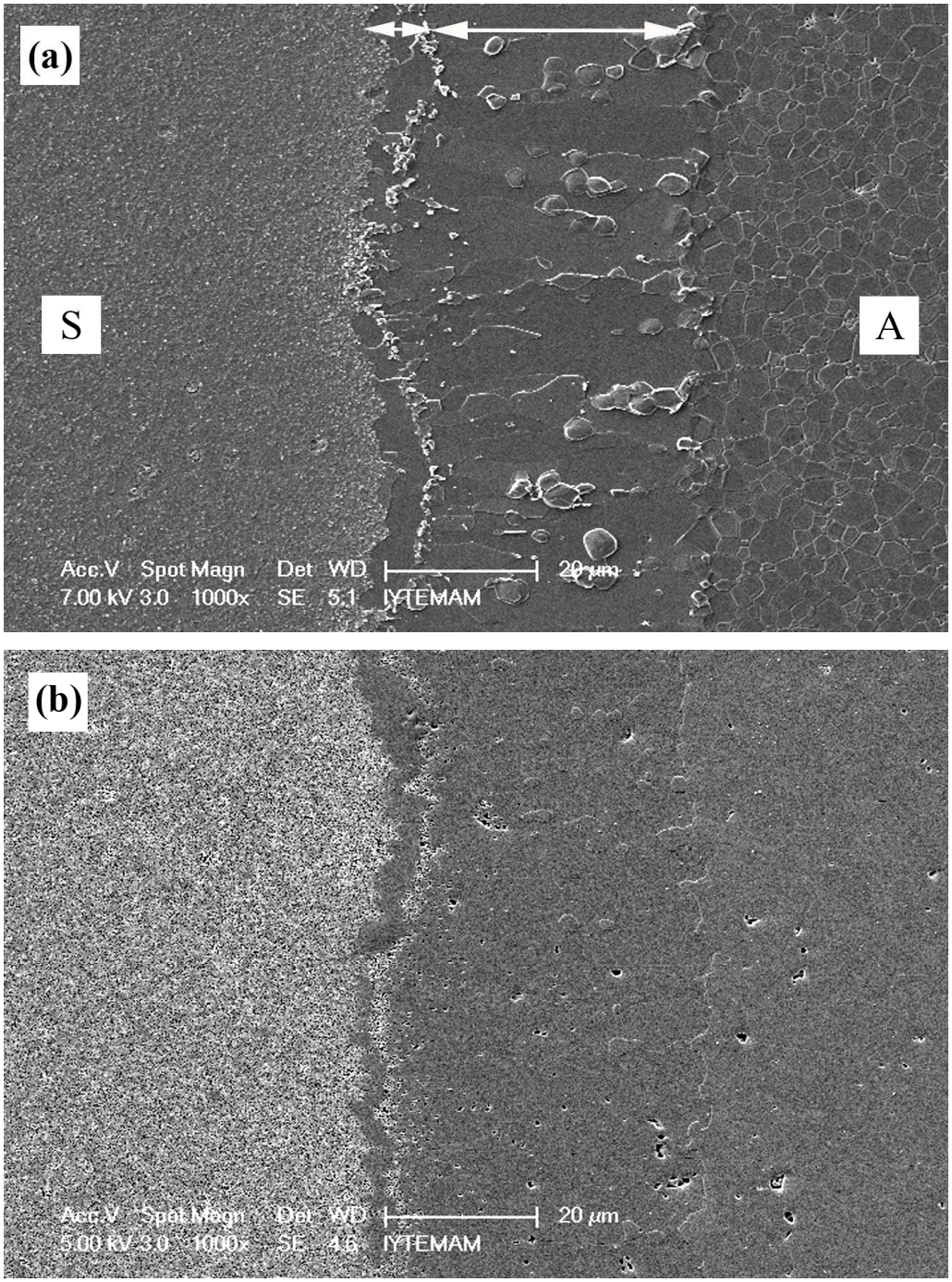

Figure 6.9. SEM image of alumina A – spinel bi-material interlayer after two isothermal steps co-sintering (16 hours at 1400°C + 16 hours at 1500°C) (a) thermally etched surface (b) chemically etched surface.

Micrographies MEB de la couche interfaciale de bi-matériaux alumina A – spinelle après un co-frittage en deux étapes isothermes (16 heures à 1400°C + 16 heures à 1500°C). a) surface polie attaquée thermiquement b) surface polie attaquée chimiquement.

Porous region in parent spinel end-member in alumina A – spinel was investigated in SEM after chemical etching of the polished surface. Figure 6.10 shows the increasing spinel grain size in moving away from the interface to the interior of the spinel. In the same direction, when moving into the bulk of the parent spinel, amount of pore was observed to decrease. Etching clearly revealed the more porous region near the interlayer where spinel had very fine grain size (Figures 6.10(a), (b) and (c)). On the other hand, around the center and the edge of the spinel same durations perfectly revealed the grain boundaries of fully dense spinel ceramic (Figures 6.10(d), (e) and (f)), which easily enabled measurement of average grain size.

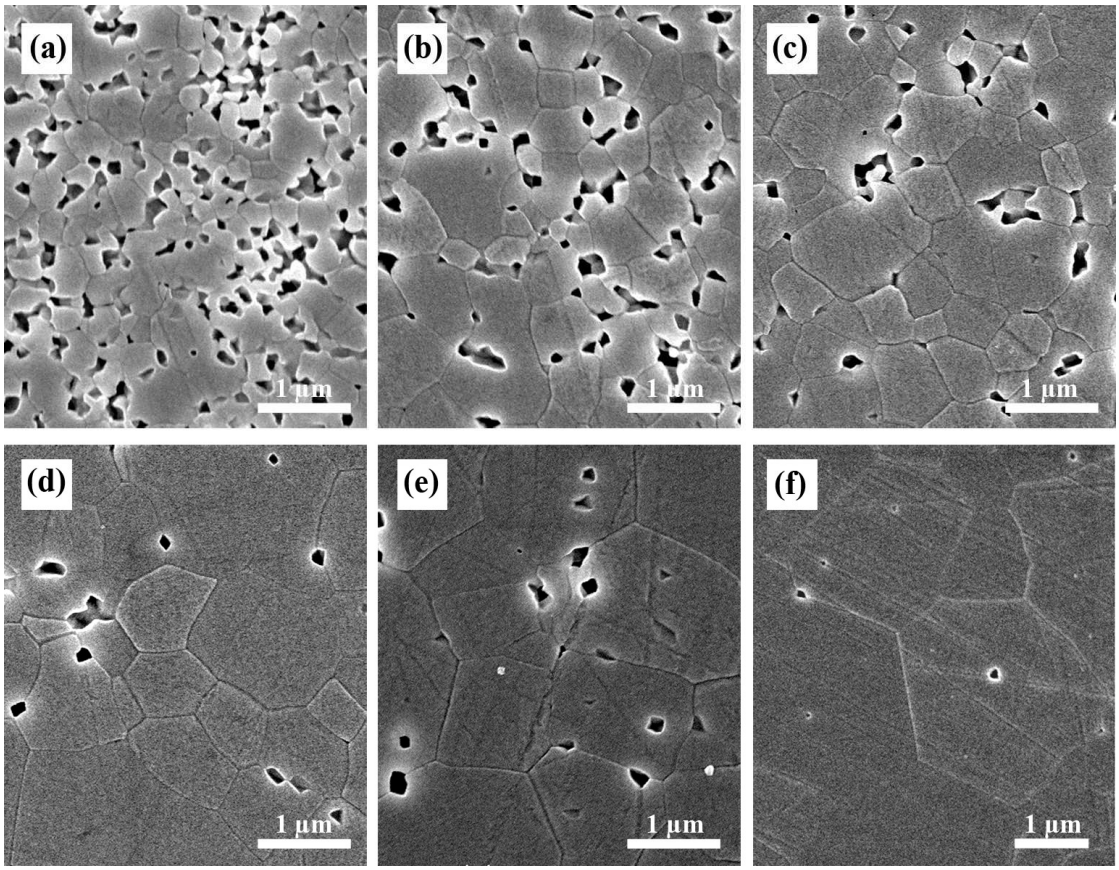

Figure 6.10. SEM images of parent spinel end-member in alumina A – spinel bi-material (a) 100 µm, (b) 200 µm, (c) 300 µm, (d) 600 µm away from the interlayer into bulk of the parent spinel and (e) at the center and (f) at the edge of parent spinel. The two sintering steps were done at 1400°C for 16 hours followed by another sintering at 1500°C for 16 hours. Sample was chemically etched at 140°C for 15 min in orthophosphoric acid.

Micrographies MEB de la partie spinelle d'un bi-matériau alumine A – spinelle co-fritté en deux étapes isothermes (16 heures à 1400°C + 16 heures à 1500°C) à différentes distances de l'interface (a) 100µm, (b) 200µm, (c) 300µm, and (d) 600µm. Sections transverses polies et attaquées chimiquement : 15 minutes à 140°C dans l'acide orthophosphorique.

The amount of porosity in the middle of this porous region was measured by image analysis to be 8% on chemically etched samples. This porosity decreased to less than 2% at 300 µm away from the interface and to <1% at the body center of the spinel pellet. Size of the spinel grains far away from the interlayer and around the center of the spinel was roughly about 1300 nm (Figure 6.10(e)). On the other hand, grain size of the spinel closer to the edges was nearly 3000 nm (Figure 6.10(f)). All the porosity and grain size measurements are plotted in Figure 6.11.

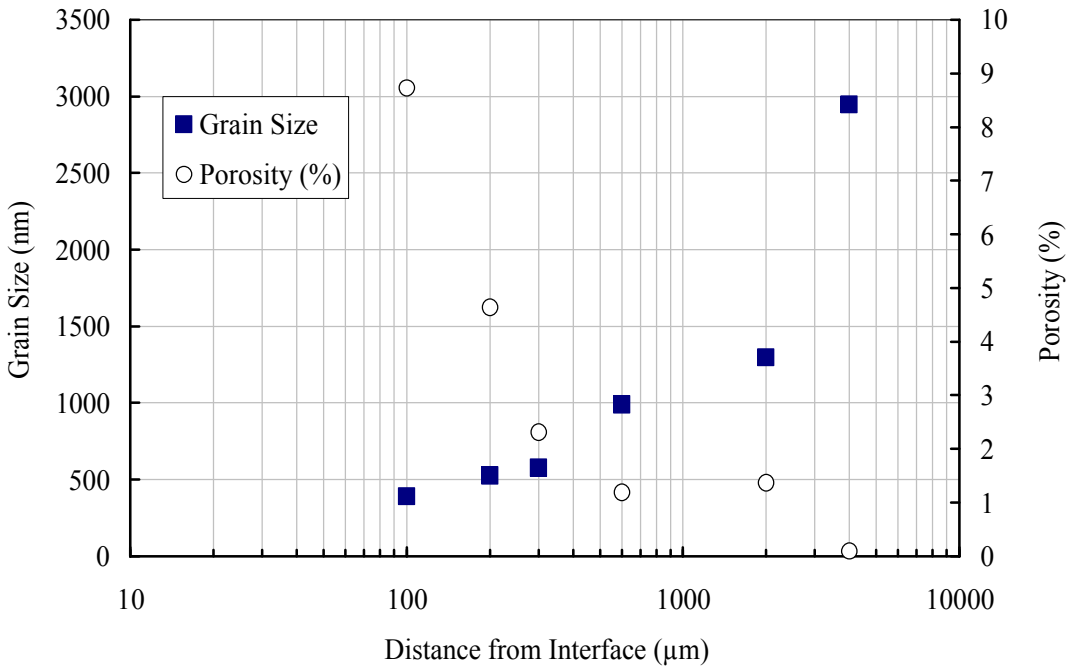

Figure 6.11. Porosity and grain size profiles from interface to interior of spinel for alumina A – spinel bi-material. The two sintering steps were done at 1400°C for 16 hours followed by another sintering at 1500°C for 16 hours. Sample was chemically etched at 140°C for 15 min in orthophosphoric acid.

Profils de porosité et de taille de grains dans la partie spinelle à partir de l'interface dans un bi-matériau alumine A – spinelle co-fritté en en deux étapes isothermes (16 heures à 1400°C + 16 heures à 1500°C). Mesures faites sur des sections transverses polies et attaquées chimiquement : 15 minutes à 140°C dans l'acide orthophosphorique.

6.3.4. Diffusion Couple Tests

Essais de couple de diffusion

Two separate tests were done to confirm the direction of diffusion and to understand the formation of columnar spinel grains from predensified ceramics. Diffusion couple tests were done as mentioned in Section 6.3.2. Schematic illustrations of diffusion couple test before and after thermal treatment are given in Figures 6.12(a) and (b). At the end of the tests, weak adhesion was observed between the two end-members which were easily separated by hand. Bare eye and optical microscope observations both showed surface ridges and nodules on the surfaces of the end-members after diffusion couple tests (Figures 6.12(b), 6.13 and 6.14).

Figures 6.13(a), (b), (c) and (d) show contact surfaces of end-members after heat treatment tests. Nodule type spots at contact points were observed on all specimen surfaces except in Figure 6.13(d) which was sintered from the green state. The surfaces of predensified alumina A end-members, as shown in Figures 6.13(a) and (c), had nearly the same appearance after diffusion couple tests. Center of the surface of the alumina end-member, as shown by area C in Figure 6.13(a), had a large cavity of about 300 μm in diameter with a matching surface ridge on the spinel surface as shown in Figure 6.13(b).

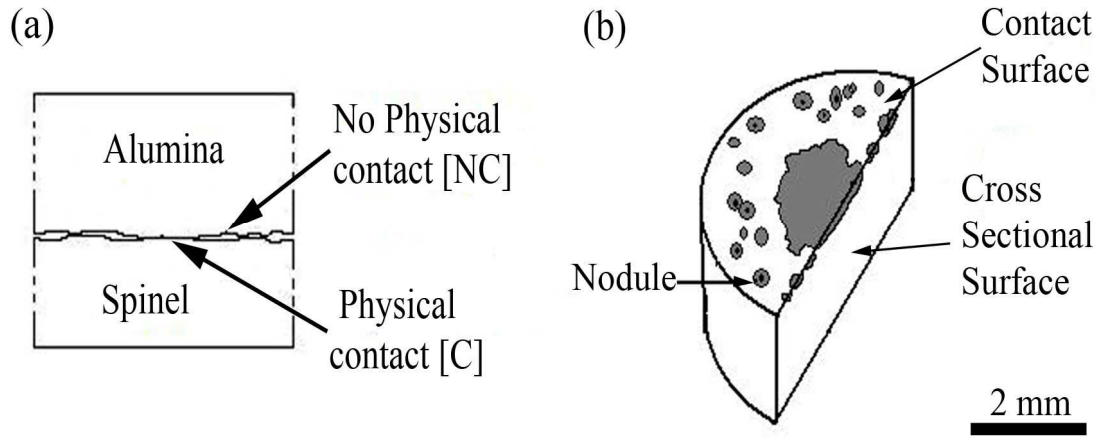

Figure 6.12. Illustration of diffusion couple test sample (a) before and (b) after thermal treatment (alumina A – spinel sintered at 1500°C for 16 hours).

Schéma d'un échantillon de couple de diffusion (a) avant et (b) après le traitement thermique (alumine A – spinelle 16 heures à 1500°C).

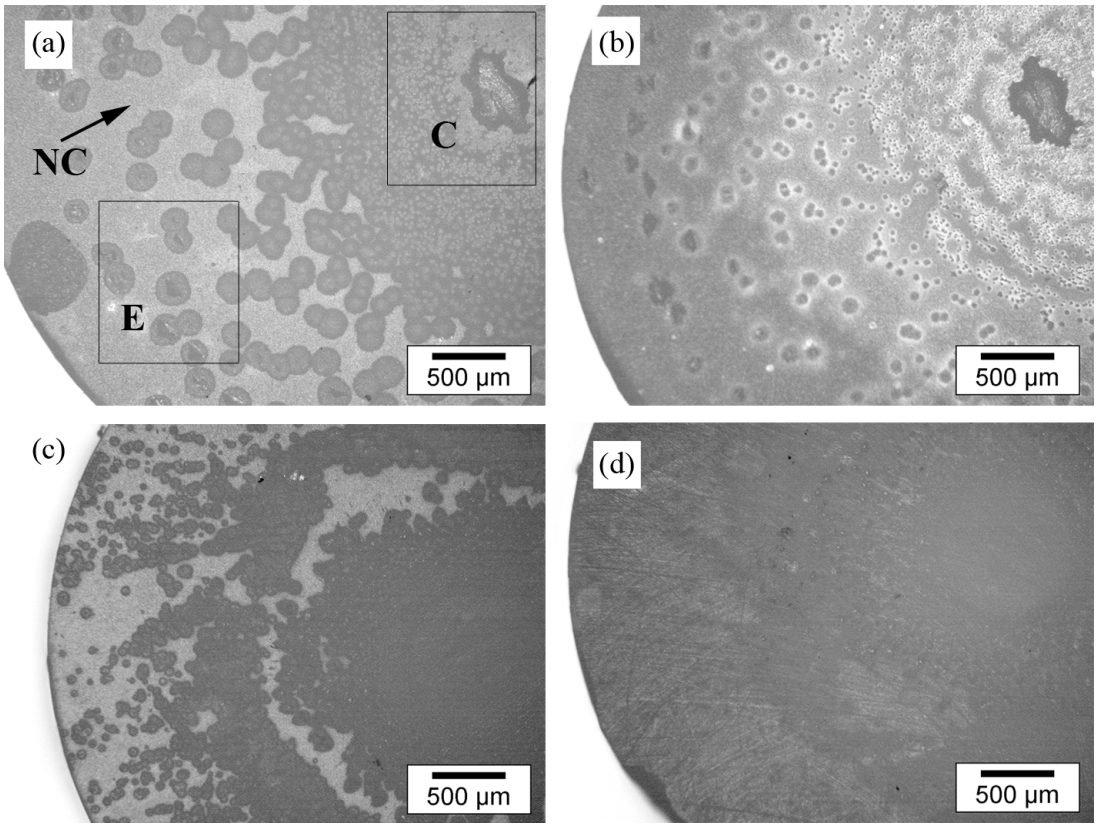

Figure 6.13. Contact surfaces of the end-members (a) predensified (95 %) alumina A (E: external part, C: central part of the sample) and (b) predensified (95%) spinel after diffusion couple test 1. Photographs show (c) predensified alumina A and (d) spinel after diffusion couple test 2 (1500°C 16 hours).

Surface de contact des deux parties de l'essai du couple de diffusion n°1 a) alumine A prédensifiée (95%) E partie extérieure, C région centrale, et b) spinelle prédensifiée (95%). Les macrographies c) et d) montrent les surfaces de contact de l'alumine A et de la spinelle après l'essai couple de diffusion n°2.

In order to investigate the diffusion between mono-materials, the contacted surfaces (see Figure 6.12(b)) were analyzed by SEM-EDS. Figures 6.14(a-e) display SEM images of contacted surfaces of predensified alumina and spinel end-members at different magnifications (experiment n° 1). Nodule type regions were observed (e.g. area E in Figure 6.13(a)) more clearly on the alumina surface in Figure 6.14(a) owing to better depth of focus of the SEM. One of the nodules is shown in more detail in greater magnification in Figure 6.14(c). EDS analysis showed that this nodule on the alumina surface consisted of spinel. There were cavities in centers of majority of the nodules indicating bonds forming by diffusion between the two end members. When the surface of the spinel pellet which was the other end-member, was observed with SEM, surface ridges with matching form were observed on the surfaces of the spinel as shown in Figures 6.14(b) and (d). Alumina and spinel parts could be matched as in Figures

6.14(c) and (d), by a cavity and a surface ridge, respectively. The spinel surface ridges on spinel pellet appeared to be formed by fracture from cavities of the nodules in alumina. So up to now, formation of nodule type spinel phase on the surface of alumina end-member by solid-state reaction mechanism in fully contacted regions is discussed. In addition to nodule type regions, surface of alumina contact surface away from nodules was also examined and displayed in Figure 6.14(e). Bright spot regions were observed among the alumina grains. The EDS analysis taken from one of them shows that there is spinel composition there. Possibly, Mg^{2+} ions evaporated from spinel end-member and diffused through the relatively rigid oxygen lattice of the Al_2O_3 in the alumina end-member. Figure 6.14(f) shows the matrix of spinel surface. Spinel grains are nearly three times bigger than the interior grains as previously mentioned in Section 6.3.1 (Figure 6.2).

The contacted surfaces of end-members after second diffusion couple test (experiment no 2) were also investigated by SEM. As seen in Figure 6.15(a), there were nodule type regions on alumina end-member that were similar to the ones observed in Figure 6.14(c). On the other hand, there were many scratch-marks like arrows pointing to the center of spinel pellet from all over the surface (Figure 6.15(b)). Some of them are shown in more detail at high magnification in Figure 6.15(d). These scratch marks are thought to originate from thermal expansion mismatch between spinel and alumina because they are always pointing to the center of the contact surface. There is a fracture at the trailing side of the scratches. These are exactly matched with the surface ridges observed on contact surface of alumina-end member as shown in Figure 6.15(c).

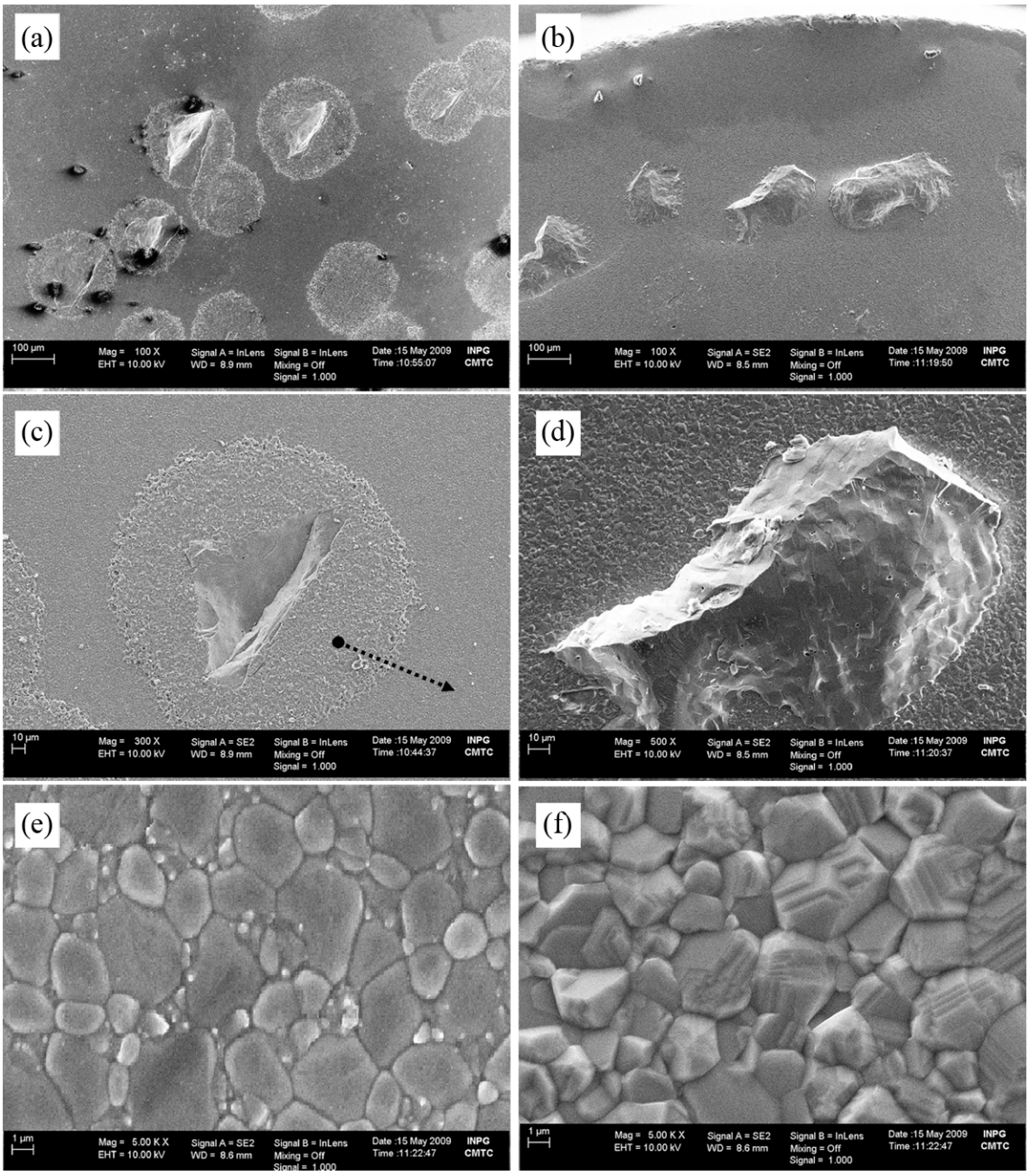

Figure 6.14. The SEM images of surfaces of predensified alumina and spinel end-members (Exp. No 1) (a), (c) and (e) alumina, (b), (d) and (f) spinel.

Micrographies MEB des surfaces de contact des parties prédensifiées (95%) alumine et spinelle de l'essai couple de diffusion n°1 a), c) et e) alumine et f) spinelle.

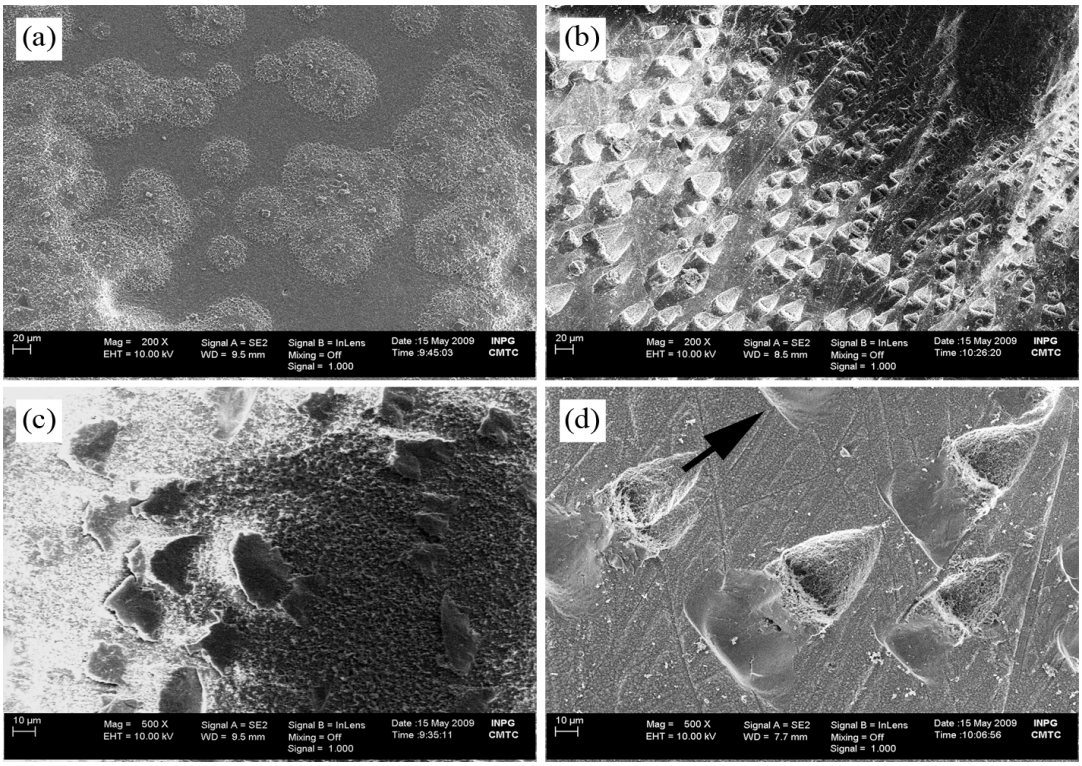

Figure 6.15. The SEM images of surfaces of the predensified alumina and spinel green compact end-members (a) and (c) alumina, (b) and (d) spinel.

Macrographies MEB des surfaces de contact entre la partie alumine prédensifiée (95%) a) et c) et la partie spinelle (initialement non prédensifiée) b) et d) après l'essai couple de diffusion n°2.

In order to analyze the diffusion of Mg and Al from contact points through the nodules to the remaining part (matrix) of the surfaces of the diffusion couples, SEM-EDS line scan analysis were applied on the dashed line as shown in Figure 6.14(c). According to the EDS line scan result, nodules were richer in Mg than Al (Figure 6.16). The oxygen content is not given in the chart. In the matrix, away from the nodules, Mg concentration was low in the grains and high in the grain boundaries where spinel formation was detected.

In addition to nodule type regions, alumina contact surface away from the nodules was also examined and displayed in Figure 6.17. Bright spot regions were observed among the alumina grains. The EDS analysis taken from one of them showed that there was spinel composition there. Possibly, Mg^{2+} ions evaporated from spinel end-member, and diffused along the grain boundaries of the alumina end-member.

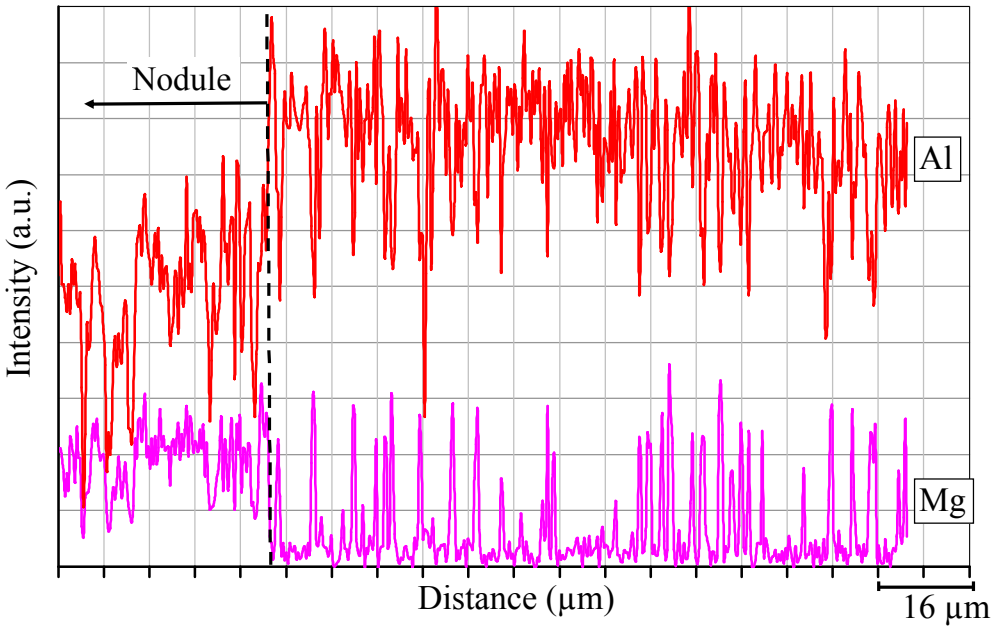

Figure 6.16. Line EDS analysis of contact surface of alumina (Exp. no 1). The surface of the nodule was richer in Mg compared to the rest of the surface.

Profil de composition en aluminium et en magnésium (analyse EDS) de la surface de contact côté alumine de l'essai couple de diffusion n°1. Le nodule est plus riche en magnésium que le reste de la surface.

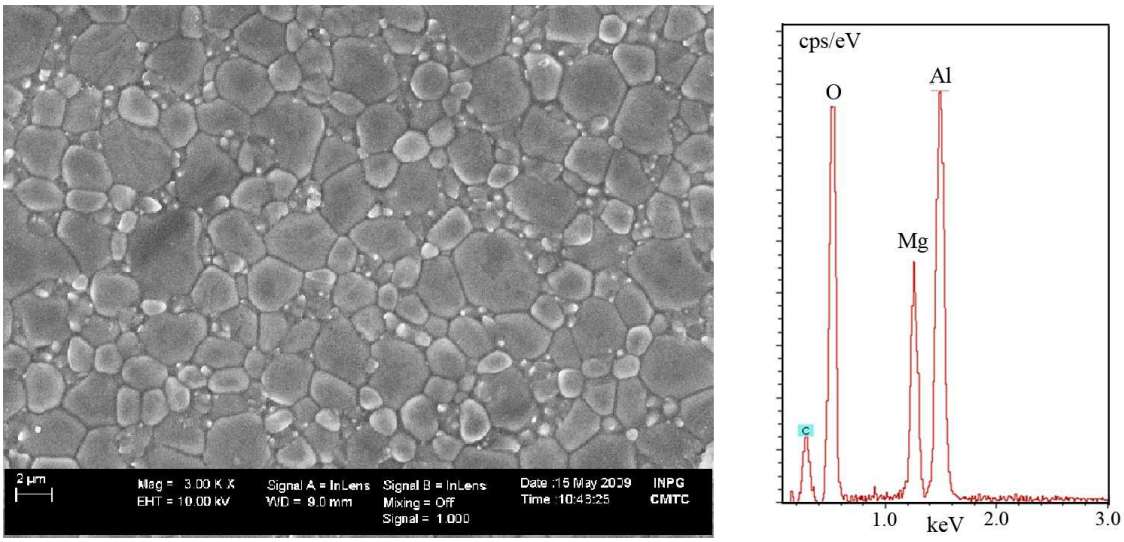

Figure 6.17. Point EDS analysis of a grain boundary of the alumina in a region out of nodules "matrix area". Image obtained from surface of alumina end-member away from nodules (in Exp. No 1).

Analyse ponctuelle (EDS) de joint de grains d'alumine dans une region éloignée des nodules. Micrographie de la surface de la partie alumine hors des nodules : essai couple de diffusion n°1.

The line scan EDS analysis was also done on the contact surface of alumina end-member after diffusion couple test 2, shown in Figure 6.18. The dashed line shows the EDS analysis line for Al and Mg. In the nodule region, Mg and Al elements were present, on the other hand, in the matrix there was almost no Mg element. This observation was different from that made in Figures 6.16 and 6.17. During the diffusion couple test the surface of spinel was rougher and more distant to spinel end member in experiment no 2 compared to experiment no 1 because spinel was in the green state in the former test.

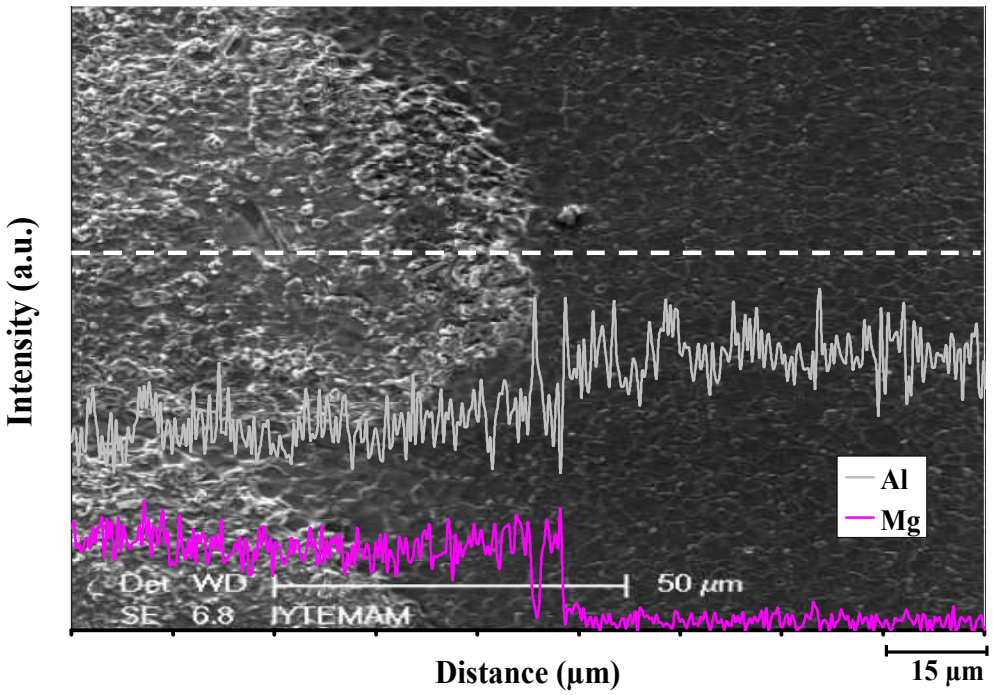

Figure 6.18. Line EDS analysis of the contact surface of alumina end-member after diffusion couple experiment 2.

Profil de composition (analyse EDS) en aluminium et en magnesium à la surface de la partie alumine (prédensifiée 95%) de l'essai couple de diffusion n°1.

In order to determine any crystal phase change or formation on the surface of the end-members after the first diffusion couple test, the end-members were analyzed by XRD technique. The XRD results are given in Figure 6.19. According to XRD results, spinel phase was detected on the surface of the alumina end-member. The detected spinel phase in the alumina end-member was an alumina rich composition ($Mg_{0.734}Al_{2.177}O_4$) with ICDD PDF-4+ Card No:04-009-7708. XRD pattern for spinel

end-member depicts two slightly separate peaks visible especially at large angles, thus it also contains slightly stoichiometric spinel ($Mg_{0.94}Al_{2.04}O_4$) phase (with ICDD PDF-4+ Card No:01-070-6979) in addition to the alumina rich phase. This was expected because Mg^{2+} concentration decreases from spinel to alumina.

In the second diffusion couple test, nearly the same XRD results were found for the end-members, except that a third spinel ($MgAl_2O_4$) phase was also detected at the spinel end-member with a stoichiometric Mg content (with ICDD PDF-4+ Card No:04-007-2712). The XRD results are not given here for the sake of brevity.

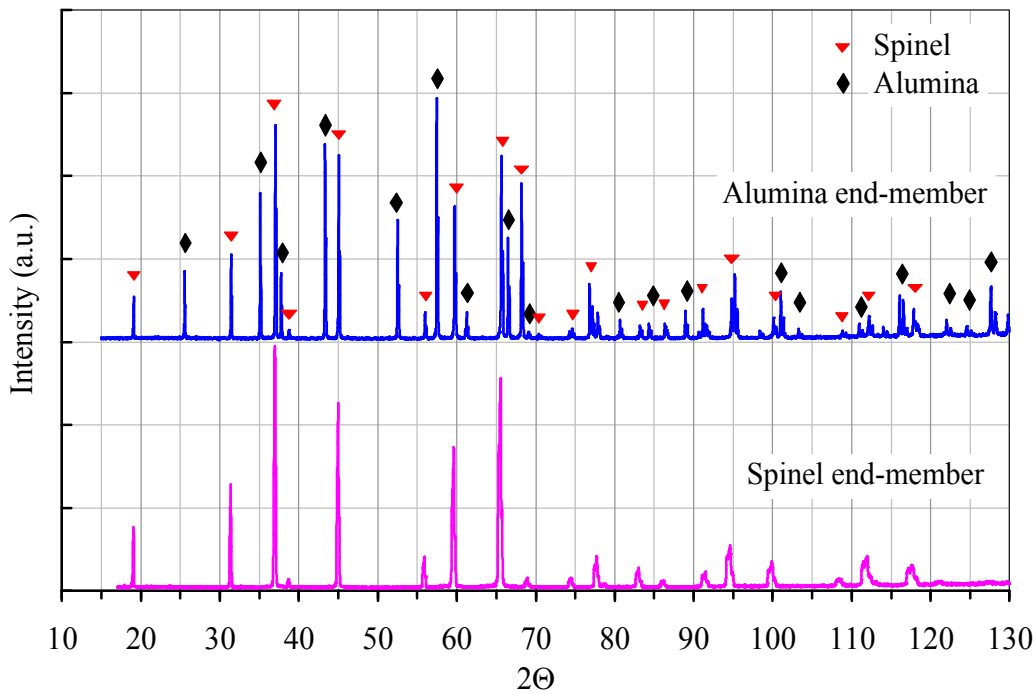

Figure 6.19. The XRD patterns of alumina and spinel end-members after diffusion couple test n°1.

Spectres de diffraction de rayons X des surfaces de contact des parties prédensifiées alumine et spinelle après l'essai couple de diffusion n°1.

We observed Mg^{2+} penetration into the alumina end-member and spinel formation on the center of alumina end-member as shown in Figures 6.12(b), 6.13(a) and (c). So in order to understand more clearly the depth of penetration of Mg^{2+} and formation of spinel in the alumina end-member, the samples were sectioned as shown in Figure 6.12(b), polished and thermally etched. Spinel grew into alumina and formed as columnar grains the lengths and widths of which were measured on SEM images.

Figure 6.20(a) shows the length of the columnar spinel grains to be about 40 μm. The spinel formation was confirmed by EDS analysis, the result is shown in Figure 6.20(b).

Widths of the columnar spinel grains were smaller than 5 μm in co-sintered samples (Figure 6.1) while they were larger than 8 μm when predensified pellets were contacted and heated (Figure 6.20(c)). The increase in the width of the columnar grains can be attributed to the smaller number of nucleating sites for spinel in predensified samples as opposed to the green pellets which obviously had smaller particles. Total lengths of the columnar spinel grains were equal to the thickness of the interlayer. This value was more or less the same in all bi-materials produced under the same sintering conditions, independent of density of the starting materials. Figure 6.20(c) shows that the phase boundaries between spinel and alumina are almost always curved with the center of curvature in alumina which indicates that the boundary tends to move into alumina. It was found that the width of the columnar spinel grains in the interlayer was small near the spinel interface and widened closer to alumina.

Non-contacted (NC) areas, where spinel formation was not detected (Figure 6.20(d)), were also observed through the cross section (NC in Figures 6.12(a) and 6.13(a)). The second diffusion couple test done with green spinel, showed that the interlayer thickness grew up to the same magnitude of roughly 40μm (Figure 6.21(a) and (b)). Interestingly, in areas where nodules cannot meet no columnar spinel formed into alumina (Figure 6.21(b)).

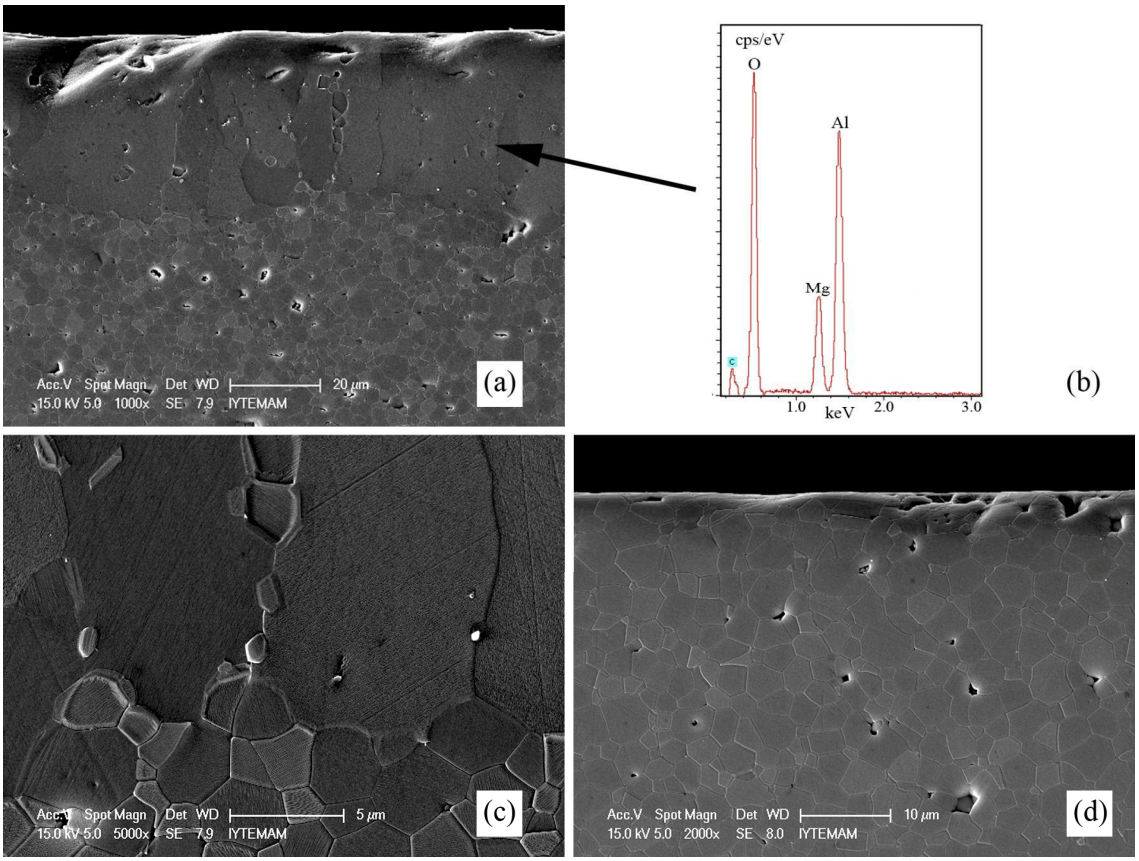

Figure 6.20. Cross-sectional images of alumina end-member and the EDS result (Experiment no 1); the width of spinel columnar grains (8 µm) is larger than in the co-sintering case (< 5 µm).

Micrographies MEB et micro-analyse (EDS) de la section transverse côté alumine de l'échantillon couple de diffusion n°1 ; la largeur (8 µm) des grains colonnaires de grains de spinelle est plus élevée que dans le cas du co-frittage (< 5 µm).

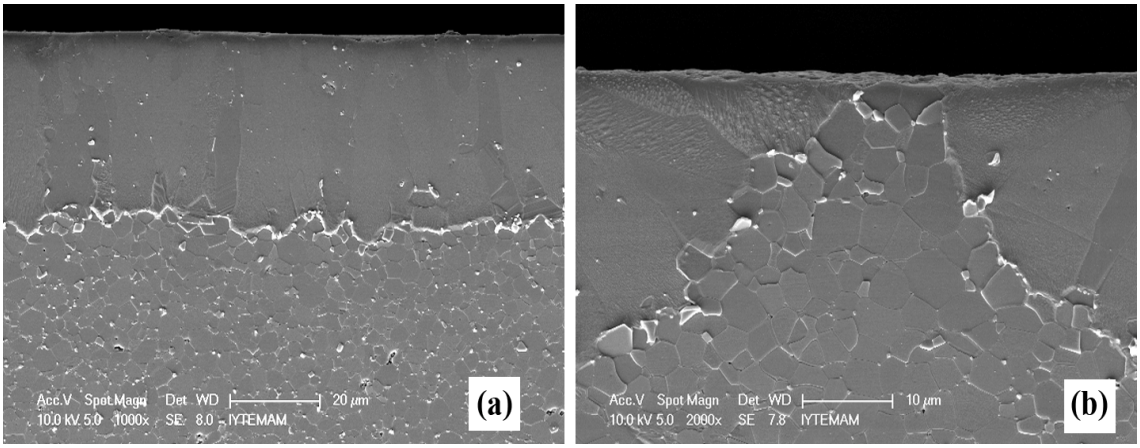

Figure 6.21. SEM cross-sectional images of alumina end-member (a) general cross section view and (b) a non-contact region among the nodules (Exp. no 2).

Micrographie MEB de section transverse côté alumine de l'essai couple de diffusion n°2 : a) vue générale b) zone de non contact entre nodules.

6.4. General Interpretation and Discussion

Interprétation et discussion générales

A good mechanical bond can be formed between spinel and alumina in co-sintered samples. Microstructural analysis of the interface revealed that a spinel interlayer of columnar grains forms between alumina and spinel regardless of the type of test. Widths of these columnar grains were less than 5 µm in co-sintered samples. In our configuration (alumina – spinel bi-materials) diffusion of Mg^{2+} and O^{2-} ions necessarily occurs from spinel to alumina through the columnar grained spinel interlayer and this volume oxygen diffusion is likely the limiting mechanism of the interlayer growth kinetics.

Spinel grain size and porosity were found to vary depending on the location in the spinel part of co-sintered samples and on the sintering temperature. At high temperature the equilibrium vapor pressure of magnesium increases rapidly ; the vapor pressure of Mg is 10 times larger at 1500°C than at 1400°C (Sasamoto, et al. 1981). Carter and separately Navias were able to grow a spinel layer on alumina through vapor transport of Mg (Carter 1961, Navias 1961). Hallstedt (1992), and especially Sasamoto et.al., (1981) and Altman (1963), reported on the vapor pressure of Mg over different Mg containing oxides. In the case of co-sintering experiments, before spinel body completes densification, evaporation of Mg from spinel fine grains, fast vapor diffusion on rather long distances and condensation at the interface are also expected in addition to transport of Mg by solid state diffusion. Such mechanisms can explain the gradient of spinel grain size and porosity in co-sintered samples from the interface towards the center of spinel part. The evolution of the microstructure (grain size and porosity) in the final-stage sintering of spinel with a gradient of magnesium content appears very complicated and depends on various parameters as shown by Ting and Lu (2000). The thin layer of porosity observed in the spinel part of co-sintered samples in two steps (Figure 6.9) can be considered as a Kirkendall effect (Smigelkas and Kirkendall 1947) due to the solid state diffusion of magnesium from spinel part towards the alumina part during the 16 hours soak at 1500°C. In the case of one step co-sintering at 1500°C, this "classical" Kirkendall effect is hidden by the long distance diffusion of magnesium vapor which leads to the grain size and porosity gradients in the spinel end-member.

In diffusion couple tests the same columnar spinel interlayer formed into alumina end- member at its contact points with the spinel end-member where Mg^{2+} was found to rapidly diffuse into alumina. On the other hand, O^{2-} diffusion into alumina is considerably slower, as confirmed by activation energy calculations, thus O^{2-} diffusion appears to control the diffusion mechanism. Similar conclusions were stated by Bratton (1971) and Ting and Lu (2000). Widths of the columnar grains were more than 8 µm in diffusion couple tests of predensified end-members. However, when the spinel end-member was in the green state and the alumina end-member in the predensified state, the diffusion couple test resulted in columnar interlayer grains of less than 5 µm thickness. It is thought that smaller columnar grain thickness was due to larger number of initial nucleation sites offered by green spinel end-member for growth of the interlayer.

Columnar grains are so formed probably due to concentration gradient of Mg^{2+} and Al^{3+} between the end-members. They are thought to nucleate on the surface of spinel and grow into alumina. When single crystal alumina is brought into a high temperature contact with single crystal of MgO, on the other hand, the interlayer grows in both directions (Rossi and Fulrath 1963, Watson and Price 2002). When the temperature is increased, the columnar grains will grow longer due to improved diffusion kinetics (Carry, et al. 2010). The diffusion mechanism for columnar grain growth is reported to be due to volume (also called lattice diffusion) diffusion (Watson and Price 2002), and less effectively by vapor transport because columnar grains extend almost all the way through the interlayer.

Columnar grains grow in an opposite direction to spinel, down the concentration gradient for Mg^{2+}. Their lengths are almost equal to the thickness of the interlayer which varies parabolically with time thus suggesting a diffusion controlled process. It was proposed that the reaction rate (thickness of interlayer) was independent of crystallographic orientation of parents oxides (Rossi and Fulrath 1963). However, columnar grains are observed to slightly decrease in number as they move away from spinel, indicating some coalescence of grains.

Similar columnar grain formation was observed in YAG samples by Buscaglia et.al., (1997) in their study on Y_2O_3 – Fe_2O_3 reaction couples. Columnar grains of $Y_3Fe_5O_{12}$ interlayer phase formed between Fe_2O_3 end-member and the in-situ formed $YFeO_3$. Another study on spinel also showed the formation of columnar spinel grains that grew between new in-situ formed equiaxed spinel grains and the corundum end-

members (Pettit, et al. 1966, Watson and Price 2002). Thus columnar spinel grains in the interlayer phase appear to always grow between spinel and corundum.

Reactions at the interfaces between alumina and magnesia were studied by several researchers by using either single or polycrystalline components (Rossi and Fulrath 1963, Watson and Price 2002, Zhang, et al. 1996). Other relevant studies involved magnesia and spinel interfaces (Whitney and Stubican 1971), interfaces between oxides like NiO – Al_2O_3 (Pettit, et al. 1966) and Y_2O_3 – Fe_2O_3 (Buscaglia, et al. 1997). But no study was found in the literature regarding the reaction at the interface between polycrystalline alumina and polycrystalline spinel. Hence this study fills this gap in the literature.

When alumina and magnesia are heated in contact, they are observed to develop two distinct spinel interlayers. An equiaxed spinel forms on magnesia side and a thicker layer of columnar spinel forms on the alumina side (Rossi and Fulrath 1963, Watson and Price 2002). A question may arise as to how the interlayer would grow if a single crystal of alumina and a polycrystalline spinel were heated together. Based on the data collected in this study, the spinel interlayer is expected to form as polycrystalline columnar grains if a single crystal of alumina is brought into contact with polycrystalline spinel. This is a priori supported by data of Rossi and Fulrath (1963) as well as the data of Watson and Price (2002). Another possible scenario is if polycrystalline alumina is contacted with single crystal of spinel at high temperature. In this case a single crystal interlayer of spinel is expected to form because the interlayer nucleates on the surface of spinel and grows into alumina. Direction of propagation of the interlayer was observed to occur into alumina both in this study and previously by Watson and Price (2002).

Whitney and Stubican (1971) studied the system MgO – $MgAl_2O_4$ using diffusion couples of single or polycrystals of MgO and spinel. They proposed that no new spinel phase forms between MgO and spinel end-members. However, Rossi and Fulrath (1963), and later Watson and Price (2002) reported on the formation of a thin spinel layer composed of equiaxed grains. The authors expect formation of a spinel interlayer with equiaxed grains between MgO and spinel if the two oxides are heated together at 1500°C.

6.5. Conclusions

Conclusions

When alumina and spinel are co-sintered at 1500°C, a good bond was observed to form between the two in the form of a new generation spinel interlayer. A much weaker bond formed during the diffusion couple test at the same temperature but the same interlayer spinel was observed although discontinuously. This interlayer spinel layer nucleated from original spinel – alumina interface and grew into alumina in the form of columnar grains up to about 40 μm after 16 hours of sintering at 1500°C. The growth of columnar grained spinel layer as a function of time was found to follow parabolic diffusion kinetics and diffusion of O^{2-} ions was proposed as the rate limiting species. These columnar grains had widths of less than 5 μm in co-sintered samples and more than 8 μm in diffusion couple experiment no 1. Smaller columnar grain thickness in the former samples was due to larger number of initial nucleation sites offered by green spinel end-member for growth of the interlayer. The center of curvature of the phase boundary between columnar spinel grains and alumina was always located in alumina, indicating that the interlayer was in the process of growing into alumina. As far as the mechanism for formation and growth of the spinel interlayer, all two scenarios are thought to occur. These are volume diffusion inside the columnar grains and magnesium vapor transport inside the fine grained and porous spinel part.

Spinel grain size was found to vary depending on the location in the spinel part of co-sintered samples. The grain size was 400 nm near the interlayer where there was roughly 8% porosity. The porosity decreased to less than 1% at the center of the spinel part. The grain size was 800 nm farther into the bulk of spinel and was larger than 3000 nm around the outer edges of the spinel where loss of Mg occurs by evaporation. No such change in grain size of alumina was observed in the alumina part of the co-sintered samples.

Two isothermal steps co-sintering was found to lead to the formation of an interlayer with two distinct forms.

In diffusion couple tests the same columnar spinel interlayer formed into alumina end member at its contact points with the spinel end-member where Mg^{2+} was found to rapidly diffuse into alumina. This finding proved that the columnar spinel interlayer nucleated from the original spinel – alumina interface and proceeded to

alumina. Another argument for the direction of propagation of the interlayer was the center of curvature of the phase boundary between interlayer spinel and alumina end-member.

CHAPTER 7

CONCLUSIONS

Conclusions

7.1. Summary and Conclusions

Sommaire et Conclusions

Alumina, zirconia and spinel powders were fine powders of high purity with a large BET surface area. The powders showed different compaction behaviors from each other, alumina B had the highest green density at any applied pressure but spinel showed the highest increase in green density difference (5%) upon increasing pressure. On the other hand, cold isostatic pressing (CIP) produced higher initial green density values than UP. The initial green density differences slightly affected the final sintered density. MgO doped alumina (alumina A) was found to have a smaller grain size than undoped alumina after sintering. The apparent activation energies for densification (Q_d) of the powders were 680 kJ/mol for alumina A and 660 kJ/mol for alumina B.

In the sintering of zirconia Z-3Y powder, an unexpected bump was observed in the shrinkage rate versus temperature diagrams. This bump was thought to originate from the very fine particle size fraction of the powder. The activation energy value for zirconia was 530 kJ/mol for the Z-3Y powder. TZ-2Y powder had an activation energy value of 740 kJ/mol. More experiments at different heating rates could provide more precise activation energy measurements and confirm the decrease of apparent densification activation energies of zirconia for increasing relative density. Such high apparent activation energies at the beginning of the densification could be related to an interface reaction controlled mechanism as long as the crystallite sizes are lower than 100 nm.

Two bumps (peak) and a minimum in-between were observed in the densification rate versus temperature plots of the spinel powder in vertical dilatometer tests. A value of m=2.75 was found for the grain growth exponent versus time. This result was different from those reported in literature possibly due to the presence of pores.

Apparent activation energy for densification of the spinel powder was measured and calculated by using Arrhenius plots and master sintering curve (MSC) methods to be 860 kJ/mol. The activation energy was found to gradually decrease by increasing relative densities. The other technique yielded an activation energy value of 863 kJ/mol. The two values for Q were in good agreement. The activation energy values reported in the study of Benameur et al., (2010) were also in agreement with the results reported here. A potential explanation could be the characteristic of the powder used in the study which was also manifested in its sintering behavior. Abnormal grain growth on the microstructure was observed near the surface of spinel ceramic due to MgO evaporation on the surface.

For nearly fully dense spinel ceramic, 15 minutes of chemical etching in orthophosphoric acid gave the best etching results by avoiding grain growth during thermal etching. For samples with low densities, however, fracture surfaces can give more accurate information on porosity and average grain size.

Precoarsening treatments at 1100-1200°C of the spinel powder led to elimination of one of the shoulders in time versus densification rate curve. However, no noticeable effect was observed on the bulk properties of the ceramic. Two step sintering technique showed an increase in relative density up to 96% without an increase in grain size (<460 nm). A slightly higher density was possible with combined use of pretreatment and TSS.

The alumina – zirconia and alumina – spinel oxide-oxide bi-material systems were investigated. The alumina B – zirconia TZ-2Y bi-material yielded poor adhesion at the interface while alumina-spinel pair possessed relatively strong adhesion at the interface. In the first case, mechanical bonding by interlocking was the adhesion mechanism. On the other hand, in the second case, chemical bonding by diffusion was the adhesion mechanism. However, alumina B – zirconia Z-3Y pairs separated after co-sintering process. The reason for separation of these bi-combinations can be explained by severe shrinkage mismatches between these pairs.

Type of production of green compact bi-material compaction processes was tested. The powders firstly, uniaxially co-pressed (Co-UP) at low pressures (50 MPa) followed by compaction at high cold isostatic pressure (Co-UP+CIP) and less cracks formed in the interface.

In-situ new generation spinel interlayer was detected between alumina and spinel end-members after co-sintering at elevated temperature. This diffusion layer

nucleated from original spinel - alumina interface and grew into alumina in the form of columnar grains up to about 40 μm after 16 hours of sintering at 1500°C. The interlayer supplied a strong bond between the end-members. The growth of columnar grains as a function of time was found to follow parabolic diffusion kinetics with diffusion of O^{2-} ions as the rate limiting species.

Spinel grain size and porosity were found to vary depending on the location in the spinel part of co-sintered samples. Two isothermal steps co-sintering was found to lead to the formation of an interlayer with two distinct forms. After the second isothermal step, the thin layer of porosity observed in the spinel part can be considered as a Kirkendall effect due to the solid state diffusion of magnesium from spinel part towards the alumina part during the 16 hours soak at 1500°C. In the case of single step co-sintering at 1500°C, this "classical" Kirkendall effect is hidden by the long distance diffusion of magnesium vapor which leads to the grain size and porosity gradients in the spinel end-member.

In diffusion couple tests the same columnar spinel interlayer formed into alumina end member at its contact points with the spinel end-member where Mg^{2+} was found to rapidly diffuse into alumina. This finding proved that the columnar spinel interlayer nucleated from the original spinel-alumina interface and proceeded to alumina. Another argument for the direction of propagation of the interlayer was the center of curvature of the phase boundary between interlayer spinel and alumina end member.

7.2. Future Work

Travaux futurs

The following studies can be done in the future:

Grain growth kinetics of spinel can be investigated in more detail in additional longer soaking time tests such as 24 or 36 hours.

Precoarsening might be done at low temperatures (~800°C) without any densification by this way the two peak formation can be examined. Then spinel can be sintered at higher temperature (>1600°C) by this way to obtain fully dense ceramics (99.5%).

In TSS, the T1 temperature might be further increased (>1550°C) to get higher density at that temperature and then full density with still fine grain size can be obtained during holding at T2 temperature.

Bi-materials have been highly promising advanced materials to develop new generated materials that can have superior thermal, mechanical or electrical properties. However, due to the challenging problems with processing, it is very hard to identify the type of appropriate processing (tape casting or dry co-pressing) to achieve a strong bond to obtain crack free bi-materials. Therefore, the type of bi-material green body production methods can be compared in the future. Adhesion strength between alumina and spinel bi-materials might be measured.

Predicted interlayer formation between potentially suggested single crystal alumina and single crystal spinel in diffusion couple tests might be investigated. Interface can be investigated with TEM to understand in more detail the Kirkendall effect and the columnar grain formation.

REFERENCES

Aloca, Inc., 2010, *Alumina*, http://www.alcoa.com, (accessed March 12, 2010).

Altman, R., 1963, Vaporization of magnesium oxide and its reaction with alumina, *Journal of the American Ceramic Society*. 67: p. 366- 369.

Anderson, M. P., Srolovitz, D. J., Grest, G. S. and Sahni, P. S., 1984, Computer-Simulation of Grain-Growth. 1. Kinetics, *Acta Metallurgica*. 32(5): p. 783-791.

Ashby, M. F., 1969, On Interface-Reaction Control of Nabarro-Herring Creep and Sintering *Scripta Metallurgica*. 3(11): p. 837-842.

Atkinson, H. V., 1988, Theories of Normal Grain-Growth in Pure Single-Phase Systems, *Acta Metallurgica*. 36(3): p. 469-491.

Baikowski, 2010, *Spinel Technical Information Data for Alumina and Spinel*, http://www.baikowski.com, (accessed March 10, 2010).

Bartha, P. and Klischat, H.J. , 1999, Present State of the Refractory Lining for Cement Kilns, *CN-Refractories*. 6(3): p. 31–38.

Bateman, C. A., Bennison, S. J. and Harmer, M. P. , 1989, Mechanisms for the Role of Magnesia in the Sintering of Alumina Containing Small Amounts of Liquid Phase, *Journal of the American Ceramic Society.* 72(7): p. 1241-44.

Baumgartner, R. and Tan, L.K., 2002, MIM Merries Metals, *Metal Powder Report*: p. 38-42.

Benameur, N., Bernard-Granger, G., Addad, A., Raffy, S. and Guizard, C., 2010, Sintering Analysis of A Fine-grained Stoichiometric Alumina–Magnesia Spinel Powder, submitted for publication to *Journal of the American Ceramic Society*.

Bennison, S. J. and Harmer, M. P., 1990, A History of the Role of MgO in the Sintering of α-Al_2O_3 *Ceramic Transactions*. 7: p. 13-49.

Bernard-Granger, G., Benameur, N., Addad, A., Nygren, M., Guizard, C. and Deville, S., 2009, Phenomenological analysis of densification mechanism during spark plasma sintering of $MgAl_2O_4$, *Journal of Materials Research*. 24(11): p. 3469-3470.

Bernard-Granger, G. and Guizard, C., 2007a, Spark plasma sintering of a commercially available granulated zirconia powder: I. Sintering path and hypotheses about the mechanism(s) controlling densification, *Acta Materialia*. 55(10): p. 3493-3504.

Bernard-Granger, G. and Guizard, C., 2007b, Apparent activation energy for the densification of a commercially available granulated zirconia powder, *Journal of the American Ceramic Society*. 90(4): p. 1246-1250.

Bernard-Granger, G. and Guizard, C., 2008b, New relationships between relative density and grain size during solid-state sintering of ceramic powders, *Acta Materialia*. 56(20): p. 6273-6282.

Bernard-Granger, G., Guizard, C. and Addad, A., 2008a, Influence of co-doping on the sintering path and on the optical properties of a submicronic alumina material, *Journal of the American Ceramic Society*. 91(5): p. 1703-1706.

Blaine, D. C., Park, S. J. and German, R. M., 2009, Linearization of Master Sintering Curve, *Journal of the American Ceramic Society*. 92(7): p. 1403-1409.

Bodisova, K., Sajgalik, P., Galusek, D. and Svancarek, P., 2007, Two-stage sintering of alumina with submicrometer grain size, *Journal of the American Ceramic Society*. 90(1): p. 330-332.

Boonyongmaneerat, Y. and Schuh, C. A., 2006, Contributions to the interfacial adhesion in Co-sintered Bilayers, *Metallurgical and Materials Transactions a-Physical Metallurgy and Materials Science*. 37A(5): p. 1435-1442.

Bratton, R. J., 1971, Sintering and Grain-Growth Kinetics of $MgAl_2O_4$, *Journal of the American Ceramic Society*. 54(3): p. 141-143.

Burton, B., 1972, Interface Reaction Controlled Diffusional Creep- Consideration of Grain-Boundary Dislocation Climb Sources, *Materials Science and Engineering*. 10(1): p. 9-14.

Buscaglia, V., Caracciolo, F., Bottino, C., Leoni, M. and Nanni, P., 1997, Reaction diffusion in the Y_2O_3-Fe_2O_3 system, *Acta Materialia*. 45(3): p. 1213-1224.

Cai, P. Z., Green, D. J. and Messing, G. L., 1997a, Constrained densification of alumina/zirconia hybrid laminates .1. Experimental observations of processing defects, *Journal of the American Ceramic Society*. 80(8): p. 1929-1939.

Cai, P. Z., Green, D. J. and Messing, G. L., 1997b, Constrained densification of alumina/zirconia hybrid laminates .2. Viscoelastic stress computation, *Journal of the American Ceramic Society*. 80(8): p. 1940-1948.

Carry, C., Yalamaç, E. and Akkurt, S., 2010, Co-Sintering Behaviours of Oxide Based Bi-Materials, ed. E. A. Olevsky and R. K. Bordia, Advances in Sintering Science and Technology, 209, 307-320, Wiley.

Carter, C.B. and Norton, M.G., 2007, Ceramic Materials: Science and Engineering, Springer.

Carter, R.E. , 1961, Mechanism of solid-state reaction between magnesium oxide and aluminium oxide and between magnesium oxide and ferric oxide, *Journal of the American Ceramic Society*. 44: p. 116-20.

Chen, I. W. and Wang, X. H., 2000, Sintering dense nanocrystalline ceramics without final-stage grain growth, *Nature*. 404(6774): p. 168-171.

Chiang, Y. M. and Kingery, W. D., 1989, Grain-Boundary Migration in Nonstoichiometric Solid-Solutios of Magnesium Aluminate Spinel: 1. Grain-Growth Studies, *Journal of the American Ceramic Society*. 72(2): p. 271-277.

Chiang, Y. M. and Kingery, W. D., 1990, Grain-Boundary Migration in Nonstoichiometric Solid-Solutios of Magnesium Aluminate Spinel: 2. Effects of Grain-Boundary NonStoichiometry, *Journal of the American Ceramic Society*. 73(5): p. 1153-1158.

Chiang, Y.M., Birnie III, D. and Kingery, W.D., 1997, Physical Ceramics: principles for ceramic science and engineering, Wiley.

Chu, M. Y., Dejonghe, L. C., Lin, M. K. F. and Lin, F. J. T., 1991, Precoarsening to Improve Microstructure and Sintering of Powder Compacts, *Journal of the American Ceramic Society*. 74(11): p. 2902-2911.

Coble, R. L., 1962a, Sintering of Alumina: Effect of Atmosphere, *Journal of the American Ceramic Society*. 45: p. 123-127.

Coble, R.L., 1962b, Transparent Alumina and Method of Preparation, U.S., No. 3026210.

Cook, S. G., Little, J. A. and King, J. E., 1995, Etching and Microstructure of Engineering Ceramics, *Materials Characterization*. 34(1): p. 1-8.

De Jonghe, L.C. and Rahaman, M.N., 2003, Sintering of Ceramics, ed. S. Somiya, Materials Science, 1, 187-264, Elsevier Science.

Demartin, M., Herard, C., Carry, C. and Lemaitre, J., 1997, Dedensification and anomalous grain growth during sintering of undoped barium titanate, *Journal of the American Ceramic Society*. 80(5): p. 1079-1084.

Elssner, G., Hoven, H. , Kiessler, G. and Wellner, P., 1999, Ceramics and Ceramic Composites: Materialographic Preparation, Elsevier.

Ewsuk, K. G., Ellerby, D. T. and DiAntonio, C. B., 2006, Analysis of nanocrystalline and microcrystalline ZnO sintering using master sintering curves, *Journal of the American Ceramic Society*. 89(6): p. 2003-2009.

German, R.M., 1996, Sintering Theory and Practice, John Wiley & Sons. Inc.

Hallstedt, B., 1992, Thermodynamic Assessment of the System $MgO-Al_2O_3$, *Journal of the American Ceramic Society*. 75(6): p. 1497-1507.

Hansel, J.D., Rusin, R.P., Teng, M.H. and Johnson, D. L., 1992, Combined Stage Sintering Model, *Journal of the American Ceramic Society*. 73(5): p. 1129-35.

He, Z. M. and Ma, J., 2003a, Constitutive modeling of the densification and grain growth of fine-grained alumina ceramics, *Materials Science and Engineering a-Structural Materials Properties Microstructure and Processing*. 361(1-2): p. 130-135.

He, Z. M. and Ma, J., 2003b, Constitutive modeling of the densification of PZT ceramics, *Journal of Physics and Chemistry of Solids*. 64(2): p. 177-183.

He, Z. M. and Ma, J., 2005, Constitutive modeling of alumina sintering: grain-size effect on dominant densification mechanism, *Computational Materials Science*. 32(2): p. 196-202.

Hesabi, Z. R., Haghighatzadeh, A., Mazaheri, M., Galusek, D. and Sadrnezhaad, S. K., 2009, Suppression of grain growth in sub-micrometer alumina via two-step sintering method, *Journal of the European Ceramic Society*. 29(8): p. 1371-1377.

Hillman, S. H. and German, R. M., 1992, Constant Heating Rate Analysis of Simultaneous Sintering Mechanisms in Alumina, *Journal of Materials Science*. 27(10): p. 2641-2648.

Jalota, S., Bhaduri, S. B. and Tas, A. C., 2007, Osteoblast proliferation on neat and apatite-like calcium phosphate-coated titanium foam scaffolds, *Materials Science & Engineering C-Biomimetic and Supramolecular Systems*. 27(3): p. 432-440.

Kellett, B. and Lange, F. F., 1984, Stresses Induced by Differential Sintering in Powder Compacts, *Journal of the American Ceramic Society*. 67(5): p. 369-371.

Kieback, B., Neubrand, A. and Riedel, H., 2003, Processing techniques for functionally graded materials, *Materials Science and Engineering a-Structural Materials Properties Microstructure and Processing*. 362(1-2): p. 81-105.

Kingery, W. D., Bowen, H.K. and Uhlmann, D.R., 1976, Introduction to Ceramics, John Wiley.

Kleebe, H. J., Reimanis, I. E. and Cook, R. L., 2005, Processing and microstructure characterization of transparent spinel monoliths, ed. C. B. DiAntonio, Ceramic Transactions, 157, p. 61-68.

Kohl, W.H., 1964, Ceramics and ceramic-to-metal sealing *Vacuum*. 14(9): p. 333-354.

Kutty, T. R. G., Khan, K. B., Hegde, P. V., Banerjee, J., Sengupta, A. K., Majumdar, S. and Kamath, H. S., 2004, Development of a master sintering curve for ThO_2, *Journal of Nuclear Materials*. 327(2-3): p. 211-219.

Lannutti, J. J., Deis, T. A., Kong, C. M. and Phillips, D. H., 1997, Density gradient evolution during dry pressing, *American Ceramic Society Bulletin*. 76(1): p. 53-58.

Legros, C., Carry, C., Bowen, P. and Hofmann, H., 1999, Sintering of a transition alumina: Effects of phase transformation, powder characteristics and thermal cycle, *Journal of the European Ceramic Society*. 19(11): p. 1967-1978.

Li, D., Chen, S., Shao, W. Q., Ge, X. H., Zhang, Y. H. and Zhang, S. S., 2008, Densification evolution of TiO_2 ceramics during sintering based on the master sintering curve theory, *Materials Letters*. 62(6-7): p. 849-851.

Li, D. X., Pirouz, P., Heuer, A. H., Yadavalli, S. and Flynn, C. P., 1992, A High-Resolution Electron-Microscopy Study of MgO/Al_2O_3 Interface and $MgAl_2O_4$ Spinel Formation, *Philosophical Magazine a-Physics of Condensed Matter Structure Defects and Mechanical Properties*. 65(2): p. 403-425.

Li, J. G., Ikegami, T., Lee, J. H. and Mori, T., 2000, Fabrication of translucent magnesium aluminum spinel ceramics, *Journal of the American Ceramic Society*. 83(11): p. 2866-2868.

Lin, F. J. T., DeJonghe, L. C. and Rahaman, M. N., 1997, Initial coarsening and microstructural evolution of fast-fired and MgO-doped Al_2O_3, *Journal of the American Ceramic Society*. 80(11): p. 2891-2896.

Maca, K., Pouchly, V. and Zalud, P., 2010, Two-Step Sintering of oxide ceramics with various crystal structures, *Journal of the European Ceramic Society*. 30(2): p. 583-589.

Matsui, K., 2007a, Sintering Kinetics at Isothermal Shrinkage: Effect of Specific Surface Area on the Initial Sintering Stage of Fine Zirconia Powder, *Journal of the American Ceramic Society*. 90(1): p. 44-49.

Matsui, K., Ohmichi, N. and Ohgai, M., 2005, Sintering Kinetics at Constant Rates of Heating: Effect of Al_2O_3 on the Initial Sintering Stage of Fine Zirconia Powder, *Journal of the American Ceramic Society*. 88(12): p. 3346-3352.

Meir, S., Kalabukhov, S., Froumin, N., Dariel, M. P. and Frage, N., 2009, Synthesis and Densification of Transparent Magnesium Aluminate Spinel by SPS Processing, *Journal of the American Ceramic Society*. 92(2): p. 358-364.

Morita, K., Kim, B. N., Yoshida, H. and Hiraga, K., 2009, Spark-Plasma-Sintering Condition Optimization for Producing Transparent $MgAl_2O_4$ Spinel Polycrystal, *Journal of the American Ceramic Society*. 92(6): p. 1208-1216.

Morrell, R., 1985, Handbook of Technical and Engineering Ceramics, Part 1, An Introduction for the Engineer and Designer, Her Majesty's Stationery Office.

Mroz, T. J., Hartnett, T. M., Wahl, J. M., Goldman, L. M., Kirsch, J. and Lindberg, W. R., 2005, Recent advances in spinel optical ceramic, ed. R. W. Tustison, Proceedings of the Society of Photo-Optical Instrumentation Engineers (Spie), 5786, p. 64-70.

Navias, L., 1961, Preparation and Properties of Spinel Made by Vapor Transport and Diffusion in the System $MgO-Al_2O_3$, *Journal of the American Ceramic Society*. 44(9): p. 434-46.

Niesz, D. E., McCoy, G. L. and Wills, R. R, 1978, Processing of Crystalline Ceramics, H. Palmour, III., R. F. Davis and T. M. Hare, 11, 41-48.

Okada, H., Kawakami, H., Hashiba, M., Miura, E., Nurishi, Y. and Hibino, T., 1985, Effect of Physical Nature of Powders and Firing Atmosphere on $ZnAl_2O_4$ Formation, *Journal of the American Ceramic Society*. 68(2): p. 58-63.

Patterson, M. C. L., DiGiovanni, A. A., Fehrenbacher, L. and Roy, D. W., 2003, Spinel: Gaining momentum in optical applications, ed. R. W. Tustison, Proceedings of the Society of Photo-Optical Instrumentation Engineers (Spie), 5078, 71-79.

Pettit, F.S., Randklev, E.H. and Felten, E.J., 1966, Formation of $NiAl_2O_4$ by Solid State Formation, *Journal of the American Ceramic Society*. 49(4): p. 199-203.

Rahaman, M. N., 1995, Ceramic Processing and Sintering, Marcel Dekker.

Rahaman, M. N. and Jonghe, L. C. De, 1993, Reaction sintering of zinc ferrite during constant rates of heating, *Journal of the American Ceramic Society*. 76: p. 1739-1744.

Ravi, D. and Green, D. J., 2006, Sintering stresses and distortion produced by density differences in bi-layer structures, *Journal of the European Ceramic Society*. 26(1-2): p. 17-25.

Reimanis, I. and Kleebe, H. J., 2009, A Review on the Sintering and Microstructure Development of Transparent Spinel ($MgAl_2O_4$), *Journal of the American Ceramic Society*. 92(7): p. 1472-1480.

Rossi, R.C. and Fulrath, R.M., 1963, Epitaxial Growth of Spinel by Reaction in the Solid State, *Journal of the American Ceramic Society*. 46: p. 145–149.

Rozenburg, K., Reimanis, I. E., Kleebe, H. J. and Cook, R. L., 2008, Sintering kinetics of a $MgAl_2O_4$ spinel doped with LiF, *Journal of the American Ceramic Society*. 91(2): p. 444-450.

Sasamoto, T., Hara, H. and Sata, T., 1981, Mass-Spectrometric Study of the Vaporization of Magnesium-Oxide from Magnesium Aluminate Spinel, *Bulletin of the Chemical Society of Japan*. 54(11): p. 3327-3333.

Sato, E. and Carry, C., 1995, Effect of Powder Granulometry and Pretreatment on Sintering Behavior of Submicron-Grain Alpha-Alumina, *Journal of the European Ceramic Society*. 15(1): p. 9-16.

Sato, E. and Carry, C., 1996, Yttria Doping and Sintering of Submicrometer-Grained α-Alumina, *Journal of the American Ceramic Society.* 79(8): p. 2156-60.

Shao, W. Q., Chen, S. O., Li, D., Cao, H. S., Zhang, Y. C. and Zhang, S. S., 2008, Apparent activation energy for densification of alpha-Al_2O_3 powder at constant heating-rate sintering, *Bulletin of Materials Science*. 31(6): p. 903-906.

Shaw, N. J., 1989, Densification and Coarsening during Solid-State Sintering of Ceramics - A Review of the Models 1. Densification, *Powder Metallurgy International*. 21(3): p. 16-21.

Siao, C. Y., Lee, H. W. and Lu, H. Y., 2009, Kirkendall porosity in barium titanate-strontium titanate diffusion couple, *Ceramics International*. 35(7): p. 2951-2958.

Simchi, A., 2006b, Densification and Microstructural Evolution during Co-sintering of Ni-Base Superalloy Powders, *Metallurgical and Materials Transactions A*. 37A: p. 2549-2557.

Simchi, A., Rota, A. and Imgrund, P., 2006a, An investigation on the sintering behavior of 316L and 17-4PH stainless steel powders for graded composites, *Materials Science and Engineering a-Structural Materials Properties Microstructure and Processing*. 424(1-2): p. 282-289.

Smigelkas, A.D. and Kirkendall, E.O., 1947, Zinc diffusion in alpha brass, *The AIME Transactions* 171.

Srolovitz, D. J., Anderson, M. P., Sahni, P. S. and Grest, G. S., 1984, Computer-Simulation of Grain-Growth. 2. Grain-Size Distribution, Topology, and Local Dynamics, *Acta Metallurgica*. 32(5): p. 793-802.

Su, H. H. and Johnson, D. L., 1996, Master sintering curve: A practical approach to sintering, *Journal of the American Ceramic Society*. 79(12): p. 3211-3217.

Sumitomo Chemical, Co. Ltd., 2010, *Alumina*, http://www.sumitomo-chem.co.jp/english/products/index.html, (accessed March 15, 2010).

Sun, L., Sneller, A. and Kwon, P., 2008, Fabrication of alumina/zirconia functionally graded material: From optimization of processing parameters to phenomenological constitutive models, *Materials Science and Engineering a-Structural Materials Properties Microstructure and Processing*. 488(1-2): p. 31-38.

Teng, M.H., Lai, Y.C. and Chen, Y.T., 2002, A Computer Program of Master Sintering Curve Model to Accurately Predict Sintering Results, *Western Pacific Earth Sciences*. 2(2): p. 171-180.

Ting, C. J. and Lu, H. Y., 1999a, Hot-pressing of magnesium aluminate spinel - I. Kinetics and densification mechanism, *Acta Materialia*. 47(3): p. 817-830.

Ting, C. J. and Lu, H. Y., 1999b, Defect reactions and the controlling mechanism in the sintering of magnesium aluminate spinel, *Journal of the American Ceramic Society*. 82(4): p. 841-848.

Ting, C. J. and Lu, H. Y., 2000, Deterioration in the final-stage sintering of magnesium aluminate spinel, *Journal of the American Ceramic Society*. 83(7): p. 1592-1598.

Tosoh, Corporation, 2010, *Zirconia*, http://www.tosoh.com/Products/basic_grades.htm, (accessed March 12, 2010).

Tummala, R. R., 1988, Ceramics in Microelectronic Packaging, *American Ceramic Society Bulletin*. 67(4): p. 752-758.

Wang, C. J., Huang, C. Y. and Wu, Y. C., 2009, Two-step sintering of fine alumina-zirconia ceramics, *Ceramics International*. 35(4): p. 1467-1472.

Wang, J. D. and Raj, R., 1990, Estimate of the Activation Energies for Boundary Diffusion from Rate-Controlled Sintering of Pure Alumina, and Alumina Doped with Zirconia or Titania, *Journal of the American Ceramic Society*. 73(5): p. 1172-1175.

Wang, J. D. and Raj, R., 1991, Activation-Energy for the Sintering of Two-Phase Alumina Zirconia Ceramics, *Journal of the American Ceramic Society*. 74(8): p. 1959-1963.

Wang, X. H., Chen, P. L. and Chen, I. W., 2006a, Two-step sintering of ceramics with constant grain-size, I. Y_2O_3, *Journal of the American Ceramic Society*. 89(2): p. 431-437.

Wang, X. H., Deng, X. Y., Bai, H. L., Zhou, H., Qu, W. G., Li, L. T. and Chen, I. W., 2006b, Two-step sintering of ceramics with constant grain-size, II: $BaTiO_3$ and Ni-Cu-Zn ferrite, *Journal of the American Ceramic Society*. 89(2): p. 438-443.

Watson, E. B. and Price, J. D., 2002, Kinetics of the reaction $MgO+Al_2O_3$ -> $MgAl_2O_4$ and Al-Mg interdiffusion in spinel at 1200 to 2000 degrees C and 1.0 to 4.0 GPa, *Geochimica Et Cosmochimica Acta*. 66(12): p. 2123-2138.

Whitney, W. P. and Stubican, V. S., 1971, Interdiffusion in System $MgO-MgAl_2O_4$, *Journal of the American Ceramic Society*. 54(7): p. 349-&.

Yangyun, S. and Brook, R. J., 1985, Preparation of Zirconia-Toughened Ceramics by Reaction Sintering, *Science of Sintering*. 17(1): p. 35-47.

Young, W. S. and Cutler, I. B., 1970, Initial Sintering with Constant Rates of Heating, *Journal of The American Ceramic Society*. 53(12): p. 659-663.

Zhang, P., Debroy, T. and Seetharaman, S., 1996, Interdiffusion in the $MgO-Al_2O_3$ spinel with or without some dopants, *Metallurgical and Materials Transactions a-Physical Metallurgy and Materials Science*. 27(8): p. 2105-2114.

Sintering, Co-Sintering and Microstructure Control Of Oxide Based Materials : Zirconia, Alumina, Spinel, Alumina - Zirconia and Spinel - Alumina

Abstract: Densification and microstructural evolution during co-sintering of alumina (Al_2O_3) – zirconia (Y-ZrO_2) and alumina – spinel ($MgAl_2O_4$) co-pressed bi-materials were investigated. Before co-sintering studies of bi-materials, sintering behaviors of the submicron powders of alumina, spinel and zirconia were studied separately by vertical dilatometer. The effects of precoarsening and two-step sintering treatments on the densification and microstructure of spinel ceramics were also investigated. The interface layer development between alumina and spinel during thermal treatment in 1400-1500°C temperature range were carefully investigated. Crack-free bonds were observed in alumina – spinel bi-materials after compaction by UP+CIP. A spinel interlayer with columnar grains was observed. Growth of this interlayer from spinel toward alumina was found to follow parabolic kinetics. Diffusion couple tests produced the same columnar spinel grains at the interface with the same kinetics as in co-sintering experiments.

Key words : spinel, alumina, zirconia, precoarsening, two-step sintering, co-pressing, co-sintering, interface microstructure, activation energy

Frittage, cofrittage et maîtrise des microstructures de matériaux à base d'oxydes : zircone, alumine, spinelle, alumine-zircone, spinelle-alumine

Résumé : La densification et l'évolution microstructurale de bimatériaux copréssés alumine (Al_2O_3) – zircone (Y-ZrO_2) and alumine – spinelle ($MgAl_2O_4$) ont été étudiées. Avant les études de co-frittage, les comportements en frittage des poudres submicroniques d'alumine, de spinelle et de zircone mises en œuvre ont été étudiés par dilatométrie verticale Les effets de traitements de pré coalescence et de frittage en deux étapes sur la densification et la microstructure des céramiques spinelle ont été caractérisés. Le développement de couches interfaciales entre la spinelle et l'alumine a été étudié lors de traitements thermiques dans la gamme de température 1400-1500°C. Des liaisons sans fissures ont été observées dans des bimatériaux spinelle – alumine mis en forme par UP + CIP. Une intercouche de grains colonnaires de spinelle a été mise en évidence. Il a été montré que la croissance de cette intercouche à partir de la partie spinelle au détriment de la partie alumine suivait une loi cinétique parabolique. Les essais de couples de diffusion de matériaux prédensifiés ont montrés le développement de grains colonnaires de spinelle avec la même cinétique que dans les bimatériaux cofrittés.

Mots clés : spinelle, alumine, zircone, précoalescence, frittage en deux étapes, co-pressage, co-frittage, microstructure d'interface, énergie d'activation